

# The 1-D Lyman alpha power spectrum from eBOSS and DESI EDR data sets

Thesis by  
Holman Daniel Quintero Salazar

In Partial Fulfillment of the Requirements for the  
Degree of  
Master of Science in Astrophysics



Adviser  
PhD. Alma Xóchitl González-Morales

Co-adviser  
PhD. César Augusto Caretta

UNIVERSIDAD DE GUANAJUATO  
Guanajuato, Guanajuato

2024  
Defended February



## CONTENTS

Contents	iii
Agradecimientos	iv
Abstract	v
Resumen	vi
Nomenclature	vii
List of Figures	viii
List of Tables	xi
<b>Chapter I: Introduction</b>	1
<b>Chapter II: Cosmology background</b>	3
2.1 Brief historical review	3
2.2 The standard model	12
2.3 Structure formation	24
2.4 Matter power spectrum	28
<b>Chapter III: The Lyman-<math>\alpha</math> forests and the flux power spectrum</b>	36
3.1 Active galactic nuclei	36
3.2 The intergalactic medium	40
3.3 Lyman- $\alpha$ forests	42
3.4 The one-dimensional flux power spectrum	53
<b>Chapter IV: Sample description and <math>P_{\text{FID}}</math> computation</b>	63
4.1 Quasar catalogs	63
4.2 Sample extraction	70
4.3 $P_{\text{FID}}$ computation pipeline description	75
<b>Chapter V: Results</b>	85
5.1 $P_{\text{FID}}$ from eBOSS	85
5.2 $P_{\text{FID}}$ from DESI	92
<b>Chapter VI: Discussion and general conclusions</b>	99
References	101
<b>Appendix A: Addendum on cosmology</b>	113
A.1 $\Lambda$ CDM parameters	113
A.2 Warm dark matter	117
A.3 $\Lambda$ CDM $_{\nu}$	118
<b>Appendix B: Instruments description</b>	121
B.1 The extended Baryon Oscillation Spectroscopic Survey (eBOSS)	121
B.2 The Dark Energy Spectroscopic Instrument (DESI)	124
Declaration	130

## AGRADECIMIENTOS

Desearía comenzar agradeciendo a la persona que me ha apoyado de manera incondicional a lo largo de mi vida y a quien dedico este trabajo con el más profundo cariño: mi madre, todo el júbilo sea para ella. Del mismo modo, quisiera hacer mención de aquellos miembros de mi familia cuyo consejo y apoyo han sido fundamentales en mi desarrollo.

Quisiera agradecer a mi directora de tesis, la Dra. Alma González, por su orientación, paciencia, dedicación y, sobre todo, por haberme brindado la oportunidad de trabajar en esta área y expandir mis horizontes académicos. De igual manera, quiero expresar mi gratitud al Dr. César Caretta por su colaboración y acompañamiento a lo largo de este trabajo, así como por las herramientas técnicas y académicas que me proporcionó durante mi estancia de posgrado.

Igualmente, deseo brindar un sentido agradecimiento al Instituto CONAHCYT y al gobierno mexicano por la beca de posgrado que recibí durante mi periodo de maestría, apoyo sin el cual la realización de este proyecto no sería posible. Agradezco también a todos los profesores que compartieron sus conocimientos y experiencias durante mi formación académica en la Universidad de Guanajuato.

Asimismo, quiero dar las gracias a mi comité sinodal, cuyas sugerencias, comentarios y discusiones mejoraron la calidad de este escrito de gran manera. Quisiera hacer especial hincapié en el Dr. Corentin Ravoux, cuyo acompañamiento fue clave en el desarrollo de este proyecto.

Finalmente, no podría dejar de mencionar a mis compañeros de generación y amigos de los departamentos de astronomía y física, quienes me brindaron su apoyo, comprensión y ánimo en momentos de regocijo como de desaliento.

A todas estas personas, y a aquellas que, aunque no mencionadas, contribuyeron de alguna manera en este proyecto, les expreso mi más sincero agradecimiento.



## ABSTRACT

When the light of distant quasars passes through the intergalactic medium (IGM) (mainly composed by primordial hydrogen) it undergoes gradual absorption as it travels through the cosmic web. This absorption produces a flux decrement in the region bluewards  $\sim 1216 \text{ \AA}$  (at rest), as a product of the Ly- $\alpha$  resonance line transition *i.e.* the Ly- $\alpha$  forests. Ly- $\alpha$  forests are especially valuable to constrain cosmological models and to unveil the evolution and properties of the IGM due to the range of scales they cover ( $\sim 0.5 - 50 h^{-1} \text{ Mpc}$ ), being the one-dimensional flux power spectrum ( $P_{\text{FID}}$ ) one of the most important probes linked to this pattern of absorption lines. This work presents the recomputation of the  $P_{\text{FID}}$  based on SDSS-IV/eBOSS (DR14 & DR16) and DESI (EDR) quasars, considering the influence of three particular systematics: broad absorption line (BAL) quasars, damped Ly- $\alpha$  absorption (DLA) systems and skylines. I used `picca`, a software written in Python and designed to obtain cosmological correlation patterns out of the IGM. Satisfactorily, it was possible to re-process eBOSS data, from publicly available data and code, getting reasonably comparable  $P_{\text{FID}}$  results to those obtained by [Chabanier et al. \(2019b\)](#). In the same way, the estimation of  $P_{\text{FID}}$  based on eBOSS DR16 was made, obtaining consistent results with those obtained from DR14. Likewise, the  $P_{\text{FID}}$  from the initial public data release of DESI was estimated, achieving an improvement in resolution at smaller scales, also getting consistent results compared with those obtained by [Ravoux et al. \(2023\)](#). Finally, the evaluation of the systematics was carried out for the three samples showing a great influence of BALs and DLAs at large scales, and a contribution of skylines at  $z = 3.6 - 3.8$ . The results are consistent enough to refine them and couple with hydrodynamical simulations and other cosmological probes to make relevant inferences to the area.

## RESUMEN

Cuando la luz de los cuásares distantes pasa a través del medio intergaláctico (IGM: *Intergalactic Medium*) (compuesto principalmente por hidrógeno primordial) sufre una absorción gradual a medida que viaja a través de la red cósmica. Esta absorción produce una disminución de flujo en la región hacia el azul de los  $\sim 1216 \text{ \AA}$  (en reposo), como producto de la transición de la línea de resonancia Ly- $\alpha$  *i.e.* los bosques Ly- $\alpha$ . Los bosques Ly- $\alpha$  son especialmente valiosos para restringir modelos cosmológicos y revelar la evolución y las propiedades del IGM debido al rango de escalas que cubren ( $\sim 0.5 - 50 h^{-1} \text{ Mpc}$ ), siendo el espectro de potencia de flujo unidimensional ( $P_{\text{F1D}}$ ) uno de los observables más importantes vinculados a este patrón de líneas de absorción. Este trabajo presenta el recálculo del  $P_{\text{F1D}}$  a partir de cuásares provenientes de los SDSS-IV/eBOSS DR14 y DR16 y el DESI EDR, considerando la influencia de tres sistemáticos particulares: cuásares BAL (*broad absorption line*), sistemas DLA (*Damped Ly- $\alpha$* ) y líneas de cielo. Se usó *picca*, un software escrito en Python y diseñado para obtener patrones de correlación cosmológica a partir del IGM. De manera satisfactoria, fue posible reprocesar los datos de eBOSS a partir de datos y códigos disponibles al público, obteniendo resultados razonablemente comparables a los obtenidos por [Chabanier et al. \(2019b\)](#). De la misma manera, se realizó la estimación de  $P_{\text{F1D}}$  con base en eBOSS DR16, obteniendo resultados consistentes con los obtenidos a partir de DR14. Igualmente, se estimó el  $P_{\text{F1D}}$  a partir de los primeros datos públicos de DESI, logrando una mejora en resolución a pequeñas escalas, obteniendo también resultados consistentes en comparación con los obtenidos por [Ravoux et al. \(2023\)](#). Finalmente, se llevó a cabo la evaluación de los sistemáticos para las tres muestras mostrando una gran influencia de BALs y DLAs a gran escala, y una contribución de las líneas de cielo a  $z = 3.6 - 3.8$ . Los resultados son lo suficientemente consistentes como para refinarlos y combinarlos con simulaciones hidrodinámicas y otros observables cosmológicos con tal de hacer inferencias relevantes para el área.

## NOMENCLATURE

- $z$ .** Spectroscopic redshift.
- AGN.** Active Galactic Nucleus.
- BAL.** Broad Absorption Line quasar.
- CMB.** Cosmic Microwave Background.
- DESI.** The Dark Energy Spectroscopic Instrument.
- DLA.** Damped Ly- $\alpha$  Absorber system.
- DR.** Data Release.
- eBOSS.** The extended Baryon Oscillation Spectroscopic Survey.
- EDR.** Early Data Release.
- EFEs.** Einstein's field equations.
- FGPA.** Fluctuating Gunn-Peterson Approximation.
- FLRW.** Friedmann-Lemaître-Robertson-Walker.
- GR.** General relativity.
- HI.** Neutral Hydrogen.
- IGM.** Intergalactic Medium.
- LSS.** Large Scale Structure.
- Ly- $\alpha$ .** Lyman alpha line transition.
- $P_{F1D}$ .** One-dimensional flux power spectrum.
- $P_{F3D}$ .** Three-dimensional flux power spectrum.
- $P_m$ .** Matter power spectrum.
- picca.** Package for Igm Cosmological-Correlations Analyses.
- QSO.** Quasi-Stellar Objects.
- SDSS.** Sloan Digital Sky Survey.
- SNR.** Signal-to-noise ratio.

## LIST OF FIGURES

<i>Number</i>	<i>Page</i>
2.1 Original distance-velocity Hubble diagram. . . . .	4
2.2 CMB blackbody spectrum measured by COBE satellite. . . . .	5
2.3 Rotation curves for several spiral galaxies. . . . .	6
2.4 Matter content in the Bullet cluster. . . . .	7
2.5 Hubble-Lemaître diagram - accelerated expansion . . . . .	8
2.6 Dark matter possible candidates . . . . .	9
2.7 Comparison between simulations and observations at large scales. . .	14
2.8 Density parameter over time . . . . .	19
2.9 Timeline of the evolution of the Universe . . . . .	23
2.10 Spatial correlation function . . . . .	29
2.11 Theoretical 3D linear matter power spectrum . . . . .	31
2.12 The 3D linear matter power spectrum at $z = 0$ . . . . .	33
2.13 CMB temperature anisotropy map. . . . .	35
3.1 AGN schematic representation . . . . .	38
3.2 Quasar spectrum . . . . .	39
3.3 Thermal history of the IGM. . . . .	41
3.4 Ly- $\alpha$ forest detail . . . . .	45
3.5 First Ly- $\alpha$ forest ever observed . . . . .	48
3.6 Gunn-Peterson trough at $z \sim 6$ . . . . .	48
3.7 BAL quasar spectrum . . . . .	50
3.8 DLA system in a quasar spectrum . . . . .	51
3.9 Metals systems in a quasar spectrum . . . . .	52
3.10 Hydrodynamical simulations of the IGM. . . . .	54
3.11 Flux power spectrum at different redshifts . . . . .	56
3.12 Matter power spectrum recovered from Ly- $\alpha$ forests . . . . .	57
3.13 One-dimensional flux power spectrum out of eBOSS DR14 . . . . .	59
3.14 One-dimensional flux power spectrum out DESI EDR + two months .	60
3.15 $P_{\text{FID}}$ measurements at different resolutions . . . . .	62
4.1 eBOSS quasar records over time . . . . .	64
4.2 eBOSS catalogs statistics . . . . .	66

4.3	Number of targets in DESI SV . . . . .	67
4.4	DESI EDR redshift distribution and BAL proportion . . . . .	69
4.5	eBOSS-DESI spectra comparison . . . . .	69
4.6	Statistics of DR14Q sample . . . . .	72
4.7	Statistics of DR16Q sample . . . . .	72
4.8	Sky projection of DR14Q sample . . . . .	73
4.9	Sky projection of DR16Q sample . . . . .	73
4.10	Statistics of DESI sample . . . . .	74
4.11	Sky projection of DESI sample . . . . .	74
4.12	BAL and DLAs proportion in eBOSS and DESI samples as function of $z$ bins. . . . .	75
4.13	$P_{\text{FID}}$ computation pipeline . . . . .	76
4.14	Quasar continuum fitting . . . . .	77
4.15	DLA correction . . . . .	79
4.16	Skylines in eBOSS . . . . .	80
4.17	Skylines in DESI . . . . .	80
4.18	General $P_{\text{FID}}$ computation pipeline . . . . .	84
5.1	$P_{\text{FID}}$ from the DR14 sample . . . . .	85
5.2	$P_{\text{FID}}$ eBOSS DR14 literature comparison . . . . .	87
5.3	Rejection stats in eBOSS . . . . .	88
5.4	$P_{\text{FID}}$ eBOSS DR14 results and DR16 results comparison. . . . .	89
5.5	$P_{\text{FID}}$ eBOSS DR14 systematics ratio . . . . .	90
5.6	$P_{\text{FID}}$ eBOSS DR6 systematics ratio . . . . .	91
5.7	$P_{\text{FID}}$ DESI EDR literature comparison . . . . .	94
5.8	$P_{\text{FID}}$ DESI EDR literature comparison (velocity units and $2.1 < z \lesssim 3.1$ ) . . . . .	95
5.9	$P_{\text{FID}}$ DESI EDR literature comparison (velocity units and $3.1 < z \lesssim 3.9$ ) . . . . .	96
5.10	Mean SNR and resolution of the forests in the three samples . . . . .	97
5.11	$P_{\text{FID}}$ DESI EDR systematics ratio . . . . .	98
A.1	Hubble tension . . . . .	114
A.2	Warm Dark Matter power spectrum . . . . .	118
A.3	Influence of neutrino bounds on the matter power spectrum . . . . .	119
B.1	BOSS spectrograph . . . . .	122
B.2	Sloan telescope . . . . .	123
B.3	eBOSS plates . . . . .	124
B.4	Mayall telescope internal structure . . . . .	125
B.5	Mayall telescope configuration . . . . .	126

B.6	DESI spectrograph . . . . .	127
B.7	DESI focal plane system . . . . .	128

## LIST OF TABLES

<i>Number</i>	<i>Page</i>
2.1 Solution of the Friedmann equations for different species. . . . .	17
2.2 Timeline of the evolution of the Universe . . . . .	23
3.1 IGM redshift-temperature evolution since recombination. . . . .	42
3.2 HI Lyman series lines. . . . .	43
3.3 Quasar absorption line system properties . . . . .	51
3.4 Astrophysical and cosmological parameters obtained from eBOSS Ly- $\alpha$ forests . . . . .	59
4.1 Subcatalog construction query attributes (eBOSS) . . . . .	70
4.2 Subcatalog construction query attributes (DESI) . . . . .	71
B.1 DESI CCD cameras resolution. . . . .	125

## Chapter 1

# INTRODUCTION

Cosmology is a captivating and interdisciplinary field at the intersection of physics and astronomy which principal focus is to unravel the origin and evolution of the Universe as a whole. With the significant improvements in theoretical research in the last century and the notorious technological advances during the last decades, including the improvement of observation techniques and the colossal amount of data collected by recent sky surveys, cosmology emerges today as a vibrant science full of open research fields and problems to solve *e.g.* the nature the dark matter, the nature of dark energy, the Hubble tension, the  $S_8$  tension, structure formation inconsistencies at small scales, etc.

Several probes have been proving highly useful for calibrating cosmological models and addressing outstanding problems and unsolved questions, including the cosmic microwave background, galaxy surveys, cosmic shear (weak lensing), gravitational waves, 21-cm radio astronomy, among many others (Reid et al., 2010; Pritchard and Loeb, 2012; Ezquiaga and Zumalacárregui, 2018; Troxel et al., 2018; Di Valentino et al., 2021; Francfort, 2022; Perivolaropoulos and Skara, 2022). Among these observables there is one of particular relevance for small scales, that is, the Lyman- $\alpha$  (Ly- $\alpha$ ) forests, a pattern of absorption lines in the spectrum of distant quasars (Rauch, 1998; Berk et al., 2001; Meiksin, 2009).

Since its discovery in the early seventies (Lynds, 1971) (and subsequent justification by Sargent et al. (1980)), Ly- $\alpha$  forests have been very useful in observational cosmology given their sensitivity to study the structure of uncollapsed baryonic matter at scales of  $\sim 0.5 - 50 h^{-1}$  Mpc, and the properties of the intergalactic medium (IGM) *i.e.* gas between galaxies, such as temperature and column density of HI (neutral hydrogen) at different redshifts, *i.e.* different values of cosmic time. The study of Ly- $\alpha$  forests has recently become a remarkable way to constrain cosmological models and study the properties of the IGM (Weinberg et al., 2003; Seljak et al., 2006; Meiksin, 2009; Palanque-Delabrouille et al., 2013; McQuinn, 2016; Arinyo-i Prats et al., 2015; Chabanier et al., 2019b; Walther et al., 2019; Zavarygin and Webb, 2019; Bourboux et al., 2020; Ravoux et al., 2020; Qin et al., 2021; Youles, 2021; Villasenor et al., 2023; Gerardi et al., 2023; Goldstein et al., 2023; Moon et al., 2023).



The modern conception of Ly- $\alpha$  forests suggests that these absorption features are produced by the interaction of the light of the quasar with baryonic matter, which follows the gravitational potentials modeled by the dark matter backbone. Given that the optical depth of these absorptions is highly dependant of many high non-linear physical processes, it is quite useful to take this flux fluctuation field into Fourier space, this in order to constrain models of structure formation and the properties of the IGM. The result of this procedure is called the one-dimensional flux power spectrum, or  $P_{\text{F1D}}$  for simplicity. The measurement of the  $P_{\text{F1D}}$  has been made for almost two decades with different instruments and spectral resolution power (Croft et al., 1997, 1998; McDonald et al., 2000; Croft et al., 2002; Jamkhedkar et al., 2003; Kim et al., 2004; Zhan et al., 2005; McDonald et al., 2006; Palanque-Delabrouille et al., 2013; Walther et al., 2017; Irsic et al., 2017; Walther et al., 2019; Chabanier et al., 2019b; Karaçaylı et al., 2020, 2022, 2023; Ravoux et al., 2023; Villaseñor et al., 2022; Mishra and Gnedin, 2022), providing relevant information about the nature of dark matter and valuable hints on the history of the IGM.

The main objective of this thesis is to re-compute the  $P_{\text{F1D}}$  calculation made by Chabanier et al. (2019b) using Ly- $\alpha$  forests of quasars from the Data Releases (DR) 14 and 16 of SDSS-IV/eBOSS. In the same way, DESI Early Data Release (EDR) spectra was used to compute the  $P_{\text{F1D}}$  with the aim of reproducing the results obtained by Ravoux et al. (2023) (the most recent  $P_{\text{F1D}}$  measurement using a FFT estimator). Furthermore, the analysis of statistical contrasts and the influence of the intervening variables, like BAL quasars, DLA systems and skyline corrections, on the results of the three samples is presented.

Thus, chapters 2 and 3 are aimed to give the reader a brief description of the main ideas of modern cosmology and some important properties of the Universe at the largest scales in the context of the IGM and the  $\Lambda$ CDM model. Many features of the current paradigm are supported by well-established theoretical concepts and key observations that have to be cited to take a whole panorama of the issue. Chapter 4 is intended to give a description of the scientific scope, the data sets used, and the methodology applied in the computation of the  $P_{\text{F1D}}$ . Chapters 5 and 6 present the obtained results, the discussion based on previous/similar works, and general conclusions. Finally, appendix A and B serve as support for the discussion of the cosmological model and the instruments referred in the main chapters.

## COSMOLOGY BACKGROUND

### 2.1 Brief historical review

The theoretical foundation of modern cosmology was provided by the theory of general relativity (GR), developed between 1915 and 1917 by Albert Einstein ([Einstein, 1917](#)), and many significant contributors including David Hilbert, Henri Poincaré, Marcel Grossman, Karl Schwarzschild, among others. In turn, the first cosmological models developed within the framework of GR emerged in the 1920s, primarily through the works of Albert Einstein, Alexander Friedmann, Georges Lemaître and Willem de Sitter. Independently, Friedmann and Lemaître developed the theoretical background of a homogeneous, isotropic, and non-static Universe ([Friedman, 1922](#); [Friedmann, 1924](#); [Lemaître, 1927](#)). Around the same years, Lemaître proposed that an expanding universe would have to go back in time to a single point of origin, the so-called "primitive atom" or the Big Bang singularity. Lemaître found observational evidences of this expansion, but his publications on the topic were only rescued recently<sup>1</sup>.

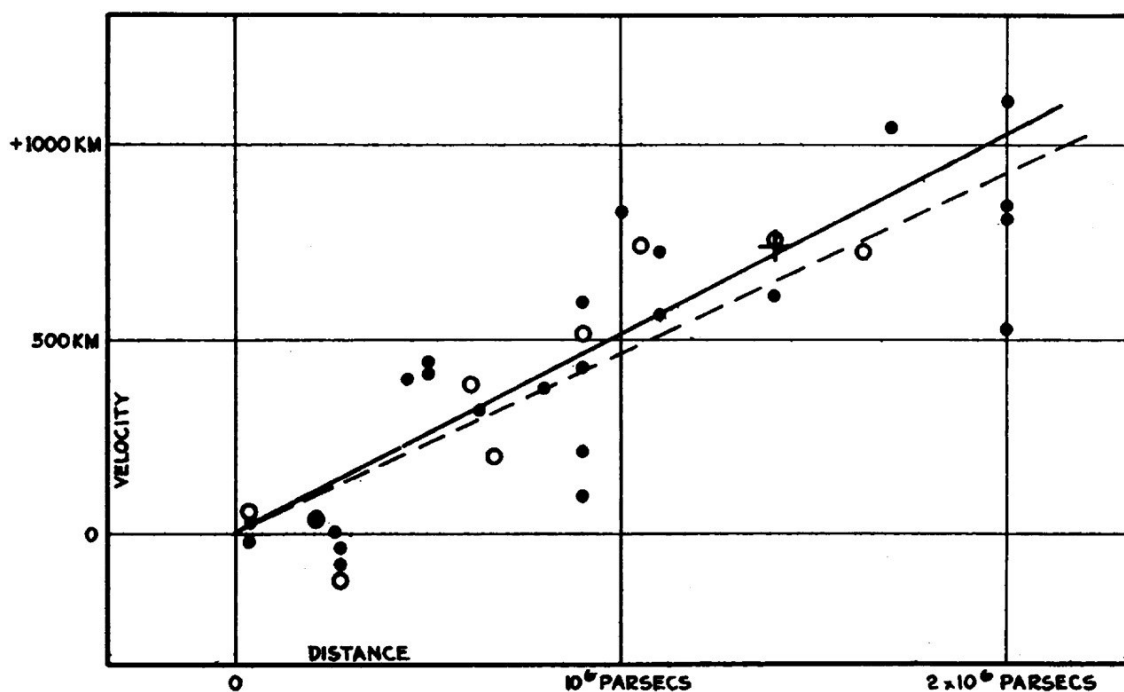
Later in 1929, Edwin Hubble presented the famous empirical law about the recession of galaxies, a fact that confirmed and popularized the idea of the existence of an expanding Universe ([Hubble, 1929](#)). The Hubble-Lemaître law<sup>2</sup> states that the speed of a distant galaxy (today understood as the product of the expansion of the Universe only, neglecting local gravitational effects) is proportional to its distance multiplied by a constant. That is

$$v = H_0 r . \tag{2.1}$$

Figure [2.1](#) exhibits one of the first measurements (by Hubble) showing the linear relationship of equation [\(2.1\)](#).

<sup>1</sup>See the [IAU Resolution B4](#) voted at the XXXth General Assembly.

<sup>2</sup>In 2018 the General Assembly of the International Astronomical Union (IAU) proposed the renaming of this law for historical reasons ([Kragh, 2018](#)) in the way that Georges Lemaître had to be cited for his important contributions.



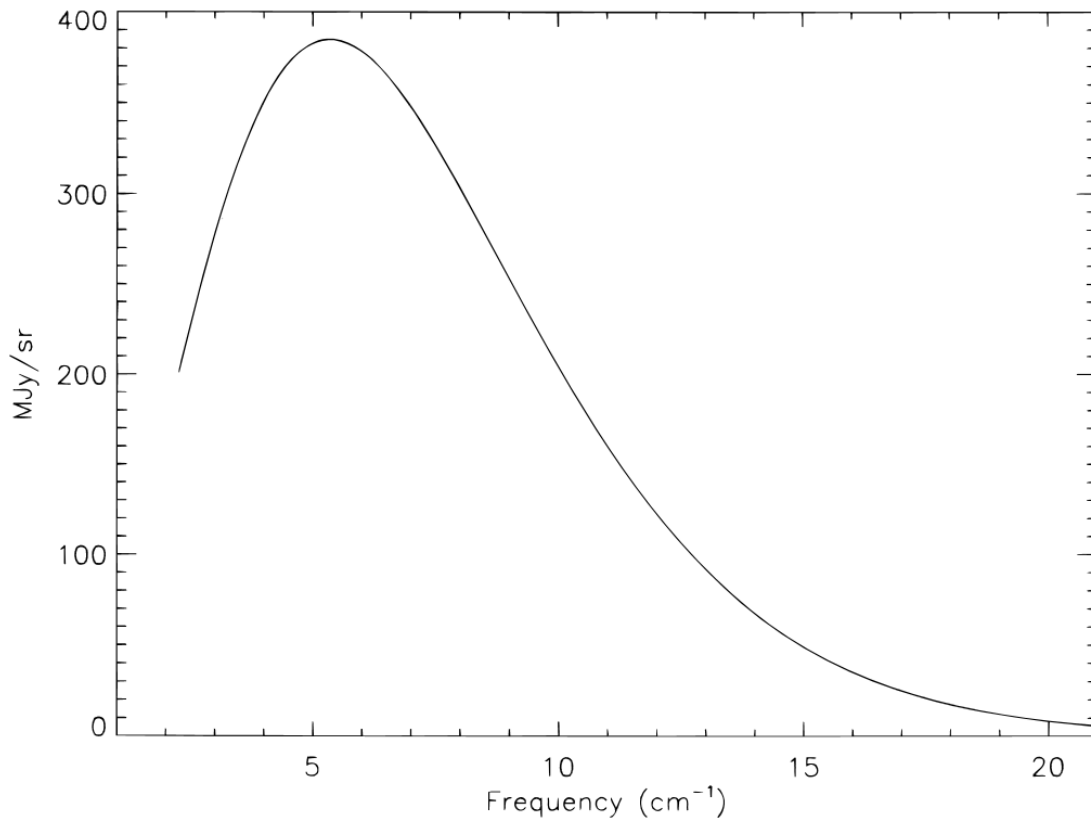
Source: Hubble (1929)

**Figure 2.1:** Nearby galaxies distance-velocity relation found by Hubble from measuring the period-luminosity (P-L) relation out of one kind of Cepheid variable stars. The constant of proportionality in the relation  $v \propto r$  is  $H_0$ , a.k.a the Hubble constant, the rate of the expansion of the Universe.

Years later, Howard P. Robertson (Robertson, 1935, 1936a,b) and Arthur Geoffrey Walker (Walker, 1937) contributed to developing what is known today as the Friedmann-Lemaître-Robertson-Walker (FLRW) metric, the formal mathematical framework that supports modern cosmology.

After that, in the 40s decade, George Gamow, Ralph Alpher, and Hans Bethe published the renowned  $\alpha$ - $\beta$ - $\gamma$  paper where they proposed the idea of a hot and dense thermonuclear primitive Universe capable of generating the entirety of elements of the periodic table (Gamow, 1946; Alpher et al., 1948). Despite this idea being theoretically imprecise (because just the lightest elements could have been formed in such conditions), the foundation for an isotropic and archaic cosmic radiation background was put on the table<sup>3</sup>. In this order of ideas, A. A. Penzias and R. W. Wilson discovered the smooth Cosmic Microwave Background (CMB) in the 60s (an almost perfect black body measurement) (Penzias and Wilson, 1965).

<sup>3</sup>See figures 2.2 and 2.13a for reference.



Source: [Fixsen et al. \(1996\)](#)

**Figure 2.2:** Measurement of the isotropic blackbody spectrum ( $T = 2.728 \pm 0004$  K) of the CMB made by the FIRAS instrument on board of the COBE satellite. Uncertainties are a small fraction of the fit line thickness, making this observation one of the best measurements of a blackbody spectrum ever made.

The Hubble-Lemaître law, the CMB, and the primordial nucleosynthesis (the cosmic origin of a significant fraction of helium, deuterium, tritium, lithium and beryllium) are the three main pieces of observational evidence for a Hot Big Bang Universe. In general terms, the cosmological model that fits on this observations is the so-called standard cosmological model, a model that encompasses a gravitational framework based on GR, the cosmological principle (homogeneity and isotropy) and the perfect fluid model (continuity equation) for the contents of the Universe. Although this cosmological framework is well established by observations and theory, it has several nuances that the model itself can not cover like those mentioned below.

Virialized systems like galaxy clusters ([Zwicky, 1933](#); [Battaner and Florido, 2000](#);

Dekel et al., 2005), flat rotation curves of spiral galaxies (see Figure 2.3; Rubin and Ford Jr, 1970; Battaner and Florido, 2000; Zasov et al., 2017) and structure formation in N-body/hydrodynamical simulations (cosmic evolution rates) (see Figure 2.7; Springel et al., 2005; Boylan-Kolchin et al., 2009; Vogelsberger et al., 2014; Fazio et al., 2018; Chacón et al., 2020), among other indirect evidence (like gravitational lensing, see Figure 2.4) suggest that there is a lack of luminous/baryonic matter in the Universe. This apparent absence of matter is understood as a gravitational-only interacting type of (possibly) non-baryonic<sup>4</sup> matter called dark matter. Simulations and observations of the Large Scale Structure (LSS) (Einasto, 2009) point towards two possible models as candidates for dark matter: CDM (Cold Dark Matter, non-relativistic, leading to a structure formation occurring bottom-up; Jenkins et al., 1998) and WDM (Warm Dark Matter, moderately relativistic, with an associated free-streaming scale<sup>5</sup>; Lovell et al., 2012).

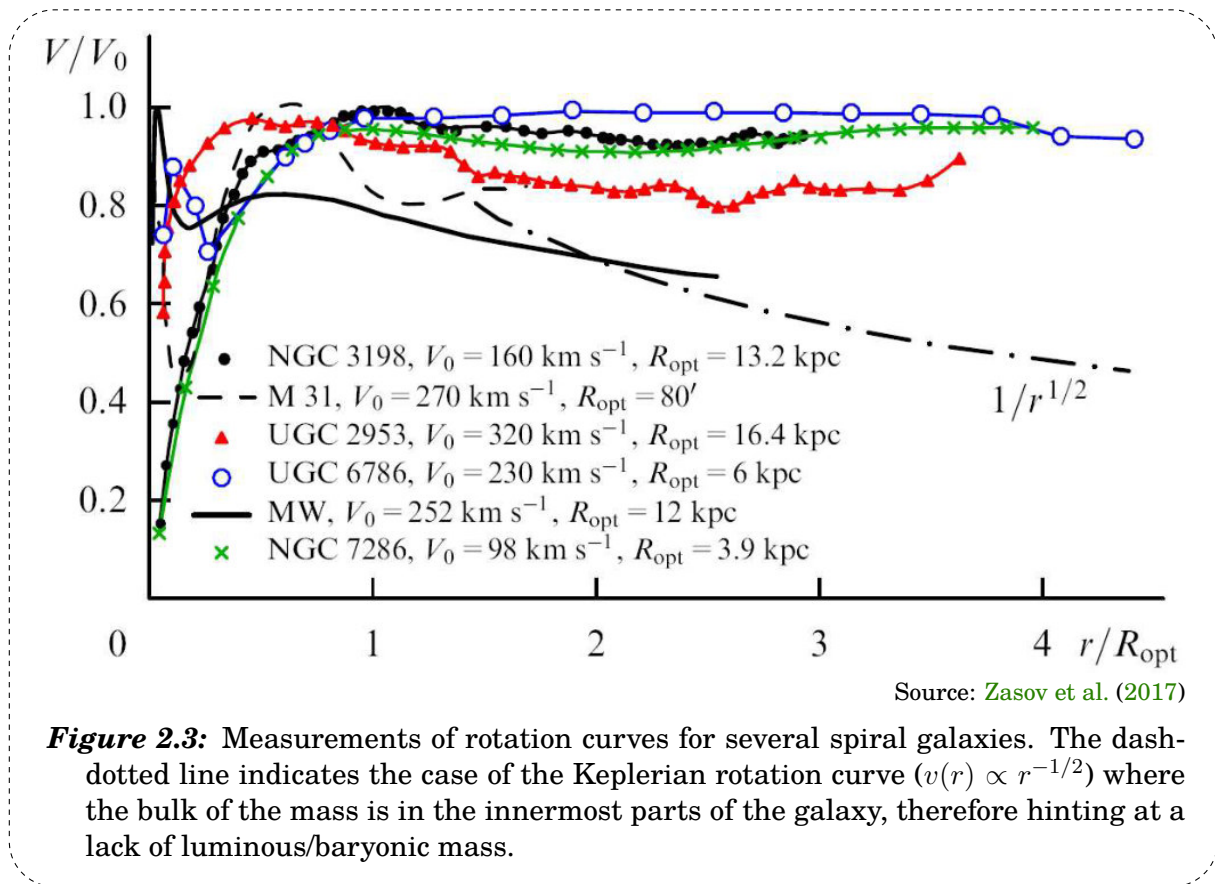
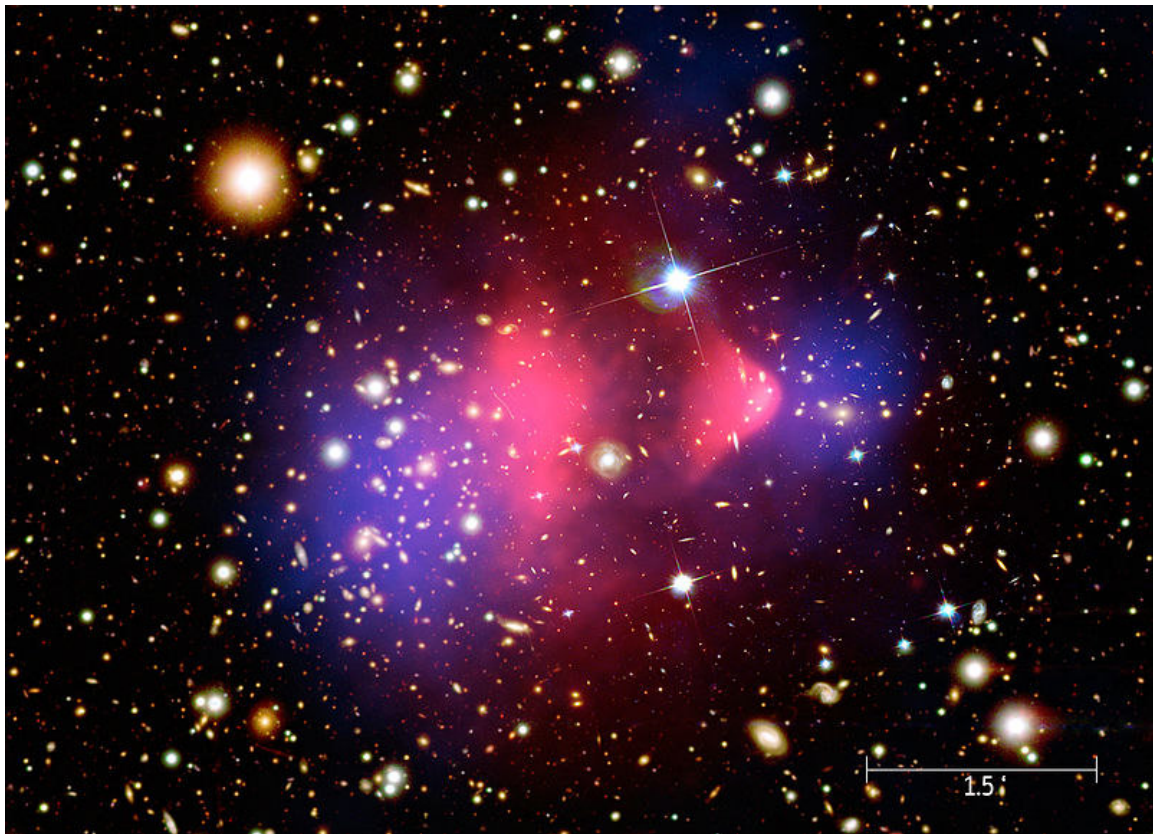


**Figure 2.3:** Measurements of rotation curves for several spiral galaxies. The dash-dotted line indicates the case of the Keplerian rotation curve ( $v(r) \propto r^{-1/2}$ ) where the bulk of the mass is in the innermost parts of the galaxy, therefore hinting at a lack of luminous/baryonic mass.

<sup>4</sup>Non-baryonic, cold/warm, dissipationless and collisionless.

<sup>5</sup>See appendix A





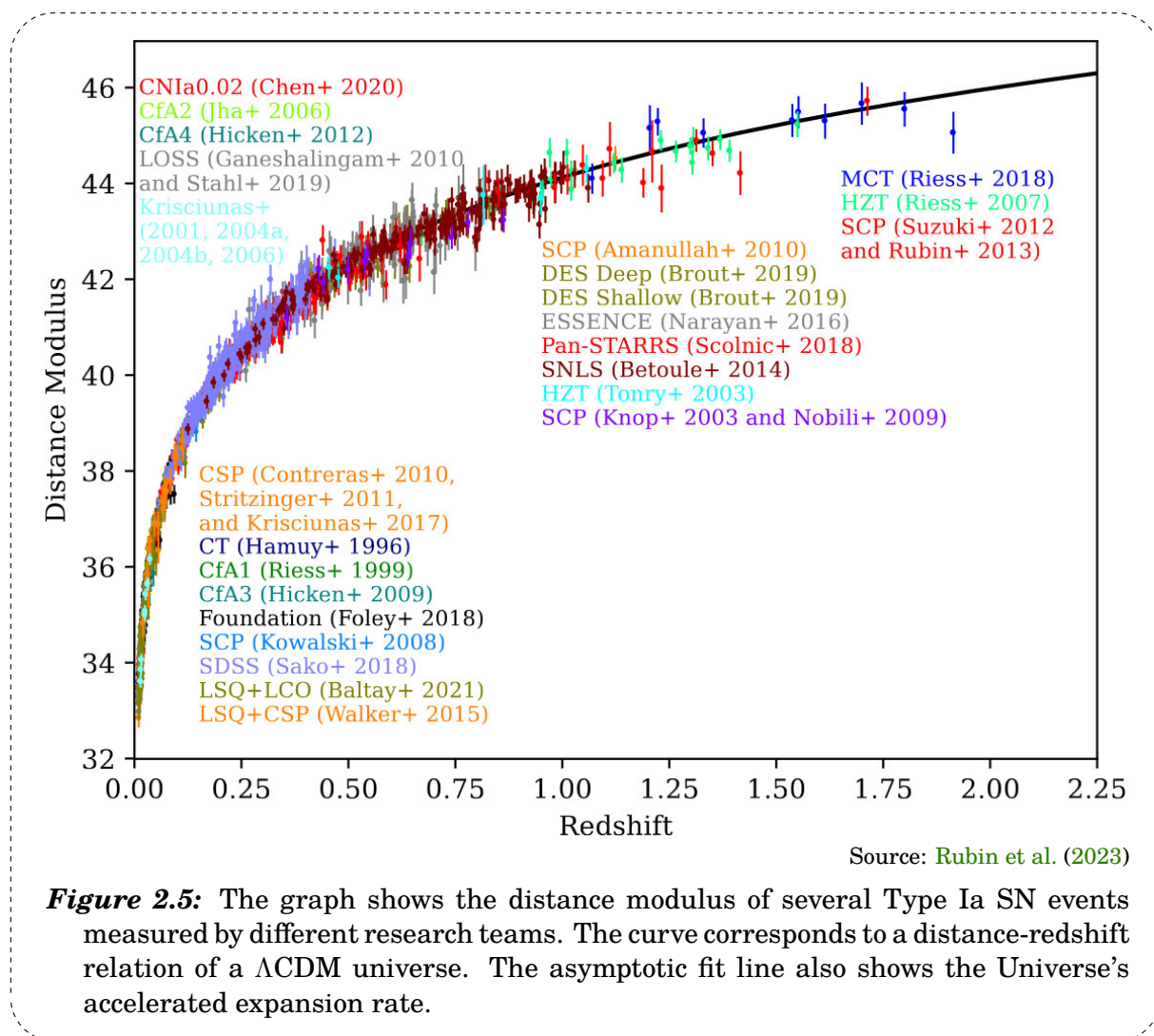
Source: CHANDRA X-Ray Observatory (2006)

**Figure 2.4:** An image overlay showing the dynamic components of the Bullet cluster (1E 0657-56). The visible light image shows the galaxies, in red/pink the ionized gas mapped with X-rays and, in blue, the distribution of dark matter reconstructed from gravitational lensing. The spatial offset of the center of the total mass from the center of the baryonic mass peaks (the gas lags behind) is a strong indication of a collisionless and non-baryonic kind of matter causing the gravitational potential wells of the cluster.

In addition, measurements of the current Universe expansion rate (the Hubble constant  $H_0$ ) in the 90s decade, using very far away Type Ia supernovae events as standard candles, showed that the Universe is not only expanding but that it is expanding at an accelerated rate (Riess et al., 1998; Perlmutter et al., 1999). Figure 2.5 shows a recent measurement of this observable featuring the behaviour mentioned before.

This outstanding result is supposed to be a consequence of the permeating presence of a mysterious and unknown type of substance called dark energy that produces

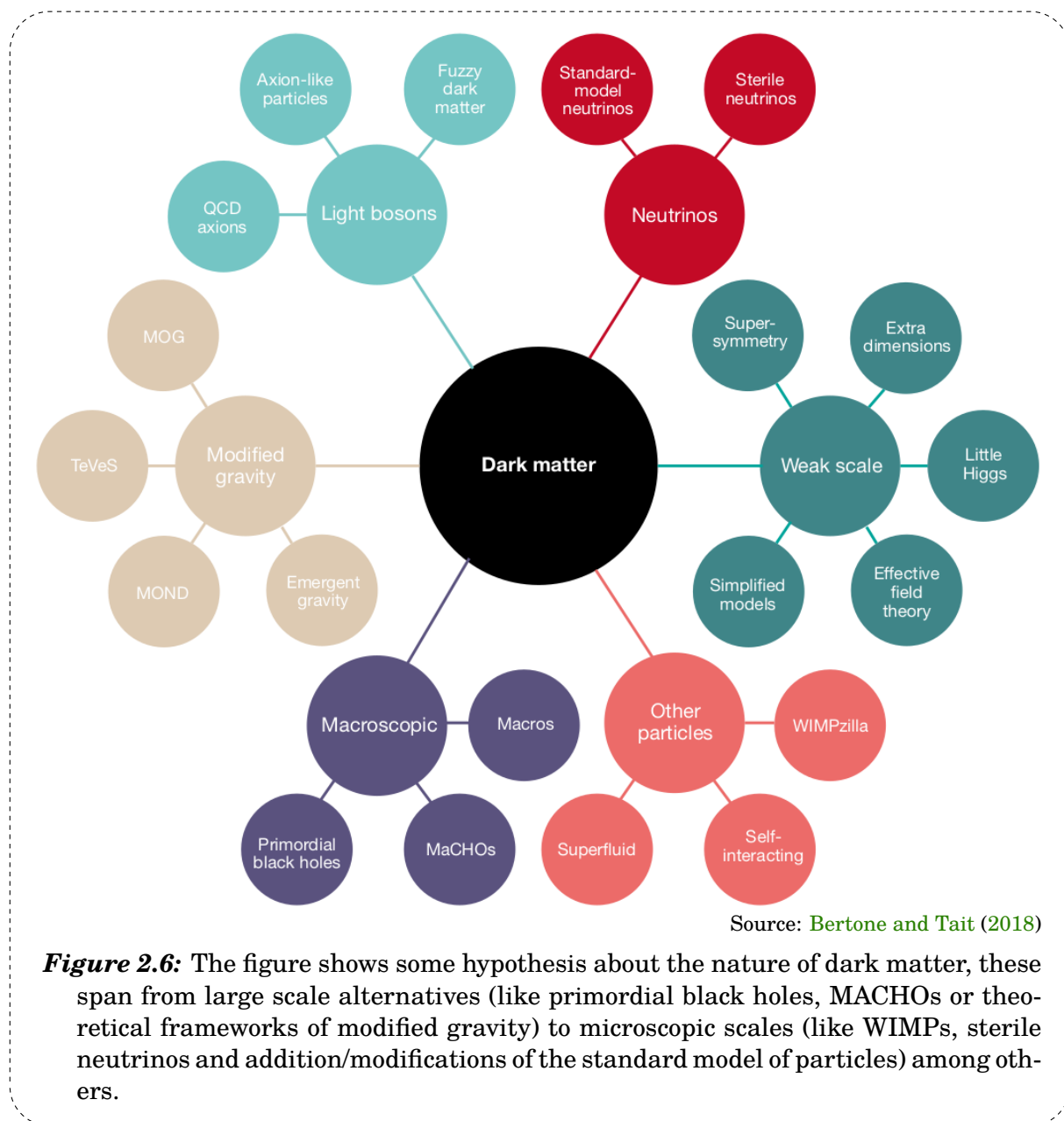
negative pressure and whose energy density is not diluted with the expansion of the Universe<sup>6</sup>.



Both dark matter and dark energy are of unknown nature to physics and astronomy. Many adjacent/alternative perspectives and models have been proposed to demystify these substances, however, to this day, there is no clear scientific consensus about them.

<sup>6</sup>This substance is sometimes associated with the cosmological constant,  $\Lambda$ , present in the original Einstein field equations. Historically, Einstein included the term  $\Lambda$  to force his field equations in order to represent a static Universe (Klimchitskaya and Mostepanenko, 2022), however, today's theoretical nature and origin of dark energy are much more profound, having implications even on QFT in the so-called cosmological constant problem or vacuum catastrophe (Weinberg, 1989; Sola Peracaula, 2022)

Figure 2.6 shows several hypotheses about the nature of dark matter. As it is shown in the graph, the range of possibilities is quite extensive, this being (along with the nature dark energy) one of the broadest questions in fundamental physics. The works of [Novosyadlyj et al. \(2015\)](#); [Arun et al. \(2017\)](#); [Bertone and Tait \(2018\)](#); [Tawfik and El Dahab \(2019\)](#) and [Martins et al. \(2023\)](#), present further dissertations about the "dark" components of the Universe.





Thus, the current paradigm of cosmology is the standard  $\Lambda$ CDM cosmological model (or just  $\Lambda$ CDM for simplicity). This model encompasses the theory of a Hot Big Bang and fits remarkably well with observations given the descriptions before<sup>7</sup>. Under the  $\Lambda$ CDM model, the Universe is essentially composed by dark energy ( $\sim 68.3\%$ ) and dark matter ( $\sim 26.8\%$ ), followed by baryonic matter ( $\sim 4\%$ ) in the form of intergalactic gas (hydrogen and helium) and small traces of other substances such as heavy elements, radiation and neutrinos (Planck-Collaboration et al., 2018). Furthermore, the  $\Lambda$ CDM model can be characterized by six free independent parameters (Lahav and Liddle, 2004; Liddle, 2004). Those are:

$$\Theta_{\Lambda\text{CDM}} = \{\Omega_b h^2; \Omega_{\text{CDM}} h^2; H_0; n_s; \sigma_8; \tau\}. \quad (2.2)$$

- Baryon density ( $\Omega_b h^2$ )
- Dark matter density ( $\Omega_{\text{CDM}} h^2$ )
- Hubble constant ( $H_0$ )
- Scalar spectral index ( $n_s$ )
- Fluctuation amplitude ( $\sigma_8$ )
- Reionization optical depth ( $\tau$ )

Measuring these parameters, the cosmological model is tested and proved to be consistent with observations. All parameters are related to the LSS and the study of the Universe at different wavelengths. A brief description of each one of them and some probes related are described on appendix A, further explanations can be found in following sections.

On the other hand, the model also considers that LSS is the product of the evolution of matter density perturbations coming from quantum density fluctuations in the early Universe. A brief description of this phenomenon is discussed next.

Recalling Figure 2.2, there is no physical mechanism that could produce the CMB's thermal uniformity without breaking causality effects (this considering two points separated by  $1^\circ$  on the sky). The possible answer to this predicament could rely on

---

<sup>7</sup>See figures 2.7, 2.12 y 2.13b for reference.

the inflation hypothesis, this postulate proposes a fast exponential growth of the horizon scale of the newborn Universe. It also could explain the large-scale correlations in the CMB, associated with the perturbation seeds for forming structures from a zero-order/smooth Universe.

Inflation appeared at the beginning of the 80s (Guth, 1981; Linde, 1982; Albrecht and Steinhardt, 1982) as a method to solve various problems related to the ancient Universe (the horizon problem, the flatness problem and the magnetic-monopole problem). Although inflation is an extension of the  $\Lambda$ CDM model, its crucial role in the structure formation and global properties of today's Universe is worth noting. To this day there is no cluing evidence that firmly supports this idea being correct and, so forth, remains as a hypothesis and an open field of discussion.

In addition to the aforementioned unknowns,  $\Lambda$ CDM has several important unsolved tensions and/or inconsistencies (observed in simulations and measurements), that could come intrinsically from the theory itself or could be strongly influenced by observational biases. Some relevant ones are:

- The Hubble tension: a discrepancy in the measurement of the rate of expansion of the Universe from different methods (the distance ladder vs high red-shift probes) (Di-Valentino et al., 2021).
- The  $S_8$  tension: a discrepancy between the value of the present day level of clustering estimated out of CMB anisotropies, and that obtained from galaxy clusters at  $z < 1$  (Akarsu et al., 2024).
- Cosmic dipoles observations: apparent violations of the cosmological principle (Bengaly et al., 2018).
- The Missing Satellites Problem: a greater number of dark matter halos reported in simulations compared with those observed (Del Popolo and Le Delliou, 2017).
- Too-Big-to-Fail: a discrepancy between the expected mass of dark matter sub-haloes and the actual central mass observed in the brightest satellite galaxies within the Local Group or in the Andromeda Galaxy (Kaplinghat et al., 2019).
- Cores vs. Cusps: a difference between dark matter halo density profiles ( $\rho(r) \propto r^{-x}$ ) coming out of simulations (cusp type:  $1 \lesssim x \lesssim 1.5$ ) and those observed in low-mass galaxies (core type:  $x \sim 0$ ) (Del Popolo and Le Delliou, 2017).

- Planes of Satellite Galaxies: evidence for a favoured plane of the orbits of satellite galaxies around massive ones (Del Popolo and Le Delliou, 2017).
- Galaxies in voids: there are much fewer galaxies in voids than expected from  $\Lambda$ CDM theory in contrast to simulations (Tikhonov and Klypin, 2009).

The main assumption is that these conflicts could be resolved over time with the aid of technological, observational, and theoretical advances, a scenario within which the work presented here is involved. However, although the  $\Lambda$ CDM model has achieved many successes, López-Corredoira and Marmet (2022); Schöneberg et al. (2022); Akarsu et al. (2024) and Jeakel et al. (2024) discuss a series of alternatives as possible solutions to the questions and discrepancies previously mentioned.

In these terms, previous paragraphs gave a brief historical review and a shallow description of the current cosmological paradigm, so forth, the following sections are intended to give a more precise explanation of the theoretical foundations of the model. The content is mainly based on the following references: Peebles (1993); Peacock (2003); Lambourne (2010); Knobel (2012); Schneider (2014); Liddle (2015); Fazio et al. (2018); Dodelson and Schmidt (2020); Youles (2021); Baumann (2022) and those explicitly cited through the text.

## 2.2 The standard model

If one studies the Universe at the largest scales, the only dominant force is gravity, and the current best-tested gravitational theory to date is GR (Dyson et al., 1920; Clemence, 1947; Pound and Rebka Jr, 1960). In GR, with the aim of measuring the separation between two events in four-dimensional space-time<sup>8</sup>, it is convenient to define an invariant quantity denoted as  $ds$ , or the so-called line element, in the form of,

$$ds^2 = \sum_{\mu,\nu=0}^3 g_{\mu\nu} dx^\mu dx^\nu . \quad (2.3)$$

In equation (2.3), the  $g_{\mu\nu}$  is the metric tensor which accounts for the geometry (curvature) of space-time. In special relativity (an euclidean space-time), the metric used is that which follows a Minkowski space, that is,

---

<sup>8</sup> $\mathbf{x} = (x^0, x^1, x^2, x^3)$ , containing one temporal and three spatial coordinates.

$$g_{\mu\nu} = \eta_{\mu\nu} = \begin{pmatrix} -1 & 0 & 0 & 0 \\ 0 & 1 & 0 & 0 \\ 0 & 0 & 1 & 0 \\ 0 & 0 & 0 & 1 \end{pmatrix}. \quad (2.4)$$

One can measure distances and angles between coordinate systems using a metric, in the same way, a metric gives a clue and puts some constraints on the context of what we are developing in GR (Schutz, 2022). The FLRW metric mentioned earlier, could be settled on three spatial coordinates linked to a spherical polar system  $(r, \theta, \phi)$  and a temporal coordinate related to the cosmic time  $t$ . Thus, the line element for the FLRW metric follows,

$$ds^2 = -dt^2 + a^2(t) \left[ \frac{dr^2}{1 - kr^2} + r^2(d\theta^2 + \sin^2\theta d\phi^2) \right], \quad (2.5)$$

and the correspondent metric tensor could be expressed as,

$$g_{\mu\nu} = \begin{pmatrix} -1 & 0 & 0 & 0 \\ 0 & \frac{a^2(t)}{1 - kr^2} & 0 & 0 \\ 0 & 0 & a^2(t)r^2 & 0 \\ 0 & 0 & 0 & a^2(t)r^2 \sin^2\theta \end{pmatrix}, \quad (2.6)$$

where  $k$  represents the spatial curvature of the Universe, and, depending on the value it assumes  $(-1, 0, +1)$ , it defines whether the Universe is going to be open, flat, or closed<sup>9</sup>. The common convention, and measurements of the CMB (Planck-Collaboration et al., 2020a) and LSS (Mortonson, 2009), attend to the idea of a Universe topologically flat ( $k = 0$ ).

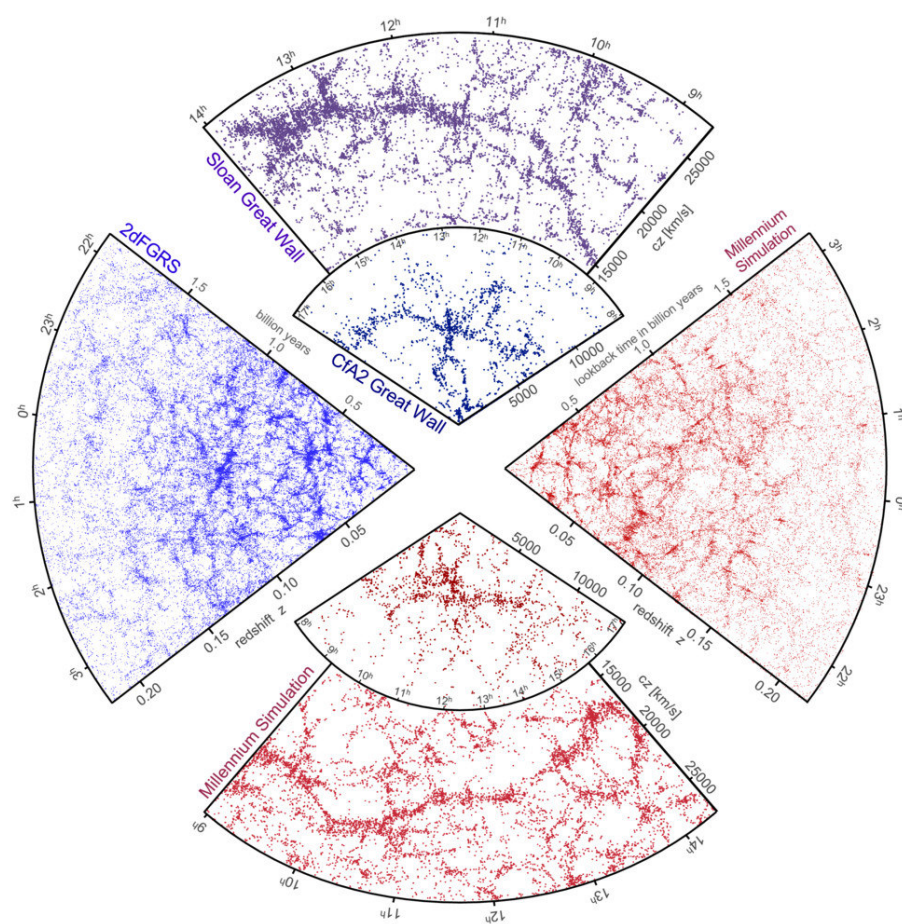
Moreover, the  $a$  term in equation (2.5) is the scale factor; this parameter normalizes the size of the Universe and controls the rate of its contraction/expansion. For convention,  $a$  is set to 1 at present, which means  $a_0 = 1$ . One key property of  $a$  is that, because of its time dependence, if it is back in time, it eventually goes to zero

---

<sup>9</sup>Hyperbolic (negative) curvature [open Universe], plane (zero) curvature [flat Universe] or spherical (positive) curvature [closed Universe].

*i.e.* what we usually refer to as the the Big Bang singularity (or the primitive atom proposed by Lemaître).

Given that the FLRW metric does not have space/time crossed terms (not special directions), and is spherically symmetric, it follows the cosmological principle. This is very important because this gives an isotropic (invariant under rotations) and homogeneous (invariant under translations) Universe as a result, properties that in fact we can measure and observe (as it is depicted in Figure 2.7 considering slices of  $1^\circ$  at equal  $\Delta z$ ). This also corresponds to one of the main assumptions of the  $\Lambda$ CDM model.



Source: [Springel et al. \(2006\)](#)

**Figure 2.7:** Comparison between some galaxy surveys (blue/purple) plotted on redshift space maps and the same plot produced out of the N-body cosmological Millennium simulation results (red). A great agreement can be seen between the observations and simulations based on the  $\Lambda$ CDM model.

On the other hand, GR is formulated by Einstein's field equations (EFEs) represented by,

$$G_{\mu\nu} + \Lambda g_{\mu\nu} = R_{\mu\nu} - \frac{1}{2}Rg_{\mu\nu} + \Lambda g_{\mu\nu} = \frac{8\pi G}{c^4}T_{\mu\nu}, \quad (2.7)$$

where the left hand side of the equation represents the geometry of the space-time and the right hand side expresses the matter-energy content that is present. That is, EFEs link how space-time behaves according to the matter and energy content it has. In equation (2.7),  $G_{\mu\nu}$  is the Einstein tensor composed in turn by the Ricci tensor ( $R_{\mu\nu}$ ), the Ricci scalar ( $R$ ) and a cosmological constant ( $\Lambda$ ).

Likewise, considering the contents of the Universe as an ideal fluid (recalling once again the cosmological principle), one can make use of the energy-momentum tensor ( $T_{\mu\nu}$ ) expressed as,

$$T_{\mu\nu} = \left( \rho + \frac{p}{c^2} \right) u_\mu u_\nu + p g_{\mu\nu}. \quad (2.8)$$

So, in this expression,  $u^\mu$  is the four-velocity,  $\rho$  is the proper energy density and  $p$  is the pressure of the fluid.

Thus, if one wants to investigate how the Universe behaves through time (or if at least it does), and in the same manner investigate how the Universe behaves depending on the stuff it contains, one needs to solve the EFEs using the FLRW metric.

For the left hand side of equation (2.7), it is necessary calculate the Christoffel symbols ( $\Gamma_{ji}^l$ ) in order to derive the Riemann tensor (and to find the components different from 0 for  $R_{tt}$ ,  $R_{rr}$ ,  $R_{\theta\theta}$  and  $R_{\phi\phi}$ ) and then calculate the Ricci scalar in the form of  $R = g^{\mu\nu} R_{\mu\nu}$ . For the right hand side of the equation, the assumption of a perfect fluid for the energy momentum tensor gives  $T_{tt} = -\rho c^2 g_{tt}$  and  $T_{ii} = p g_{ii}$ <sup>10</sup>.

Solving the temporal part ( $_{tt}$ ) and the spatial part ( $_{ii}$ ) of the EFEs leads to the renowned Friedmann equations presented in equations (2.9) and (2.10). These differential equations describes how the scale factor changes through time according to the energy-matter contents in consideration, also as function of curvature and the cosmological constant.

---

<sup>10</sup>For a thorough derivation and a comparison with the classic Newtonian counterpart see [Arnau Romeu \(2014\)](#)



The first Friedmann equation, conventionally known just as the Friedmann equation, relates the rate of expansion of the Universe (left hand side) and its contents and curvature (right hand side) as a function of time, as expressed by:

$$H^2(t) = \left(\frac{\dot{a}(t)}{a(t)}\right)^2 = \frac{8\pi G}{3}\rho(t) - \frac{kc^2}{a^2(t)} + \frac{\Lambda c}{3}. \quad (2.9)$$

For the particular case of a flat Universe (the scalar curvature term is equal to  $k = 0$ ), the second term in the equation vanishes and only the contributions of the different kinds of matter-energy contents are taken into account. The first term in the equation is called the Hubble parameter and it is worth noting that if we set  $t = 0$  (the present epoch) and  $a = 1$ , the value for  $H$  we obtain is the Hubble constant or  $H_0$ , the current rate of expansion of the Universe, which is one of the most important observables in cosmology<sup>11</sup>.

The second Friedmann equation is called the acceleration equation and could be stated as,

$$\dot{H}(t) + H^2(t) = \frac{\ddot{a}(t)}{a(t)} = -\frac{4\pi G}{3}\left(\rho(t) + \frac{3p(t)}{c^2}\right) + \frac{\Lambda c}{3}. \quad (2.10)$$

Enclosed in this equation is the relation between the matter-energy content pressure (plus dark energy contribution) and the change in the rate of expansion in time. Note that in the absence of pressure contributions, the expansion would be decelerating.

An additional relation could be derived by applying energy conservation arguments to the energy-momentum tensor of equation (2.8) ( $\nabla_\mu T^{\mu\nu} = 0$ ). Considering perfect fluid assumptions this leads to

$$\frac{\partial\rho(t)}{\partial t} + \frac{3\dot{a}(t)}{a(t)}\left(\rho(t) + \frac{p(t)}{c^2}\right) = 0, \quad (2.11)$$

and is known as the continuity or fluid equation. As it can be seen, this expression shows how different matter-energy content densities change over time. The first term expresses the dilution in density produced by a volume change and the second term in brackets corresponds to a loss of energy caused by the change in pressure, both related by the  $a$  factor change.

<sup>11</sup>Hubble constant is often parameterized as  $H_0 = 100 h \frac{\text{km/s}}{\text{Mpc}}$ , where  $h$  is the reduced Hubble constant which encompasses the uncertainty in the measurements (Croton, 2013).

## Kinematics of an expanding universe

As mentioned before, cosmology is not limited to the analysis of space-time alone. The  $\Lambda$ CDM model implies the existence of different species with their own physical characteristics. These are: the relativistic ones (photons  $[\gamma]$  and neutrinos  $[\nu]$ ), non-relativistic matter (including baryons plus leptons <sup>12</sup> $[b]$ , and dark matter  $[CDM]$ ), dark energy  $[\Lambda]$  and the contribution of curvature  $[k]$  to the expansion dynamics of the Universe.

To solve equations (2.10) to (2.11), it is necessary an expression that specifies the relation between the pressure and density of the fluid we are considering. Such mathematical expression is the equation of state expressed as,

$$p(t) = wc^2\rho(t) . \quad (2.12)$$

Thus, Table 2.1 shows solutions of the Friedmann equations for the different matter-energy contents discussed above.

<i>Content</i>	<i>Equation of state</i>	<i>Scale factor</i>	<i>Energy density</i>
Non-relativistic matter ( $m$ )	$w = 0$	$a(t) \propto t^{2/3}$	$\rho(t) \propto a^{-3}$
Relativistic species ( $r$ )	$w = 1/3$	$a(t) \propto t^{1/2}$	$\rho(t) \propto a^{-4}$
Dark energy ( $\Lambda$ )	$w = -1$	$a(t) \propto e^{H/t}$	$\rho(t) \propto \text{constant}$
Curvature ( $k$ )	$w = -1/3$	$a(t) \propto t$	$\rho(t) \propto a^{-2}$

**Table 2.1:** Solution of the Friedmann equations for different species.

Solving Friedmann's equations for a Universe composed of mixtures of different species is the key to understand how the Universe evolve. In order to do that it is worth noting that the term  $\rho$  on equations (2.9) and (2.10) should be expressed as

$$\rho(t) = \sum_i \rho_i = \rho_m + \rho_r + \rho_\Lambda , \quad (2.13)$$

---

<sup>12</sup>In cosmology, both baryons and leptons are treated as baryonic content.



recalling that the  $k$  term is not included given its absence in the acceleration equation. It is also important to note that  $\rho_m = \rho_{CDM} + \rho_b$  and  $\rho_r = \rho_\gamma + \rho_\nu$ .

Moreover, by setting  $k = 0$  and  $\Lambda = 0$  in equation (2.9) it is possible to derive the critical density of the Universe, that is  $\rho_c = 3H^2/8\pi G$ <sup>13</sup>. This parameter represents the density of matter-energy content for a spatially flat universe ( $k = 0$ ). From this, the density parameter  $\Omega$  can be defined, this is the ratio of the density  $\rho$  and  $\rho_c$ . So forth, for the case of different species one has,

$$\Omega_m = \frac{8\pi G}{3H^2}\rho_m, \Omega_r = \frac{8\pi G}{3H^2}\rho_r, \Omega_\Lambda = \frac{\Lambda c}{3H^2} \text{ and } \Omega_k = \frac{-kc^2}{(aH)^2}. \quad (2.14)$$

Two important results can be yielded by inserting the density parameters into Friedmann's equations. On one hand, we consider that, for a flat Universe,  $\Omega_r + \Omega_m + \Omega_k + \Omega_\Lambda = 1$  is true for all times, and, on the other hand, by setting  $a = 1$  for the present epoch one can derive

$$H^2(a) = H_0^2 (\Omega_{0,r}a^{-4} + \Omega_{0,m}a^{-3} + \Omega_{0,k}a^{-2} + \Omega_{0,\Lambda}), \quad (2.15)$$

which gives the rate of expansion of the Universe at any given time in accordance to the present rate of expansion and the current density parameter values (see Figure 2.8).

Equation (2.15) and Figure 2.8 give the general behaviour of the evolution of the Universe. For very early times, that means a small value of  $a$ , the Universe is dominated by radiation, when the scale factor is growing in such way that the matter density parameter for matter becomes predominant, that is  $a \geq a_{eq}$ <sup>14</sup>, it is said that the Universe is matter dominated. At last, for larger values of  $a$ , dark energy dominates.<sup>15</sup>

<sup>13</sup> $\rho_c = 1.87834 \times 10^{-29} h^2 \text{ g cm}^{-3}$  for  $h = 0.674$  under [Planck-Collaboration et al. \(2018\)](#) results.

<sup>14</sup> $a_{eq}$  means the time when matter and radiation density were equal as it is shown in Figure 2.8.

<sup>15</sup>For  $k \neq 0$ , the curvature term would dominate between the matter and the dark energy epoch, but it is not presumably the case for the  $\Lambda$ CDM model.

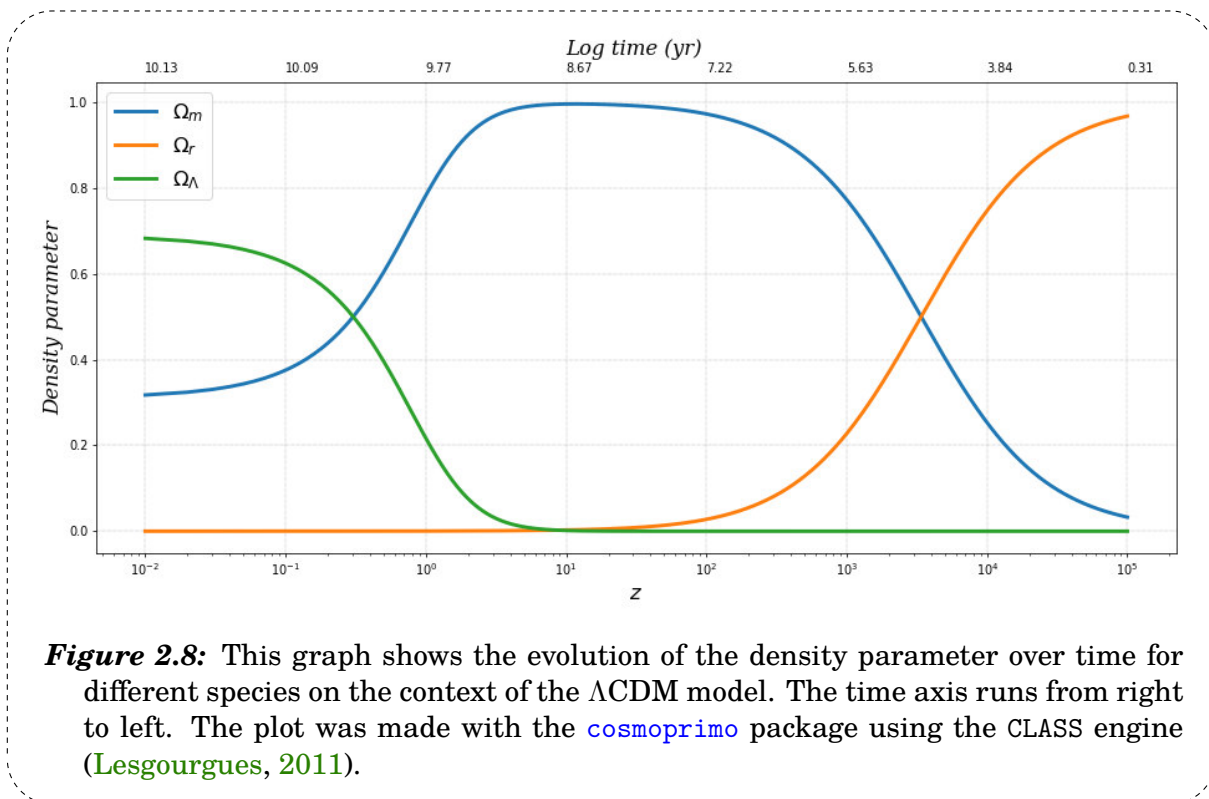


**Figure 2.8:** This graph shows the evolution of the density parameter over time for different species on the context of the  $\Lambda$ CDM model. The time axis runs from right to left. The plot was made with the `cosmoprime` package using the CLASS engine (Lesgourgues, 2011).

## Cosmological redshift

Light follows null geodesics (zero proper time), therefore,

$$c^2 dt^2 = a^2(t) dr^2 \quad \rightarrow \quad r = \int \frac{c dt}{a(t)}. \quad (2.16)$$

If a photon of a distant galaxy is emitted at a certain time  $t_e$  at a wavelength  $\lambda_e$ , and is observed/received at  $t_r$  and  $\lambda_r$ , given that the comoving distance is constant for these photons (see equation (2.24), this implies the events between the observer and the galaxy suffer time dilation. Taking  $t_e$  and  $t_r$  as integration limits in equation (2.16), it is possible to conclude that

$$1 + z = \frac{\lambda_{\text{received}}}{\lambda_{\text{emitted}}} = \frac{a(t_{\text{received}})}{a(t_{\text{emitted}})}. \quad (2.17)$$

As a result, an expression for the redshift ( $z$ ) and the scale factor ( $a$ ) is obtained. Equation (2.17) holds great significance as it conveys that the higher the redshift of

a specific object, the further back in time we are observing. Thus, with this expression, it is possible to study the Universe on different time scales. Equation (2.17) is also called cosmological redshift. Moreover, setting  $a_0 = 1$  for today's Universe one can notice that  $a(t) = (1 + z)^{-1}$ , hence, equation (2.15) can be rewritten as

$$H^2(z) = H_0^2 (\Omega_r(1 + z)^4 + \Omega_m(1 + z)^3 + \Omega_k(1 + z)^2 + \Omega_\Lambda). \quad (2.18)$$

Finally, taking equations (2.15), (2.17) and (2.18), and making a change of variable as  $H = \dot{a}/a = 1/t$  and  $H_0 = 1/t_0$ , the age of the Universe, *i.e.* the time back to the Big Bang singularity, can be obtained through <sup>16</sup>

$$t_0 = \int_0^\infty \frac{dz}{(1 + z)H(z)}. \quad (2.19)$$

### Thermal history of the Universe

From the previous section, it could be recognized that going back in time means the Universe gets hotter and denser. Consequently, collisions between particles become more common and more energetic, therefore, it is expected that baryonic matter was ionized and nuclear reactions were occurring in the early Universe. To approach this statement, it is worth noting to consider the fate of the energy density of photons of frequency  $\nu_1$  in a black-body spectrum at temperature  $T_1$  for  $t_1$  through the Planck's function ( $B(\nu, T)$ ), or expressed in a mathematical form,

$$B(\nu, T) = \frac{2h\nu^3}{c^2} \frac{1}{e^{\frac{h\nu}{k_B T}} - 1}. \quad (2.20)$$

In equation (2.20),  $h$  is the Planck constant and  $k_B$  is the Boltzmann constant. Recalling the basic radiative transfer equation where no photons get absorbed/scattered nor produced ( $dI_\nu/ds = 0$ ), it is expected that in a posterior time  $t_2$  where  $t_2 > t_1$ , each photon will appear redshifted according to  $\nu_1 = (1 + z)\nu_2$  and the following energy distribution will be function of  $T_2 = T_1/(1 + z)$ . That means, the temperature of the blackbody is going to preserve its shape but its temperature is

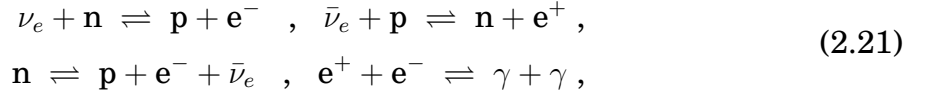
---

<sup>16</sup>The age of the Universe can also be obtained using models of stellar evolution applied to old globular clusters and measuring the angular power spectrum of temperature fluctuations of the CMB (Freedman and Madore, 2010), among other methods.

going to decrease by a  $1 + z$  factor and the energy density decreased by a factor of  $(1 + z)^4$  (Theuns, 2016).

### • Big Bang Nucleosynthesis (BBN)

Under the consideration of an expanding Universe, particle interactions should go out of equilibrium, this phenomena is called the freeze-out. In order to approach this, it is convenient to consider the scenario where  $H$ , the Hubble parameter, is higher than  $\Gamma$ , the reaction rate. At  $T \lesssim 10^{12}$  K, the early Universe is essentially a full ionized plasma mixture composed by relativistic species (electrons, positrons, neutrinos and photons) and non-relativistic species (protons and neutrons) (Grohs et al., 2019; Grohs and Fuller, 2023). For a Universe in an equilibrium state it holds that



where  $\mathbf{p}$  stands for protons,  $\mathbf{n}$  for neutrons,  $\gamma$  for photons,  $\mathbf{e}^-$  for electrons,  $\mathbf{e}^+$  for positrons,  $\nu_e$  are electronic neutrinos and  $\bar{\nu}_e$  electronic antineutrinos. Reaching temperatures of  $T \sim 10^{10}$  K, the weak interaction rate become small to maintain equilibrium so the freeze-out of neutrinos occurs. They get decoupled from the plasma and their abundance is fixed. Then, reaching temperatures between  $T \sim 8 \times 10^9$  K and  $T \sim 10^8$  K, the decay of neutron and the production of heavier elements by fusion occurs. The deuterium production reaction is possible because the photon density is low enough to prevent the inverse reaction. The creation of heavy elements could be possible given the annihilation reactions of the remaining positrons with electrons that heat the plasma (Steigman, 2007; Baumann, 2022; Grohs and Fuller, 2023).

Then, the main composition of the Universe is set to  $\sim 73\%$  hydrogen,  $\sim 24\%$  helium and traces of deuterium, tritium, lithium and beryllium ( $\sim 3\%$ ). The rest of heavier elements are produced later through stellar nucleosynthesis and stellar evolution events like supernovas or kilonovas (Patrignani et al., 2016).

### • Cosmic Microwave Background (CMB)

Under the previous considerations, if the CMB is about  $T = 2.7$  K today (recalling

Figure 2.2), at redshift  $\sim 1100$  the temperature of the CMB was about  $\sim 3000$  K. At this temperature, the energy level of the atoms is sufficient to be ionized, that means, at even higher redshift the Universe is fully ionized. Moreover, because of photons are constantly scattering off the free electrons, at this stages the Universe is totally opaque (Theuns, 2016).

Now, considering that the Universe is expanding and cooling, the typical collision energy will progressively lose the ability to ionize hydrogen, therefore the gas little by little becomes neutral *i.e.* the recombination epoch. It is expected that ionization ends when the energy of the gas reaches the binding energy of the hydrogen atom, that is  $k_B T \sim 13.6/3$  eV, because of the Boltzmann distribution, and again  $T \sim 3 \times 10^3$  K. At  $\sim 2900$  K, the photo-ionization rate becomes  $\Gamma < H$ , the photons decouple from the plasma and the electrons recombine forming atoms. Those photons that escape from the plasma are the CMB, they are emitted from the last scattering surface (Dodelson and Schmidt, 2020; Baumann, 2022; Grohs and Fuller, 2023).

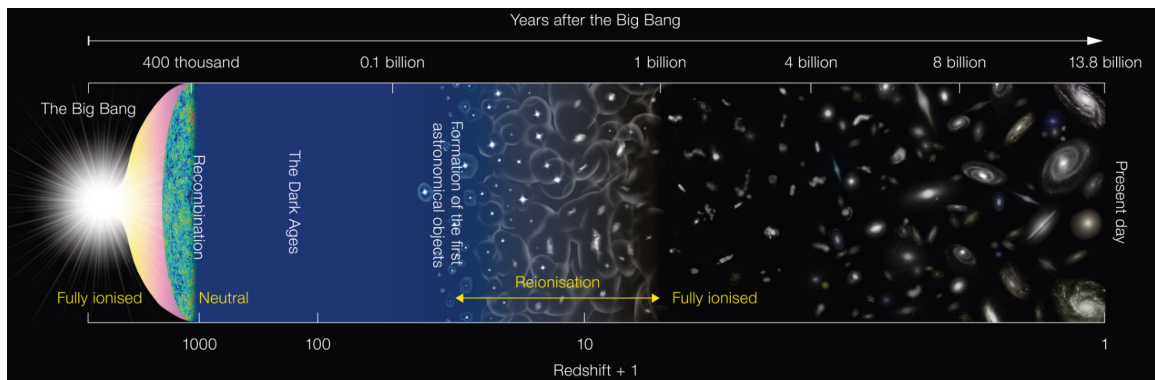
It is possible to define an optical depth to constrain the reionization process through

$$\tau = \int_{t_{\text{rec}}}^{t_0} n_e(t) \sigma_T dt = \int_0^{z_{\text{rec}}} \frac{n_e \sigma_T X_e(z)}{(1+z)H(z)} dz, \quad (2.22)$$

where  $\sigma_T$  is the Thompson scattering cross section,  $n_e$  is the electron number density and  $X_e = n_e/n_b$  assuming a value of 0.5 at recombination.

It is worth noting that, before recombination, the primordial plasma was suffering a competition between radiative pressure forces fighting against gravitational collapse, this phenomena produced the so-called baryonic acoustic oscillations (BAO), the propagation of acoustic waves. After the recombination, acoustic waves are "frozen" and spatially fixed at a characteristic scale of about  $\sim 100 h^{-1}$  Mpc. Measuring the properties of the BAO is an important probe to constrain cosmological models.

Summarizing the thermal history of the Universe, Table 2.2 shows the evolution history of the Universe in order to get a general idea about the physical processes discussed in this section. In the same way, Figure 2.9 depicts the evolution of the Universe in a timeline.



Source: NOAJ

**Figure 2.9:** Timeline of the evolution of the Universe

<i>Era</i>	<i>Time</i>	<i>Temperature</i>
Big Bang	0 s	-
Inflation	$< 10^{-32}$ s	$10^{27} - 10^{22}$ K
Neutrino decoupling	1 s	$10^{10}$ K
Primordial Nucleosynthesis (BBN)	$10 - 10^3$ s	$10^9 - 10^7$ K
Matter-Radiation Equality	10 s – 0.37 Myr	$10^9 - 10^3$ K
Recombination	0.37 Myr	$< 3500$ K
Photon decoupling (CMB)	0.38 Myr	$\sim 2900$ K
Dark ages	0.38 – 150 Myr	$3500 - 60$ K
Earliest AGNs and Population III stars	150 – 400 Myr	$\sim 60$ K
Reionization	200 – 900 Myr	$60 \sim 19$ K
Galaxy formation and evolution	1 Gyr	$19 \sim 4$ K
Matter-Dark Energy equality	10 Gyr	$\gtrsim 3.8$ K
Today	13.8 Gyr	$\sim 2.7$ K

**Table 2.2:** Timeline of the evolution of the Universe

### 2.3 Structure formation

The Universe looks homogeneous and isotropic above  $\gtrsim 100$  Mpc, however, as depicted in Figure 2.7, below this particular scale the Universe gets mostly anisotropic and inhomogeneous. In fact, galaxies and similar/related kind structures like clusters or superclusters are not randomly distributed. They are distributed in the form of the so-called cosmic web composed of filaments, sheets, nodes and voids (White et al., 2012; Schneider, 2014). These structures are understood as the product of the evolution of primordial gravitational instabilities defined by

$$\delta(\mathbf{x}, t) = \rho(\mathbf{x}, t)/\bar{\rho}(t) - 1, \quad (2.23)$$

where  $\langle \rho \rangle$  or  $\bar{\rho}$  is the globally average density of the Universe at that particular epoch (Peacock, 2003; Knobel, 2012).

In general terms, the two inquiries to solve under the previous assumptions are, what is the physical process or phenomenon behind the primordial perturbations and, how they have evolved through time. As mentioned before, the answer to the first question may be related to inflation, a discussion beyond this work. On the other hand, the evolution of gravitational instabilities in an expanding Universe, which in fact is related with the scope of this work, is very important because this helps to define the general characteristics of the Universe. Therefore, this section is intended to give a brief summary of the physical background of gravitational instabilities, serving also as a preamble of the next section.

First of all, it is necessary to define a dynamical framework that encompasses the Hubble expansion, this could be made setting a comoving coordinates framework as

$$\mathbf{r}(\mathbf{x}, t) = a(t)\mathbf{x}(t), \quad (2.24)$$

where  $\mathbf{r}$  is the physical (proper) coordinate of the system and  $\mathbf{x}$  is the comoving coordinate. Taking the temporal derivative of the previous expression gives

$$\mathbf{v}_0 = \dot{\mathbf{r}} = \dot{a}\mathbf{x} + a\dot{\mathbf{x}} = H\mathbf{r} + a\dot{\mathbf{x}} = H\mathbf{r} + \mathbf{u}, \quad (2.25)$$

that is, the characteristic Hubble flow represented by  $H\mathbf{r}$  and peculiar velocities of the system led by local gravitational effects  $a\dot{\mathbf{x}}(\mathbf{u})$ .

Furthermore, energy-matter evolution can be described using the treatment of a perfect fluid<sup>17</sup> with density  $\rho(\mathbf{r}, t)$ , velocity  $\mathbf{v}_0(\mathbf{r}, t)$  and pressure  $P$ , which follows

$$\begin{aligned}
 \text{Continuity equation: } & \frac{\partial \rho}{\partial t} + \nabla \cdot (\rho \mathbf{v}_0) = 0, \\
 \text{Euler equation: } & \frac{\partial \mathbf{v}_0}{\partial t} + (\mathbf{v}_0 \cdot \nabla) \mathbf{v}_0 + \frac{\nabla P}{\rho} + \nabla \Phi = 0, \\
 \text{Poisson equation: } & \nabla^2 \Phi = 4\pi G \rho.
 \end{aligned} \tag{2.26}$$

The set of equations (2.26) is expressed in terms of proper coordinates, so they have to be transformed into a comoving framework. The velocity field and the local gravitational potentials have to be derived plugging equations (2.24) and (2.25) into (2.26). Thus, considering small perturbations in the form of  $\delta\rho = \bar{\rho}(t)(1 + \delta(\mathbf{r}, t))$  and  $\delta v$ , associated with a perturbed potential  $\phi$ , and keeping only first-order terms, it is possible to derive the following relations

$$\begin{aligned}
 \text{Continuity equation: } & \frac{\partial \delta}{\partial t} + \frac{1}{a} \nabla \cdot \delta = 0, \\
 \text{Euler equation: } & \frac{\partial \delta \mathbf{u}}{\partial t} + \frac{\dot{a}}{a} \mathbf{u} + \frac{1}{a} \nabla \phi + \frac{1}{a} c_s^2 \nabla \delta = 0, \\
 \text{Poisson equation: } & \nabla^2 \phi = 4\pi G \rho a^2 \delta.
 \end{aligned} \tag{2.27}$$

where  $c_s$  is the speed of sound in the form of  $c_s^2 = \partial P / \partial \rho$ . In these derivations, the Newtonian perturbation theory on the linear regime ( $\delta \ll 1$ ) is followed. These assumptions are sufficient and equivalent to the relativistic case due to the scales ( $l \ll cH^{-1}$ ), velocities ( $v \ll c$ ) and redshift ranges treated in this dissertation. Once  $|\delta| \sim 1$ , as the product of the evolution of gravitational instabilities, the linear regime is no longer valid.

Finally, getting rid of peculiar velocities and taking  $\nabla = 0$  in Euler's equation in (2.27) (once more neglecting high order terms in  $\delta$ ), it is possible to obtain the equation that describes the evolution of perturbations in the linear regime, that is

---

<sup>17</sup>This recalling the main features of the standard cosmological model.



$$\ddot{\delta} + 2H\dot{\delta} + 4\pi G\bar{\rho}\delta - \frac{c_s^2}{a}\nabla^2\delta = 0. \quad (2.28)$$

Expressing equation (2.28) in Fourier space<sup>18</sup> and treating each  $k$  mode as independent, one can obtain

$$\ddot{\hat{\delta}} + 2H\dot{\hat{\delta}} + \left[ \frac{c_s^2 k^2}{a^2} - 4\pi G\bar{\rho} \right] \hat{\delta} = 0. \quad (2.29)$$

The term proportional to  $H$  acts similar to a friction term and is called the Hubble drag or expansion dilution. This term, together with the pressure term  $c_s^2 k^2/a^2$ , fight against the collapse of the perturbations imposed by the gravity term.

Moreover, equation (2.29) has two types of solutions considering the terms in the brackets. On one side, if the  $c_s^2 k^2/a^2$  dominates, the solutions for  $\hat{\delta}$  are sinusoidal, that means pressure forces are sufficiently strong to resist gravity, therefore, the behaviour is oscillatory. On the other hand, if the  $4\pi G\bar{\rho}$  term dominates, the solutions for  $\hat{\delta}$  are monotonic in time increasing or decreasing the density perturbation. Given this, if the monotonic solution increase with time, gravity wins against pressure, and density perturbations can form bound structures.

The dividing line between this two possible solutions is the so-called Jeans criterion. Setting  $c_s^2 k^2/a^2 = 4\pi G\bar{\rho}$  one could derive a characteristic scale in the form

$$k_J = \frac{a}{c_s} \sqrt{4\pi G\bar{\rho}} \quad \therefore \quad \lambda_J = \frac{2\pi}{k_J} \quad \text{thus,} \quad M_J = \frac{4\pi}{3} \left( \frac{\lambda_J}{2} \right)^3 \bar{\rho}. \quad (2.30)$$

The insight behind these equations is that perturbations which are more massive than the Jeans mass are able to grow, and also that the Jeans criterion is proportional to the speed of sound of the fluid.

Now, if just larger Fourier modes ( $k > k_J$ ) are taken into account, that also means  $c_s^2 k^2/a^2$  term vanishes in (2.29), one can obtain a general solution expressed as

$$\delta(\mathbf{k}, t) = \delta_+(\mathbf{k})D_+(t) + \delta_-(\mathbf{k})D_-(t). \quad (2.31)$$

---

<sup>18</sup>This Fourier decomposition to the perturbations follows:  $\delta(t, \mathbf{k}) = \int \delta(t, \mathbf{x}) e^{-i\mathbf{k}\mathbf{x}} d\mathbf{x}^3$ ,  $\delta(t, \mathbf{x}) = \frac{1}{(2\pi)^3} \int \delta(t, \mathbf{k}) e^{i\mathbf{k}\mathbf{x}} d\mathbf{k}^3$ , where  $\mathbf{k}$  are the comoving Fourier modes.

In this expression, + and – indexes represents the growing and the decaying modes, the former increases with time, whereas the latter decreases. Eventually, the increasing term will dominate at later times, whereas the decaying one will become irrelevant. Under those considerations, the growing term is called the linear growth function and could be normalized in such way that  $D_+(t_0) = 1$ . The growth factor can be expressed as

$$D_+(a) \propto \frac{H(a)}{H_0} \int_0^a \frac{da'}{\left[\frac{\Omega_m}{a'} + \Omega_\Lambda a'^2 - (\Omega_m + \Omega_\Lambda - 1)\right]^{\frac{3}{2}}}. \quad (2.32)$$

Furthermore, one can express the density contrast like

$$\delta(\mathbf{x}, t) = D_+(t)\delta_0(\mathbf{x}). \quad (2.33)$$

considering the decaying mode in equation (2.31) vanishes. Now, regarding equation (2.33), one can states that, in linear perturbation theory, the spatial shape of the density perturbations is frozen in comoving coordinates and just their amplitude increases. The  $\delta_0(\mathbf{x})$  term is denoted as the linearly extrapolated density fluctuation field.

Finally, recalling equation (2.32), one can notice that the growth function is dependant of matter and dark energy but no radiation terms appears. For this, it could be considered that,

$$\delta(t, \mathbf{k}) \propto \frac{1}{H^2(t)a^2(t)} \propto \begin{cases} a^2(t) & \text{(radiation domination),} \\ a(t) & \text{(matter domination),} \end{cases} \quad (2.34)$$

which expresses how the scale factor behaves in a radiation/matter dominated Universe.

During matter domination, perturbations grow proportional to the scale factor (outside and inside the causal horizon  $R_H(z)$  <sup>19</sup>). To take into consideration the case of a radiation dominated Universe it is necessary to define a transfer function ( $T(k)$ ), that is,

---

<sup>19</sup>  $R_H(z) = \int_0^t c dt/a(t)$

$$\delta(t, \mathbf{k}) = \delta(t_{\text{in}}, \mathbf{k}) T(k) \frac{D_+(t)}{D_+(t_{\text{in}})} . \quad (2.35)$$

$T(k)$  takes into account the deviations in the evolution of the primordial perturbations which happen at early times during radiation domination and within the horizon (that is the *in* term in equation (2.35)). For a mode  $\mathbf{k}$  which enters within the matter dominated regime *i.e.* after decoupling, by definition one gets  $T(k) \simeq 1$  for modes outside the horizon and  $T(k) \simeq (kR_{\text{H}})^{-2}$  for modes inside the horizon (Knobel, 2012).

## 2.4 Matter power spectrum

The overdensity field  $\delta(t, \mathbf{x})$  should contain the whole panorama of structure formation about LSS formation. In order to characterize the structure formation in the Universe and find a way to compare theory with observations, it is useful to set  $\delta$  as a realization of a stochastic process, that should be postulated on the consideration that  $\delta$  exists in a homogeneous and isotropic universe. Therefore, the statistical properties of  $\delta$  should also be homogeneous. In order to fulfill the previous statement, one should consider that the  $\delta$  field is ergodic, that means the volume average is interchangeable with the ensemble average ( $\langle \cdot \cdot \cdot \rangle$ ) (Knobel, 2012; Primack, 2015).

According to Peacock (2003), if there is a density fluctuation field produced by the evolution of primordial gravitational instabilities given by equation (2.23), the level of structure of the aforementioned field could be defined measuring the spatial correlation function  $\xi$ , expressed as

$$\xi(\mathbf{r}) = \langle \delta(\mathbf{x})\delta(\mathbf{x} + \mathbf{r}) \rangle . \quad (2.36)$$

The concept of correlation function usually refers to the two-point auto-correlation function of the field. In the realm of galaxies,  $\xi$  represents the excess probability of finding two galaxies at a particular scale, surpassing the probability that would occur if the galaxies were randomly and uniformly scattered independent of each other. As Figure 2.10 shows, for the  $\Lambda$ CDM model, two peaks appear in the correlation function; the former represents the hierarchical nature of structure formation in the Universe led by gravitational potentials. On the other hand, the second peak

(at about  $100 h^{-1}$  Mpc), shows what is known as the BAO peak, previously pointed in section 2.2.

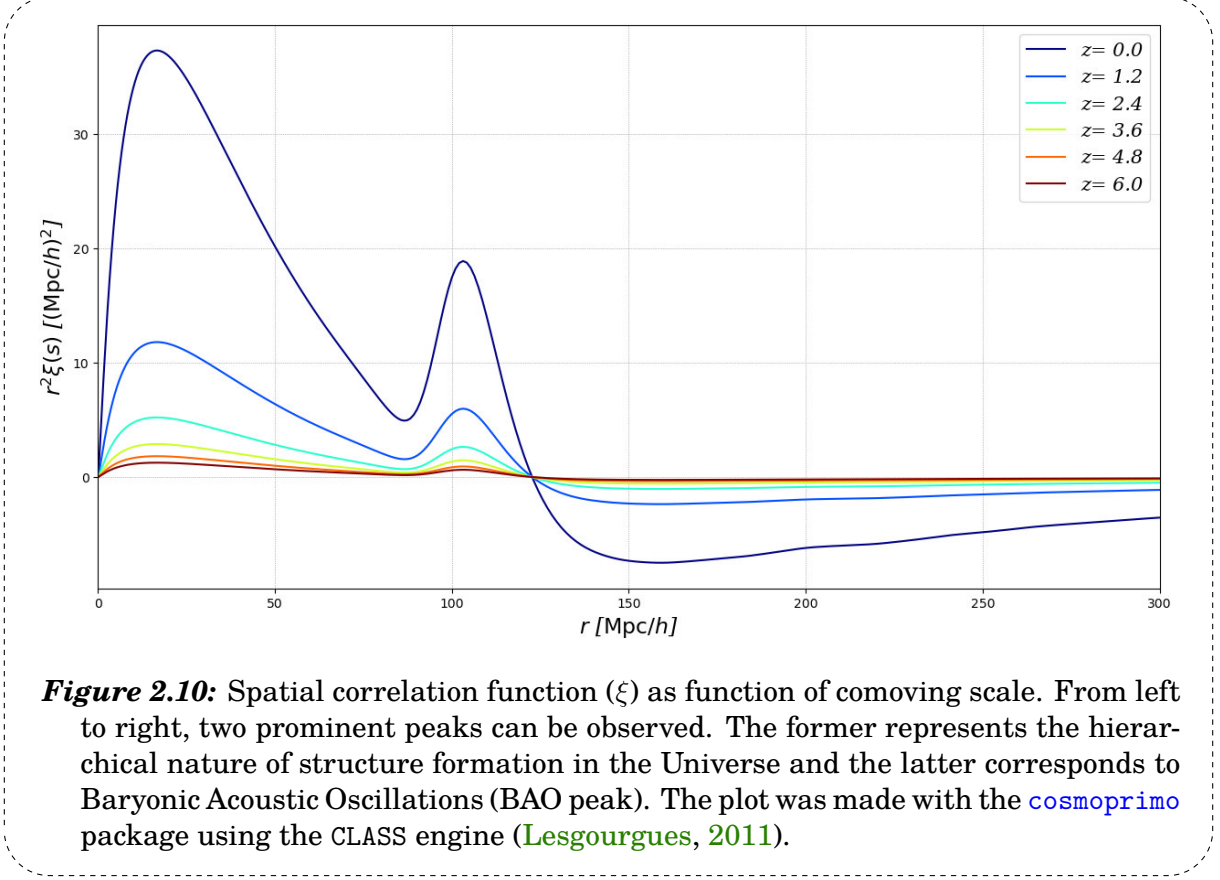


**Figure 2.10:** Spatial correlation function ( $\xi$ ) as function of comoving scale. From left to right, two prominent peaks can be observed. The former represents the hierarchical nature of structure formation in the Universe and the latter corresponds to Baryonic Acoustic Oscillations (BAO peak). The plot was made with the `cosmoprime` package using the CLASS engine (Lesgourgues, 2011).

The scale of the BAO peak is related to the sound horizon at the time when recombination occurred. Observations of this peak in galaxy surveys provide what is called a "standard ruler" that can be used to measure distances and constrain cosmological parameters (Eisenstein et al., 2005; Delubac et al., 2013).

Reciprocally, it is possible to decompose the density fluctuations in Fourier modes such that

$$\xi(\mathbf{r}) = \frac{V}{(2\pi)^3} \int |\delta_{\mathbf{k}}|^2 e^{-i\mathbf{k}\cdot\mathbf{r}} d^3k, \quad (2.37)$$

and reciprocally,

$$\delta(\mathbf{k}) = \frac{1}{2\pi} \int \delta(\mathbf{x}) e^{-i\mathbf{k}\cdot\mathbf{x}} dx. \quad (2.38)$$

In equation (2.38),  $k$  represents the comoving wavenumber (*i.e.* length scale  $2\pi/k$ ) and the term  $\langle |\delta_k|^2 \rangle$  is the renowned matter power spectrum ( $P_m(k)$ ) which is an observable of wide interest in cosmology given its ability to constrain models.  $P_m(k)$  is formally defined as

$$\langle \delta(\mathbf{k})\delta^*(\mathbf{k}') \rangle = (2\pi)^3 \delta_D(\mathbf{k} - \mathbf{k}') P(\mathbf{k}) \quad \text{or} \quad P(\mathbf{k}) = \int \xi(\mathbf{x}) e^{-i\mathbf{k}\cdot\mathbf{x}} d\mathbf{x}^3. \quad (2.39)$$

It should be noted that, by general convention and visualization purposes, the matter power spectrum can be represented in terms of the dimensionless quantity  $\Delta^2$ , expressed as

$$\Delta^2 = \frac{V}{(2\pi)^3} 4\pi k^3 P(k) = \frac{2}{\pi} k^3 \int_0^\infty \xi(r) \frac{\sin(kr)}{kr} r^2 dr; \quad (2.40)$$

$\Delta^2 = 1$  means there are order-unity density fluctuations from modes in the logarithmic bin around wavenumber  $k$ .

In the absence of a mechanism producing the initial perturbation field, an *ansatz* should be set in order to approach the initial power spectrum characteristics. The initial power spectrum proposed for the time before inflation was postulated is the Harrison-Peebles-Zel'dovich spectrum (Harrison, 1970; Peebles and Yu, 1970; Zel'Dovich, 1970) which takes the form

$$P(k) \propto k^n, \quad (2.41)$$

where  $n$  is the spectral index. The Harrison-Peebles-Zel'dovich spectrum assumes  $n = 1$ , which means is scale invariant. After inflation hypothesis was postulated, the spectral index is dependent of the considered inflation field (Knobel, 2012; Schneider, 2014).

As represented in Figure 2.11, for a  $\Lambda$ CDM universe, the power spectrum asymptotes to  $P(k) \sim k^1$  for small  $k$  while  $P(k) \sim k^{-3}$  for large values of  $k$ . There is a prominent peak at  $k_{eq} \sim 2 \times 10^{-2} h \text{ Mpc}^{-1}$ , corresponding to  $\lambda_{eq} \sim 350 h \text{ Mpc}^{-1}$ , this is the characteristic length-scale where the matter-radiation equality happens. The peak is smooth because the transition from radiation to matter domination era is not instantaneous (Norman, 2010; Primack, 2015). Moreover, the oscillations seen in Figure 2.11, around  $\sim 0.02 - 0.3 h\text{Mpc}^{-1}$ , are the spectral manifestations of the baryonic acoustic oscillations.

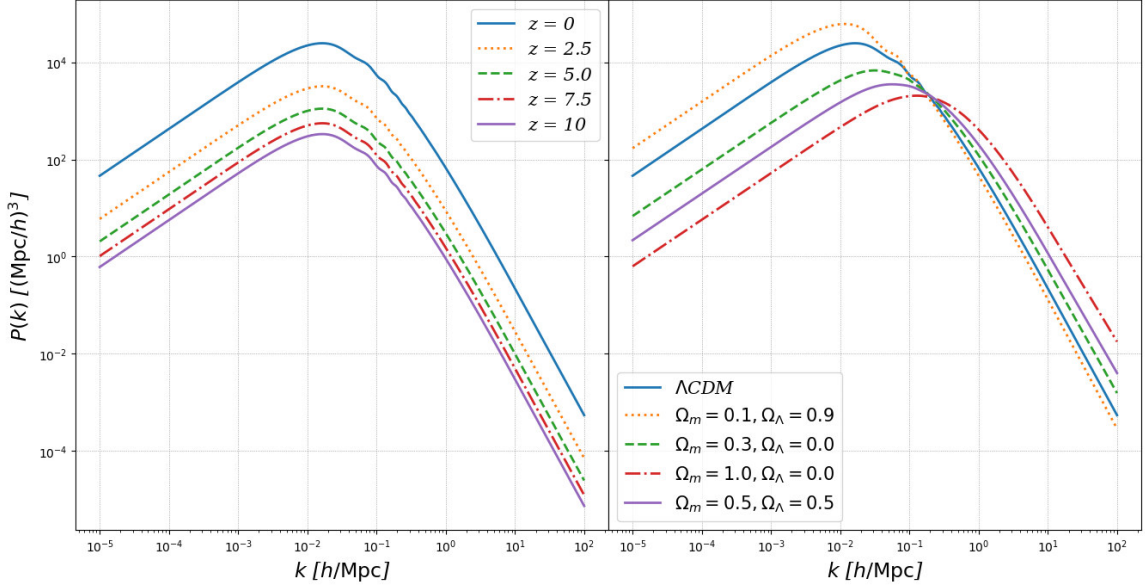


**Figure 2.11:** Three-dimensional linear matter power spectrum estimation at different  $z$  values for the  $\Lambda$ CDM model and the estimation for universes with different density parameter proportions at  $z = 0$ . The plot was made with the `cosmoprime` package using the CLASS engine (Lesgourgues, 2011).

From the estimation of the amplitude and the shape of the matter power spectrum, it is possible to retrieve cosmological and general statistical characteristics of the Universe. Taking the left panel of Figure 2.11 as reference, one can observe that the level of structure of the Universe *i.e.* its clumpiness, grows as time increases. Then again, from the right panel of the figure it can be seen that, as the density parameter proportion changes, the shape and amplitude of the power spectrum changes as well.

The  $P_m(k)$  showed in Figure 2.11 is the representation of the linear regime only, but the power spectrum, at a given time, has contributions of linear and non-linear features of structure formation, that is,

$$P(t, k) = P_{\text{linear}}(t, k) + P_{\text{non-linear}}(t, k), \quad (2.42)$$

however, in order to consider scales where the non-linear regime dominates, the linear regime is extrapolated.

In this order of ideas, the linear matter power spectrum is a function of the amplitude of fluctuations at  $z = 0$  ( $A_0$ ), an initial power spectrum, a transfer function and the growing mode of structure formation evolution. Or mathematically,

$$P_{\text{linear}}(t, k) = A_0 k^n T^2(k) D_+^2(t) . \quad (2.43)$$

Figure 2.12 shows the linear matter power spectrum (black line) for the  $\Lambda$ CDM model (equation (2.43)) and a consistency check from different probes including: CMB temperature, polarization (Planck-Collaboration et al., 2020b) and lensing reconstruction (Planck-Collaboration et al., 2020c) power spectra, cosmic shear (Troxel et al., 2018), galaxy clustering (Reid et al., 2010) and Ly- $\alpha$  forests (Chabanier et al., 2019b). These probes covers several scale ranges and different cosmic epochs. The plot expresses the great accordance between theory and observations.

Finally, the matter power spectrum of Figure 2.12 represents a three-dimensional inference of the level of structure of the Universe. According to Lumsden et al. (1989) and Kaiser and Peacock (1991), in the particular case of having a power spectrum along a one-dimensional density field (*e.g.*, "pencil-beam" type surveys (Giovanelli and Haynes, 1991) or the Ly- $\alpha$  forest of section 3.4), it is possible to recover the three-dimensional power spectrum through

$$P_{3D}(k) = -\frac{2\pi}{k} \frac{dP_{1D}(k)}{dk} , \quad (2.44)$$

while the one-dimensional power spectrum magnitude is the integral of the three-dimensional spectrum along a specific line of sight<sup>20</sup>, implying that,

$$P_{1D}(k_{\parallel}) = \frac{k_{\perp}}{2\pi} \int_0^{\infty} P_{3D}(k_{\parallel}, k_{\perp}) dk_{\perp} . \quad (2.45)$$

---

<sup>20</sup>Consequently, the dimensionless variance  $\Delta^2$  takes the form of  $\Delta^2(k) = (1/\pi)kP(k)$ , for the one-dimensional case.

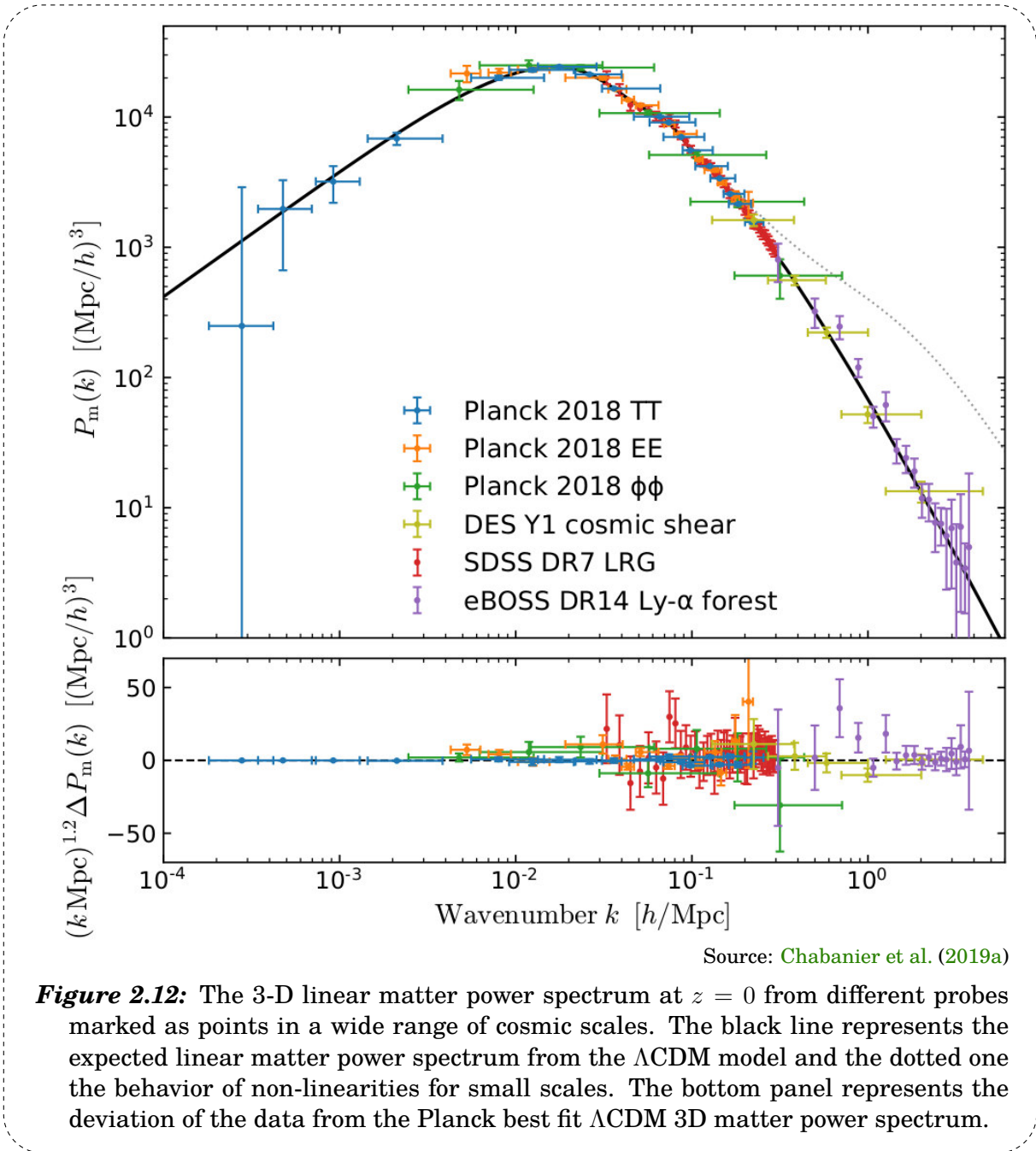


**Figure 2.12:** The 3-D linear matter power spectrum at  $z = 0$  from different probes marked as points in a wide range of cosmic scales. The black line represents the expected linear matter power spectrum from the  $\Lambda$ CDM model and the dotted one the behavior of non-linearities for small scales. The bottom panel represents the deviation of the data from the Planck best fit  $\Lambda$ CDM 3D matter power spectrum.



## CMB power spectrum

CMB is not completely smooth, instead, it presents a series of temperature anisotropies with respect to its blackbody distribution (see Figure 2.2) expressed in the form of

$$\frac{\delta T}{T}(\theta, \phi) = \frac{T(\theta, \phi) - \langle T \rangle}{\langle T \rangle}, \quad (2.46)$$

these anisotropies are of the order of  $\delta T \sim 10^{-5}$  (Figure 2.13a show these anisotropies exaggerated with respect of the mean CMB temperature). The CMB can be projected onto a 2D spherical surface and its anisotropies are commonly analyzed by expanding them in spherical harmonics such that:

$$\frac{\delta T}{T}(\theta, \phi) = \Theta(\hat{n}) = \sum_{l=0}^{\infty} \sum_{m=-l}^l a_{lm} Y_{lm}(\hat{n}), \quad (2.47)$$

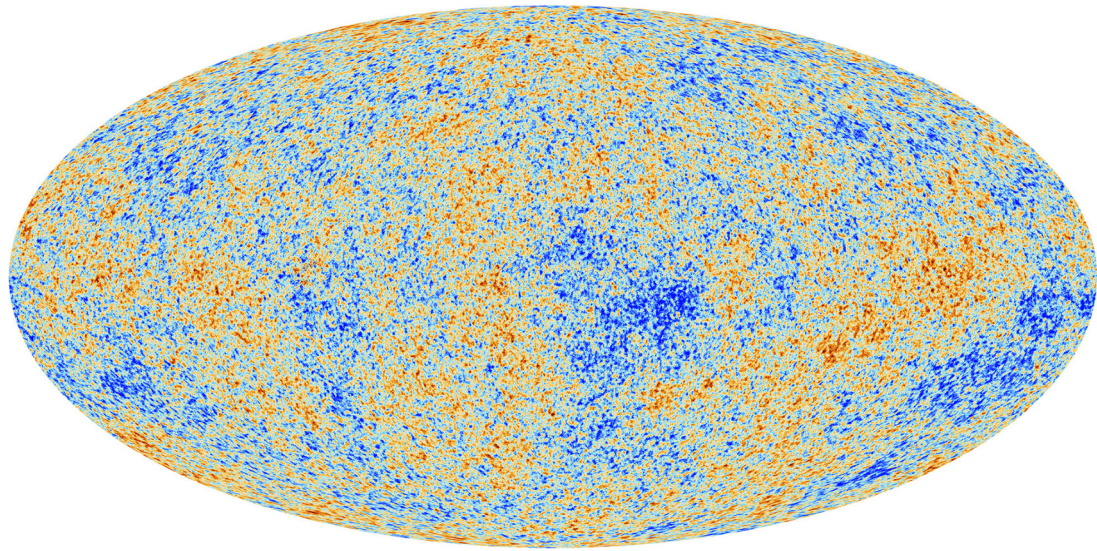
$$\text{where } Y_{lm} = \left( \frac{2l+1}{4\pi} \frac{(l-m)!}{(l+m)!} \right)^{0.5} P_m^l(\cos\theta) e^{im\theta}, \quad (2.48)$$

The set of equations in (2.47) represents the spectral decomposition of the CMB temperature anisotropies<sup>21</sup>. In equations (2.47) and (2.48),  $P_m^l$  are the Legendre polynomials,  $l$  runs from 0 to  $\infty$ ,  $-l \leq m \leq l$  and the multipole moment  $l$  is function of angular separation as  $l = \pi/\Delta\theta$ <sup>22</sup>. The angular power spectrum is the variance as  $C_l = \langle |a_{lm}|^2 \rangle$  for each spherical harmonic  $Y_{lm}$ .

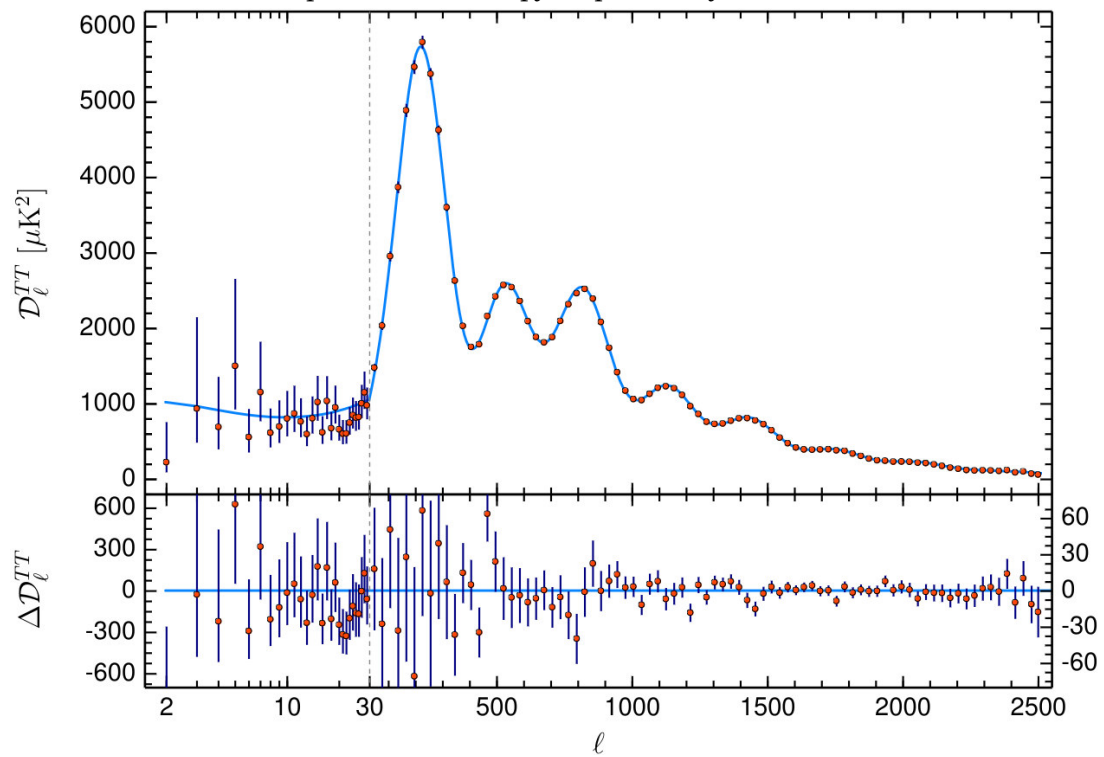
Figure 2.13b shows the great accordance between the  $\Lambda$ CDM model expected value and the observations. The peaks are the result of sound waves in the primordial plasma and their relative positions and heights give constraints to the cosmological parameters.

<sup>21</sup>The spherical harmonic decomposition of the CMB is similar to the three dimensional decomposition of the  $P_m(k)$  into Fourier modes mentioned before (Dodelson and Schmidt, 2020).

<sup>22</sup>Also contemplating that  $a_{lm} = \int_{\theta=-\pi}^{\pi} \int_{\phi=0}^{2\pi} \Theta(\hat{n}) Y_{lm}^*(\hat{n}) d\Omega$ .



(a) CMB temperature anisotropy map taken by the Planck satellite



(b) Angular power spectrum of the CMB temperature anisotropy in terms of multipolar moment (angular scale)

Source: (a) [ESA \(2013\)](#) (b) [Planck-Collaboration et al. \(2020a\)](#)

**Figure 2.13:** CMB temperature anisotropy map.

## THE LYMAN- $\alpha$ FORESTS AND THE FLUX POWER SPECTRUM

### 3.1 Active galactic nuclei

Back to the first decade of the XX century, astronomers were observing strong emission lines in the spectra of some spiral galaxies (Fath, 1909). Carl Seyfert began the systematic study of these particular objects in the 40s decade (Seyfert, 1943); he is also credited for the detection of galaxies featuring highly luminous central regions, a kind of galaxies named Seyfert in his honor.

Due to the technological advances in radio antennas and radars led by the historical context at that epoch, radio astronomy emerged as a new way to study the sky during the 30s decade (Jansky, 1933; Reber, 1944; Bolton, 1948; Bolton et al., 1949). Objects similar to Seyfert galaxies were exhibiting spectra characterized by a continuous emission, exceptionally broad emission lines, and occasional absorption lines. These emission patterns were being observed within the optical spectrum and, on occasion, extend into the realm of radio frequencies.

In 1963, Schmidt (1963) reported the 3C273 star-like<sup>1</sup> radio emitting object, also featuring four broad emission lines and an extremely large redshift for that time ( $z = 0.158$ ). Many theoretical models were developed over time aiming to explain the physical foundation of these objects and the observational properties they showed (Alfven and Herlofson, 1950; Salpeter, 1964; DeYoung and Axford, 1967; Lynden-Bell, 1969; Khachikian and Weedman, 1974; Fanaroff and Riley, 1974; Miller et al., 1978; Heckman, 1980). This led to what we know today as the the orientation unified scheme of Active Galactic Nuclei (Shields, 1999; Beckmann and Shrader, 2012).

An Active Galactic Nucleus (AGN) is a compact and exceptionally energetic region at the center of a galaxy, characterized by the presence of a supermassive black hole (SMBH) surrounded by an accretion disk of gas and dust (Figure 3.1). The intense gravitational forces exerted by the black hole cause the infalling material to release enormous amounts of energy. This is one of the most efficient radiation production

---

<sup>1</sup>Point-like or not resolved

mechanisms in the Universe ( $\eta = 10 - 40\%$ ) (Ananna et al., 2020) being even more efficient than nuclear fusion ( $\eta \sim 0.8\%$ )<sup>2</sup>.

The process of energy generation in AGNs is driven by accretion, and it results in the production of extremely bright and variable emission that can outshine the entire galaxy in which the AGN resides (in some cases even  $\sim 10^3$  times brighter than its host galaxy). AGNs are crucial objects of study in astrophysics, as they have a profound impact on the dynamics and evolution of their host galaxies, and their emission provide valuable insights into the physical processes occurring in the vicinity of supermassive black holes (Elvis, 2009; Beckmann and Shrader, 2012).

In the same order of ideas, under the paradigm of the unified AGN model, these objects are characterized by having gas rotating around them at different velocities (broad line region and narrow line region), a toroidal zone made of dust and a synchrotron emission jet, as depicted in Figure 3.1.

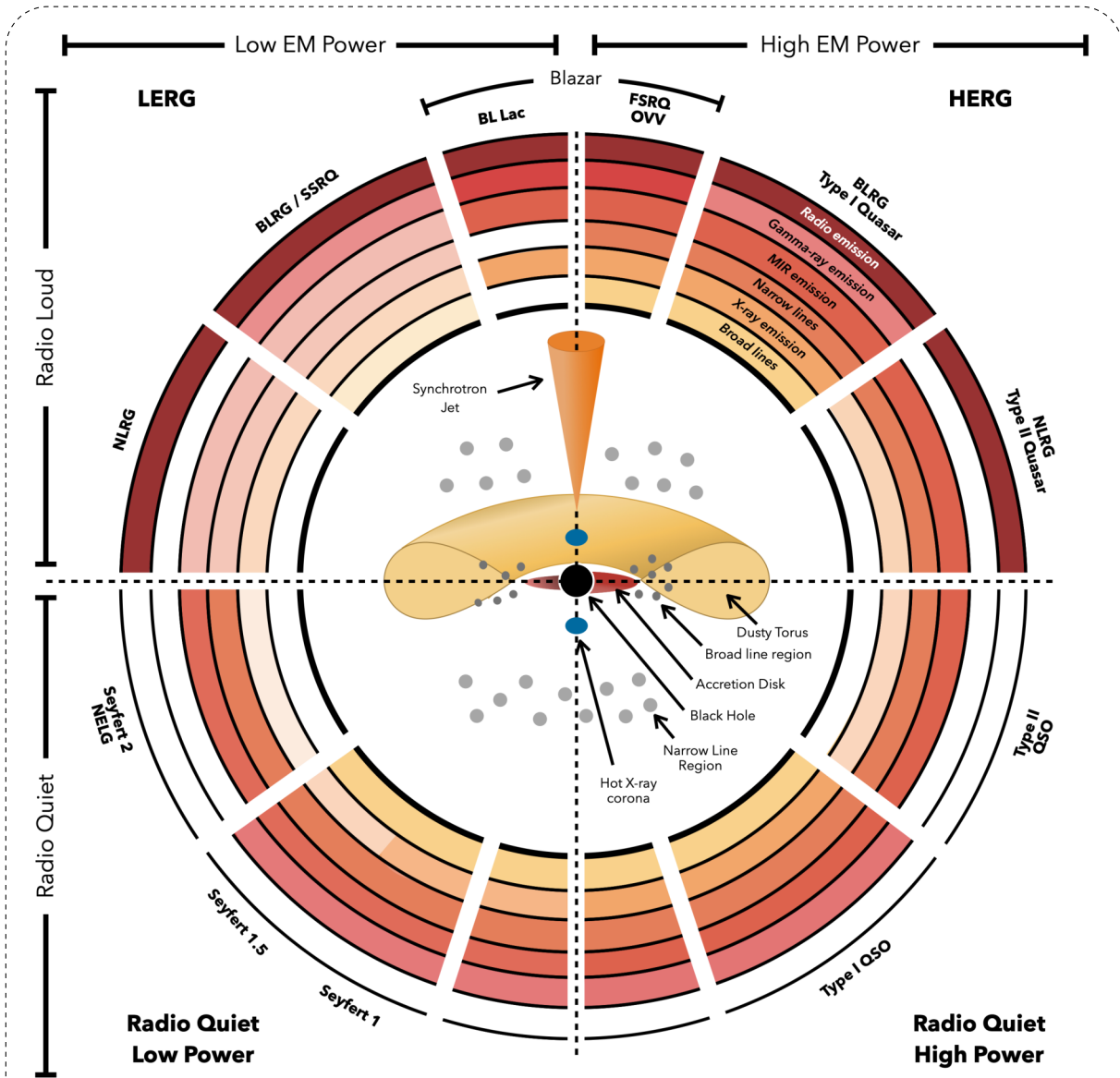
As Figure 3.1 suggests, the orientation of the AGN to one particular observer line of sight defines its spectral features. The focus of this work is centered on a particular type of AGN called quasars ("quasi-stellar objects") or QSO<sup>3</sup>. A quasar is a class of extremely luminous type of AGN that exhibits exceptional radiative output across a broad range of the electromagnetic spectrum, spanning from radio waves to gamma rays.

As Figure 3.2 shows, the spectra of quasars in the optical range is characterized by a (non-stellar) continuum mostly generated by the accretion disk of the quasar (Elvis, 2009) which follows a power law in the form of  $F_\nu \propto \nu^{\alpha_\nu}$  between  $\sim 1200 - 5000 \text{ \AA}$ , where  $\alpha_\nu \sim 0.44$  (Risaliti and Elvis, 2004) and a set of broad emission lines ranging between  $1\,000$  to  $40\,000 \text{ km}\cdot\text{s}^{-1}$ . These emission lines are associated with the rotating heated gas very close to the central engine of the quasar (broad line region in Figure 3.1), that is, radiation from the disc absorbed by these gas clouds and re-emitted as broad emission peaks in the spectrum.

---

<sup>2</sup>Energy conversion efficiency:  $\eta = P_{\text{out}}/P_{\text{in}}$ .

<sup>3</sup>Although there is a difference between QSO and quasar objects (radio quiet and radio loud respectively), through the text the terms could be interchanged indistinctively.



Source: [Thorne et al. \(2022\)](#)

**Figure 3.1:** Schematic representation of the current paradigm of AGNs in the orientation unified scheme. The type of object observed (the spectrum) depends on factors like the viewing angle and presence of significant jet emission (radio loud or quiet). The terms LERGs and HERGs (low/high excitation radio galaxies) refers to the radiative efficiency of accretion into the SMBH. A thorough definition of BLRG, NLRG, NELG, FSRQ, SSRQ, OVV, QSO and Seyfert objects can be found in [Thorne et al. \(2022\)](#) and [Beckmann and Shrader \(2012\)](#).



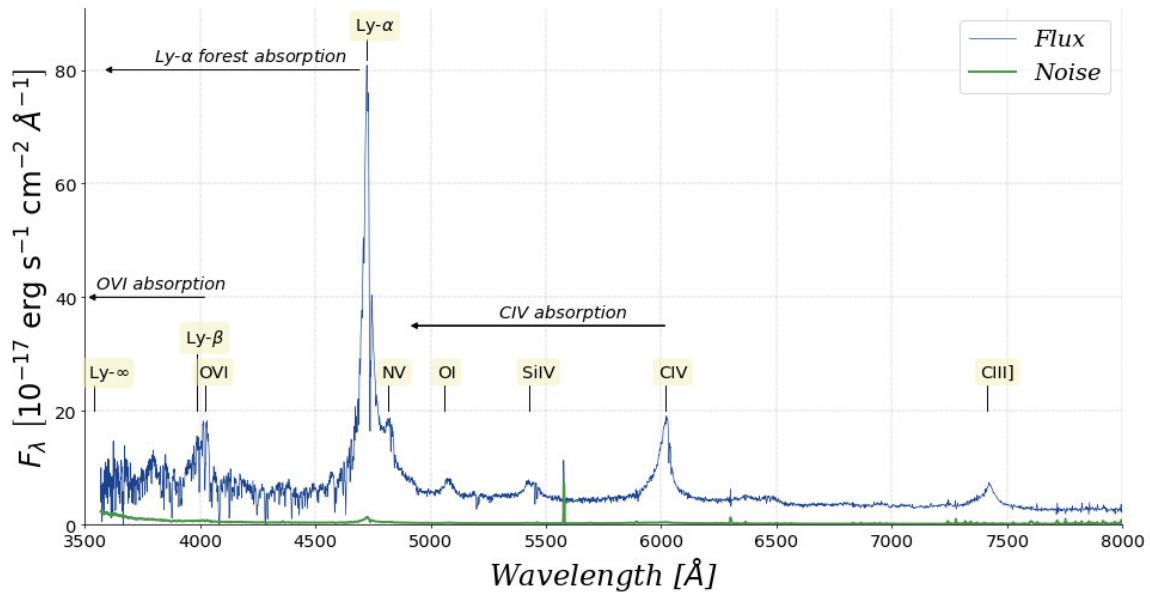


**Figure 3.2:** A quasar spectrum (plate-mjd-fiberid = 7339-56799-0379) from eBOSS DR14 at redshift  $z = 2.884$ . The quasar continuum, a set of broad emission lines and the pattern of associated absorption lines can be seen.

In the same way, these objects are characterized by their point-like appearance and are among the most radiant entities observed in the universe ( $10^{11} - 10^{14} L_{\odot}$ ). Quasars' cores are primarily distinguished by the presence of a supermassive black hole in a volume of radius about 10 parsecs, these black holes typically have masses ranging from  $10^6$  to  $10^9 M_{\odot}$  (Schneider, 2014)<sup>4</sup>.

Given their distinctive high luminosity, quasars are among the most distant and oldest observable objects in the night sky. The furthest quasar ever detected until 2021 had a redshift of  $z = 7.642$  (Wang et al., 2021), however, on August 7, 2023, Whalen et al. (2023) reported a quasar with a supermassive black hole mass of  $4 \times 10^7 M_{\odot}$  at redshift of  $z = 10.3$ , this using the JWST NIRcam brand new facility and data from the Chandra X-ray observatory. This measurement represents the furthest quasar detection ever made corresponding to a cosmic time of 450 Myr after the Big Bang.

<sup>4</sup> $M_{\odot} \sim 2 \times 10^{30}$  kg and  $L_{\odot} \sim 3.828 \times 10^{26}$  W stand for solar mass and solar luminosity respectively.

### 3.2 The intergalactic medium

The vast expanse of intergalactic space is permeated by a continuous medium of ionized gas known as the Intergalactic Medium (IGM). Simulations indicate that the IGM serves as the primary repository of baryonic matter originating from the Big Bang, making it the primary source of material from which galaxies were born. The presence of metal systems<sup>5</sup> within the IGM also reveals that it underwent early enrichment from stellar evolution events, underscoring a close link between galaxy formation and the IGM itself (Meiksin, 2009; McQuinn, 2016).

Although intergalactic medium is essentially ionized, the gas has a neutral fraction ( $x_{HI}$ ) of less than  $\sim 1/10^5$  (Meiksin, 2009; Dijkstra, 2019). This proportion arises considering the equilibrium between charged and neutral particles and electronic collisional ionization and recombination rates given by

$$x_{HI} = \frac{\alpha_A(T) n_e}{\Gamma} \quad (3.1)$$

where  $\alpha_A(T)$  is the radiative recombination coefficient<sup>6</sup>,  $n_e$  is the electron number density, and  $\Gamma$  is the HI photoionization rate (Madau, 2001; Meiksin, 2009; McQuinn, 2016).

Furthermore, the IGM assumes a crucial role in our understanding of galaxy evolution. The formation of stars within galaxies depends on their matter content, and the IGM serves as an extensive reservoir of this material, supplying galaxies with the essential resources needed for their long-term development. From a cosmological viewpoint, exploring the distribution of baryons within the IGM is very useful because it reflects the density and structure of dark matter (Miralda-Escude et al., 1996; Mucket, 1996; Tomlinson et al., 2018).

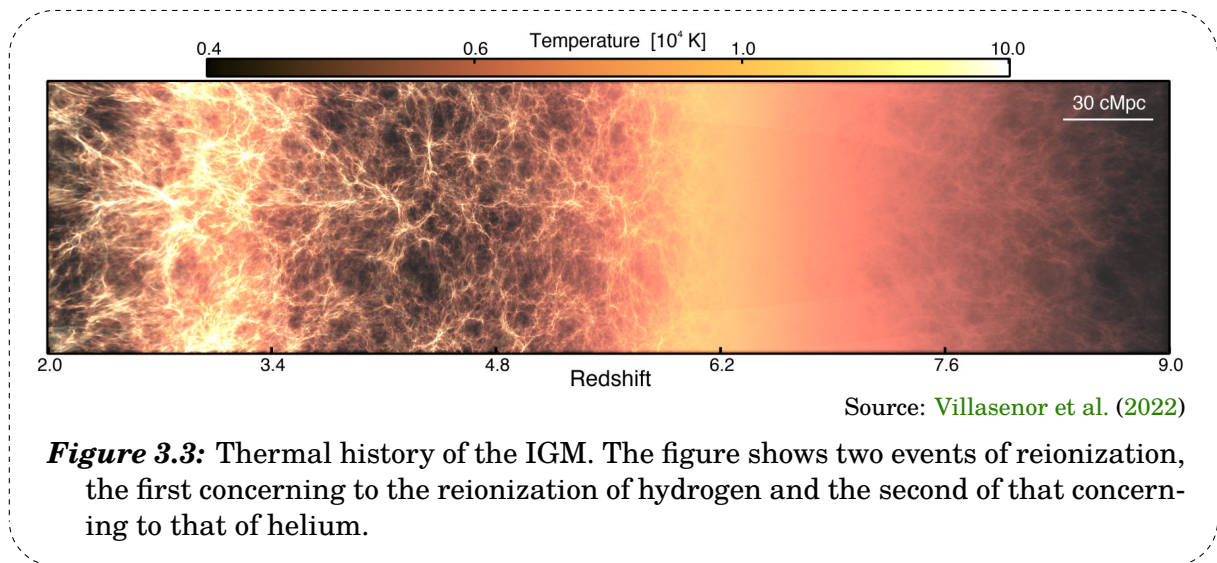
Characterizing the temperature of the gas is a key topic of research in the study of the IGM, this because it provides constraints on the conditions for the formation of structures in the Universe and serves as a proxy for other physical properties of the IGM *e.g.* ionization level. Hui and Gnedin (1997) suggested an empirical semi-analytical relation describing the temperature-density relation of the IGM,

<sup>5</sup>In cosmology, and astronomy in general, elements with an atomic number  $Z > 2$  are called metals.

<sup>6</sup>The electron cross section ( $\sigma_n$ ) times the electron velocity ( $v_e$ ), taking the average across a thermal distribution and adding up across all atomic levels *i.e.*  $\alpha_A(T) = \sum \langle \sigma_n v_e \rangle$ .

$$T(\rho, z) = T_0(z) \times \left( \frac{\rho}{\langle \rho \rangle} \right)^{\gamma(z)-1}, \quad (3.2)$$

commonly useful for  $\delta_b \lesssim 5$  and  $z = 2 - 4$ , where  $\rho$  is the baryonic density,  $T_0(z)$  is a normalization temperature (temperature at average density) and  $\gamma(z)$  is the logarithmic slope that describes the temperature-density relation. In the same way, equation (3.2) ceases to be valid in regions where overdensities are high enough to render the IGM physics highly non-linear. In the context of hydrodynamical simulations,  $T_0(z)$  and  $\gamma(z)$  are varied to fit observations.



Given that the ionization degree and the thermal properties of the IGM are governed by a not completely understood UV background (AGNs and star-forming galaxies), the study of the IGM is an open field of research. Finally, Figure 3.3 and Table 3.1 depict the history and evolution of the intergalactic medium within the framework of the  $\Lambda$ CDM model.



<i>Redshift (z)</i>	<i>Gas temperature</i>	<i>Description</i>
1100 – 147	$\gtrsim 10^3 - 400 \text{ K}$	The temperature of the gas is linked to the temperature of the CMB through Compton scattering.
147 – 20	$\sim 2 \text{ K}$	The gas no longer cools adiabatically as there are not enough free electrons to effectively link its temperature with that of the CMB photons.
20 – 6	$\sim 10^4 \text{ K}$	During the Epoch of Reionization, which spans $\sim 500 \text{ Myr}$ , the IGM is exposed to X-rays and UV radiation from the earliest stars and AGNs. This radiation ionizes the HI and HeI, transforming them into HII and HeII, thus raising the temperature of the IGM through photoionization heating.
6 – 4.5	$\sim 5000 \text{ K}$	UV photons travel freely through the IGM over vast distances. The IGM stays in ionization balance with this ambient radiation, and it cools as the universe expands.
4.5 – 3	$\sim 14000 \text{ K}$	The activity of AGNs reaches its peak, resulting in the ionization of HeII to HeIII and the subsequent re-warming of the IGM.
3 – 0	$\sim 10000 \text{ K}$	The IGM again cools through adiabatic expansion.

**Table 3.1:** IGM redshift-temperature evolution since recombination. Adapted from Youles (2021).

### 3.3 Lyman- $\alpha$ forests

#### Ly- $\alpha$ radiative transfer

The Lyman atomic series is a sequence of spectral lines in the electromagnetic spectrum, which corresponds to transitions of electrons within hydrogen atoms between higher energy levels ( $n > 1$ ) and the first energy level ( $n = 1$ ). Electrons can transit

between these levels by either absorbing or emitting energy in the form of photons. In the Lyman series, these transitions (emitted photons) have specific energies and wavelengths, that fall in the ultraviolet part of the spectrum. One can derive these energy levels from a Hamiltonian for a hydrogenic ion with charge  $Ze$  in the form of,

$$H^{(0)} = \frac{-\hbar^2 \nabla^2}{2\mu} - \frac{Ze^2}{r}, \quad (3.3)$$

and the associated energy levels behaves as,

$$E_n = -\frac{1}{2} \mu c^2 \frac{(Z\alpha)^2}{n^2}. \quad (3.4)$$

In equation (3.3),  $\mu$  is the reduced mass and  $\alpha$  in (3.4) is the fine-structure constant. Lyman series are transitions linked to the ground state  $E_1$ , so, in order to get the wavelengths values shown in Table 3.2 one need to solve the  $\lambda$  value at rest as,

$$\lambda_{rest,n} = \frac{hc}{E_n - E_1}. \quad (3.5)$$

<b>Transition</b>	<b><math>n</math></b>	<b><math>E_n - E_1</math> (eV)</b>	<b><math>\lambda_{rest}</math> (Å)</b>
Ly- $\alpha$	2	10.20	$\sim 1216$
Ly- $\beta$	3	12.10	$\sim 1026$
$\vdots$	$\vdots$	$\vdots$	$\vdots$
Ly- $\infty$	—	13.60	$\sim 911.75$

**Table 3.2:** HI Lyman series lines.

The Lyman- $\alpha$  (Ly- $\alpha$ ) line corresponds to the shift between the first excited state and the fundamental state, while the Lyman- $\beta$  (Ly- $\beta$ ) line corresponds to the transition between the second excited state and the fundamental state. The rest frame wavelength for these transitions measure  $\sim 1216$  Å and  $\sim 1026$  Å respectively. As the quantum number  $n$  approaches infinity, the Lyman series gradually converges to a fixed wavelength, denoted as Ly- $\infty$ , which is also known as the Lyman limit, with

a value of 911.75 Å. As one approach Ly-∞, the individual Lyman lines become progressively less distinct eventually blending together (Dijkstra, 2019). This transitions can be viewed as emission lines in a quasar spectra produced by the heated gas of the AGN (see Figure 3.2).

Now, considering a free-streaming photon with frequency  $\nu = c/\lambda$ , it is convenient to define what is known as the optical depth ( $\tau$ ). The optical depth quantifies how opaque a medium is to radiation along its path, indicating the extent of light absorption as it travels through the medium. Intensity decreases exponentially with increasing optical depth: a higher optical depth implies greater opacity ( $\kappa(\nu)$ ) and/or a greater cross section coefficient ( $\sigma(\nu)$ ) along the radiation path. This means,

$$d\tau(\nu) = (\kappa(\nu) + \sigma(\nu))dr . \quad (3.6)$$

Optical depth varies with wavelength and represents the specific effects of light traveling through a particular material, with greater optical depth indicating greater effects, especially over extended distances. An optical depth much greater than 1 (optically thick medium) indicates that photons along this path are predominantly absorbed or scattered, whereas an optical depth much less than 1 (optically thin medium) suggests that photons tend to pass through the medium. Optical depth is calculated by integrating the product of the material's absorption coefficient ( $\alpha_\nu$ ) over the path traversed by the light in such way that,

$$\tau_\nu(r) = \int_{r_0}^r \alpha_\nu(r')dr' , \quad (3.7)$$

where  $\alpha_\nu = n\sigma_\nu + \rho\kappa_\nu$ ,  $n$  represents numerical density and  $\rho$  is volumetric mass density. Additionally, optical depth is a proxy of the number of mean free paths a photon undergoes as it passes through the medium, accounting for variations in opacity and density along the path (Rybicki and Lightman, 1991). The fraction of transmitted flux for a frequency  $\nu$  is given by

$$F_\nu = \frac{f_{out}(\nu)}{f_{in}(\nu)} = e^{-\tau(\nu)} . \quad (3.8)$$

Finally, one can estimate the column density of the material the light is interacting with, integrating the numerical density ( $n$ ) along the light path, that is,

$$N = \int_{r_0}^r n(r') dr' . \quad (3.9)$$

The Ly- $\alpha$  cross section coefficient is modeled as

$$\sigma_\alpha(\nu) = \left( \frac{\pi e^2}{m_e c} \right) \left[ \frac{1}{4\pi\epsilon_0} \right] f_\alpha \frac{\mathcal{V}}{\pi^{1/2} \Delta\nu_D} , \quad (3.10)$$

with  $\Delta\nu_D \equiv \frac{\nu_{1-n}}{c} \sqrt{\frac{2kT}{m}} ,$

where  $\mathcal{V}$  is a Voigt profile which encompasses the Lorentzian contribution by pressure broadening and resonance effects (damping wings), and a Maxwell profile (gaussian core) linked to thermal broadening (Dijkstra, 2019; Ravoux, 2022).

Considering the continuum radiation of a distant quasar under an expanding universe metric, it can be seen that its light undergoes a consequent redshift with respect to a locally at-rest observer. Reciprocally, the wavelength of some of these photons would coincide with the rest-wavelength of the Ly- $\alpha$  line at intermediate positions and it could be absorbed by neutral hydrogen at the exact value of  $z$  along a line of sight (Bahcall and Salpeter, 1965; Gunn and Peterson, 1965). That is, the positive detection of a flux decrement at rest wavelengths bluewards of the quasar Ly- $\alpha$  emission line (Madau, 2001; Dijkstra, 2019), as can be seen in Figure 3.4.

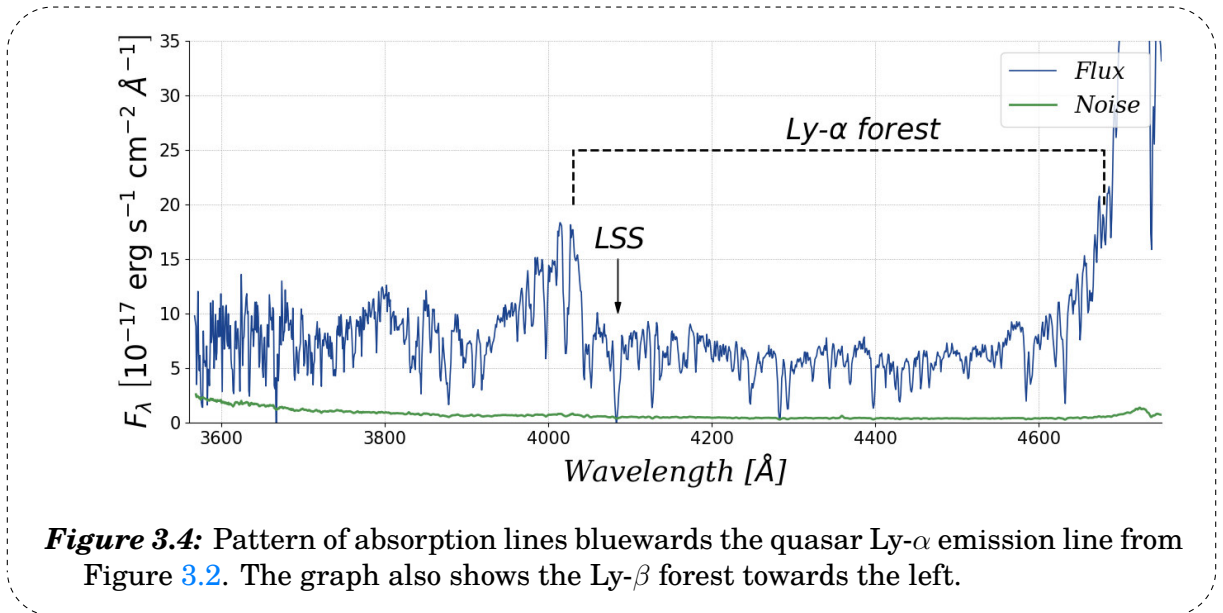


**Figure 3.4:** Pattern of absorption lines bluewards the quasar Ly- $\alpha$  emission line from Figure 3.2. The graph also shows the Ly- $\beta$  forest towards the left.

One can evaluate equations (3.7) to (3.10) considering a neutral hydrogen cloud capable of absorbing some of the radiation coming out of a radiation source (like, for example, a quasar). HI absorbs photons at  $\lambda_{\text{Ly-}\alpha} = 1216 \text{ \AA}$ , now given that some photons of the quasar are redshifted in the way that  $\lambda_{\text{Ly-}\alpha}(1 + z_{\text{QSO}})^{-1} < \lambda < \lambda_{\text{Ly-}\alpha}$ , every photon bluewards the Ly- $\alpha$  should appear absorbed in the spectrum (see also equation 3.14). The name of this phenomena is called the Gunn-Peterson effect (Gunn and Peterson, 1965; Schneider, 2014) and can be described as

$$\tau_{\alpha}(\nu) = \int n_{\text{HI}}(r)\sigma_{\alpha}(r, \nu)\delta_{\text{D}}\left(1 + z_{\text{abs}} - \frac{\nu_{\alpha}}{\nu}\right) dr . \quad (3.11)$$

Likewise, the formation of analogous forest-like structures occurs for different spectral lines due to the same underlying mechanism. Recalling Figure 3.4, we can use a similar approach to define the Ly- $\beta$  forest and the corresponding set of spectral features associated with other elements (metals) found in the IGM ( $\sim 5000 - 6000 \text{ \AA}$  in Figure 3.2).

The modern cosmological conception of the Ly- $\alpha$  forests proposes that the observed level of opacity comes from the baryonic matter density<sup>7</sup> (mainly ionized gas led by extragalactic ultraviolet background radiation), which, by its turn, follows the dark matter density fluctuations. With the previous statements, and within the optically thin approximation (low optical depth), this concept has led to the development of the formalism referred as the fluctuating Gunn-Peterson approximation or FGPA (Reisenegger and Miralda-Escude, 1995; Hui and Gnedin, 1997; Faucher-Giguère et al., 2007; Kooistra et al., 2022) defined as,

$$\tau \propto \rho_b^2 T^{-0.7} \equiv A(\rho_b/\bar{\rho}_b)^{\beta} . \quad (3.12)$$

In equation (3.12), the term  $A$  represents,

$$A \propto \left(\frac{1+z}{4}\right)^6 \left(\frac{\Omega_b h^2}{0.0125}\right)^2 \left(\frac{T_0}{10^4 \text{ K}}\right)^{-0.7} \left(\frac{\Gamma}{10^{-12} \text{ s}^{-1}}\right)^{-1} \left(\frac{H(z)}{100 \text{ km s}^{-1} \text{ Mpc}^{-1}}\right)^{-1} , \quad (3.13)$$

where  $\tau$  represents the optical depth of the Ly- $\alpha$  forest, the remaining parameters have been previously defined through the text.

<sup>7</sup>In fact, Ly- $\alpha$  forest contain about  $\sim 85\%$  of the total baryonic matter between  $2 \lesssim z \lesssim 4$ , for the local Universe, the majority of baryonic matter in form of gas is very difficult to detect given its temperature ranges (recall Table 3.1) (Meiksin, 2009; Schneider, 2014; McQuinn, 2016).

## Ly- $\alpha$ forests detection

When the light of distant quasars passes through the IGM it can be absorbed by intervening objects and hydrogen clouds that remain uncollapsed (Rauch, 1998; Meiksin, 2009)<sup>8</sup>. The pattern of absorption lines appearing bluewards the Lyman- $\alpha$  (Ly- $\alpha$ : 1216 Å at rest; Berk et al., 2001), particularly between  $2.0 \lesssim z \lesssim 6.0$ , allow us to infer the individual distance of these clouds and some of their attributes as a function of their redshift, that is,

$$\lambda = (1 + z_{\text{absorption}})\lambda_{\alpha} . \quad (3.14)$$

Thus, offering a proxy of the matter structure and distribution throughout the Universe at intermediate and small scales, properties of the IGM, the epoch of reionization, among others; as mentioned in previous sections, this characteristic pattern of absorption lines is known as Ly- $\alpha$  forests. The name "forests" alludes to the fact that this collection of absorption peaks in redshift space forms a forest of lines.

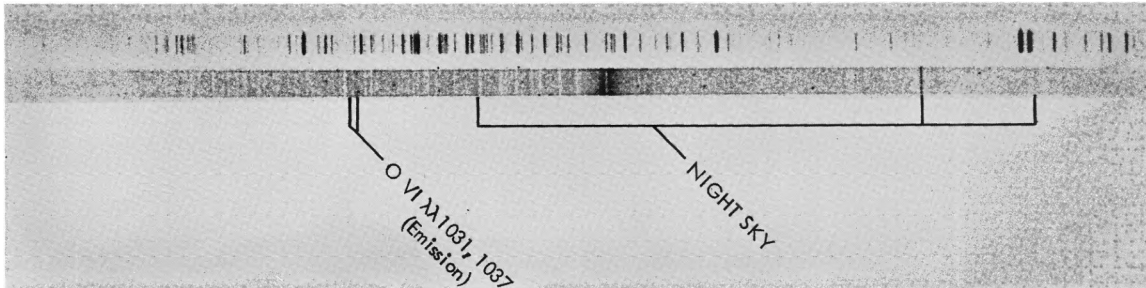
The first report of this phenomenon was made by Lynds (1971) for a quasar at  $z = 2.877$ . Figure 3.5 shows this characteristic pattern between the OVI and the Ly- $\alpha$  emission lines. Posteriorly, Sargent et al. (1980) studying a sample of six quasars between  $2.2 \lesssim z \lesssim 3.3$ , demonstrated that Ly- $\alpha$  forests originated by the interaction of the quasars' light with the IGM and did not belong to internal physical phenomena like outflows of ejected material in the AGNs.

That said, a second phenomenon emerged from the study of quasars' spectra with  $z \gtrsim 6.0$ . In this redshift regime, it can be observed a lack of flux in the range of wavelengths less than the line Ly- $\alpha$  at rest. This flux suppression is a consequence of the late appearance of the reionization epoch. After the dark ages (post-recombination era), the Universe gets entirely reionized as a product of the UV emission from the first radiating structures of baryonic matter (Population III stars and primordial AGNs; Meiksin, 2009; McQuinn, 2016). The medium through which this pristine light transits is optically thick because it is essentially HI. In the late epochs of the reionization of the Universe, this process produces a total suppression in the region corresponding to the Ly- $\alpha$  forest of quasars (Meiksin, 2009). The evidence of

---

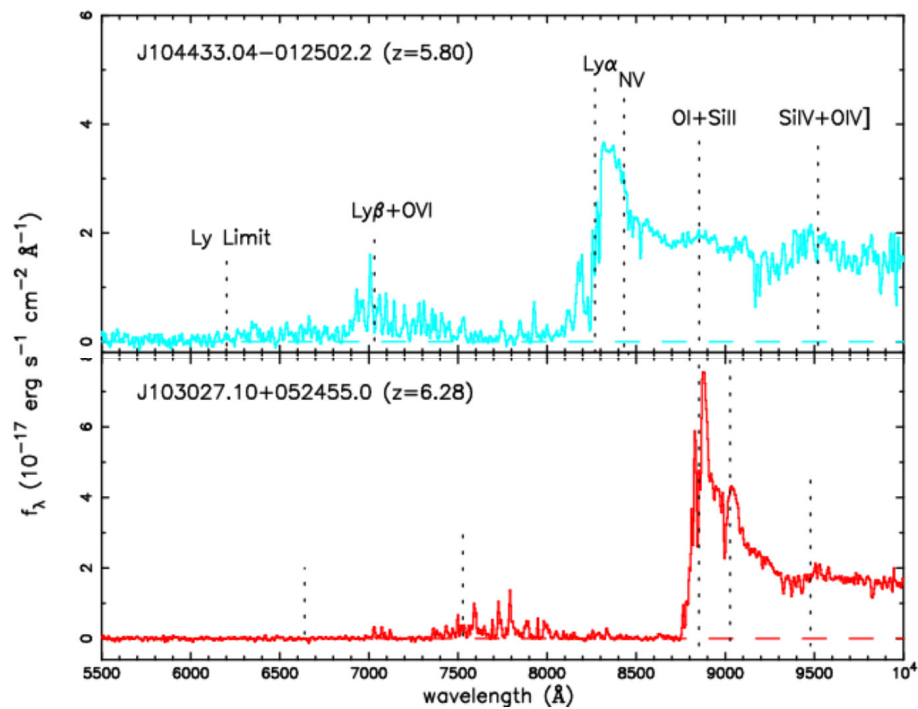
<sup>8</sup>An Andrew Pontzen animation showing the Ly- $\alpha$  absorption through IGM can be found [on this link](#).

this phenomenon was confirmed by [Becker et al. \(2001\)](#) (see [Figure 3.6](#)) and is also known as the [Gunn and Peterson trough](#).



Source: [Lynds \(1971\)](#)

**Figure 3.5:** The spectrum of the quasar 4C 05.34 taken at the Kitt Peak National Observatory. Aside from the central Ly- $\alpha$  and OVI emissions lines, the pattern of characteristic absorption lines can be seen.



Source: [Becker et al. \(2001\)](#)

**Figure 3.6:** Spectra of  $z \gtrsim 5.8$  quasars taken with the Keck/ESI instrument, featuring a lack of transmitted flux bluewards the Ly- $\alpha$  line (the [Gunn and Peterson trough](#)). The most prominent emission lines as well as the Ly- $\alpha$  limit are represented as dashed lines.



If one wants to study Ly- $\alpha$  forests in the optical range of the electromagnetic spectrum, it is mandatory to restrict the range of redshifts to values of  $z \gtrsim 2.0$ . This is because the Ly- $\alpha$  line and its associated forest is transmuted into values of  $\lambda \gtrsim 3650 \text{ \AA}$  as a product of the Universe's expansion (shorter wavelengths are absorbed by the atmosphere, quasars with  $z < 2$  must be analyzed with space telescopes). Moreover, the number of hydrogen clouds is much greater as the value of  $z$  increases, producing a denser and more compact pattern of absorption lines (Charlton and Churchill, 2001).

Likewise, for practicality, it is common to rule out quasars with  $z \gtrsim 6.0$ , because a total suppression of emission is observed at wavelengths less than the Ly- $\alpha$  line and they are very faint (poor quality values of transmitted flux).

### High column density objects

It is convenient to mention that the Ly- $\alpha$  forests belongs to a family of absorption lines that appears in quasar spectra. One can define two general classes of absorption line patterns in the spectra of quasars: (i) those generated by internal processes in the quasar and (ii) those produced by the interaction of quasar' light with the IGM.

In the first class, one can find the Broad Absorption Line or BAL quasars. BAL quasars are a type of quasar characterized by the presence of broad and often deep absorption lines in its spectral features (few thousand to tens of thousands of  $\text{km} \cdot \text{s}^{-1}$ ). These absorption lines arise due to the presence of high-velocity outflows of ionized gas in the vicinity of the supermassive black hole at the center of the quasar; these outflows are believed to be accelerated out from the outskirts of quasar accretion disks by radiative forces (Hamann et al., 2013; Rankine et al., 2020).

The outflowing gas absorbs light emitted by the quasar across a range of wavelengths, resulting in the distinctive absorption line patterns observed in the quasars' spectrum. These winds contain a variety of elements and ions, and they commonly absorb light emitted by the quasar in a set of specific wavelength ranges (C IV  $\lambda \sim 1549 \text{ \AA}$ , Si IV  $\lambda \sim 1397 \text{ \AA}$ , N V  $\lambda \sim 1240 \text{ \AA}$  and O IV  $\lambda \sim 1034 \text{ \AA}$ ). Figure 3.7 shows a typical spectrum of a BAL quasar.



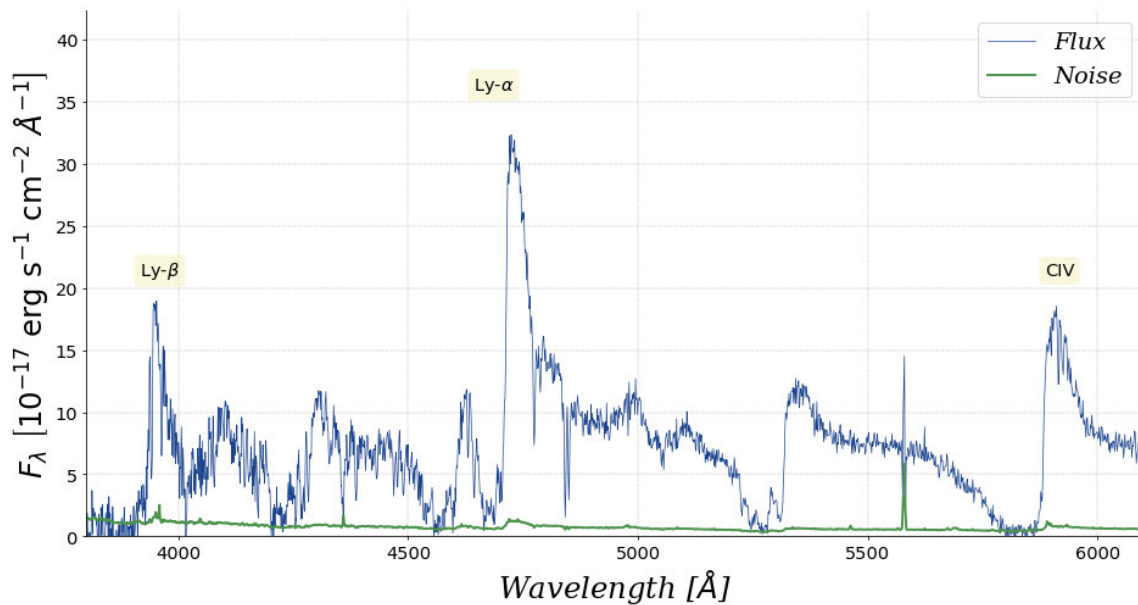


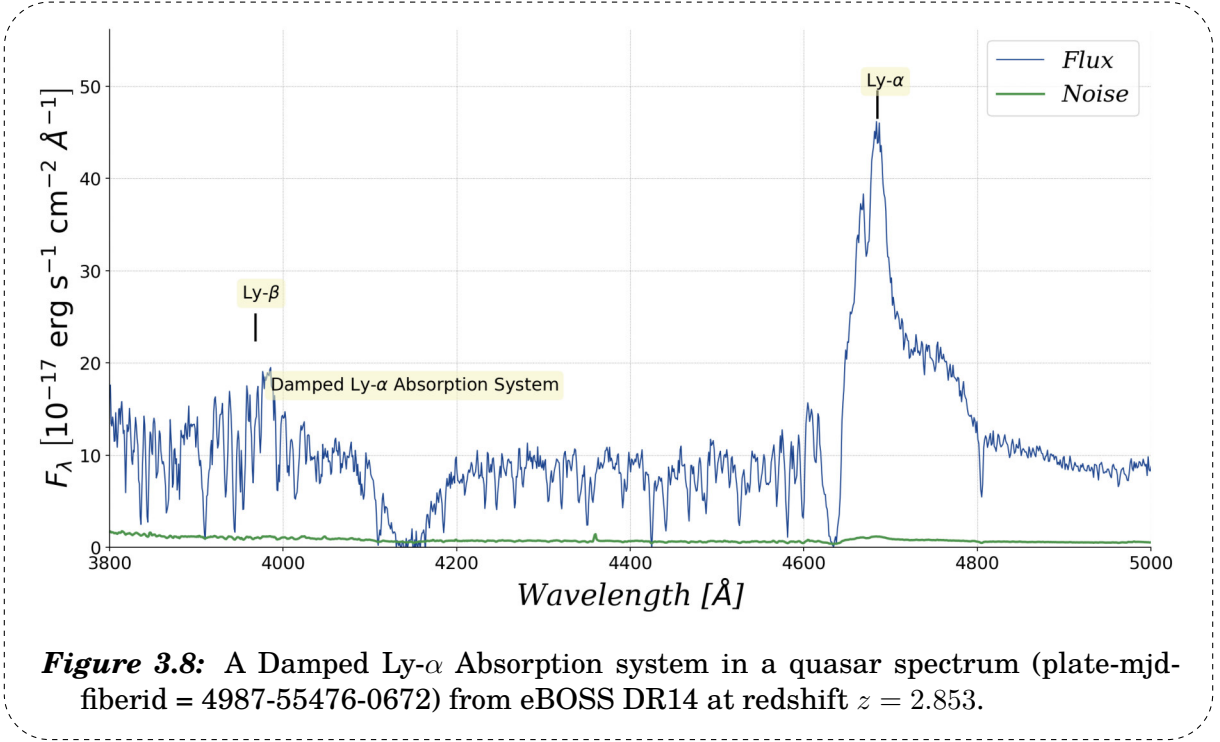
**Figure 3.7:** A Broad Absorption Line quasar spectrum (plate-mjd-fiberid = 6392-56331-0942) from eBOSS DR14 at redshift  $z = 2.829$ . The set of broad absorption features can be seen. A notable difference can be seen compared to the absorption patterns present in figures 3.2 and 3.4.

The second class of absorption lines are those related with the IGM. The main feature of distinction is the HI column density (in the case of HI absorption features) or their metallic origin:

- **Ly- $\alpha$  forests:** Ly- $\alpha$  forests correspond to absorption features with column density of  $\lesssim 10^{17} \text{cm}^{-2}$ <sup>9</sup> and are related to the filamentous structure of the gas in the Universe.
- **Lyman limit systems (LLS):** System with a higher column density than Ly- $\alpha$  forest (see Figure 3.4). These systems can not be disentangle from Ly- $\alpha$  forest absorption and are able to absorb photons above the Lyman limit.
- **Super Lyman limit systems (Super LLS):** They are commonly associated with the external part of galaxy halos and are the intermediate step between Ly- $\alpha$  systems and DLAs.

<sup>9</sup>Their column density is insufficient to saturate the absorption at  $2 \leq z \lesssim 6$  and their line profile could be fitted with a Gaussian function. In the same way, systems with  $N_{\text{HI}} \lesssim 10^{12} \text{cm}^{-2}$  are not currently observable (Ravoux, 2022).

- **Damped Ly- $\alpha$  Absorption systems (DLA):** The highest Ly- $\alpha$  column density systems. These systems are associated to the circumgalactic medium (they are essentially and almost completely composed by HI) and are used to model and constrict galaxy formation and evolution (Nagamine, 2007; Pontzen et al., 2008; Meiksin, 2009; Garratt-Smithson et al., 2021). Their line profile has to be fitted with a Voigt profile (Wolfe et al., 2005) (see Figure 4.15). Figure 3.8 shows a typical DLA system in a quasar spectrum.

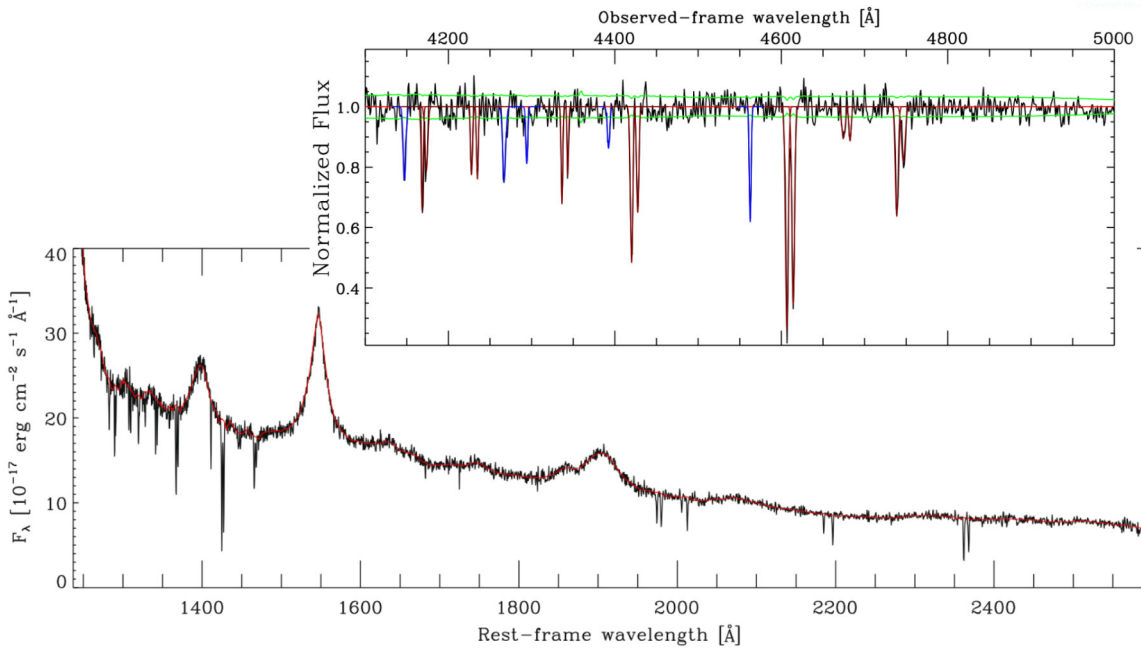


Absorber class	$N_{\text{HI}}(\text{cm}^{-2})$	T (K)	Size (kpc)	$b$	$N_0$	$\gamma$
Ly- $\alpha$ forest	$\lesssim 10^{17}$	5000 – 50000	$15 - 10^3$	15 – 60	6.1	2.47
LLS	$10^{17} - 10^{19}$	$\sim 30000$	-	$\sim 15$	0.3	1.50
Super LLS	$10^{19} - 2 \times 10^{20}$	$\sim 10000$	-	$\sim 15$	0.03	1.50
DLA	$> 2 \times 10^{20}$	100 – 10000	$\sim 10 - 20$	$\sim 15$	$\sim 0.03$	$\sim 1.5$

**Table 3.3:** Quasar absorption line system properties. In this table,  $b$  is the Doppler parameter of thermal velocity ( $\text{km}\cdot\text{s}^{-1}$ ) and  $\gamma$  is from  $dN/dz = N_0(1+z)^\gamma$  (distribution function). Adapted from Meiksin (2009).

Table 3.3 gives a brief description of HI absorbers, where  $N_{\text{HI}}$  is the column density of HI and  $T(\text{K})$  their characteristic temperature ranges.

- **Metal systems:** As figures 3.2 and 3.9 show, for each metallic emission line, there is an associated forest attached to it (following the reasoning of section 3.3). These metal forests can be used separately as an additional tracer of matter and are commonly merged with the Ly- $\alpha$  absorption bluewards the Ly- $\alpha$  emission line.



Source: Pan et al. (2014)

**Figure 3.9:** The figure shows a SDSS quasar spectrum at  $z = 2.2536$ , with a pseudo-continuum fit (continuous red line in lower panel), and the detail of metal absorption features (upper panel) of MgII (blue lines) and CIV (red lines). The green lines are the flux uncertainties.

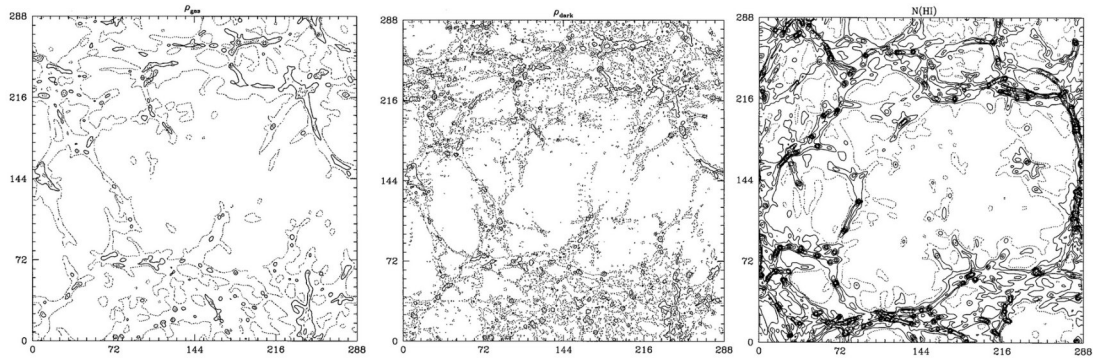
### 3.4 The one-dimensional flux power spectrum

The current structure formation model and the results obtained by the N-body hydrodynamical simulations from the early 90s (take as reference Figure 3.10a from Miralda-Escude et al. (1996)) say that neutral gas collapses under the gravitational influence of dark matter into flat and filamentous structures that are observed and interpreted as Ly- $\alpha$  forests in the spectra of quasars (Hernquist et al., 1996; Miralda-Escude et al., 1996; Weinberg et al., 2003). From Figure 3.10a it is evident how the gas distribution follows the dark matter distribution.

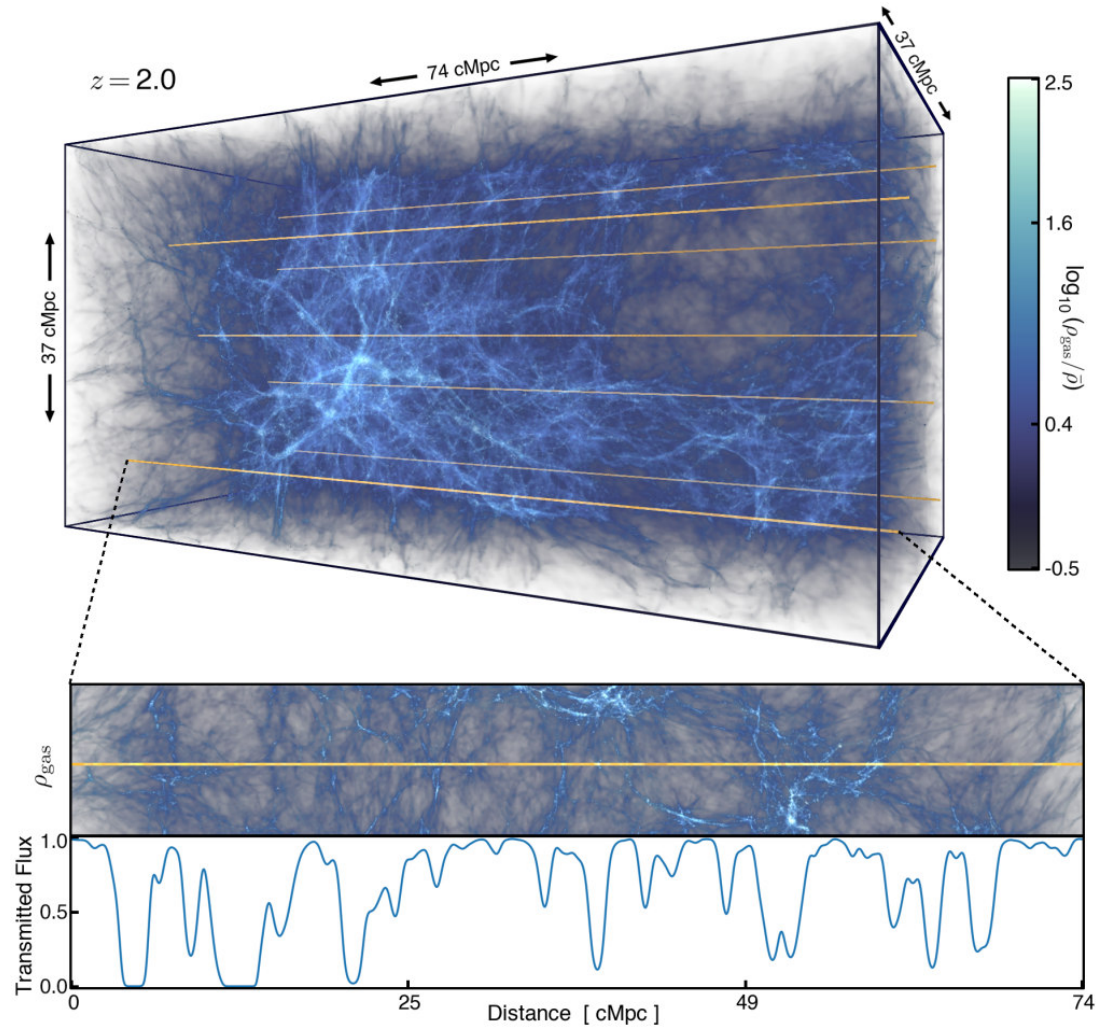
In the same way, Figure 3.10b shows the expected distribution of HI throughout the Universe as a result of a recent hydrodynamical simulation considering  $\Lambda$ CDM constraints. The figure also shows a fluctuation field of matter for a particular line of sight.

The absorption features in the Ly- $\alpha$  forests (like shape, depth and position) are influenced by the UV background (see section 3.2) and by the density and velocity field shaped by gravity. In these terms, dark matter serves as the large-scale backbone structure, which web-like shape is the product of an initial fluctuation field and the evolution of non-linear gravitational interactions (Villasenor et al., 2022), as discussed in chapter 2.

This argument implies that studying the neutral gas density structure is a good proxy of the dark matter structure. Alternatively, these structures could be visualized approximately as a density field along the line of sight of the quasar (see equation 2.45). Therefore, it is possible to recover a matter fluctuation power spectrum given the tight relation between the optical depth of the forest and the baryonic matter column density *i.e.* neutral hydrogen (Croft et al., 1998; Hernquist et al., 1996; Gnedin and Hamilton, 2002).



(a) Slice of a  $10 h^{-1}\text{Mpc}$  hydrodynamical cosmological simulation. From left to right, gas density ( $\rho_{gas}$ ), dark matter density ( $\rho_{CDM}$ ) and neutral column density ( $N_{HI}$ ).



(b) High-resolution cosmological simulation ( $L = 50 h^{-1}\text{Mpc}$ ,  $N = 2 \times 2048^3$ ) showing the gas density for the Universe at redshift  $z = 2$ . The absorption lines along the line of sight represent the HI column density and the quasar's flux transmitted by the IGM.

Source: (a) [Miralda-Escude et al. \(1996\)](#) (b) [Villasenor et al. \(2022\)](#)

**Figure 3.10:** Hydrodynamical simulations of the IGM.



Given that the line of sight of a quasar spectrum containing Ly- $\alpha$  forests is in essence a one-dimensional density field based on flux, it is congruent to define the transmitted flux power spectrum, from now on  $P_{\text{F1D}}$ .  $P_{\text{F1D}}$  can adopt the transmitted flux ( $F(v)$ ) as a dependent variable over a velocity interval  $v$  given the relation  $v/c = \Delta\lambda/\lambda$ . It is possible to transform wavenumber values from and to velocity units (or wavelength units) using the relation (Ravoux et al., 2023):

$$k[\text{s} \cdot \text{km}^{-1}] = k[\text{\AA}^{-1}] \times \lambda_{\alpha}[\text{\AA}](1+z)/c[\text{km} \cdot \text{s}^{-1}]. \quad (3.15)$$

In these terms, according to Croft et al. (1997, 2002),  $P_{\text{F1D}}$  can be obtained by decomposing the flux variations ( $\delta_F$ ) into Fourier modes ( $k = 2\pi/v$ ) as a function of an average normalized flux ( $\langle F \rangle$ ) expressed as,

$$\delta_F(v) = \frac{F - \langle F \rangle}{\langle F \rangle}, \text{ thus } \tilde{\delta}_F = \frac{1}{V} \int_0^V dv e^{-ikv} \delta_F(v), \quad (3.16)$$

which leads to,

$$P_F(k) = V \langle |\tilde{\delta}_F(k)|^2 \rangle. \quad (3.17)$$

According to Croft et al. (1997), one possible approach to obtain the fluctuations in the density field along the line of sight of the QSO would be reversing the relationships between the optical depth, the underlying baryonic matter distribution and the flux received, this inferring  $\tau$  from  $F$  and  $\rho$  from  $\tau$ . However, this mapping from  $\rho$  to  $F$  is not linear, involving a power law, and it relies on an unknown constant factor in the  $\tau - \rho$  relationship. Furthermore, accurately measuring  $\tau$  in saturated regions, where  $F$  is close to zero, can be challenging. The advantage of the Fourier decomposition method relies in the fact that the amplitude of the flux power spectrum depends almost exclusively on the amplitude of the matter power spectrum  $P_m(k)$ <sup>10</sup>.

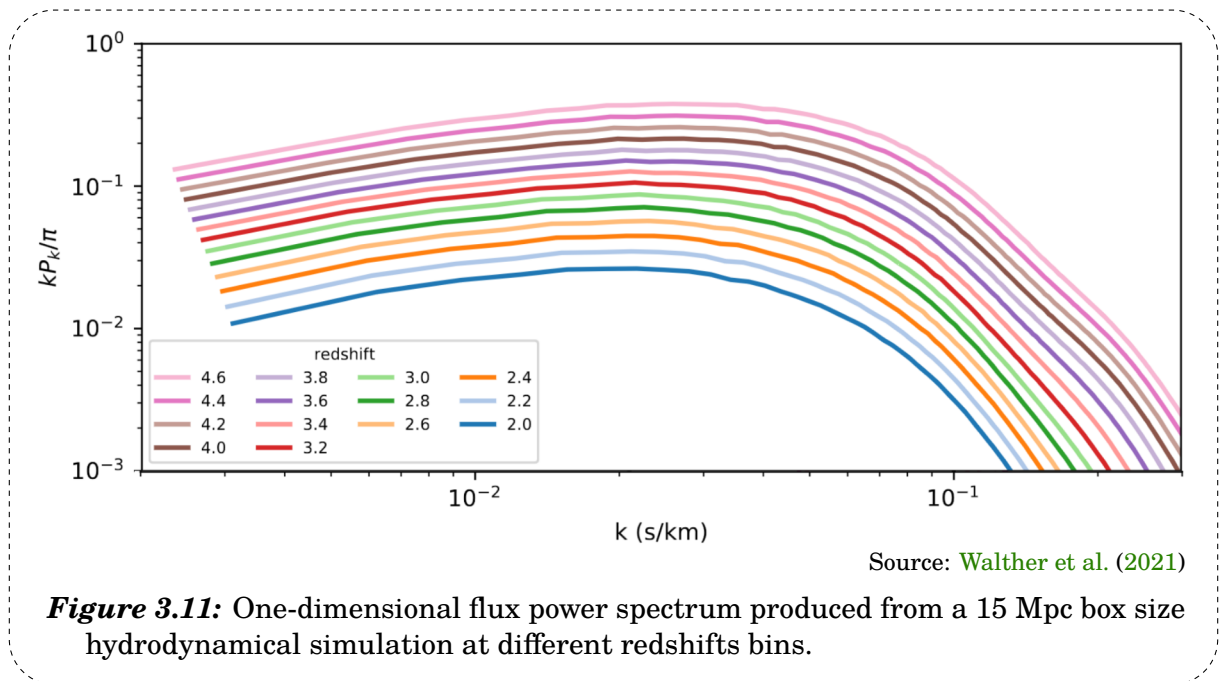
Multiple measurements with real and simulated spectra have shown that  $P_{\text{F1D}}$  estimation replicates the matter power spectrum quite well on large enough scales and ancient times, *i.e.* in the linear regime of structure formation (Croft et al., 1997;

---

<sup>10</sup>There is an alternative method to obtain the  $P_{\text{F1D}}$  out of Ly- $\alpha$  forest, this is using a maximum likelihood estimator as it is further discussed in Palanque-Delabrouille et al. (2013); Karaçaylı et al. (2020, 2022, 2023).

Weinberg et al., 2003; Kim et al., 2004; Zhan et al., 2005; McDonald et al., 2006; Palanque-Delabrouille et al., 2013; Walther et al., 2017; Irsic et al., 2017; Walther et al., 2019; Chabanier et al., 2019b; Villasenor et al., 2022; Mishra and Gnedin, 2022).

Contrary to the matter power spectrum, the amplitude of the flux power spectrum is inversely proportional to the redshift, however, normalizing the amplitude of the  $P_{\text{FID}}$  as function of the optical depth, one recovers the original pattern of increasing values at lower redshifts (Kim et al., 2004) (take Figure 3.11 as reference).



Coupled with hydrodynamic simulations (and different kinds of cosmological probes like the CMB or gravitational lensing), the  $P_{\text{FID}}$  measurements could be very useful in retrieving cosmological and astrophysical parameters like the matter density fluctuations rms ( $\sigma_8$ ), the spectral index of primordial density fluctuations ( $n_s$ ), the matter density parameter ( $\Omega_m$ ), the Hubble constant ( $H_0$ ), the temperature of the IGM ( $T_0(z)$ ), and the logarithmic slope that describes the temperature-density relationship  $\gamma(z)$ <sup>11</sup>. For further dissertations about it you can see Tegmark and Zaldarriaga (2002); Seljak et al. (2006); Borde et al. (2014); Chabanier et al. (2019b).

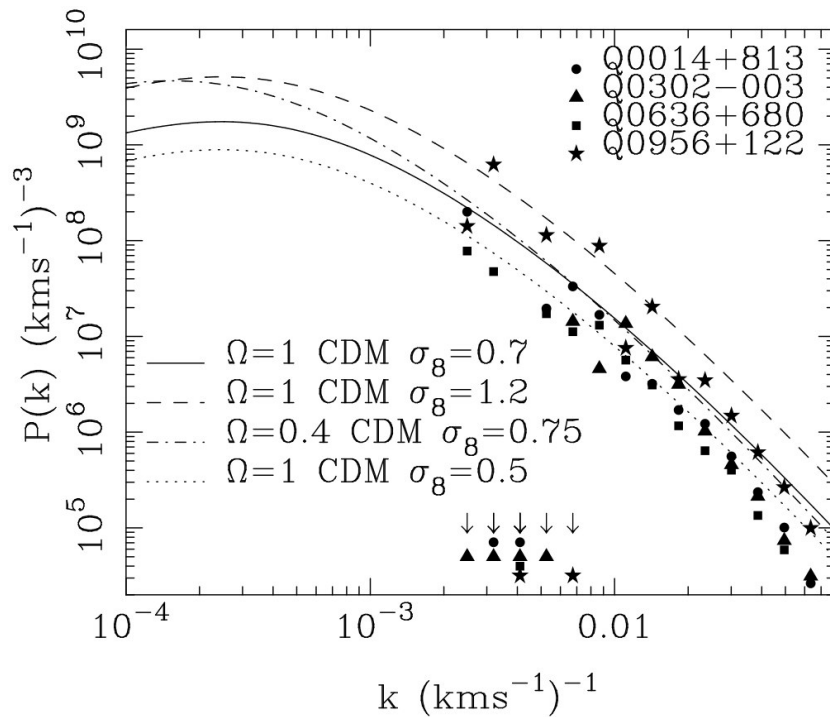
<sup>11</sup>Recalling sections A.1 and 3.2

Moreover, it is possible to retrieve an estimate of the actual matter power spectrum using the Kaiser equation, that is,

$$P_{3D}(k_{\parallel}, k_{\perp}, z) = b_{\delta}^2 P_m(k, z) \left(1 + \frac{\beta}{k_{\parallel}^2}\right)^2, \quad (3.18)$$

where  $b_{\delta}^2(k, z)$  is a density bias between baryonic matter (gas) and dark matter, and  $\beta$  is the redshift distortion parameter of the Ly- $\alpha$  forest<sup>12</sup> (Kaiser, 1987; Slosar et al., 2011; Palanque-Delabrouille et al., 2013; Chabanier et al., 2019a).

Croft et al. (1997) was the first work to present such an estimate, extracting the density field from the forest of a single quasar from the Keck telescope (HIRES). This work would mark the precedent in the estimation of the  $P_{\text{FID}}$  with Ly- $\alpha$  forests. Figure 3.12 shows one of the first comparisons between the estimation of the matter power spectrum and one extracted from Ly- $\alpha$  forests.



Source: Croft et al. (1998)

**Figure 3.12:** Matter power spectrum recovered from the Ly- $\alpha$  forest in four QSO. The theoretical linear power spectrum for different CDM models at the same mean redshift  $z = 2.9$  are also shown.

<sup>12</sup> $k^2 = k_{\parallel}^2 + k_{\perp}^2$



Since then,  $P_{\text{FID}}$  has been estimated from Ly- $\alpha$  forests with intermediate (McDonald et al., 2006; Palanque-Delabrouille et al., 2013; Chabanier et al., 2019b; Ravoux et al., 2023) and high resolution (Jamkhedkar et al., 2003; Kim et al., 2004; Walther et al., 2017; Karaçaylı et al., 2022) presenting an anticorrelation between spectral resolution and sample size.

McDonald et al. (2006) was the first work that estimated  $P_{\text{FID}}$  with a statistically robust sample proportional to  $10^3$  (3 035 quasars) between  $2.0 \lesssim z \lesssim 4.0$ , product of Data Releases 1 and 2 of the SDSS project. Being a statistically significant sample, the work by McDonald et al. (2006) made it clear that the estimation of the  $P_{\text{FID}}$  is quite sensitive to astrophysical systematics and intervening variables such as the presence of DLAs along the line of sight of the quasar, the resolution of the spectrograph, removal of skylines, the adjustment method for the continuum used, metal absorption lines of the quasar, SNR, among others (as well as many similar works that point it out such as Gnedin and Hamilton (2002); Palanque-Delabrouille et al. (2013); Chabanier et al. (2019b); Day et al. (2019) or Karaçaylı et al. (2020).

In these terms, Palanque-Delabrouille et al. (2020) pointed out that sometimes cosmological measurements are so precise that the interpretation of the data is limited by systematic rather than statistical errors, so the examination of systematic budgets is very important.

Chabanier et al. (2019b) computed a  $P_{\text{FID}}$  estimation (Figure 3.13) with a sample of 43 751 quasars with  $z > 2.1$  from the Data Release 14 of SDSS-IV /eBOSS. Figure 3.13 shows the evolution of the transmitted flux (hence the optical depth) of Ly- $\alpha$  forests through different cosmic epochs ( $z$ ) *i.e.* the level of clustering of the IGM. Moreover, Chabanier et al. (2019b) results showed great agreement with the results obtained by Palanque-Delabrouille et al. (2013) who used 13 821 quasars from the Data Release 9 of SDSS-III/BOSS.

To date, Chabanier et al. (2019b) work is the publication with the largest number of quasars analyzed in a  $P_{\text{FID}}$  calculation, which means good statistical confidence *e.g.* low redshifts bins in Figure 3.13. Finally, Table 3.4 shows the best parameter fit for astrophysical and cosmological parameters for Chabanier et al. (2019b) results, retrieved out of a tree smoothed particle hydrodynamical simulation and constrained with CMB data (Planck-Collaboration et al., 2016) and another  $P_{\text{FID}}$  estimation with enhanced spectral resolution (Irsic et al., 2017).

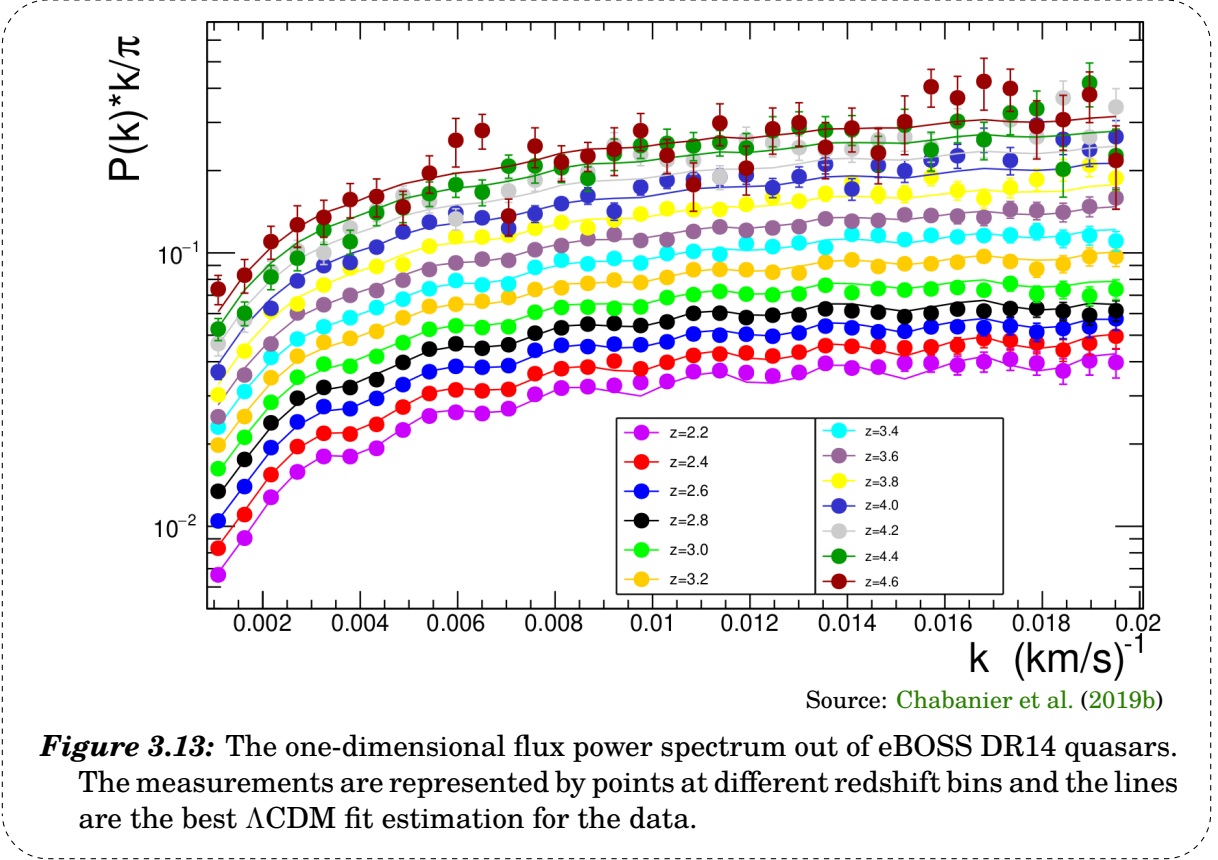


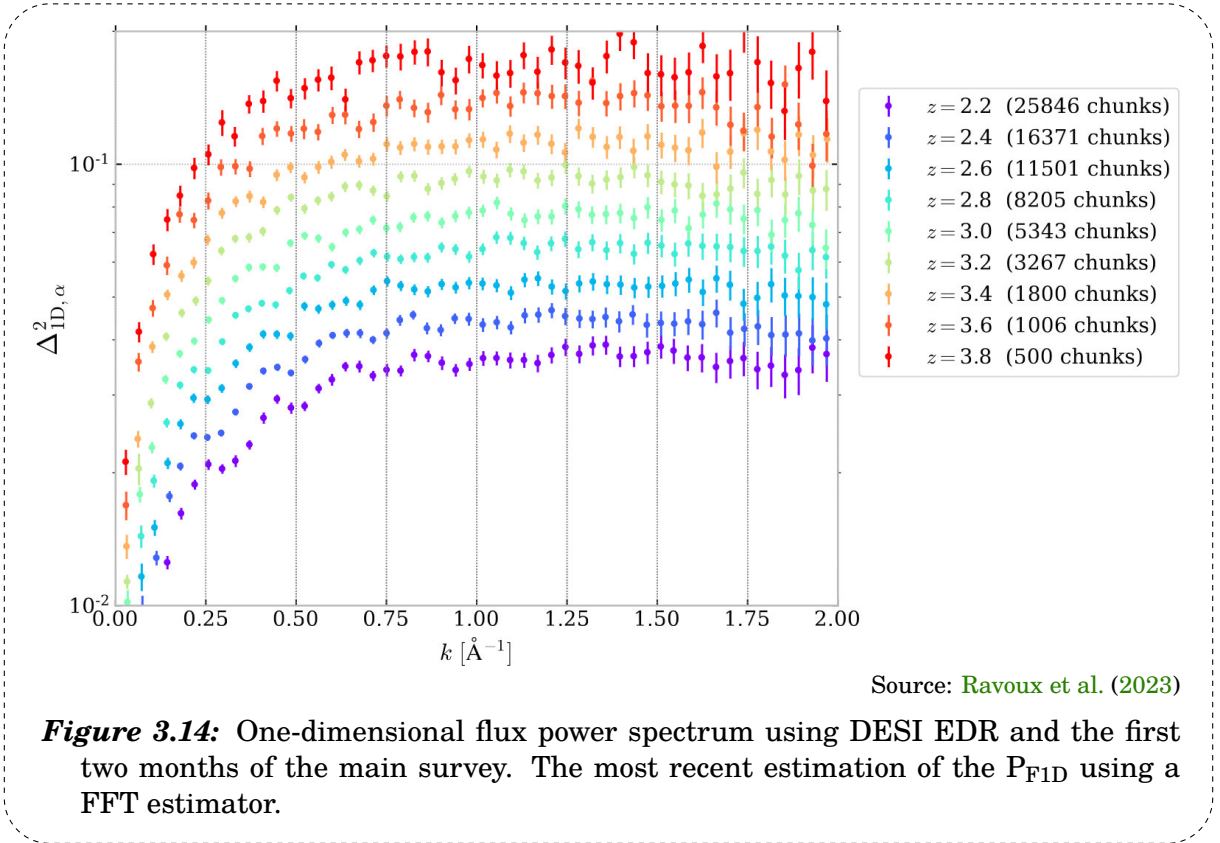
**Figure 3.13:** The one-dimensional flux power spectrum out of eBOSS DR14 quasars. The measurements are represented by points at different redshift bins and the lines are the best  $\Lambda$ CDM fit estimation for the data.

Parameter	Ly- $\alpha$ BOSS	Ly- $\alpha$ eBOSS	Ly- $\alpha$ eBOSS + XQ-100 + Planck (TT+lowE)
$T_0(z=3)$ ( $10^3\text{K}$ )	$8.9 \pm 3.9$	$10.3 \pm 1.7$	$13.7 \pm 1.5$
$\gamma$	$0.9 \pm 3.2$	$0.8 \pm 0.1$	$0.9 \pm 0.1$
$\sigma_8$	$0.855 \pm 0.025$	$0.820 \pm 0.021$	$0.804 \pm 0.008$
$n_s$	$0.937 \pm 0.009$	$0.955 \pm 0.005$	$0.961 \pm 0.004$
$\Omega_m$	$0.288 \pm 0.012$	$0.269 \pm 0.009$	$0.309 \pm 0.011$
$H_0$ ( $\text{km s}^{-1} \text{Mpc}^{-1}$ )	$67.1 \pm 1.0$	$67.1 \pm 1.0$	$67.6 \pm 0.8$

**Table 3.4:** Astrophysical and cosmological parameters obtained from eBOSS Ly- $\alpha$  forests (Chabanier et al., 2019b) and constrained with different probes (BOSS Ly- $\alpha$  forests (Palanque-Delabrouille et al., 2013), XQ-100 Ly- $\alpha$  forests (Irsic et al., 2017) and Planck data (Planck-Collaboration et al., 2016)). Adapted from Chabanier et al. (2019b).

Within the conclusions of [Chabanier et al. \(2019b\)](#), they also show the profound influence of the eight systematicities identified in the estimation of  $P_{\text{F1D}}$ . Furthermore, the authors suggest combining all the systematic errors in quadrature in order to improve the estimate of  $P_{\text{F1D}}$ .

The most recent publication about the computation of the  $P_{\text{F1D}}$  using a FFT estimator is the work presented by [Ravoux et al. \(2023\)](#), which used the brand new spectra of the DESI early data release plus two months of the main survey. They analyzed a total amount of 26 330 quasars getting an improvement in resolution on small scales given the technological advancement of the DESI instrument (Figure 3.14).

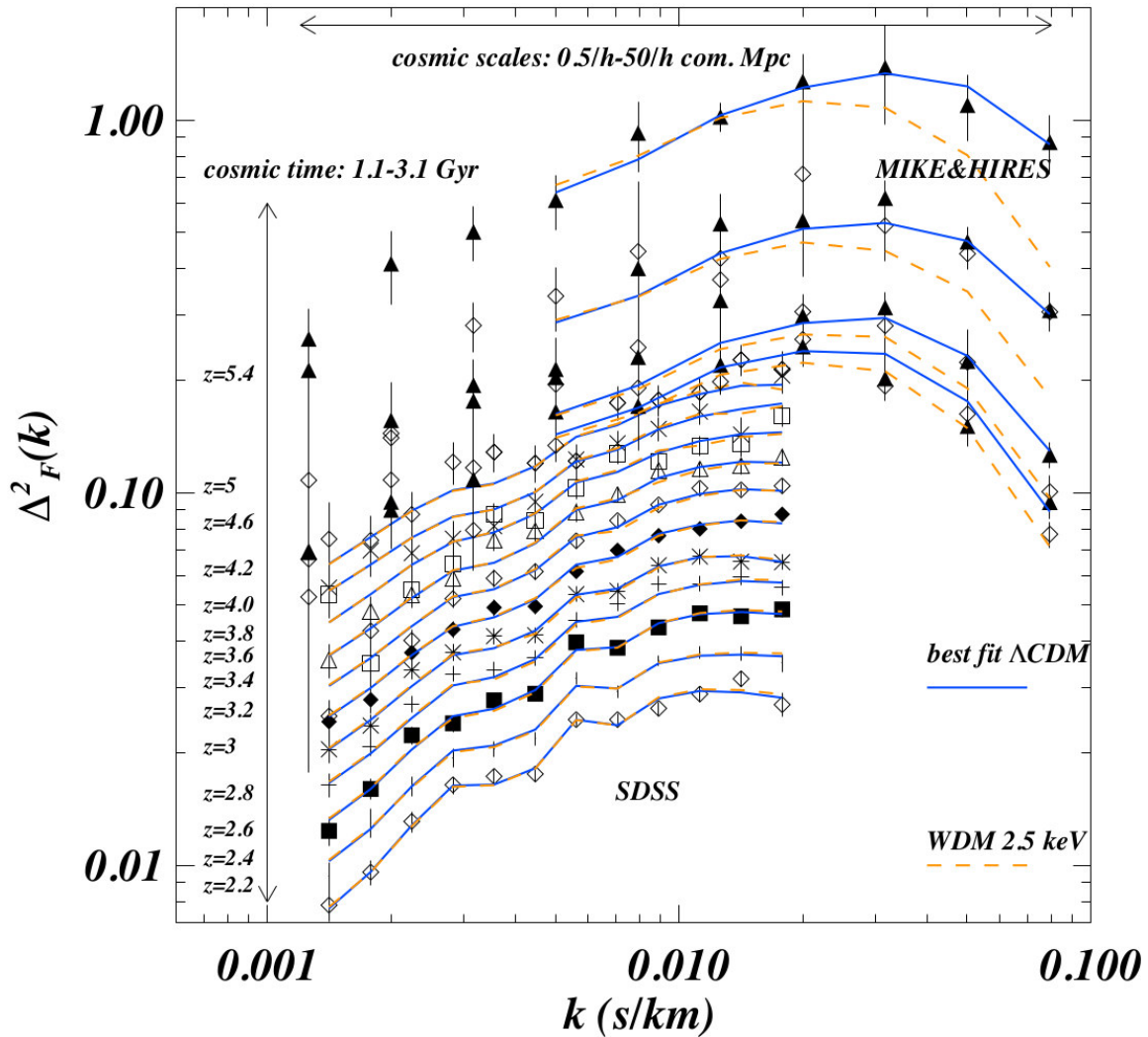


Summarizing, the computation of the  $P_{\text{F1D}}$  ([Chabanier et al., 2019b](#); [Ravoux et al., 2023](#)) along the line of sight of the quasars from Ly- $\alpha$  forests allows us to infer the three-dimensional flux power spectrum ( $P_{\text{F3D}}$ ) ([Font-Ribera et al., 2018](#); [Karim et al., 2023](#)), and the consequent matter power spectrum ( $P_m(k)$ ) ([Chabanier et al., 2019a](#)), as well as their associated cosmological parameters, *i.e.*  $P_{\text{F1D}} \rightarrow P_{\text{F3D}} \rightarrow P_m(k)$  ([Seljak et al., 2006](#); [Borde et al., 2014](#)).

Given that Ly- $\alpha$  forests are very sensitive to the thermal and dynamical state of the IGM,  $P_{\text{F1D}}$  is maybe the most important probe in cutting-edge cosmological researches at small scales on the characterization and evolution of the IGM at  $2 < z \lesssim 6$  (Meiksin, 2009; McQuinn, 2016; Walther et al., 2019; Qin et al., 2021).

In the same way, given the scale ranges it covers (some few to tens of Mpc), the  $P_{\text{F1D}}$  estimation allow us to put constraints on the masses of massive neutrinos (Palanque-Delabrouille et al., 2015, 2020), dark radiation models (Rossi et al., 2015), constrains to the nature of dark matter (Armengaud et al., 2017; Iršič et al., 2017a,b), an approach to a better understanding of the AGN feedback mechanism (Chabanier et al., 2020), among other high level impact applications. As Figure 3.15 shows,  $P_{\text{F1D}}$  estimations at different spectral resolutions and several cosmic epochs ( $z$ ), are quite handy to constrain models of dark matter at scales unreachabele to, for example, galaxy surveys.

As a final remark, some additional key applications of Ly- $\alpha$  forests besides the  $P_{\text{F1D}}$  are cited, such as the measurement of the BAO (Bourboux et al., 2020; Youles, 2021; Moon et al., 2023), tomographies of the IGM (Ravoux et al., 2020), cosmological principle tests (Zavarygin and Webb, 2019), and hints on the resolution of the Hubble tension (Goldstein et al., 2023).



Source: [Markovič and Viel \(2014\)](#)

**Figure 3.15:**  $P_{\text{F1D}}$  measurements obtained out of SDSS (large scales) and MIKE+HIRES (small scales) spectra. It is possible to visualize the range of scales (comoving) covered by the measurements and the different time scales they span. The graph also shows the best fit estimations for  $\Lambda\text{CDM}$  and WDM models. Large scales are very sensitive to cosmological parameters and small scales are sensitive to astrophysical parameters, the neutrino masses and WDM (see appendix A).

## *Chapter 4*

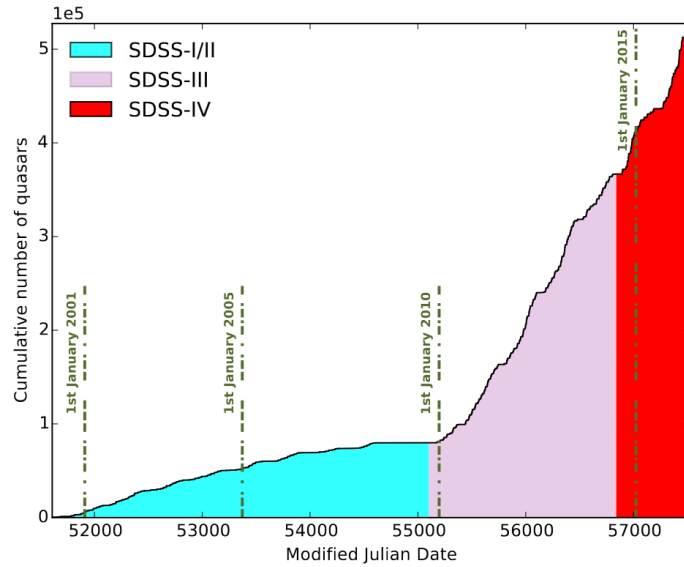
### **SAMPLE DESCRIPTION AND $P_{\text{FID}}$ COMPUTATION**

This chapter outlines the methodology for calculating the  $P_{\text{FID}}$  from both eBOSS and DESI samples. The description of the public data and additional information used is also included, alongside the general statistical characterization of the samples. Furthermore, the  $P_{\text{FID}}$  computation workflow using a dedicated software is described. Some technical concepts are cited through the chapter, to further reference and clarifications see appendix B, a general description of the instruments from which the data come from.

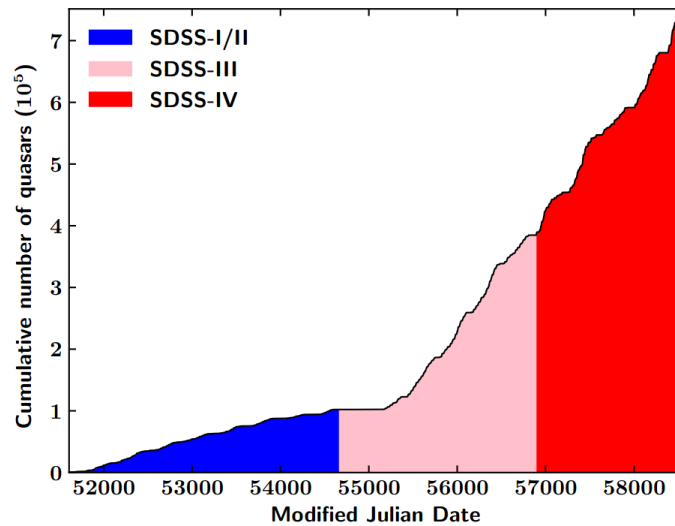
#### **4.1 Quasar catalogs**

##### **eBOSS**

For the computation of  $P_{\text{FID}}$  in eBOSS, I used publicly available spectra data from the fourteenth data release (DR14) and the sixteenth data release (DR16) of eBOSS. For DR14, the measurements were carried out from 2014 to 2016 (Abolfathi et al., 2018). In DR16, the spectra were taken between 2016 and 2019 (Ahumada et al., 2020). Because the interest of this thesis is centered on quasars specifically, I used the DR14Q quasar catalog which has a total of 526 356 visually and/or automated inspected spectra (Pâris et al., 2018), in contrast, DR16Q has a total of 750 414 spectra (225 082 new objects in comparison to DR14Q). Taking Figure 4.1 as reference, DR16Q is the largest selection of spectroscopically confirmed quasars up to 2020 (Lyke et al., 2020).



(a) DR14Q



(b) DR16Q

Source: (a) Pâris et al. (2018) (b) Lyke et al. (2020)

**Figure 4.1:** eBOSS quasar records over time for DR14 and DR16.

The catalog creation for both data releases was practically the same. They selected the targets for which the spectra would be obtained based on several photometric classifications. Then, the spectra passed to an automated classification test and (depending on the result in the first step) spectra were analyzed through visual inspection in order to confirm their relevant properties. The visual classification for eBOSS spectra was done until  $MJD = 56870$  (08/01/2014), from that point ahead



the robustness of target classification relied on automated procedures (see [Pâris et al. \(2018\)](#); [Lyke et al. \(2020\)](#)).

The redshift classification of the quasars was made using the MgII broad emission line because this line is the least affected by systematic shifts. However, additional visual/automated redshift classification methods were used in both data releases. On the other hand, the identification of BAL quasars was made measuring the balnicity index (BI) in the form of,

$$\text{BI} = - \int_{25000}^{3000} \left[ 1 - \frac{f(v)}{0.9} \right] C(v) dv . \quad (4.1)$$

The BI is calculated by taking the blueward part of the CIV emission line where  $C(v)$  represents the quasar continuum as function of velocity and  $f(v)$  is the normalized flux density as a function of velocity displacement from the emission-line center. When BI assumes a value major than 0 ( $\text{BI} > 0$ ), the associated quasar is classified as a BAL candidate.

Both quasar catalogs of the data releases<sup>1,2</sup>, and their associated spectra<sup>3,4</sup>, are available on the SDSS public website as a binary FITS table file. The main Binary-Table that contains the information of interest for this study is presented in a set of 105 columns.

Finally, in order to correct the DLA and skyline<sup>5</sup> systematic contributions, I used the DR14 & DR16 DLA catalogs (made by [Noterdaeme et al. \(2012\)](#); [Parks et al. \(2018\)](#) and [Chabanier et al. \(2022\)](#) respectively) both based on neural network algorithms, while the wavelength regions contaminated by sky emission lines were downloaded from [https://github.com/igmhub/picca/blob/master/etc/list\\_vetoline\\_Pk1D.txt](https://github.com/igmhub/picca/blob/master/etc/list_vetoline_Pk1D.txt). Figure 4.2 shows the redshift distribution and BAL quasars proportion of eBOSS general catalogs.

<sup>1</sup>[https://data.sdss.org/sas/dr14/ebooss/qso/DR14Q/DR14Q\\_v4\\_4.fits](https://data.sdss.org/sas/dr14/ebooss/qso/DR14Q/DR14Q_v4_4.fits)

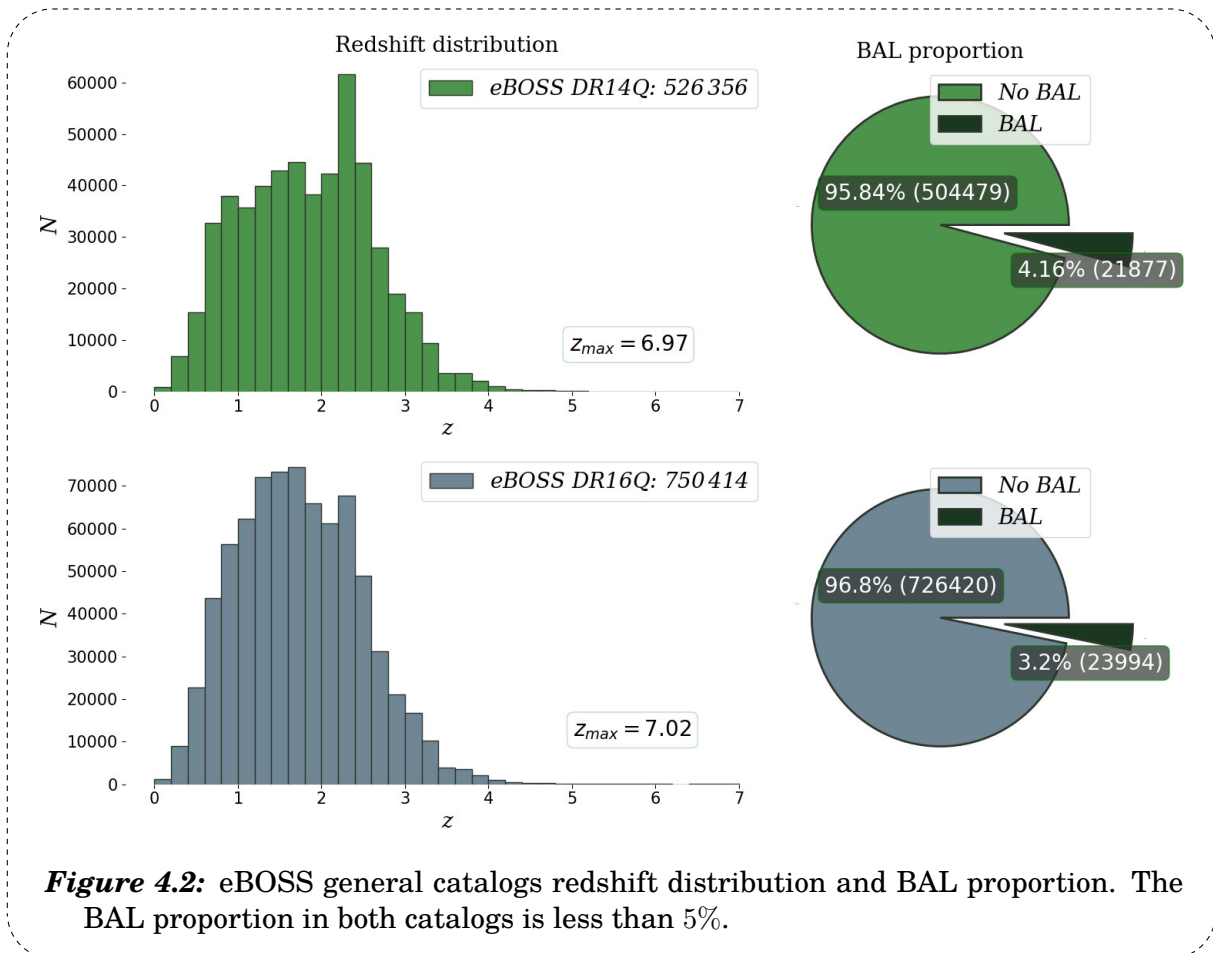
<sup>2</sup>[https://data.sdss.org/sas/dr16/ebooss/qso/DR16Q/DR16Q\\_v4.fits](https://data.sdss.org/sas/dr16/ebooss/qso/DR16Q/DR16Q_v4.fits)

<sup>3</sup>[https://data.sdss.org/sas/dr14/ebooss/spectro/redux/v5\\_10\\_0/spectra/full/](https://data.sdss.org/sas/dr14/ebooss/spectro/redux/v5_10_0/spectra/full/)

<sup>4</sup>[https://data.sdss.org/sas/dr16/ebooss/spectro/redux/v5\\_13\\_0/spectra/full/](https://data.sdss.org/sas/dr16/ebooss/spectro/redux/v5_13_0/spectra/full/)

<sup>5</sup>Skylines, or night-sky emission lines, is light emission produced by air glow, light pollution, zodiacal light among others, that appears as fixed lines in spectroscopic measurements (see figures 4.16 and 4.17).





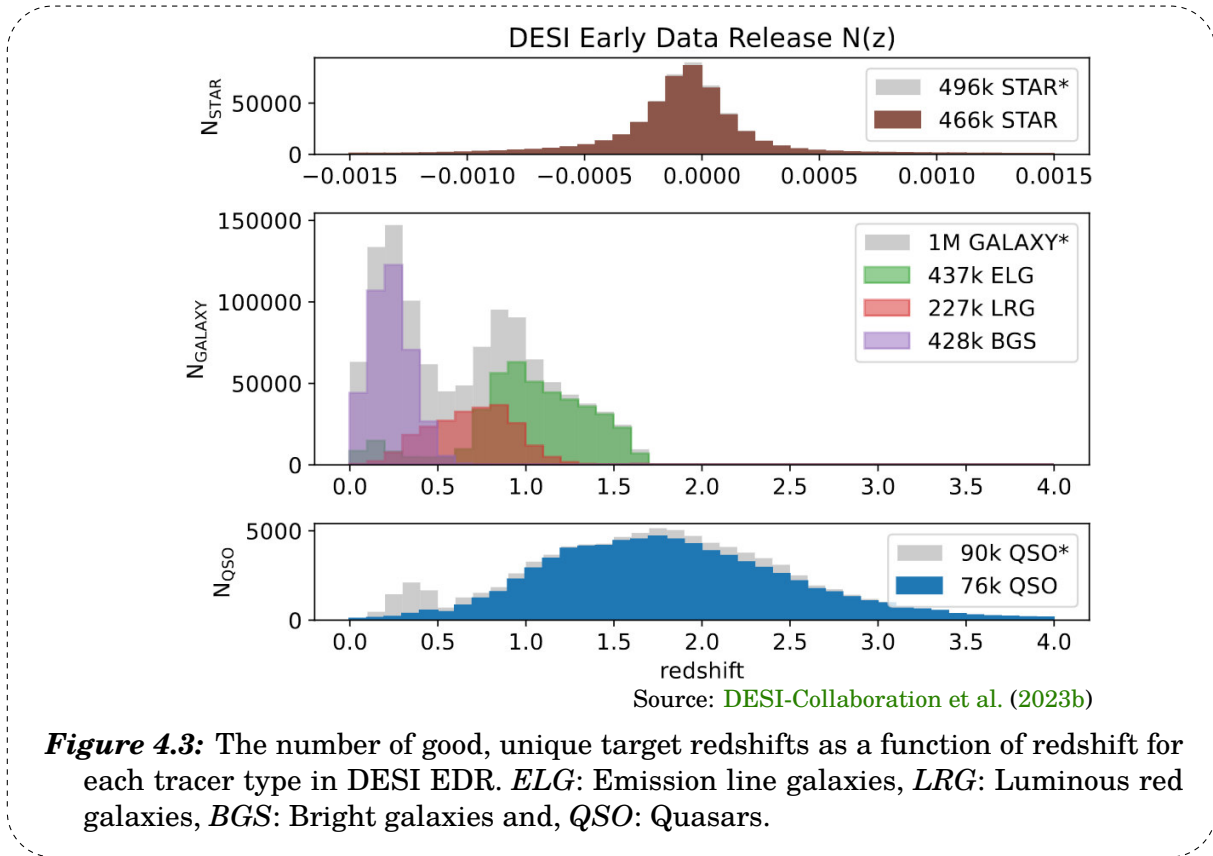
## DESI

For the computation of  $P_{F1D}$  in DESI, I used spectra from the early data release of the survey, that is, the survey validation (SV). The survey validation extended from December 2020 through mid-May 2021. In the same way, SV was divided in SV1 (first phase of survey validation with long exposure times), SV2 (operations testing: "dress rehearsal" for SV3) and SV3 (one-percent survey<sup>6</sup> with standard exposure times) (DESI-Collaboration et al., 2023b,a).

I started using the general redshift catalog published in DESI-Collaboration et al. (2023b) which contain a total of 117 771 objects classified as QSO (Figure 4.3). However, given that the general redshift catalog reported some spectra missclassifica-

<sup>6</sup>Covering 1% of the survey's projected area, the final phase of SV

tion and there was the necessity of using the Balcinity index mentioned in equation (4.1), I also used the BAL quasar catalogs<sup>7</sup> related to the survey validation of DESI.



For the purpose of classifying objects, it is worth noting that DESI had five primary target classes where the QSO type was one of them. Observations were based upon tiles, that is, a given pointing of the telescope combined with assignments of each fiber to a specific target.

Tiles were associated with a single survey, or phase of DESI operations. Moreover, tiles were grouped within a survey by their program (it could be bright or dark) indicating the observing conditions under which they should be observed. The distinction between bright and dark program is determined by the survey speed, meaning how rapidly the instrument can accumulate signal-to-noise under the observing conditions, as calculated by the exposure time calculator (DESI-Collaboration et al., 2023b). For QSO targets the selected program was dark.

<sup>7</sup>This catalog (Filbert et al. (2023)) was published later than the EDR initial catalog.

From the general redshift catalog of DESI EDR, the procedure to re-identify targets as QSOs could be summarized as follows. As reported by [Alexander et al. \(2023\)](#); [DESI-Collaboration et al. \(2023b\)](#) and [Chaussidon et al. \(2023\)](#), the spectra were taken from scratch and introduced into the redrock code in order to fit the redshift and spectral properties based on eBOSS spectra templates (QSOs, galaxies and/or stars). Then, the code Quasar-NET ([Busca and Balland, 2018](#)), which apply neural networks trained with eBOSS, was used to finally obtain the proper classification of objects (this process is iterative). The reported purity (goodness) of the classification was about 99% (the missclassification of QSO target is supposed to be due host-galaxy dominated cases). The redshift identification was based on the MgII emission line and the classification of BAL quasars was based on the BI index with the aid of an additional absorption index (AI) ([Filbert et al., 2023](#)).

Both files, the redshift and BAL quasar catalogs of the EDR<sup>8,9,10,11</sup>, and their associated spectra<sup>12,13</sup>, are available on the DESI public website as a binary FITS table file. To this day, the DLA quasar catalog is not yet publicly available, on the other hand, the wavelength regions contaminated by sky emission lines were downloaded from [https://github.com/corentinravoux/p1desi/blob/main/etc/skylines/list\\_mask\\_p1d\\_DESI\\_EDR.txt](https://github.com/corentinravoux/p1desi/blob/main/etc/skylines/list_mask_p1d_DESI_EDR.txt).

Figure 4.4 shows the redshift distribution and BAL quasars proportion of SV1 and SV3, the redshift distribution is similar to one of eBOSS and the BAL proportion is  $\sim 2.6\%$  in both cases. As a final remark, Figure 4.5 shows a comparison between the spectrum of the same QSO taken with eBOSS and DESI. An improvement in spectral resolution can be clearly seen.

<sup>8</sup><https://data.desi.lbl.gov/public/edr/spectro/redux/fuji/zcatalog/zall-pix-fuji.fits>

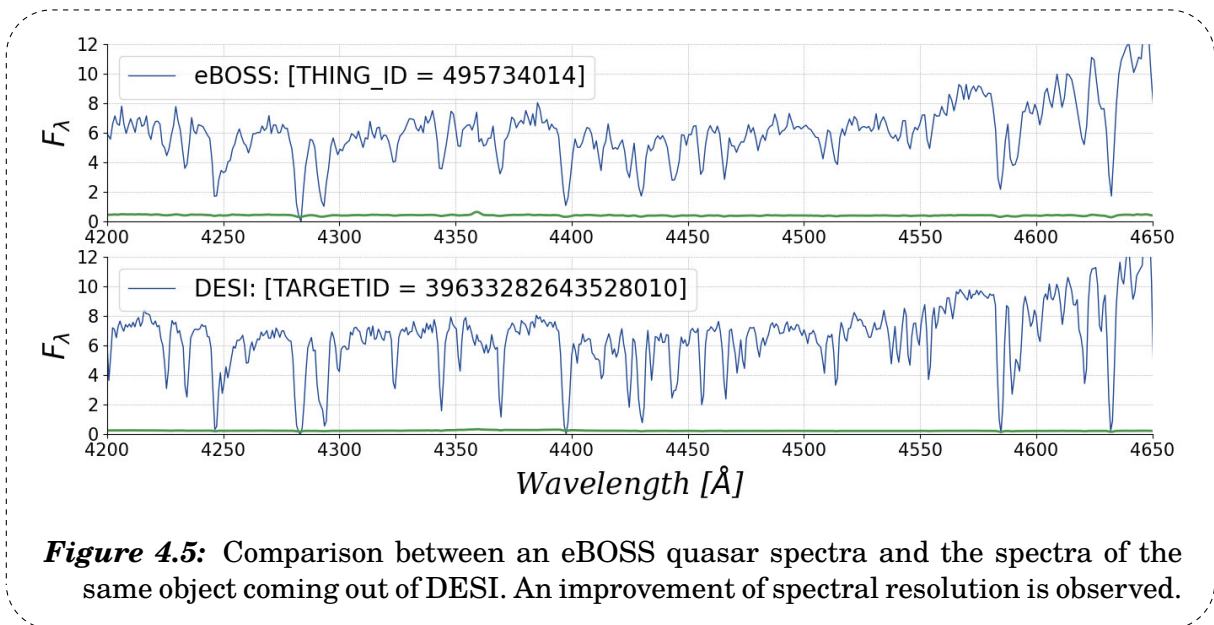
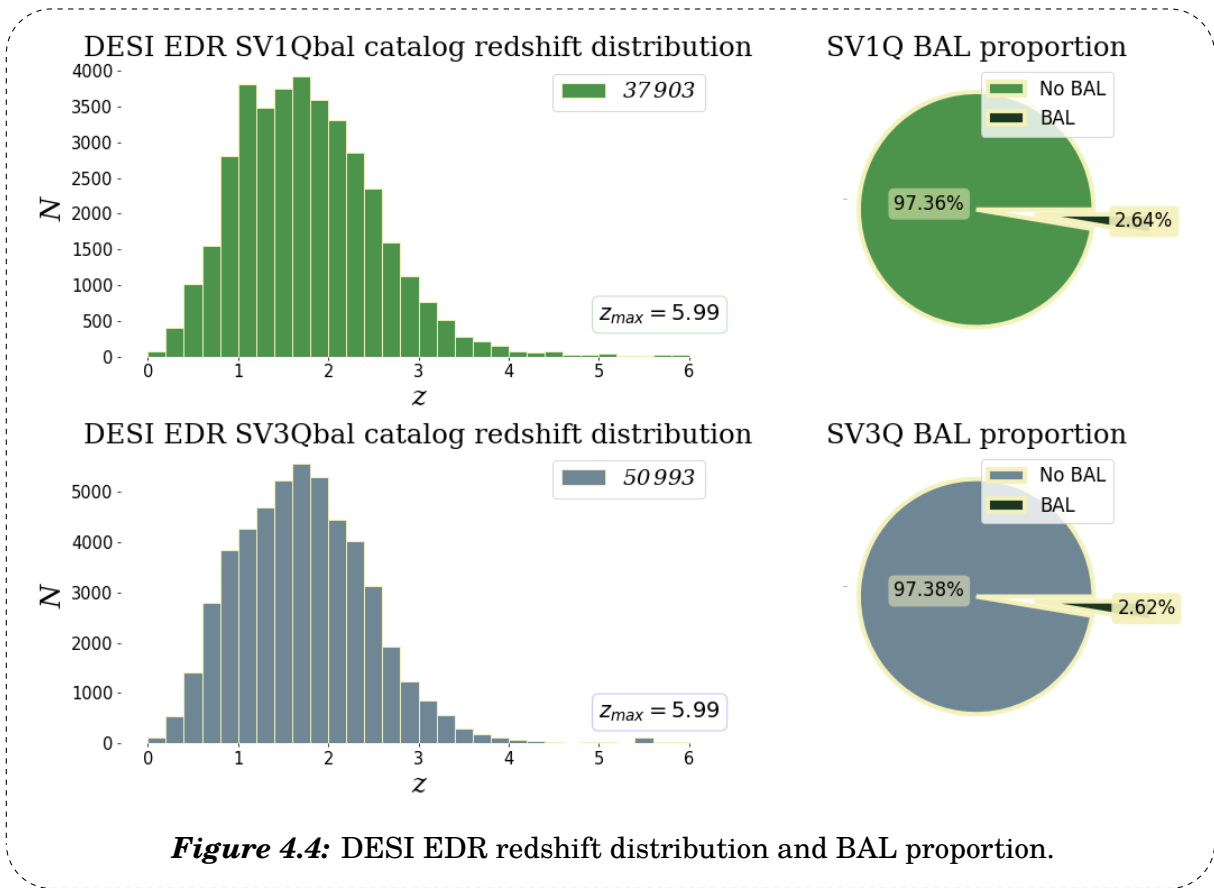
<sup>9</sup><https://data.desi.lbl.gov/public/edr/vac/edr/zcat/fuji/v1.0/zall-pix-edr-vac.fits>

<sup>10</sup>[https://data.desi.lbl.gov/public/edr/vac/edr/bal/fuji/v1.0/QSO\\_cat\\_fuji\\_sv1\\_dark\\_bal\\_mask\\_v1.0.fits](https://data.desi.lbl.gov/public/edr/vac/edr/bal/fuji/v1.0/QSO_cat_fuji_sv1_dark_bal_mask_v1.0.fits)

<sup>11</sup>[https://data.desi.lbl.gov/public/edr/vac/edr/bal/fuji/v1.0/QSO\\_cat\\_fuji\\_sv3\\_dark\\_bal\\_mask\\_v1.0.fits](https://data.desi.lbl.gov/public/edr/vac/edr/bal/fuji/v1.0/QSO_cat_fuji_sv3_dark_bal_mask_v1.0.fits)

<sup>12</sup><https://data.desi.lbl.gov/public/edr/spectro/redux/fuji/healpix/sv1/dark/>

<sup>13</sup><https://data.desi.lbl.gov/public/edr/spectro/redux/fuji/healpix/sv3/dark/>



## 4.2 Sample extraction

In order to build the sample spectra (subcatalogs) to be analyzed, it was necessary to filter the general catalogs. Each filtering process was different for each survey given how the data is stored. In the case of eBOSS, the catalogs of [Pâris et al. \(2018\)](#) and [Lyke et al. \(2020\)](#) were filtered according to Table 4.1. In the same way, this selection aimed to reproduce as much as possible the selection made by [Chabanier et al. \(2019b\)](#).

Attribute	Flag	Query
1. Unique identifier code for each quasar based on PLATE-MJD-FIBERID	THING_ID	$> 0$
2. Quasar's redshift estimation	Z	$\geq 2.1$
3. Object's right ascension	RA	$> 0$
4. Object's declination	DEC	$\neq \text{RA}$
5. Object's observation date	MJD	$< 56870$
6. Object's Balcinity Index estimation. Sorting BAL and non-BAL quasars	BI_CIV	$= 0$

**Table 4.1:** Subcatalog construction query attributes (eBOSS)

In Table 4.1, attributes 1, 3, and 4 are designed to prevent any potential anomalies, such as quasars with a right ascension  $RA < 0$  (what would not make sense), attribute 2 for redshift selection, attribute 5 to keep only visually inspected spectra and attribute 6 for BAL quasar sorting. A total of 180 485 / 180 843 spectra were chosen from eBOSS DR14 / DR16 where 12 440 / 11 093 are BAL quasars. Once the list of spectra is obtained, the individual files are downloaded based on a unique PLATE-MJD-FIBERID identifier.

For DESI, I built a new quasar catalog from the catalogs named in the previous section (the general redshift catalog and the BAL catalog). First, I merged the two quasar catalogs from [Filbert et al. \(2023\)](#), applying attributes 2 and 3 of Table 4.2.

Attribute	Flag	Query
1. Object's primary target class	SPECTYPE	QSO
2. Quasar's redshift estimation	Z	$\geq 2.1$
3. Object's observation program	PROGRAM	<i>dark</i>
4. Object's Balnicity Index estimation. Sorting BAL and non-BAL quasars	BI_CIV	= 0

**Table 4.2:** Subcatalog construction query attributes (DESI)

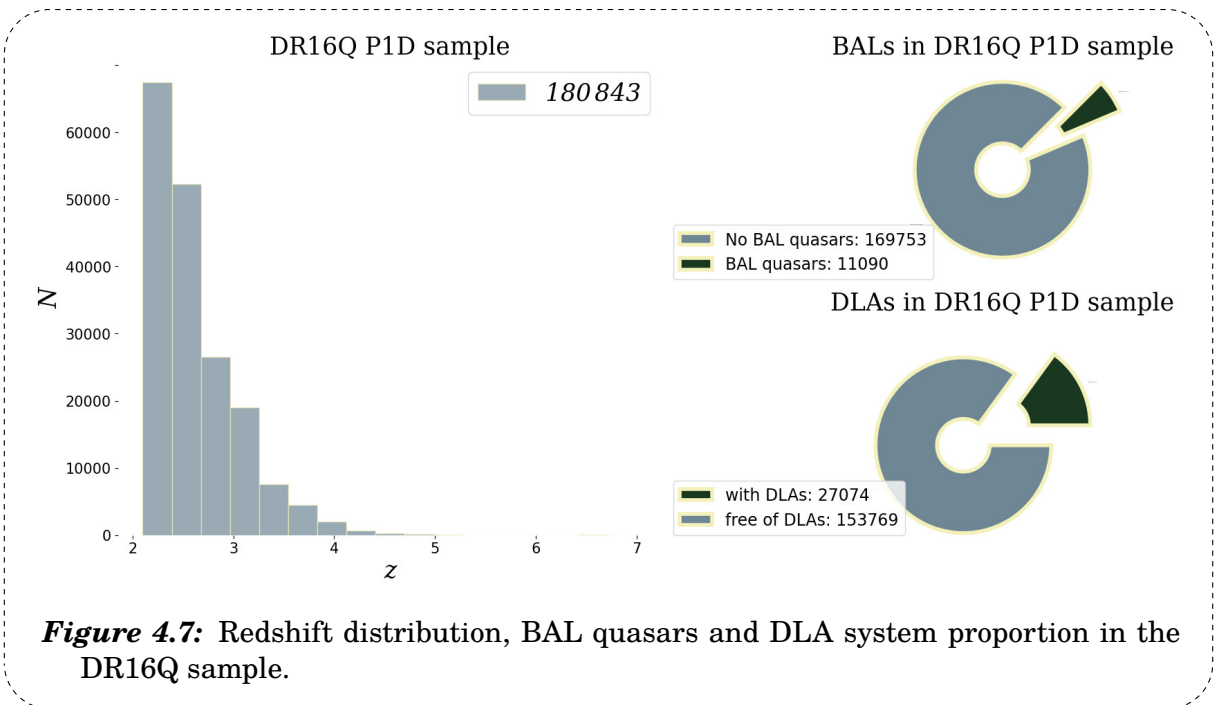
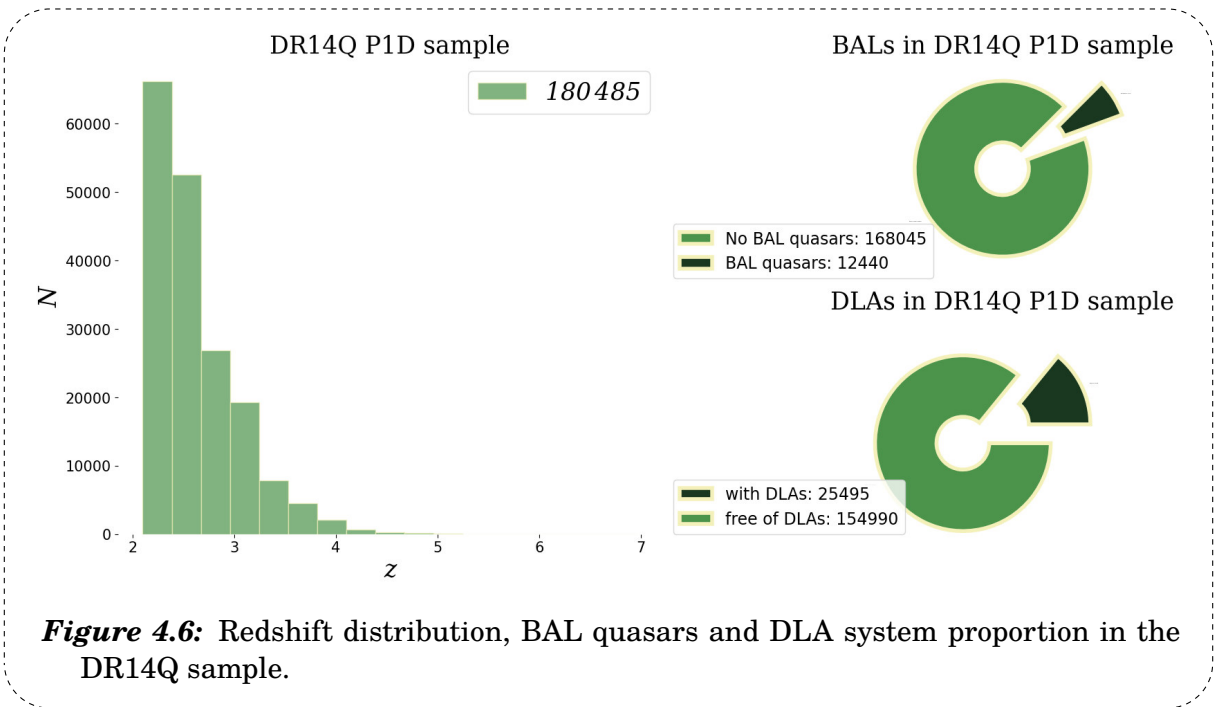
Then, from the DESI EDR redshift summary catalog, I extracted the column LAST-NIGHT<sup>14</sup>, associating each individual spectrum between catalogs, also using criteria of Table 4.2. Sometimes, the spectra of some targets were taken twice, consequently, I only chose spectra in the sample with a greater coadded exposure time and excluded the repeated ones (spectra repeated both in SV1 and SV3). A total of 26 060 spectra were chosen from DESI EDR.

The download of spectra in DESI is different because the spectrum of each object is contained in a parent file that contains all the objects in that region of the sky (HEALPix<sup>15</sup> or HPXPPIXEL as expressed as a column in the catalogs), also separated by survey and program. Therefore, I made a code in Python to download the parent file according to criteria of Table 4.2, leaving only the objects of interest and deleting those that do not belong to the sub-catalog.

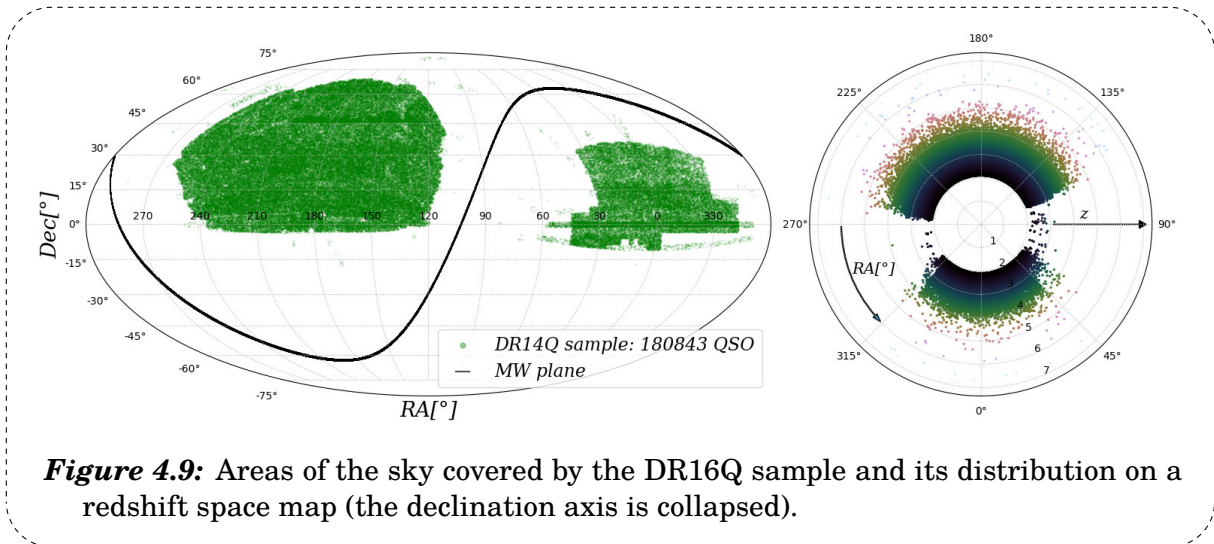
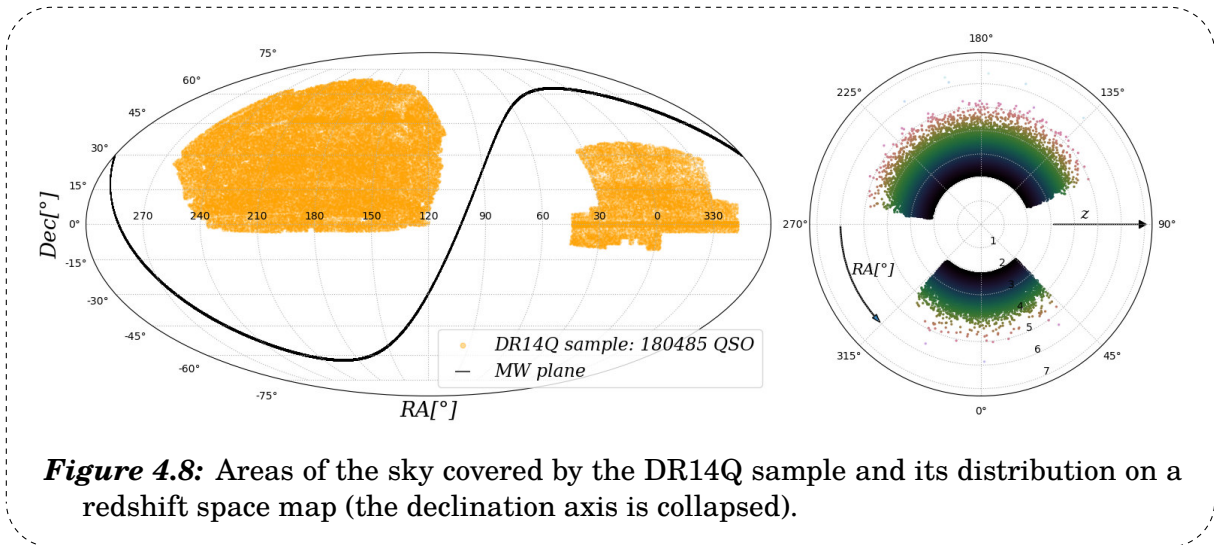
Figures 4.6 to 4.11 show the redshift distribution, BAL and DLAs proportions and distribution of the samples (sub-catalogs) in the sky.

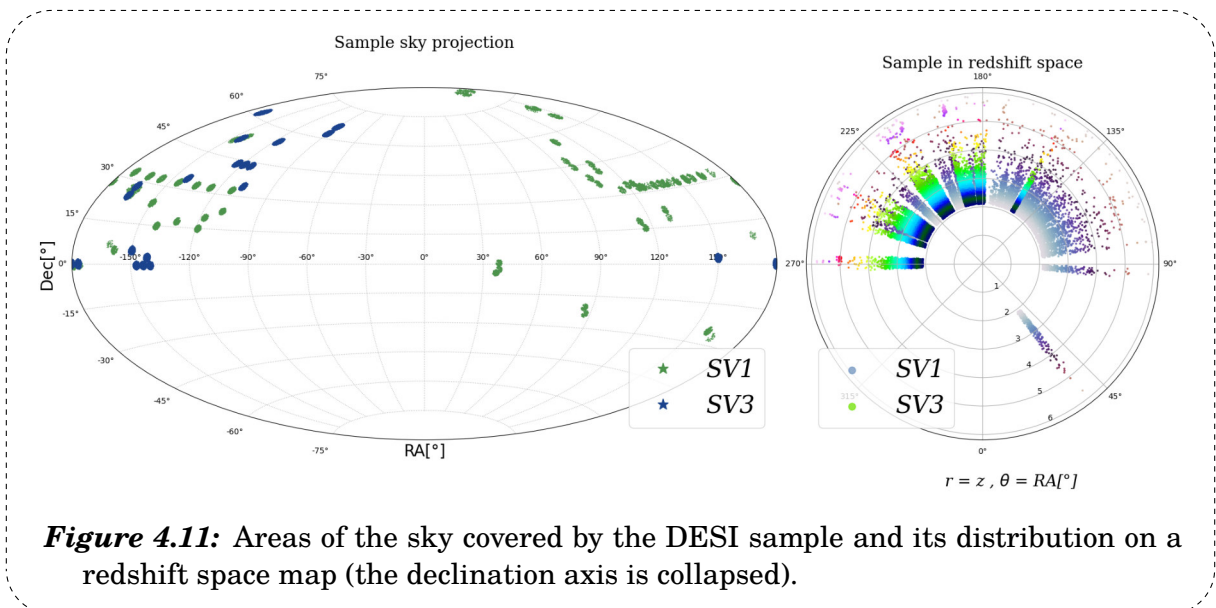
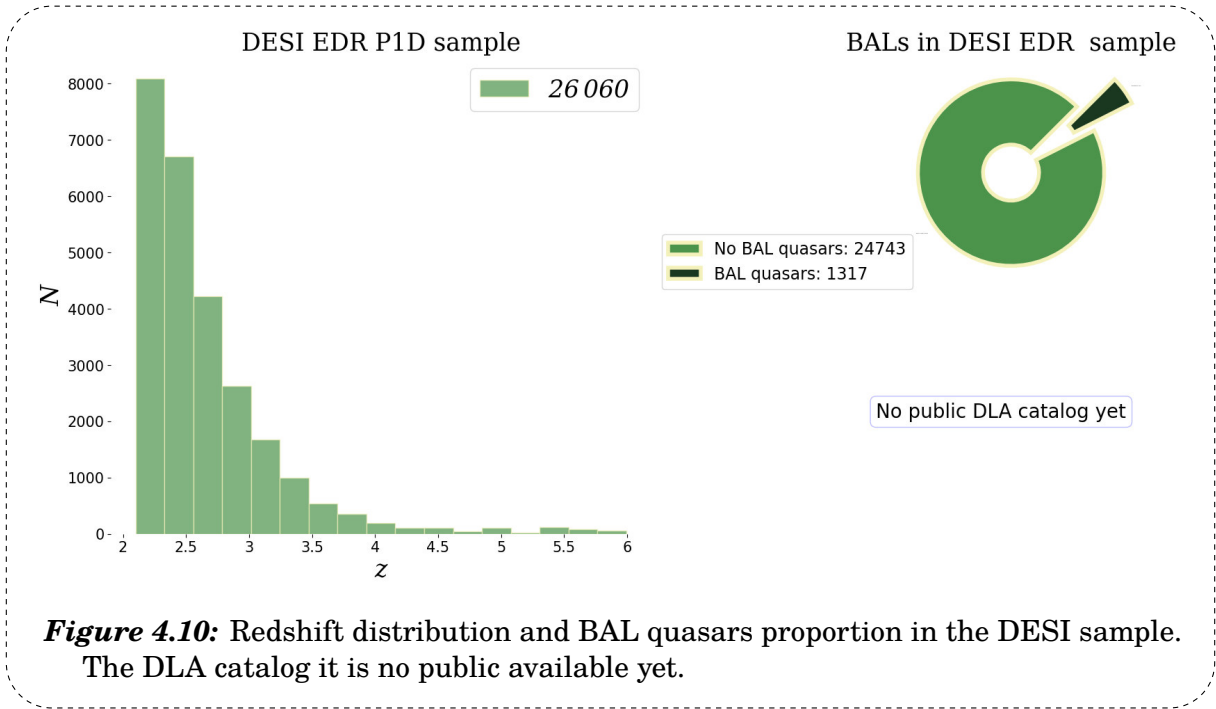
<sup>14</sup>Calendar Date when the last exposure was obtained for the tile.

<sup>15</sup>HEALPix stands for Hierarchical Equal Area isoLatitude Pixelisation of a 2-sphere. It is an algorithm used to pixelate a 2-sphere. More info on [HEALPix](#)

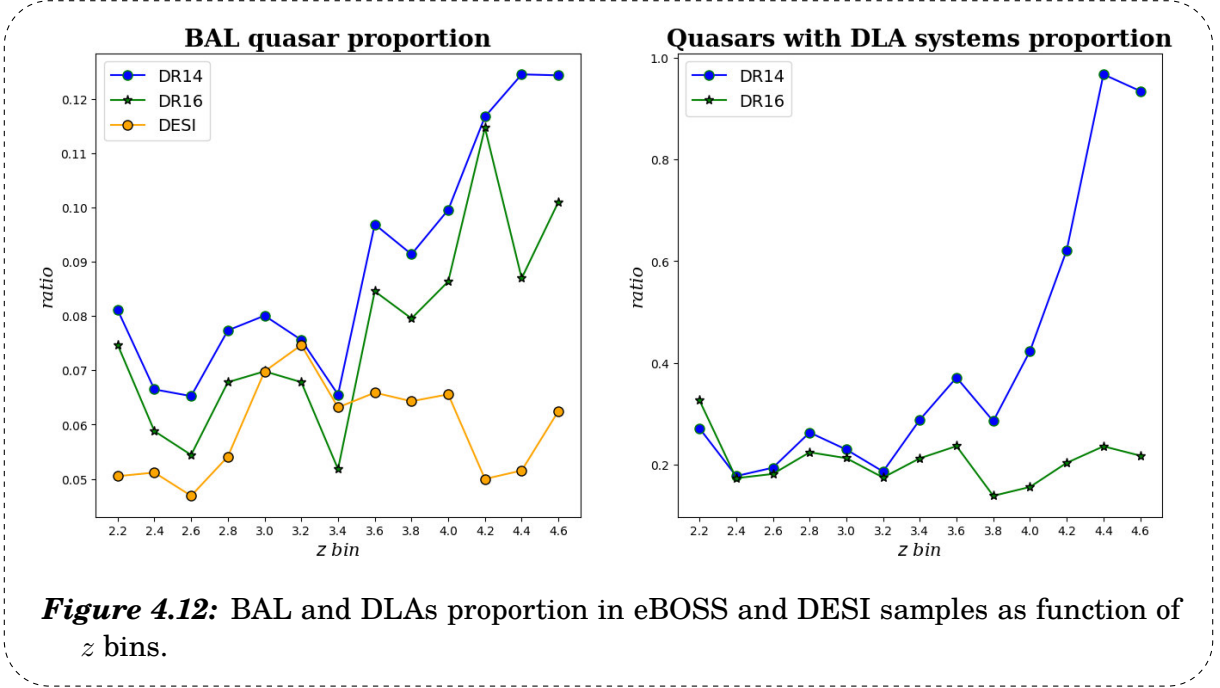








Finally, Figure 4.12 shows the BAL and DLAs proportion in each sample as function of the redshift bins evaluated<sup>16</sup>. In the case of eBOSS, the fraction of BAL quasars increases as redshift does, not being the case for DESI. For DLAs in eBOSS DR14, it is noticeable that the fraction of quasars with DLA systems increases with redshift. On the contrary, quasars with DLA systems in DR16 shows a bounded behaviour as function of redshift.



### 4.3 $P_{\text{FID}}$ computation pipeline description

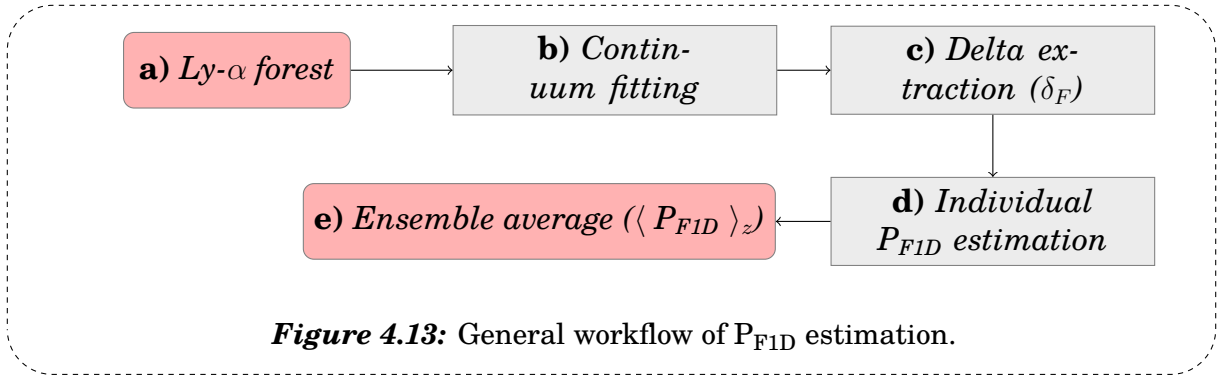
In order to compute the  $P_{\text{FID}}$  out of the Ly- $\alpha$  forests, I used `picca` (Package for Igm Cosmological-Correlations Analyzes), a package mainly designed to perform cosmological correlation analyses as referred in [du Mas des Bourboux et al. \(2021\)](#). This package performs the quasar continuum fitting, the extraction of the Ly- $\alpha$  contrasts<sup>17</sup> and the computation of the one-dimensional flux power spectrum using the FFTw algorithm ([Frigo and Johnson, 2012](#)). `picca` was designed to work with BOSS/eBOSS data and recently adapted to analyse DESI spectra.

The procedure used here to compute the  $P_{\text{FID}}$  is that based on the FFT method ex-

<sup>16</sup>This redshift binning was selected based on the computation of the  $P_{\text{FID}}$ .

<sup>17</sup>Ly- $\beta$  and metals contrast extraction included.

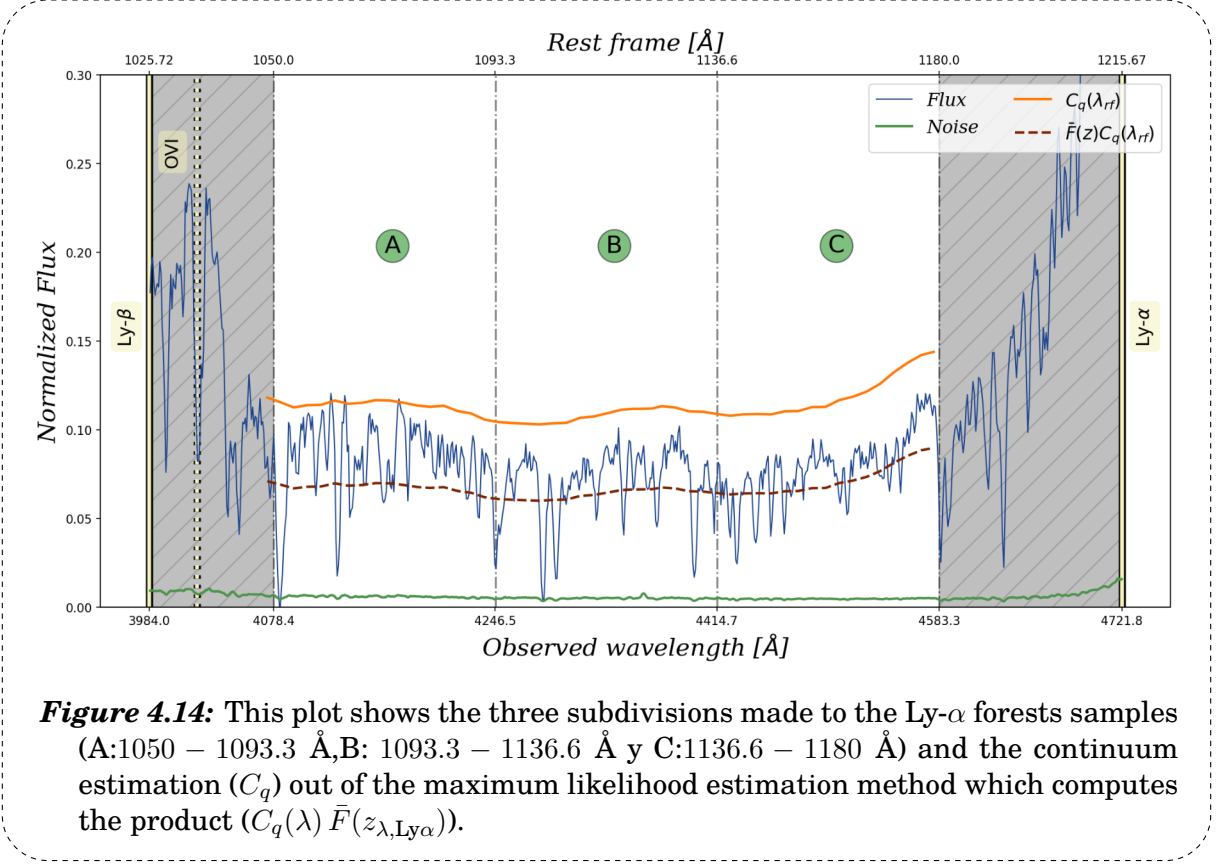
tensively used in previous works, as mentioned in chapter 2. As it is shown in Figure 4.13, the general computation of  $P_{\text{FID}}$  out of Ly- $\alpha$  forest under the FFT method could be described in five parts: **(a)** Ly- $\alpha$  forest extraction from quasar spectra, **(b)** make the continuum fitting of the spectra in order to **(c)** get the flux density fluctuation field along the line of sight of the quasar, otherwise the Ly- $\alpha$  contrast extraction ( $\delta_F$ <sup>18</sup>)<sup>19</sup>, then **(d)** make a FFT of this field taking the advantage of the discreteness of the data ( $\tilde{\delta}_F(k)$ ), and, finally, **(e)** compute the ensemble average over several redshift bins ( $\langle |\tilde{\delta}_F(k)|^2 \rangle$ ).



a) Ly- $\alpha$  forest extraction from quasar spectra: As we know, each absorption line in Figure 4.14 is produced by the interaction of the quasar light with HI in the IGM at a particular redshift *i.e.* cosmic time (equation 3.14). Therefore, in order to increase the redshift binning/resolution of the  $P_{\text{FID}}$ , the Ly- $\alpha$  forest sample ranging from 1050 Å to 1180 Å is divided into three parts (subforests). The redshift average of each line in the subforests is the contribution of that forest at a given redshift bin. Moreover, the forest were taken  $\sim 6000$  km/s ( $\sim 24$  Å) redwards and  $\sim 8500$  km/s ( $\sim 36$  Å) bluewards respectively from the Ly- $\beta$  and Ly- $\alpha$  emission lines at rest, in order to avoid additional astrophysical systematics coming out of the quasar like the OIV line close Ly- $\beta$ .

<sup>18</sup> $F$  for flux

<sup>19</sup>In these terms, the Ly- $\alpha$  contrast is equivalent to the flux fluctuation field.



b) Continuum fitting: The next step is the computation of the flux fluctuation field extracting the deltas  $\delta_F(\lambda)$  as:

$$\delta_F(\lambda) = \frac{f_i(\lambda)}{C_q(\lambda) \bar{F}(z_{\lambda, Ly\alpha})} - 1. \quad (4.2)$$

where  $f_i(\lambda)$  is the transmitted flux of the quasar per wavelength bin. So forth, it is necessary to estimate the product of the quasar continuum ( $C_q(\lambda)$ ) times the average fraction of transmitted flux ( $\bar{F}(z_{\lambda, Ly\alpha})$ ). `picca` computes this product modeling each quasar as the product of a universal continuum function, common to every quasar, and a polynomial term in wavelength. Respectively, for eBOSS a zeroth-order polynomial function was used,

$$\bar{F}(\lambda)C_q(\lambda) = a_q C(\lambda_{rest}), \quad (4.3)$$

where  $\lambda_{rest} = \lambda_0/(1 + z_q)$ , and a first-order polynomial for DESI

$$\bar{F}(\lambda)C_q(\lambda) = (a_q + b_q\Lambda(\lambda))C(\lambda_{\text{rest}}), \quad (4.4)$$

where the  $\Lambda(\lambda)$  term is used to approach variations in the amplitude and tilt of the spectrum. The terms  $a_q$  and  $b_q$  are quasar dependant normalization terms which are determined for each quasar together with the  $C$  function maximizing the likelihood function represented by

$$\mathcal{L} = - \sum_i \frac{[f_i - \bar{F}(\lambda_i)C_q(\lambda_i, z_i, a_i, b_i)]^2}{\sigma_q^2(\lambda_i)} - \sum_i \ln[\sigma_q^2(\lambda_i)]. \quad (4.5)$$

In equation (4.5) the term  $\sigma_q$  is the standard deviation estimator of the flux  $f$ , specifically,

$$\frac{\sigma_q^2(\lambda)}{((\bar{F}(\lambda)C_q(\lambda))^2)} = \eta(\lambda) \frac{\sigma_{\text{pip,q}}^2(\lambda)}{((\bar{F}(\lambda)C_q(\lambda))^2)} + \sigma_{\text{iss}}^2(\lambda) + \epsilon(\lambda) \frac{((\bar{F}(\lambda)C_q(\lambda))^2)}{\sigma_{\text{pip,q}}^2(\lambda)}, \quad (4.6)$$

where  $\sigma_q$  is also function of  $\sigma_{\text{pip,q}}$  which represents the noise coming out the spectral extraction pipeline in the surveys.

Here is a brief description of the delta extraction computation implemented by `picca`. First, a flat assumption is made for the continuum fitting, that is,  $C(\lambda_{\text{rest}}) = 1$ , then, for FFT in eBOSS and DESI  $\eta(\lambda) = 0$ ,  $\sigma_{\text{iss}}^2(\lambda) = 1$  and  $\epsilon(\lambda) = 0$ <sup>20</sup>, where  $\eta$  represents a correction term to account for inaccuracies in the pipeline noise estimation,  $\sigma_{\text{iss}}^2$  is the intrinsic variance of the Ly- $\alpha$  forest and  $\epsilon$  is a correction to compensate the observed increase of the variance at high SNR, due to the quasar diversity or variability.

Once the previous step was accomplished, the current values of the cited variables are used to estimate  $a_q$  and  $b_q$  through equation (4.5) on each individual forest. Using the current value of  $C(\lambda_{\text{rest}})$ , the delta field is computed using the expected flux obtained for the continuum of each quasar. Then, the delta field is extracted and, with that in hand, the variance functions are fitted.

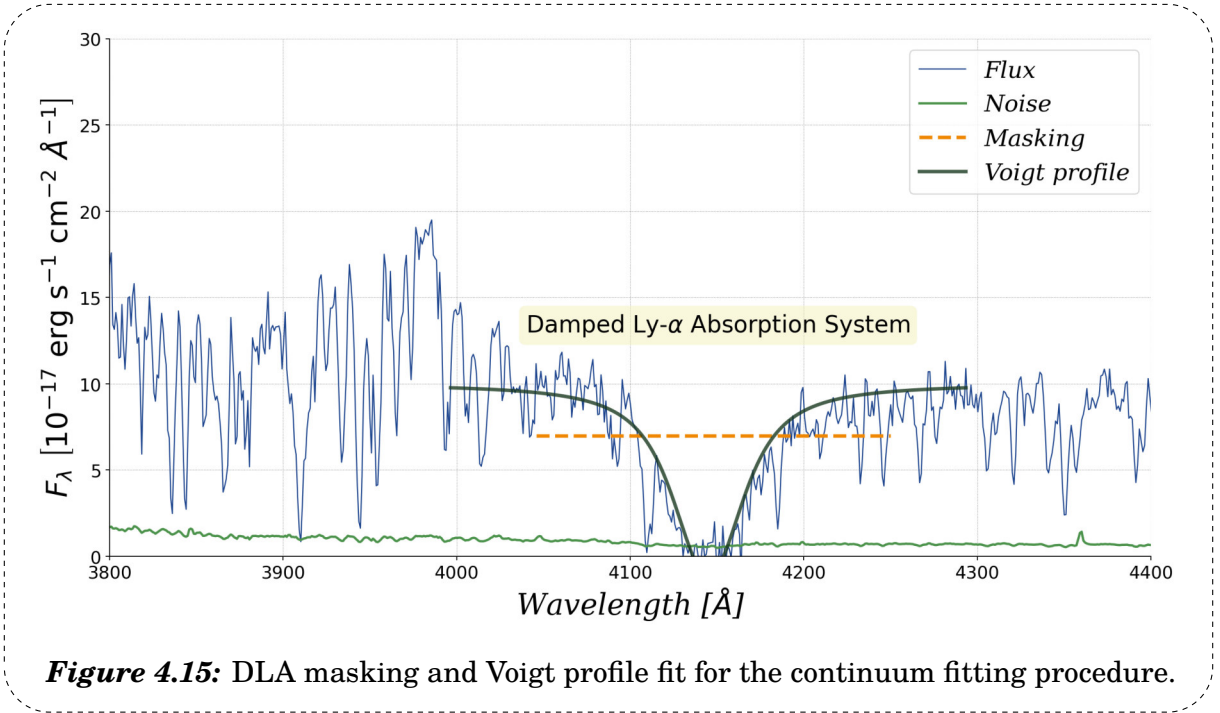
Finally, the  $C(\lambda_{\text{rest}})$  term is recomputed weighting the average of all quasars expected flux sharing the same  $\lambda_{\text{rest}}$  value. Then, the process iterates from the per-quasar parameters fitting step ( $a_q, b_q$ ), until the quality of fit is reliable

---

<sup>20</sup>In BAO correlation analyzes from Ly- $\alpha$  forests, the criteria of  $\eta(\lambda) = 1$ ,  $\sigma_{\text{iss}}^2(\lambda) = 1$  and  $\epsilon(\lambda) = 1$  is applied.

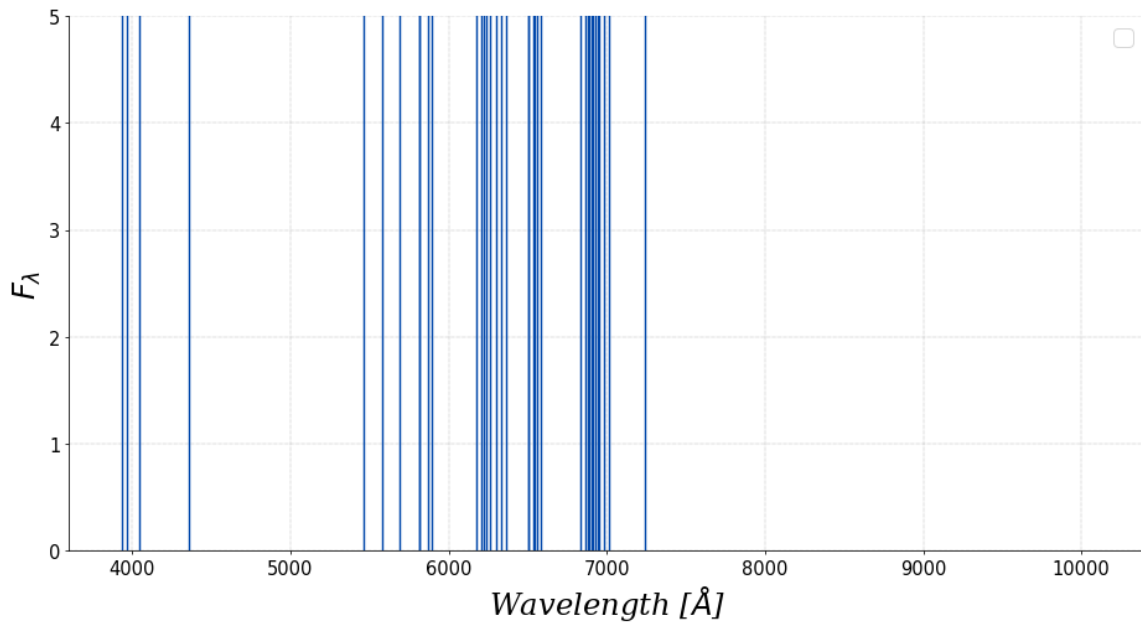
(between 5 to 7 times for converge). A thorough explanation of this process could be found in [Ramírez-Pérez et al. \(2023\)](#).

Figure 4.14 shows the estimation of the term  $\bar{F}(z_{\lambda, \text{Ly}\alpha})C_q(\lambda)$  for a quasar of the sample and the continuum estimation based on equations (3.8) and (3.12). As it is also shown in Figure 4.15, DLA systems in eBOSS quasars are masked, pixels where DLA influence is larger than 20% are removed and not included into the fitting, the remaining pixels coming out of the Lorentzian-profile damping wings are corrected with a Voigt profile<sup>21</sup>. Finally, regions affected by noise increment due to the presence of skylines (see figures 4.16 and 4.17) are also masked (but not fitted, contrary to the DLA case).



<sup>21</sup>Given that the DESI EDR DLA catalog is not public available, this correction was skipped for DESI spectra.





**Figure 4.16:** Skylines in eBOSS spectrograph reported in [Chabanier et al. \(2019b\)](#).

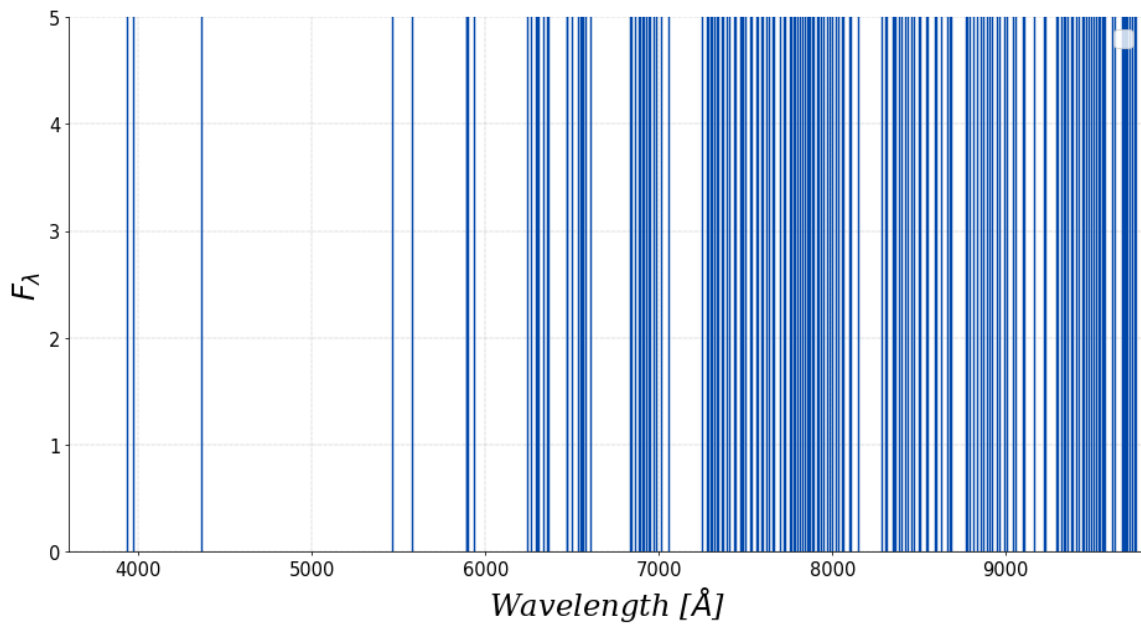


**Figure 4.17:** Skylines in DESI spectrograph reported in [Ravoux et al. \(2023\)](#).

c) Delta extraction: In ideal conditions, the flux fluctuation field stacking and the computation of individual  $P_{\text{FID}}$ s would be Ly- $\alpha$  dependant only, however, the contributions of additional factors have to be accounted for, namely,

$$\delta_F(\lambda) = \left( \delta_{\text{Ly}\alpha}(\lambda) + \delta_{\text{Ly}\alpha\text{-Si III/II}}(\lambda) + \delta_{\text{metals}}(\lambda) \right) \otimes W^2 + \delta_{\text{noise}}(\lambda) . \quad (4.7)$$

- $\delta_{\text{Ly}\alpha\text{-Si III/II}}(\lambda)$ : Absorption lines of Si III/II that occur inside the Ly- $\alpha$  forest regions. These can not be disentangled from the flux fluctuation field. Furthermore, their contribution appears as wiggles in the  $P_{\text{FID}}$  as can be seen in figures 3.13 and 3.14.
- $\delta_{\text{metals}}(\lambda)$ : As Figure 3.2 shows, each metallic emission line has a set of absorption lines attached to it. These absorptions could pass to the Ly- $\alpha$  region, like in the case of CIV (recalling Figure 3.2). Their contribution could be managed estimating side-bands ( $P_{\text{SB}}(k)$ ): the flux power spectrum redwards to the Ly- $\alpha$  forest where most of the metallic absorption occurs).
- $W^2$ : The contribution of a window function that has to be convoluted to the signal in order to account the finite spectral resolution of the instruments (further reference on appendix B). This windowing is function of the wavenumber, the resolution and the binning of the spectrograph (the spectral response). Equation (4.8) shows the windowing function for eBOSS and DESI used in Chabanier et al. (2019b) and Ravoux et al. (2023)<sup>22</sup>.

$$\text{eBOSS: } W(k, R, \Delta v) = \exp\left(-\frac{1}{2}(kR)^2\right) \times \frac{\sin(k\Delta v/2)}{(k\Delta v/2)} , \quad (4.8)$$

$$\text{DESI: } W(k, \mathbf{R}, \Delta\lambda_{\text{pix}}) = \mathbf{R}(k) .$$

- $\delta_{\text{noise}}(\lambda)$ : The contribution of noise in the spectra.

d) Individual  $P_{\text{FID}}$  estimation: Once the previous considerations were made, a FFT estimator is applied to all delta fields expressed as,

$$\begin{aligned} P_{\text{astro}}(k) &= P_{\text{Ly}\alpha}(k) + P_{\text{Ly}\alpha\text{-Si III/II}}(k) + P_{\text{metals}}(k) , \\ P_{\text{raw}}(k) &= \left( P_{\text{astro}}(k) \right) \cdot W^2(k, R, \Delta v) + P_{\text{noise}}(k) , \end{aligned} \quad (4.9)$$

---

<sup>22</sup>In equation (4.8),  $R$  is the spectrograph resolution in  $\text{km s}^{-1}$  and  $\mathbf{R}$  is a resolution matrix.

- e) Ensemble average computation: Finally, the average of the individual  $P_{\text{F1D}}$  estimation per redshift bin is taken subtracting the undesired contributions, or, in mathematical terms,

$$P_{\text{F1D}}(k) = \left\langle \frac{P_{\text{raw}}(k) - P_{\text{noise}}(k)}{W^2} \right\rangle - P_{\text{SB}}(k). \quad (4.10)$$

In this work, I just computed the average term, the  $P_{\text{SB}}(k)$  is an additional correction (having an amplitude contribution in the  $P_{\text{F1D}}$ ) posterior to the `picca` data processing.

Following [Chabanier et al. \(2019b\)](#), the final  $P_{\text{F1D}}$  computation is presented in thirteen redshift bins separated in thirty six equally spaced ( $5.4 \times 10^{-2} \text{ s km}^{-1}$ ) values of  $k$ .

The Nyquist theorem of spectral analysis states that the highest possible wavenumber to be represented is given by  $k_s = 2\pi/\Delta v$  and  $k_{\text{max}} < k_s/2$ <sup>23</sup>. In eBOSS, with a spectral resolution of  $\Delta v = 69 \text{ km/s}$ , the highest  $k$  value is  $k_{\text{max}} \sim 0.045 \text{ (km/s)}^{-1}$ , however, as [Chabanier et al. \(2019b\)](#) explain in their article, the best maximum  $k$  value is  $k = 0.02 \text{ (km/s)}^{-1}$ , beyond which the spectrograph resolution decreases (see appendix B). DESI spectra are linearly binned with a resolution of  $\Delta\lambda = 0.8 \text{ \AA}$ , so by the Nyquist theorem we get  $k_{\text{max}} \sim 4.0 \text{ \AA}$ , and taking the same consideration as in eBOSS spectrograph we have  $k = 2.0 \text{ \AA}$ .

Finally, in order to refine the calculation of the aforementioned observable, a series of quality cuts were carried out.

The quality filtering of the forests was made according to that mentioned in [Chabanier et al. \(2019b\)](#), that is, discarding forests based on a CCD cut of  $3750 \text{ \AA}$  (UV-wavelength) and  $7200 \text{ \AA}$  (see appendix B), where the spectral response of the instrument decreases. Forests where the mean spectral resolution is larger than  $85 \text{ km/s}$  and where the mean SNR was less than 2.0 in eBOSS and 1.0 for DESI were also rejected.

As mentioned before, DLA systems and skylines are masked to make the delta extraction. In the case of DLA systems, all pixels where the absorption is higher than 20% were masked, and then corrected using a Voigt profile. At last, forests

---

<sup>23</sup> $k_s$ : sampling wavenumber.

shorter than 75 pixels were rejected, and forests with more than 40/120 masked pixels (eBOSS/DESI), whether from DLA absorption, sky line masking, or flags from the SDSS pipeline, were rejected.

Since the use of a FFT to compute the power spectrum requires equally-spaced pixels, `picca` reintroduces all masked pixels in the forest before performing the Fourier transform and set their flux to zero. Moreover, the number of iterations in the continuum fitting for all run was 7 (convergence).

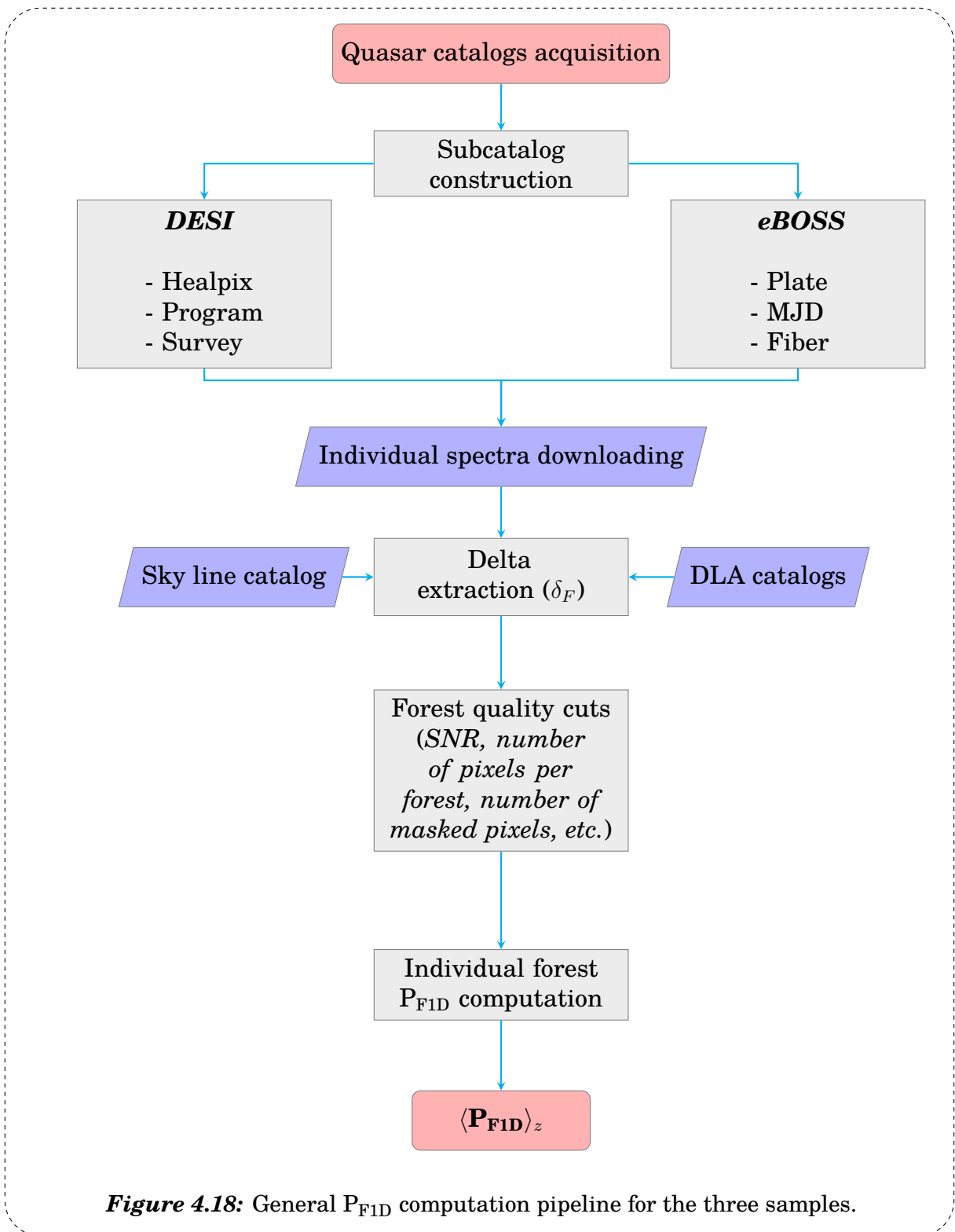
I used two versions of `picca` in the delta extraction procedure, the most recent version (master<sup>24</sup>) and an older one (v4<sup>25</sup>), this in order to achieve the closest reproduction to [Chabanier et al. \(2019b\)](#) results. In the rest of the text I used master, unless otherwise is specified.

As a summary of this chapter, [Figure 4.18](#) shows the general pipeline of the  $P_{\text{FID}}$  computation.

---

<sup>24</sup><https://github.com/igmhub/picca/tree/v8.3.0>

<sup>25</sup><https://github.com/igmhub/picca/tree/v4.alpha>



## Chapter 5

## RESULTS

5.1  $P_{\text{FID}}$  from eBOSS

Figure 5.1 shows the  $P_{\text{FID}}$  calculation out of the DR14 sample using `picca` v4. A total of 91 471 forests were used in the computation compared with the 94 558 reported by Chabanier et al. (2019b). Using the master version in the delta extraction, just 40 563 forests were used in the computation. For the sake of comparison, I only used redshift bins from  $z = 2.2$  to  $z = 4.4$ , where the statistics is best.

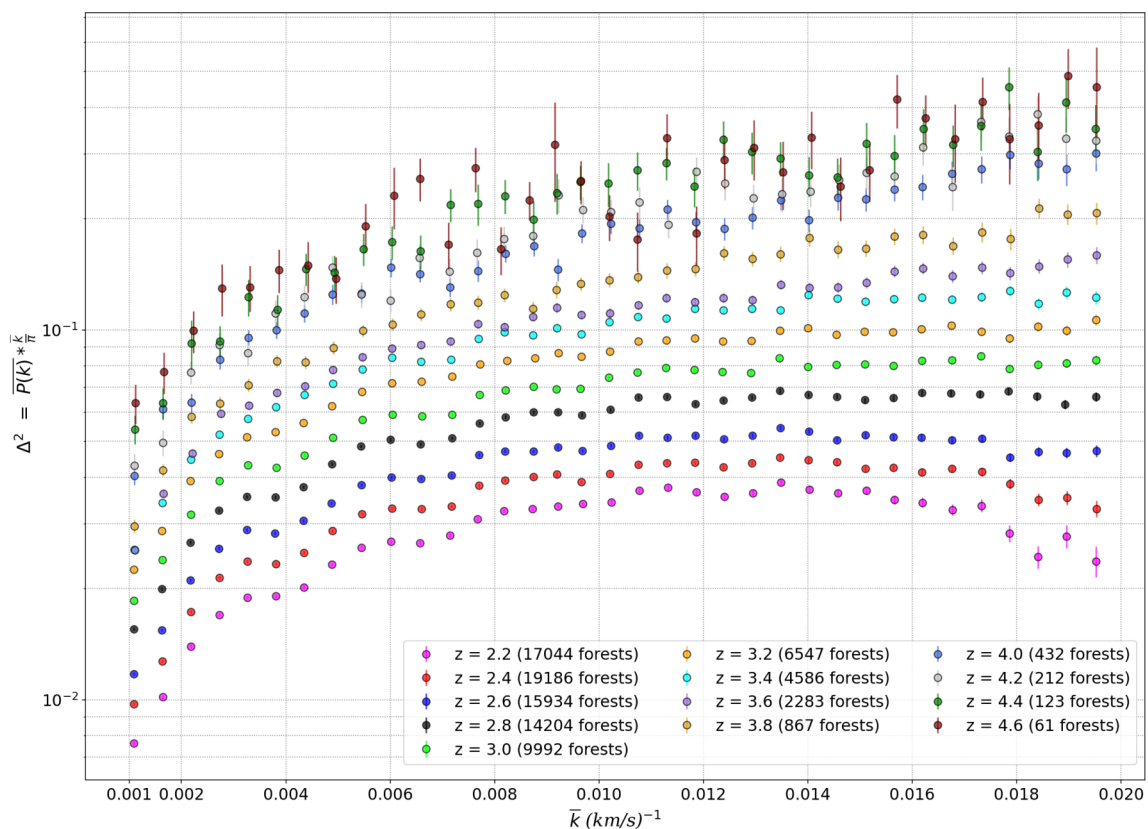


**Figure 5.1:**  $P_{\text{FID}}$  from the DR14 sample. The results shows the expected behaviour in contrast to Figure 3.11. The error (error bars) are proportional to  $z$  on almost all scales.

Figure 5.2 shows<sup>1</sup>, the comparison between my results and those obtained by [Chabanier et al. \(2019b\)](#). Although there is a good agreement between the results and the expected values, a noticeable discrepancy can be seen at lower redshift bins ( $z = 2.2, 2.4, 2.6$ ) and small scales ( $k > 0.016 \text{ s km}^{-1}$ ). This difference could be product of a missing correction of noise in the computation of the ensemble average. The exact correction or missing step have not been identified yet. As a final remark, it is appropriate to note that the results show good agreement among themselves. Using the older version of `picca` I get an average difference of 4.95%, in turn, using the master version I get an average difference of 8.78%.

In general, this difference between the results of the two versions of `picca` is a product of the quality filters that are applied when calculating the deltas. As Figure 5.3 shows, when the deltas are computed using the master version (v8.3.0), there is a greater number of forests rejected by the SNR threshold with no obvious preference for any of the three subdivisions of the forest (see Figure 4.14). Thus, for future analyzes with eBOSS, it should be necessary to review what causes this inconsistency between versions.

Once the DR14 quasar sample was analyzed, I moved to the DR16 sample. Using the quality filters and configurations mentioned in chapter 4, I successfully computed the  $P_{\text{F1D}}$  estimation for the DR16 sample. Using the older version of `picca`, a total of 104 468 forest were used in the computation, in turn, using the master version, a total of 48 331 forest were used.

The amount of new forests used into the computation is statistically significant at a level of  $\sim 10\%$  using version v4 (9910 new forests added into the computation) and  $\sim 20\%$  using the master version (7768 new forests). Comparing the results from both samples, as Figure 5.4 shows, there is a visual disagreement both for small and large scales. For the case of small scales, it is noticeable that the DR16 could suffer the same noise miss-correction as in DR14. No matter what, the results between the DR14 and DR16 samples are statistically homogeneous. The average difference obtained using the old version of `picca` was about 5.55%, and using the master version an average difference of 9.24%, so there is reasonably good accordance between the results.

---

<sup>1</sup>Lines don't represent the behaviour of the data (markers do), just plotted for visualization and clarity purposes. This apply for all comparison graphs.



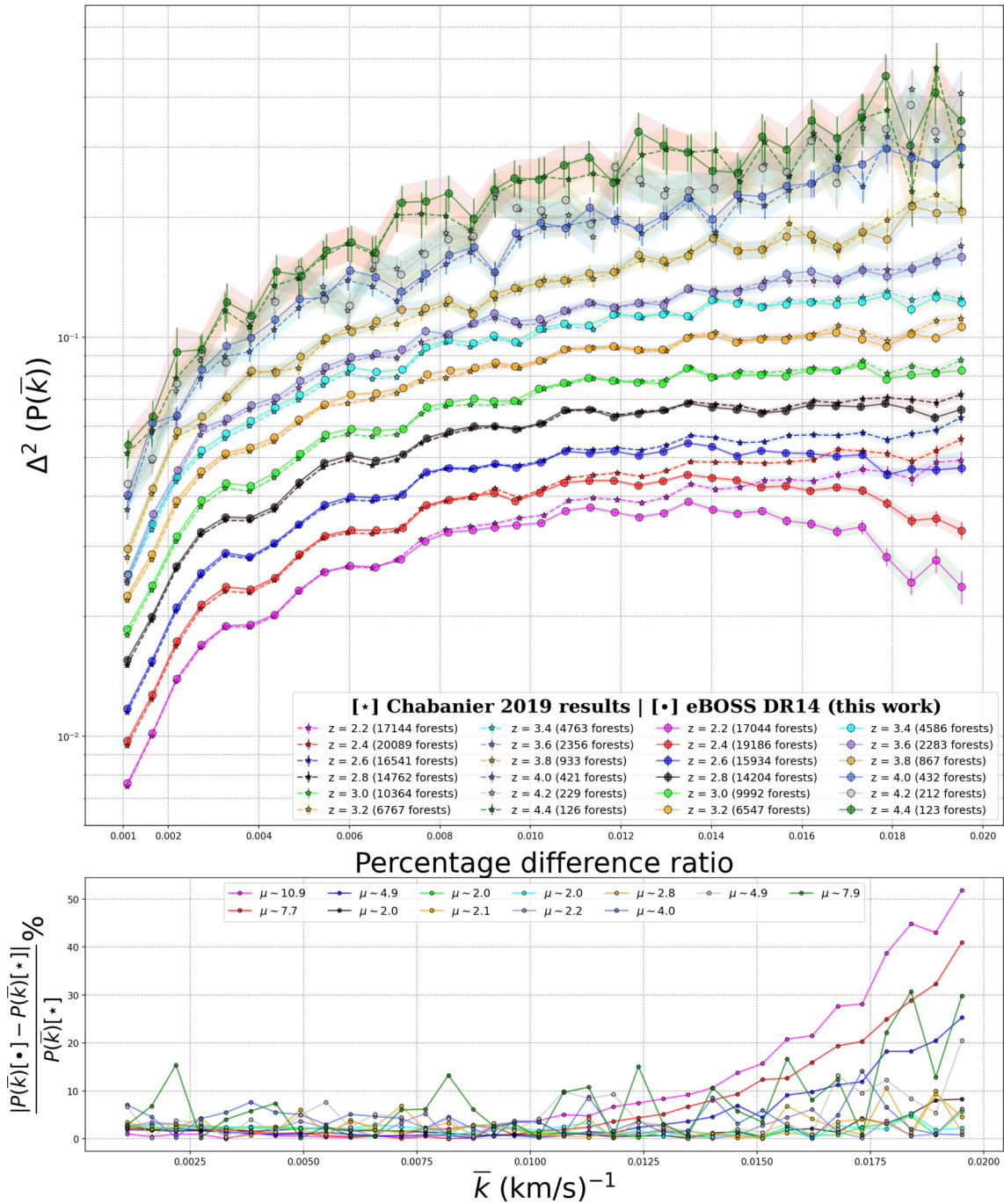


**Figure 5.2:** eBOSS DR14 results and Chabanier et al. (2019b) results comparison. An unexpected amplitude lowering for the three redshift bins at small scales can be seen.

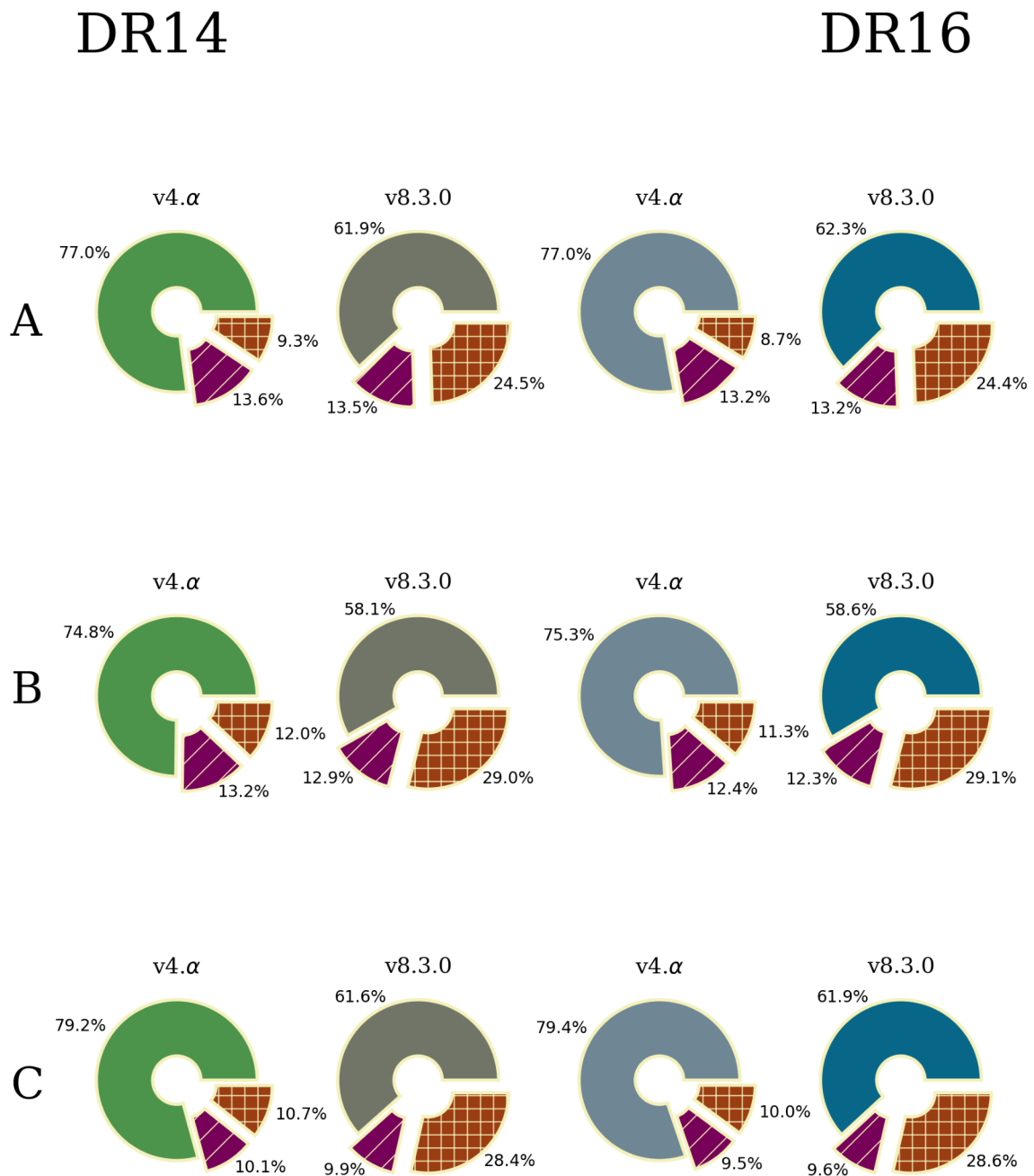


**Figure 5.3:** Proportion of rejected/accepted forests by quality filters in the two versions of `picca`. The purple hatched parts represent the forests rejected for being too short while the brown hatched parts represent those rejected due to low SNR level, the non-hatched parts represent the percentage of forests included in the computation of the  $P_{FID}$ . A substantial change is observed in the number of forests rejected due to a low level of SNR between the two versions of `picca`.

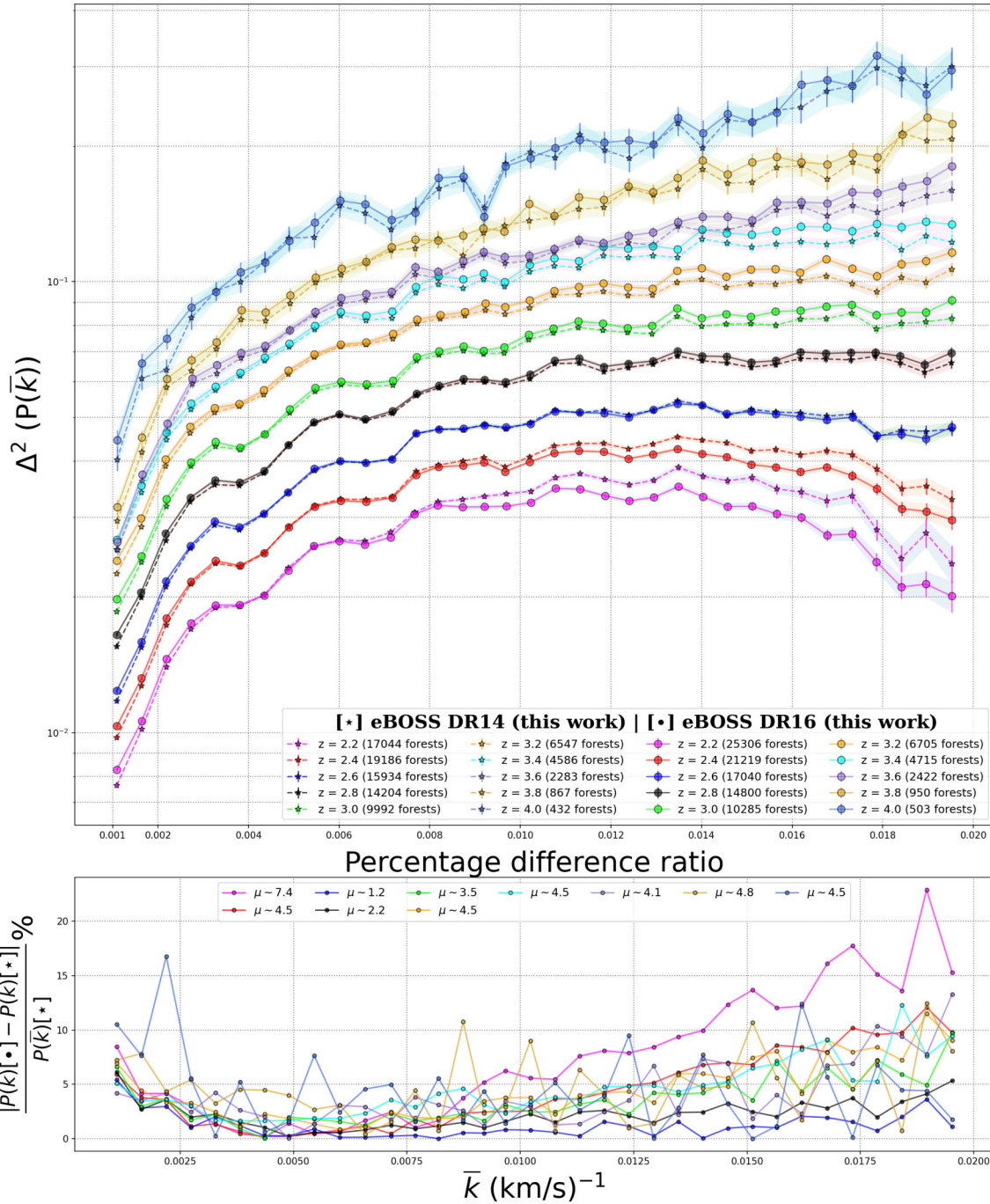


**Figure 5.4:** eBOSS DR14 results and DR16 results comparison. There is good accordance in contrast to DR14 (this work) and Chabanier et al. (2019b) except for extreme values in scale range.

## eBOSS systematic ratios

With the aim of evaluating the influence of sistematycs in the computation of the  $P_{\text{FID}}$ , I analyzed the percentage difference between the  $P_{\text{FID}}$  computation skipping corrections for DLAs, BALs and skylines in the sample, against the computation presented before (data splitting), this taking the `picca` master version computation as control group. The results are presented in figures 5.5 and 5.6.

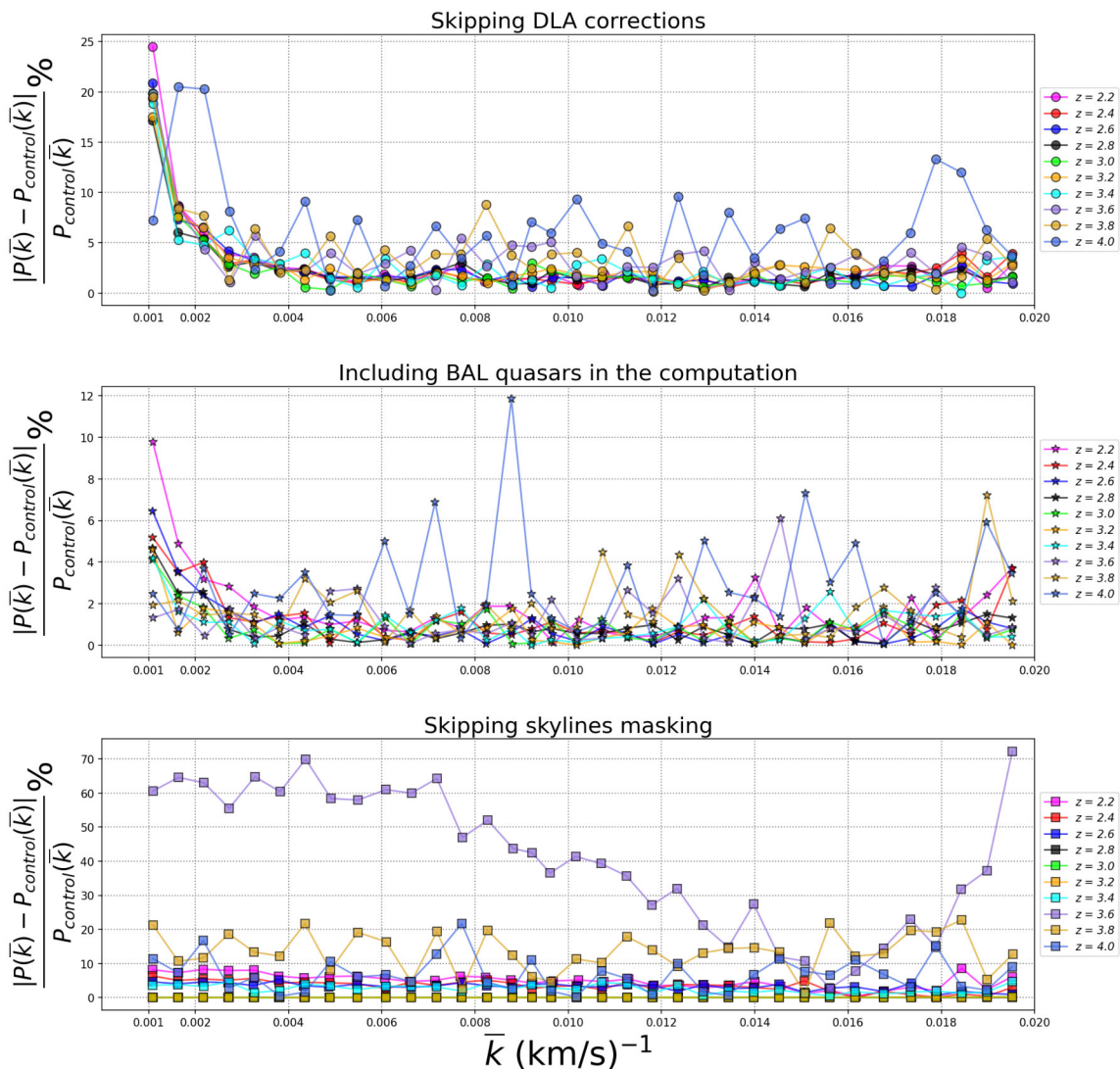


**Figure 5.5:**  $P_{\text{FID}}$  eBOSS DR14 systematics ratio. A prominent influence of DLAs and BAL quasars can be seen at large scales. On the other hand, an amplitude difference can be seen at  $z = 3.6$  skipping skylines corrections.



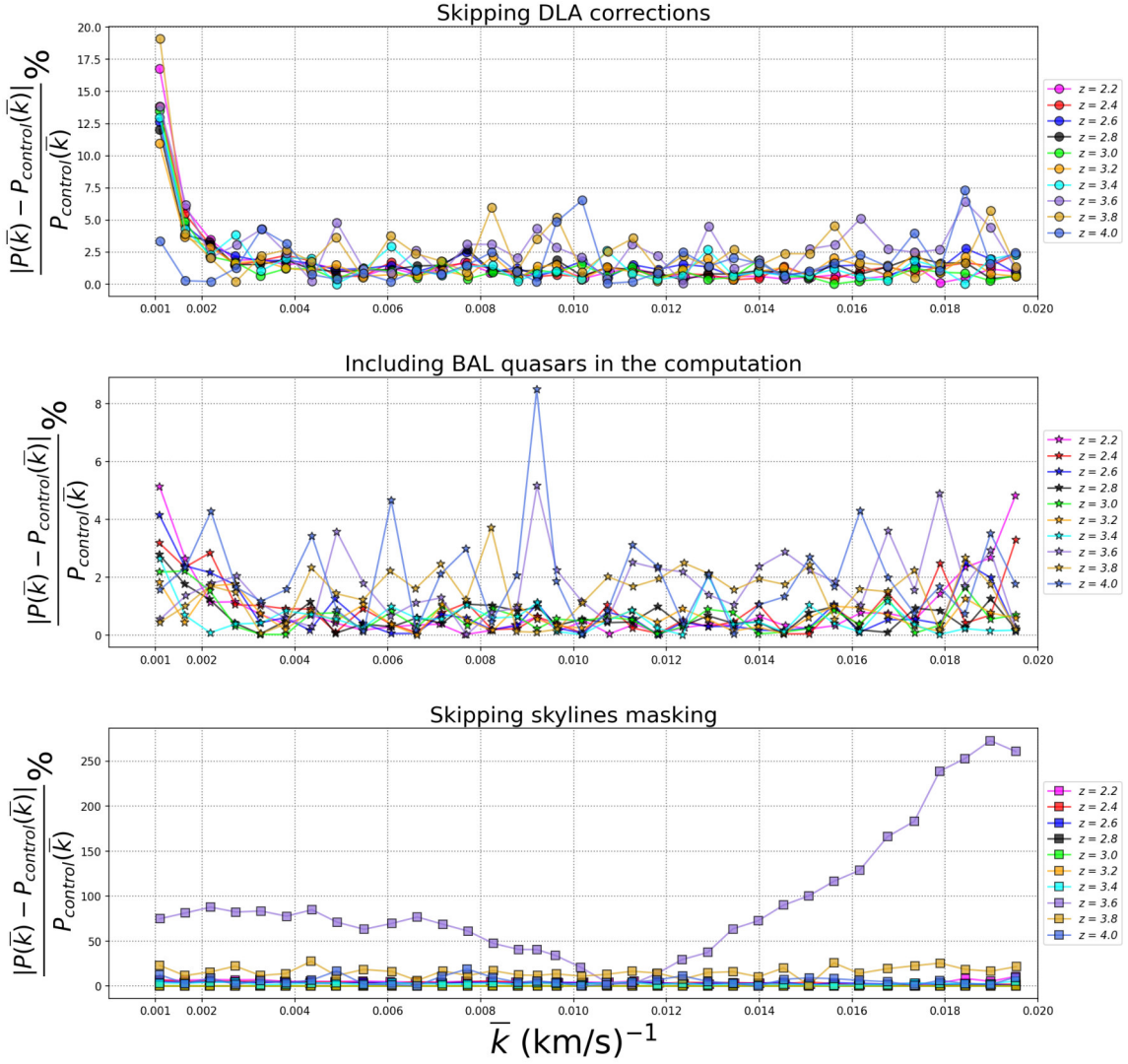


**Figure 5.6:**  $P_{\text{F1D}}$  eBOSS DR16 systematics ratio. The results are similar to those of DR14 in Figure 5.5.

As can be seen, skipping the DLA correction and BAL removing gives an undesired amplitude increment of the  $P_{\text{F1D}}$  at large scales, this is because the large scale modes are more sensitive to the contribution of broad absorption line profiles (this kind of behaviour is expected considering the absorption properties showed in figures 3.7 and 3.8), however, the DLAs' impact on large scales is more notorious than that of BAL quasars. Looking at the first panel of figures 5.5 and 5.6, for eBOSS DR14, the amplitude discrepancy for DLAs miss-correction above  $\sim 5\%$  starts at  $k \gtrsim 0.002 \text{ s km}^{-1}$ , and in DR16 about  $k \lesssim 0.002 \text{ s km}^{-1}$ . On the other hand, the discrepancy

for including BAL quasar in the  $P_{\text{FID}}$  computation is quite noticeable above  $\sim 2\%$  at  $k \sim 0.002 \text{ s km}^{-1}$  in DR14. For DR16, it is not very clear if this pattern follows the same behaviour as in DR14.

In this order of ideas, the previous statement suggests, that the DR16 catalog lacks BAL/DLA completeness, this also considering the proportions presented in Figure 5.4.

Furthermore, skipping skylines correction gives an undesired amplitude increment of the  $P_{\text{FID}}$  at all scales at certain redshift bins. Specifically, this undesired increment is present at  $z = 3.6$ , and, to a lesser extent, in the  $z = 3.8$  bin. Looking at Figure 4.16, this behaviour is expected because most of the forests at these particular redshift bins overlap with skylines. On the other hand, comparing the data splitting in the third panels of figures 5.5 and 5.6, it is quite evident that skipping skylines correction in eBOSS DR14 is less relevant to small scales than in DR16. Moreover, a possible turning point value for both DR14 ( $k \sim 0.016 \text{ s km}^{-1}$ ) and DR16 ( $k \sim 0.012 \text{ s km}^{-1}$ ) is also observed in these panels.

The results of this section are consistent with those presented in previous works like McDonald et al. (2006); Palanque-Delabrouille et al. (2013); Chabanier et al. (2019b) and Ravoux et al. (2023).

## 5.2 $P_{\text{FID}}$ from DESI

DESI spectra are linearly binned with a resolution of  $\Delta\lambda = 0.8 \text{ \AA}$ , so the natural units to make the calculation of the  $P_{\text{FID}}$  are wavelength units. Using quality criteria like in the previous section, I computed the  $P_{\text{FID}}$  out of the DESI EDR sample using a total number of 27 403 forest as is shown in Figure 5.7.

As can be seen in Figure 5.7, there is a good agreement between the results obtained by Ravoux et al. (2023) and those obtained in this work, the discrepancies at big scales presumably come from the missing DLA correction given that, as it was mentioned in the previous section, the DLA catalog for DESI is not public yet, however, the results are very consistent with an average difference ratio of 4.7%. For the computation of  $P_{\text{FID}}$  out of DESI, I only use the master version recently conditioned for DESI spectra.

On the other hand, figures 5.8 and 5.9 show the comparison between the results obtained out of DESI EDR in velocity units and Chabanier et al. (2019b). From

these figures, the improvement in scale resolution achieved by DESI in contrast to eBOSS could be noticeable. A good agreement ( $\sim 5\%$  average difference) at intermediate scales ( $k = 0.010 - 0.020 \text{ s km}^{-1}$ ) in all redshift bins can be seen.

Regarding to large scales ( $k = 0.000 - 0.010 \text{ s km}^{-1}$ ), it is also noticeable a great discrepancy mainly led by the DLA miss-correction. In the second panel of figures 5.8 and 5.9, these discrepancies reach higher values ( $\gtrsim 25\%$ ) compared with similar comparisons made in eBOSS ( $\lesssim 25\%$ , see section 5.1). Under the assumption that  $P_{\text{F1D}}$  results should be the same (or at least similar) in both eBOSS and DESI<sup>2</sup>, the difference at large scales shown in the aforementioned figures is a product of the DLAs miss-correction added to another factor (still unknown), such as the BAL catalog completeness or some error in the pipeline.

Ravoux et al. (2023) reported the same difference at large scales ( $\sim 15\%$ ), even after correcting for DLA. According to these authors, this anomaly could be due to the  $P_{\text{F1D}}$  computation pipeline and/or to the high-column density catalogs completeness (as pointed in the last paragraph). However, this is unlikely considering the  $P_{\text{F1D}}$  results presented by me use the current computation pipeline for eBOSS.

---

<sup>2</sup>This using the same pipeline provided by `picca` and also considering the possible statistical uncertainties for both surveys



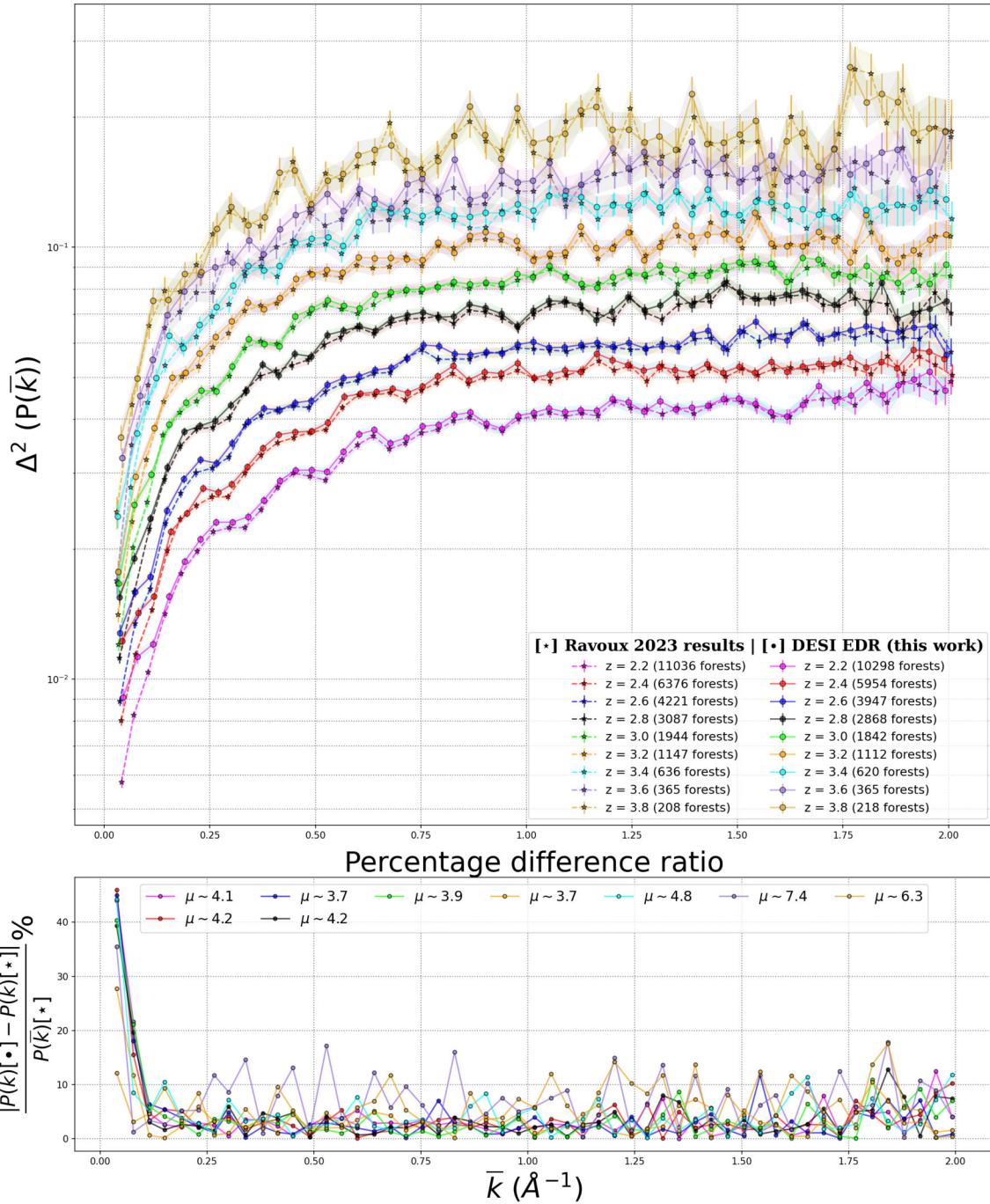


**Figure 5.7:** DESI EDR results and Ravoux et al. (2023) results comparison. There is agreement at all scales except for the largest ones product of the DLA miss-correction.

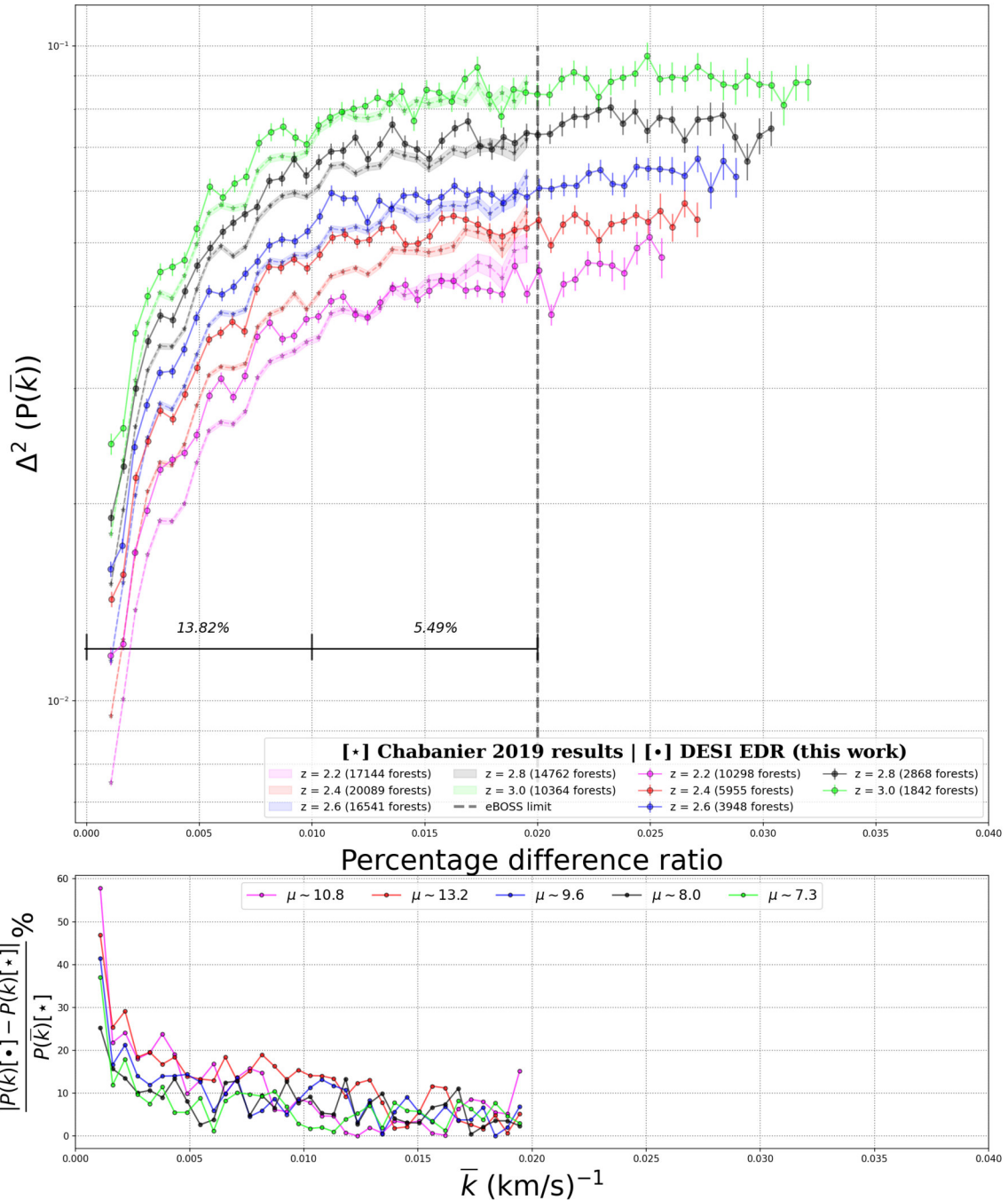


**Figure 5.8:** DESI EDR results comparison in velocity units for the first five redshift bins in contrast to Chabanier et al. (2019b) results.

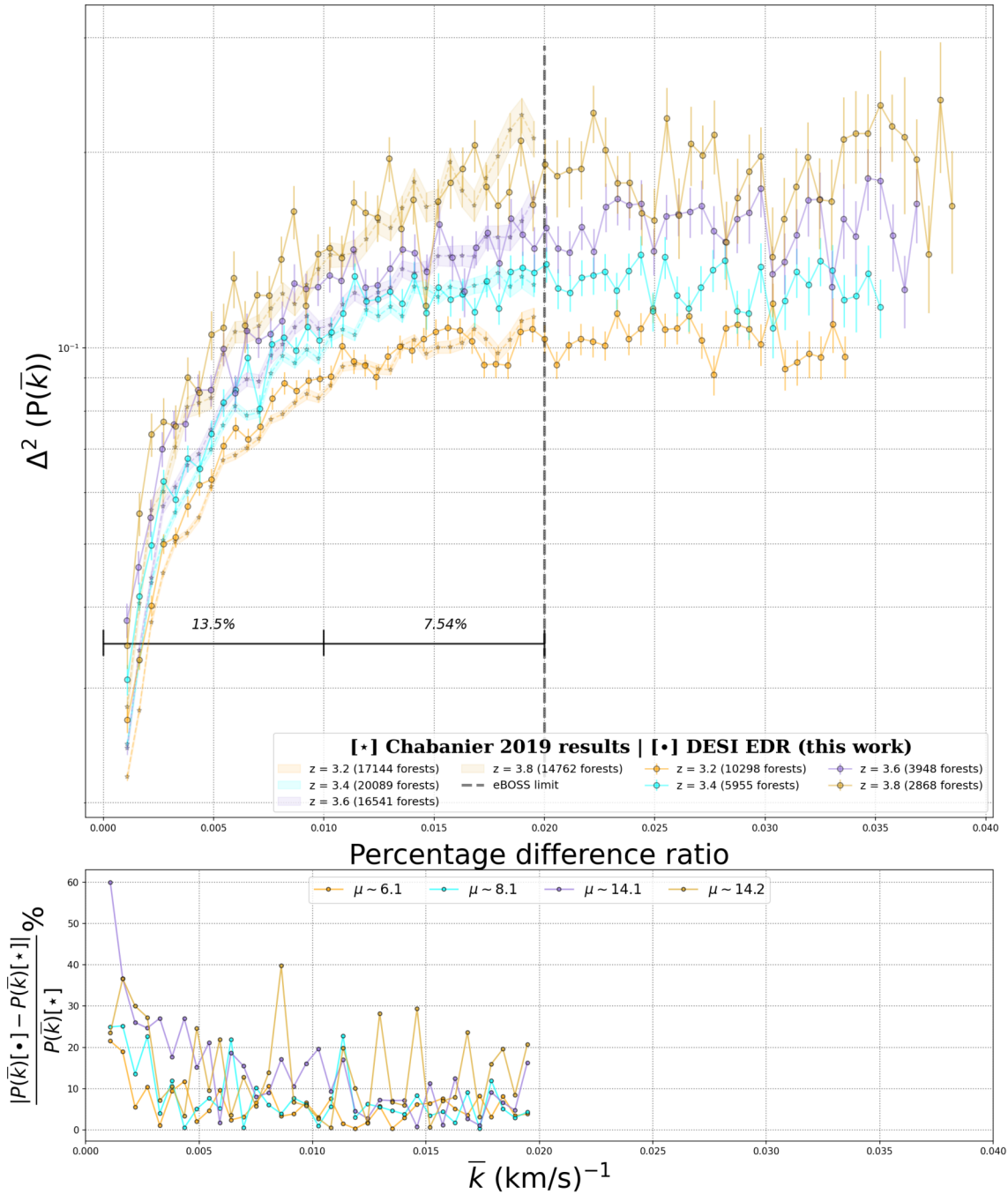
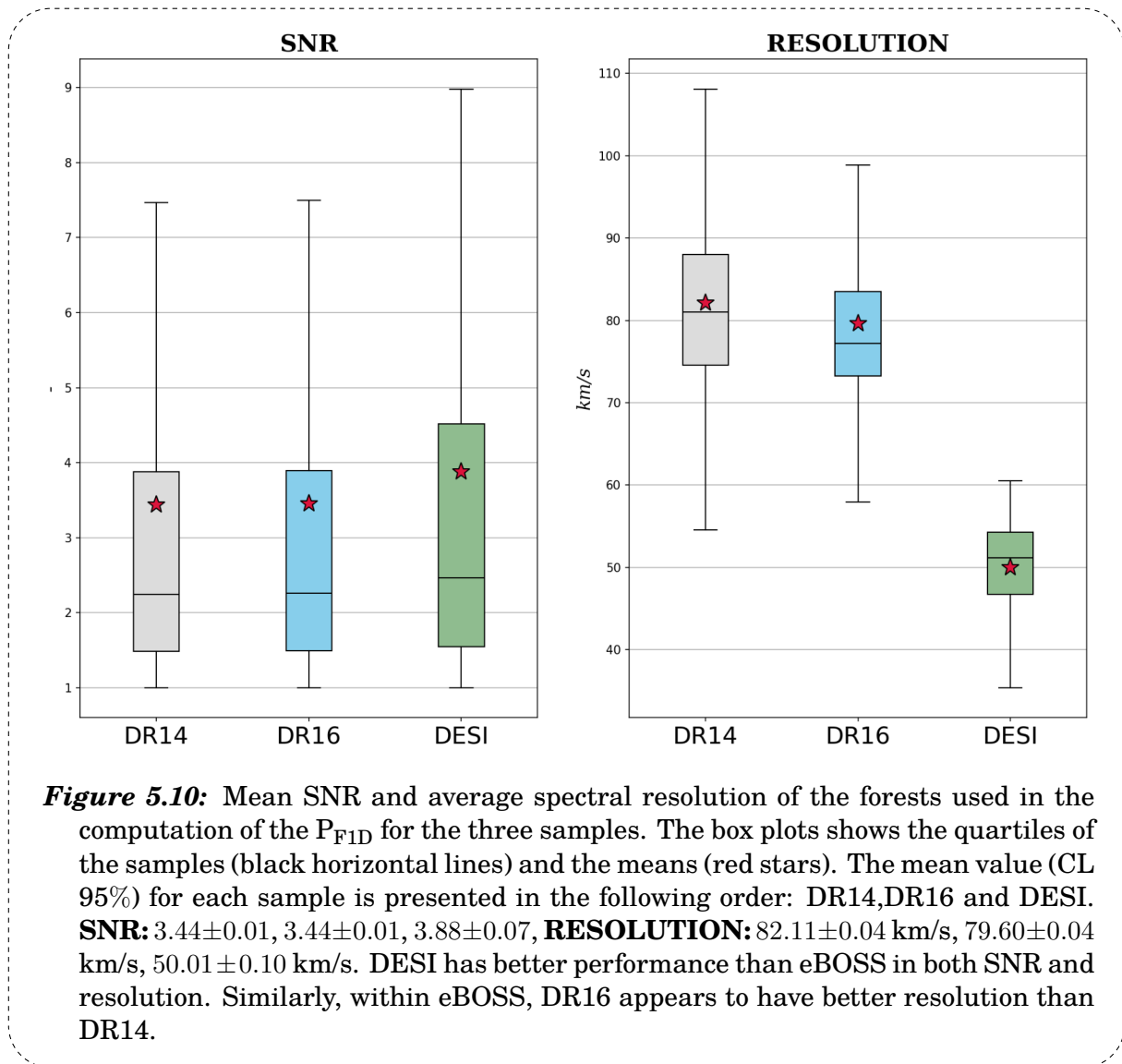


**Figure 5.9:** DESI EDR results comparison in velocity units for the last four redshift bins in contrast to Chabanier et al. (2019b).

As a final remark, Figure 5.10 shows the statistical distribution of the mean SNR and mean resolution in each forest used in the  $P_{\text{F1D}}$  computation of the three samples. As it can be seen, DESI shows a significant improvement both in spectral resolution and in the quality of the data (led by the technological advancements showed in appendix B), making the coming data releases a great opportunity to boost extragalactic and cosmological researches.



## DESI systematic ratios

Following the same procedure as in section 5.1, I computed the  $P_{\text{F1D}}$  out of DESI EDR skipping the skylines correction and including BAL quasars in the computation. As Figure 5.11 shows, skipping the corrections mentioned earlier gives similar results as in eBOSS. Including BAL quasars gives an undesired amplitude increment at large scales, and, again, skipping skylines correction gives an undesired amplitude increment of the  $P_{\text{F1D}}$  at  $z = 3.6$  and  $z = 3.8$  bins particularly at small scales. However, it is quite evident that, for DESI, the skylines influence is much smaller (and does not present a turning point value) compared with the results presented in eBOSS (figures 5.5 and 5.6).

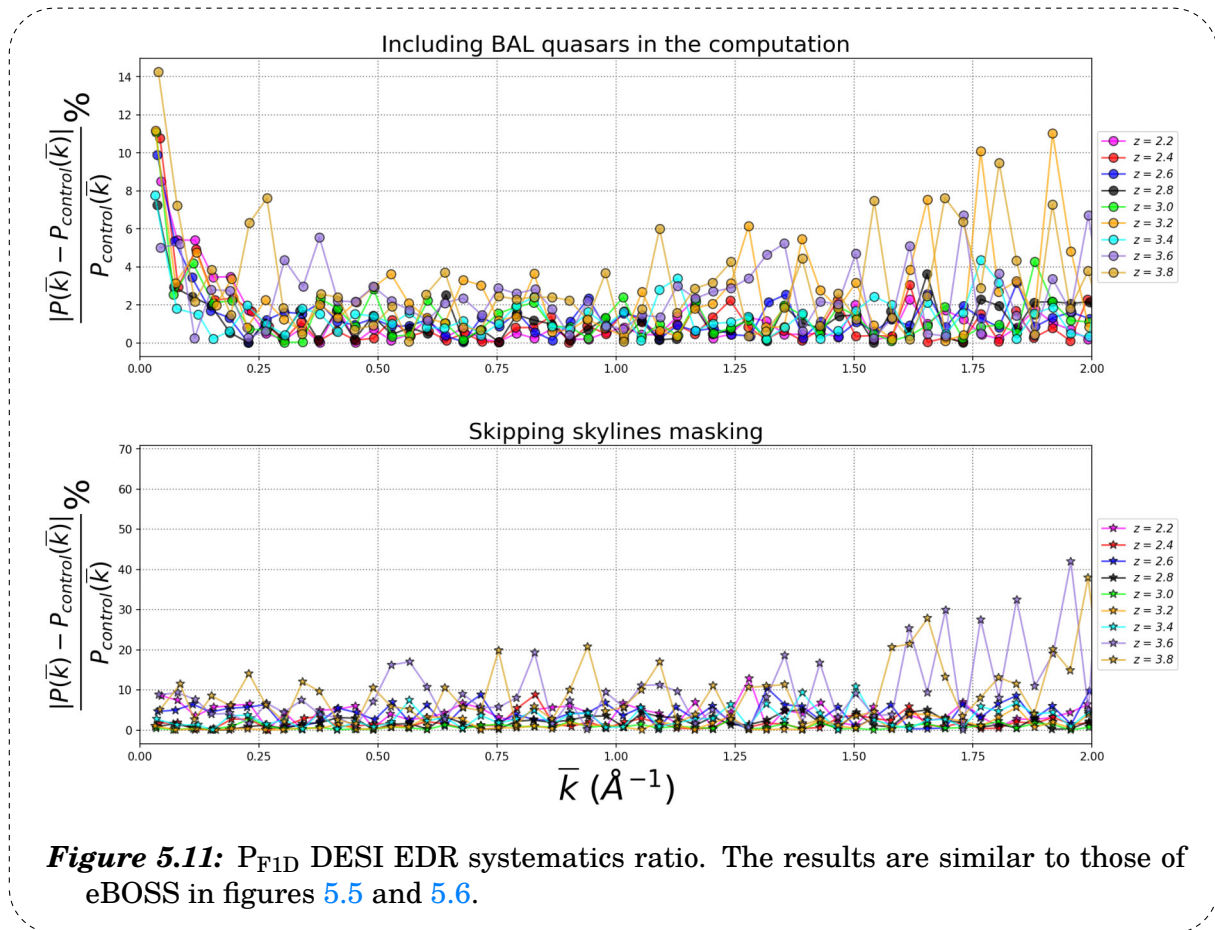


**Figure 5.11:**  $P_{\text{F1D}}$  DESI EDR systematics ratio. The results are similar to those of eBOSS in figures 5.5 and 5.6.



## DISCUSSION AND GENERAL CONCLUSIONS

Satisfactorily, it was possible to re-process eBOSS data, all from publicly available data and code, getting reasonably comparable  $P_{\text{FID}}$  results to those obtained by [Chabanier et al. \(2019b\)](#). The estimation of  $P_{\text{FID}}$  based on eBOSS DR16 was made, obtaining consistent results with those obtained from DR14 (Figure 5.4). Similarly, the  $P_{\text{FID}}$  from the initial public data release of DESI was estimated, achieving an improvement in resolution at smaller scales, as depicted in figures 5.8 and 5.9. The  $P_{\text{FID}}$  estimation from DESI is equally consistent with the results obtained by [Ravoux et al. \(2023\)](#), who used data from the early data release plus two months of the survey (Figure 5.7).

For eBOSS, there is a significant discrepancy at small scales in the first three redshift bins compared to [Chabanier et al. \(2019b\)](#) results, likely generated by a noise miss-correction. In the same way, during the computation of the P1D, two versions of the public code `picca` were used, `v4.alpha` and `v8.3.0(master)`. The results for eBOSS, generated after using each version independently, shows a discrepancy in the number of forests rejected applying the SNR quality cut. This difference, and the discrepancies presented for the three redshift bins at small scales, should be approached for future works using `picca`.

Regarding the analysis of systematic effects, it was found that BAL quasars and DLA systems in the quasar spectra lead to an increase in the amplitude of  $P_{\text{FID}}$  at large scales. Likewise, it is evident that the presence of skylines from the spectrograph is much more relevant for eBOSS forests at  $z = 3.6$ , also showing a possible turning point value ( $k \sim 0.014 \text{ s km}^{-1}$ ). The same analysis of skylines in DESI showed a large decrease in their influence on the  $P_{\text{FID}}$  computation, possibly due to an improvement in the spectra reduction pipeline compared to eBOSS.

Comparing the results obtained in eBOSS DR14 and DR16, it was observed a somewhat statistical low increase in the number of quasars available for calculating the  $P_{\text{FID}}$ . However, there is a subtle difference at large scales, possibly due to a BAL quasar miss-classification and/or to a DLA systems catalog incompleteness. This difference is also supported by Figure 4.12, where a significant difference in the

of BAL/DLA proportion is observed for each sample. Given that the eBOSS samples are supposed to be statistically homogeneous, it is expected that this behaviour would replicate on the BAL/DLA proportion.

It is worth noting that this work presents the results of the  $P_{\text{FID}}$  for eBOSS DR16, a calculation that had not been carried out by any previous research group. On the other hand, it is also convenient to emphasize that the eBOSS DR14 results presented here are a consistency check within the framework of the  $P_{\text{FID}}$  computation (scientific reproducibility). Additionally, the results from the DESI spectra sample validate the new pipeline built for this data set with `picca`.

Referring to the conclusion drawn by [Ravoux et al. \(2023\)](#), as cited in Chapter 5, it is evident that a discrepancy exists between the  $P_{\text{FID}}$  results of eBOSS and DESI on larger scales. The root cause of this disparity remains unidentified, being a current subject of debate. In line with this discussion, the present study could provide some insights into the potential factors contributing to this inconsistency.

The results presented here are consistent with previous studies; therefore, it is convenient to continue using DESI spectra due to its sensitivity on small scales and great spectra quality (figures 4.5 and 5.10). In the same way,  $P_{\text{FID}}$  measurements out of eBOSS should be refined in order to improve the results and solve the discrepancies presented in this work. In addition, there is the possibility to combine eBOSS and DESI data to achieve better results and, in turn, looking for (maybe) new instrumental systematics. This could be made by proposing new methods of continuum fitting, SNR quality cuts or data splitting like those presented in section 5.1. The  $P_{\text{FID}}$  estimation presented here could be coupled with hydrodynamical simulations and other cosmological probes to make relevant inferences to the area.



## REFERENCES

- Abareshi, B., Aguilar, J., Ahlen, S., Alam, S., Alexander, D. M., Alfarsy, R., Allen, L., Prieto, C. A., Alves, O., Ameel, J., et al. (2022). Overview of the instrumentation for the dark energy spectroscopic instrument. The Astronomical Journal, 164(5):207.
- Abbott, T., Aguena, M., Alarcon, A., Allam, S., Alves, O., Amon, A., Andrade-Oliveira, F., Annis, J., Avila, S., Bacon, D., et al. (2022). Dark energy survey year 3 results: Cosmological constraints from galaxy clustering and weak lensing. Physical Review D, 105(2):023520.
- Abdalla, E., Abellán, G. F., Aboubrahim, A., Agnello, A., Akarsu, Ö., Akrami, Y., Alestas, G., Aloni, D., Amendola, L., Anchordoqui, L. A., et al. (2022). Cosmology intertwined: A review of the particle physics, astrophysics, and cosmology associated with the cosmological tensions and anomalies. Journal of High Energy Astrophysics, 34:49–211.
- Abolfathi, B., Aguado, D., Aguilar, G., Prieto, C. A., Almeida, A., Ananna, T. T., Anders, F., Anderson, S. F., Andrews, B. H., Anguiano, B., et al. (2018). The fourteenth data release of the sloan digital sky survey: First spectroscopic data from the extended baryon oscillation spectroscopic survey and from the second phase of the apache point observatory galactic evolution experiment. The Astrophysical Journal Supplement Series, 235(2):42.
- Addison, G. E., Hinshaw, G., and Halpern, M. (2013). Cosmological constraints from baryon acoustic oscillations and clustering of large-scale structure. Monthly Notices of the Royal Astronomical Society, 436(2):1674–1683.
- Aghamousa, A., Aguilar, J., Ahlen, S., Alam, S., Allen, L. E., Prieto, C. A., Annis, J., Bailey, S., Baland, C., Ballester, O., et al. (2016). The desi experiment part ii: instrument design. arXiv preprint arXiv:1611.00037.
- Ahumada, R., Prieto, C. A., Almeida, A., Anders, F., Anderson, S. F., Andrews, B. H., Anguiano, B., Arcodia, R., Armengaud, E., Aubert, M., et al. (2020). The 16th data release of the sloan digital sky surveys: first release from the apogee-2 southern survey and full release of eboss spectra. The Astrophysical Journal Supplement Series, 249(1):3.
- Aiola, S., Calabrese, E., Maurin, L., Naess, S., Schmitt, B. L., Abitbol, M. H., Addison, G. E., Ade, P. A., Alonso, D., Amiri, M., et al. (2020). The atacama cosmology telescope: Dr4 maps and cosmological parameters. Journal of Cosmology and Astroparticle Physics, 2020(12):047.
- Akarsu, Ö., Colgáin, E. Ó., Sen, A. A., and Sheikh-Jabbari, M. (2024).  $\lambda$  cdm tensions: Localising missing physics through consistency checks. arXiv preprint arXiv:2402.04767.
- Albrecht, A. and Steinhardt, P. J. (1982). Cosmology for grand unified theories with radiatively induced symmetry breaking. Physical Review Letters, 48(17):1220.
- Alexander, D. M., Davis, T. M., Chaussidon, E., Fawcett, V., Gonzalez-Morales, A. X., Lan, T.-W., Yèche, C., Ahlen, S., Aguilar, J., Armengaud, E., et al. (2023). The desi survey validation: Results from visual inspection of the quasar survey spectra. The Astronomical Journal, 165(3):124.
- Alfvén, H. and Herlofson, N. (1950). Cosmic radiation and radio stars. In A Source Book in Astronomy and Astrophysics, 1900–1975, pages 779–781. Harvard University Press.
- Alpher, R. A., Bethe, H., and Gamow, G. (1948). The origin of chemical elements. Physical Review, 73(7):803.
- Ananna, T. T., Urry, C. M., Treister, E., Hickox, R. C., Shankar, F., Ricci, C., Cappelluti, N., Marchesi, S., and Turner, T. J. (2020). Accretion history of agns. iii. radiative efficiency and agn contribution to reionization. The Astrophysical Journal, 903(2):85.
- Arinyo-i Prats, A., Miralda-Escude, J., Viel, M., and Cen, R. (2015). The non-linear power spectrum of the lyman alpha forest. Journal of Cosmology and Astroparticle Physics, 2015(12):017.
- Armengaud, E., Palanque-Delabrouille, N., Yèche, C., Marsh, D. J., and Baur, J. (2017). Constraining the mass of light bosonic dark matter using sdss lyman- $\alpha$  forest. Monthly Notices of the Royal Astronomical Society, 471(4):4606–4614.
- Arnau Romeu, J. (2014). Derivation of friedman equations. Facultat de Fisica, Universitat de Barcelona.
- Arun, K., Gudennavar, S., and Sivaram, C. (2017). Dark matter, dark energy, and alternate models: A review. Advances in Space Research, 60(1):166–186.

- Aviles, A., Banerjee, A., Niz, G., and Slepian, Z. (2021). Clustering in massive neutrino cosmologies via eulerian perturbation theory. Journal of Cosmology and Astroparticle Physics, 2021(11):028.
- Bahcall, J. N. and Salpeter, E. (1965). On the interaction of radiation from distant sources with the intervening medium. The Astrophysical Journal, 142:1677–1680.
- Bahcall, N. A., Lubin, L. M., and Dorman, V. (1995). Where is the dark matter? The Astrophysical Journal, 447(2):L81.
- Battaner, E. and Florido, E. (2000). The rotation curve of spiral galaxies and its cosmological implications. arXiv preprint astro-ph/0010475.
- Baumann, D. (2022). Cosmology. Cambridge University Press.
- Becker, R. H., Fan, X., White, R. L., Strauss, M. A., Narayanan, V. K., Lupton, R. H., Gunn, J. E., Annis, J., Bahcall, N. A., Brinkmann, J., et al. (2001). Evidence for reionization at  $z \approx 6$ : Detection of a Gunn-Peterson trough in a  $z=6.28$  quasar. The Astronomical Journal, 122(6):2850.
- Beckmann, V. and Shrader, C. (2012). Active galactic nuclei. John Wiley & Sons.
- Bengaly, C. A., Maartens, R., and Santos, M. G. (2018). Probing the cosmological principle in the counts of radio galaxies at different frequencies. Journal of Cosmology and Astroparticle Physics, 2018(04):031.
- Berk, D. E. V., Richards, G. T., Bauer, A., Strauss, M. A., Schneider, D. P., Heckman, T. M., York, D. G., Hall, P. B., Fan, X., Knapp, G., et al. (2001). Composite quasar spectra from the Sloan Digital Sky Survey. The Astronomical Journal, 122(2):549.
- Bertone, G. and Tait, T. M. (2018). A new era in the quest for dark matter. arXiv preprint arXiv:1810.01668.
- Bocquet, S., Dietrich, J., Schrabback, T., Bleem, L., Klein, M., Allen, S., Applegate, D., Ashby, M., Bautz, M., Bayliss, M., et al. (2019). Cluster cosmology constraints from the 2500 deg<sup>2</sup> SPT-SZ survey: inclusion of weak gravitational lensing data from Magellan and the Hubble Space Telescope. The Astrophysical Journal, 878(1):55.
- Bolton, J. (1948). Discrete sources of galactic radio frequency noise. Nature, 162(4108):141–142.
- Bolton, J. G., Stanley, G. J., and Slee, O. (1949). Positions of three discrete sources of galactic radio-frequency radiation. In A Source Book in Astronomy and Astrophysics, 1900–1975, pages 777–778. Harvard University Press.
- Borde, A., Palanque-Delabrouille, N., Rossi, G., Viel, M., Bolton, J., Yèche, C., LeGoff, J., and Rich, J. (2014). Simulating the effect of cosmological parameters on the one-dimensional Ly $\alpha$  forest power spectrum. Journal of Cosmology and Astroparticle Physics.
- Bourboux, H. d. M. d., Rich, J., Font-Ribera, A., Agathe, V. d. S., Farr, J., Etourneau, T., Goff, J.-M. L., Cuceu, A., Balland, C., Bautista, J. E., et al. (2020). The completed SDSS-IV extended baryon oscillation spectroscopic survey: Baryon acoustic oscillations with Ly $\alpha$  forests. arXiv preprint arXiv:2007.08995.
- Boylan-Kolchin, M., Springel, V., White, S. D., Jenkins, A., and Lemson, G. (2009). Resolving cosmic structure formation with the Millennium-II simulation. Monthly Notices of the Royal Astronomical Society, 398(3):1150–1164.
- Busca, N. and Balland, C. (2018). Quasarnet: Human-level spectral classification and redshifting with deep neural networks. arXiv preprint arXiv:1808.09955.
- Capozzi, F., Lisi, E., Marrone, A., Montanino, D., and Palazzo, A. (2016). Neutrino masses and mixings: Status of known and unknown  $3\nu$  parameters. Nuclear Physics B, 908:218–234.
- Chabanier, S., Bournaud, F., Dubois, Y., Palanque-Delabrouille, N., Yèche, C., Armengaud, E., Peirani, S., and Beckmann, R. (2020). The impact of AGN feedback on the 1D power spectra from the Ly $\alpha$  forest using the horizon-AGN suite of simulations. Monthly Notices of the Royal Astronomical Society, 495(2):1825–1840.
- Chabanier, S., Etourneau, T., Le Goff, J.-M., Rich, J., Stermer, J., Abolfathi, B., Font-Ribera, A., Gonzalez-Morales, A. X., de La Macorra, A., Pérez-Ráfols, I., et al. (2022). The completed Sloan Digital Sky Survey IV extended baryon oscillation spectroscopic survey: The damped Ly $\alpha$  systems catalog. The Astrophysical Journal Supplement Series, 258(1):18.
- Chabanier, S., Millea, M., and Palanque-Delabrouille, N. (2019a). Matter power spectrum: from Ly $\alpha$  forest to CMB scales. Monthly Notices of the Royal Astronomical Society, 489(2):2247–2253.
- Chabanier, S., Palanque-Delabrouille, N., Yèche, C., Le Goff, J.-M., Armengaud, E., Bautista, J., Blomqvist, M., Dawson, K., Etourneau, T., Font-Ribera, A., et al. (2019b). The one-dimensional power spectrum from the SDSS DR14 Ly $\alpha$  forests. Journal of Cosmology and Astroparticle Physics, 2019(07):017.

- Chacón, J., Vázquez, J. A., and Gabbasov, R. (2020). Dark matter with n-body numerical simulations. [arXiv preprint arXiv:2006.10203](#).
- CHANDRA X-Ray Observatory, t. (2006). X-ray/optical/lensing map composites of 1e 0657-56. <https://chandra.harvard.edu/photo/2006/1e0657/more.html>.
- Charlton, J. and Churchill, C. (2001). Quasistellar objects: Intervening absorption lines. In *Encyclopedia of Astronomy & Astrophysics*, pages 1–11. CRC Press.
- Chaussidon, E., Yèche, C., Palanque-Delabrouille, N., Alexander, D. M., Yang, J., Ahlen, S., Bailey, S., Brooks, D., Cai, Z., Chabanier, S., et al. (2023). Target selection and validation of desi quasars. *The Astrophysical Journal*, 944(1):107.
- Clemence, G. M. (1947). The relativity effect in planetary motions. *Reviews of Modern Physics*, 19(4):361.
- Cooke, R. J., Pettini, M., and Steidel, C. C. (2018). One percent determination of the primordial deuterium abundance. *The Astrophysical Journal*, 855(2):102.
- Copi, C. J., Schramm, D. N., and Turner, M. S. (1995). Big-bang nucleosynthesis and the baryon density of the universe. *Science*, 267(5195):192–199.
- Costanzi, M., Rozo, E., Simet, M., Zhang, Y., Evrard, A., Mantz, A., Rykoff, E., Jeltema, T., Gruen, D., McClintock, S. A. T., et al. (2018). Dark energy survey year 1 results: methods for cluster cosmology and application to the sdss. [arXiv preprint arXiv:1810.09456](#).
- Croft, R., Weinberg, D. H., Katz, N., and Hernquist, L. (1998). Cosmology from the structure of the lyman-alpha forest. [arXiv: Astrophysics](#).
- Croft, R. A., Weinberg, D. H., Bolte, M., Burles, S., Hernquist, L., Katz, N., Kirkman, D., and Tytler, D. (2002). Toward a precise measurement of matter clustering: Ly $\alpha$  forest data at redshifts 2-4. *The Astrophysical Journal*, 581(1):20.
- Croft, R. A., Weinberg, D. H., Katz, N., and Hernquist, L. (1997). Recovery of the power spectrum of mass fluctuations from observations of the ly $\alpha$  forest. *The Astrophysical Journal*, 495(1):44.
- Croton, D. J. (2013). Damn you, little h!(or, real-world applications of the hubble constant using observed and simulated data). *Publications of the Astronomical Society of Australia*, 30:e052.
- Day, A., Tytler, D., and Kambalur, B. (2019). Power spectrum of the flux in the lyman-alpha forest from high-resolution spectra of 87 qsos. *Monthly Notices of the Royal Astronomical Society*, 489(2):2536–2554.
- Dekel, A., Stoehr, F., Mamon, G., Cox, T., Novak, G., and Primack, J. (2005). Lost and found dark matter in elliptical galaxies. *Nature*, 437(7059):707–710.
- Del Popolo, A. and Le Delliou, M. (2017). Small scale problems of the  $\lambda$ cdm model: a short review. *Galaxies*, 5(1):17.
- Delubac, T., Rich, J., Bailey, S., Font-Ribera, A., Kirkby, D., Le Goff, J.-M., Pieri, M. M., Slosar, A., Aubourg, É., Bautista, J. E., et al. (2013). Baryon acoustic oscillations in the ly $\alpha$  forest of boss quasars. *Astronomy & Astrophysics*, 552:A96.
- DESI-Collaboration, Adame, A., Aguilar, J., Ahlen, S., Alam, S., Aldering, G., Alexander, D., Alfarsy, R., Prieto, C. A., Alvarez, M., Alves, O., et al. (2023a). Validation of the scientific program for the dark energy spectroscopic instrument. [arXiv preprint arXiv:2306.06307](#).
- DESI-Collaboration, Adame, A., Aguilar, J., Ahlen, S., Alam, S., Aldering, G., Alexander, D., Alfarsy, R., Prieto, C. A., Alvarez, M., et al. (2023b). The early data release of the dark energy spectroscopic instrument. [arXiv preprint arXiv:2306.06308](#).
- DESI-Collaboration, Aghamousa, A., Aguilar, J., Ahlen, S., Alam, S., Allen, L. E., Prieto, C. A., Annis, J., Bailey, S., Balland, C., et al. (2016). The desi experiment part i: Science, targeting, and survey design. [arXiv e-prints](#).
- DeYoung, D. S. and Axford, W. (1967). Inertial confinement of extended radio sources. *Nature*, 216(5111):129–131.
- Di Valentino, E., Mena, O., Pan, S., Visinelli, L., Yang, W., Melchiorri, A., Mota, D. F., Riess, A. G., and Silk, J. (2021). In the realm of the hubble tension—a review of solutions. *Classical and Quantum Gravity*, 38(15):153001.
- Di-Valentino, E., Olga, M., Supriya, P., Luca, V., Weiqiang, Y., Alessandro, M., et al. (2021). In the realm of the hubble tension—a review of solutions. *Class. Quant. Grav.*, 38.
- Dijkstra, M. (2019). *Lyman-alpha as an Astrophysical and Cosmological Tool*, volume 46. Springer.

- Dodelson, S. and Schmidt, F. (2020). Modern cosmology. Academic press.
- Dodelson, S. and Widrow, L. M. (1994). Sterile neutrinos as dark matter. Physical Review Letters, 72(1):17.
- Dolgov, A. D. (2002). Neutrinos in cosmology. Physics Reports, 370(4-5):333–535.
- du Mas des Bourboux, H., Rich, J., Font-Ribera, A., de Sainte Agathe, V., Farr, J., Etourneau, T., Le Goff, J.-M., Cuceu, A., Balland, C., Bautista, J. E., et al. (2021). picca: Package for igm cosmological-correlations analyses. Astrophysics Source Code Library, pages ascl-2106.
- Dyson, F. W., Eddington, A. S., and Davidson, C. (1920). IX. a determination of the deflection of light by the sun's gravitational field, from observations made at the total eclipse of may 29, 1919. Philosophical Transactions of the Royal Society of London. Series A, Containing Papers of a Mathematical or Physical Character, 220(571-581):291–333.
- eBOSS Collaboration, Alam, S., Aubert, M., Avila, S., Balland, C., Bautista, J. E., Bershady, M. A., Bizyaev, D., Blanton, M. R., Bolton, A. S., Bovy, J., et al. (2021). Completed sdss-iv extended baryon oscillation spectroscopic survey: Cosmological implications from two decades of spectroscopic surveys at the apache point observatory. Physical Review D, 103(8):083533.
- Einasto, J. (2009). Dark matter. arXiv preprint arXiv:0901.0632.
- Einstein, A. (1917). Cosmological considerations on the general theory of relativity. Cosmological Constants, page 16.
- Eisenstein, D. J., Zehavi, I., Hogg, D. W., Scoccimarro, R., Blanton, M. R., Nichol, R. C., Scranton, R., Seo, H.-J., Tegmark, M., Zheng, Z., et al. (2005). Detection of the baryon acoustic peak in the large-scale correlation function of sdss luminous red galaxies. The Astrophysical Journal, 633(2):560.
- Elvis, M. (2009). The quasar continuum. Proceedings of the International Astronomical Union, 5(S267):55–64.
- ESA (2013). Planck cmb. [https://www.esa.int/ESA\\_Multimedia/Images/2013/03/Planck\\_CMB](https://www.esa.int/ESA_Multimedia/Images/2013/03/Planck_CMB).
- Ezquiaga, J. M. and Zumalacárregui, M. (2018). Dark energy in light of multi-messenger gravitational-wave astronomy. Frontiers in Astronomy and Space Sciences, 5:44.
- Fairbairn, M. (2022). Galactic anomalies and particle dark matter. Symmetry, 14(4):812.
- Fan, X., Strauss, M. A., Becker, R. H., White, R. L., Gunn, J. E., Knapp, G. R., Richards, G. T., Schneider, D. P., Brinkmann, J., and Fukugita, M. (2006). Constraining the evolution of the ionizing background and the epoch of reionization with  $z \approx 6$  quasars. ii. a sample of 19 quasars. The Astronomical Journal, 132(1):117.
- Fanaroff, B. L. and Riley, J. M. (1974). The morphology of extragalactic radio sources of high and low luminosity. Monthly Notices of the Royal Astronomical Society, 167(1):31P–36P.
- Fath, E. A. (1909). The spectra of some spiral nebulae and globular star clusters. Publications of the Astronomical Society of the Pacific, 21(126):138–143.
- Faucher-Giguère, C.-A., Prochaska, J., Lidz, A., Hernquist, L., and Zaldarriaga, M. (2007). A direct precision measurement of the intergalactic lyman- $\alpha$  opacity at  $z \approx 4.2$ . Nuovo Cimento B Serie, 122(9):1249–1252.
- Fazio, G. G., Hernquist, L., Loeb, A., and Mckee, C. (2018). Encyclopedia Of Cosmology, The (In 4 Volumes). World Scientific.
- Filbert, S., Martini, P., Seebaluck, K., Ennesser, L., Alexander, D., Bault, A., Brodzeller, A., Herrera-Alcantar, H., Montero-Camacho, P., Pérez-Ràfols, I., et al. (2023). Broad absorption line quasars in the dark energy spectroscopic instrument early data release. arXiv preprint arXiv:2309.03434.
- Fixsen, D., Cheng, E., Gales, J., Mather, J. C., Shafer, R., and Wright, E. (1996). The cosmic microwave background spectrum from the full coBE\* firas data set. The Astrophysical Journal, 473(2):576.
- Flaugher, B. and Bebek, C. (2014). The dark energy spectroscopic instrument (desi). In Ground-based and Airborne Instrumentation for Astronomy V, volume 9147, pages 282–289. SPIE.
- Font-Ribera, A., McDonald, P., and Slosar, A. (2018). How to estimate the 3d power spectrum of the lyman- $\alpha$  forest. Journal of Cosmology and Astroparticle Physics, 2018(01):003.
- Francfort, J. (2022). Observables in cosmology: Three astronomical perspectives. arXiv preprint arXiv:2207.03296.
- Freedman, W. L. and Madore, B. F. (2010). The hubble constant. Annual Review of Astronomy and Astrophysics, 48:673–710.

- Friedman, A. (1922). Über die krümmung des raumes. Zeitschrift für Physik, 10(1):377–386.
- Friedmann, A. (1924). Über die möglichkeit einer welt mit konstanter negativer krümmung des raumes. Zeitschrift für Physik, 21(1):326–332.
- Frigo, M. and Johnson, S. G. (2012). Fftw: Fastest fourier transform in the west. Astrophysics Source Code Library, pages ascl–1201.
- Gamow, G. (1946). Expanding universe and the origin of elements. Physical review, 70(7-8):572.
- Garratt-Smithson, L., Power, C., Lagos, C. d. P., Stevens, A. R., Allison, J. R., and Sadler, E. M. (2021). The distribution and properties of dlas at  $z < 2$  in the eagle simulations. Monthly Notices of the Royal Astronomical Society, 501(3):4396–4419.
- Gerardi, F., Cuceu, A., Font-Ribera, A., Joachimi, B., and Lemos, P. (2023). Direct cosmological inference from three-dimensional correlations of the lyman  $\alpha$  forest. Monthly Notices of the Royal Astronomical Society, 518(2):2567–2573.
- Giovanelli, R. and Haynes, M. P. (1991). Redshift surveys of galaxies. Annual review of astronomy and astrophysics, 29(1):499–541.
- Gnedin, N. Y. and Hamilton, A. J. (2002). Matter power spectrum from the lyman-alpha forest: myth or reality? Monthly Notices of the Royal Astronomical Society, 334(1):107–116.
- Goldstein, S., Hill, J. C., Irsic, V., and Sherwin, B. D. (2023). Canonical Hubble-Tension-Resolving Early Dark Energy Cosmologies are Inconsistent with the Lyman- $\alpha$  Forest. arXiv e-prints, page arXiv:2303.00746.
- Grohs, E. and Fuller, G. M. (2023). Big bang nucleosynthesis. arXiv preprint arXiv:2301.12299.
- Grohs, E. B., Bond, J. R., Cooke, R. J., Fuller, G. M., Meyers, J., and Paris, M. W. (2019). Big bang nucleosynthesis and neutrino cosmology. arXiv preprint arXiv:1903.09187.
- Gunn, J. E. and Peterson, B. A. (1965). On the density of neutral hydrogen in intergalactic space. Astrophysical Journal, vol. 142, p. 1633-1636, 142:1633–1636.
- Gunn, J. E., Siegmund, W. A., Mannery, E. J., Owen, R. E., Hull, C. L., Leger, R. F., Carey, L. N., Knapp, G. R., York, D. G., Boroski, W. N., et al. (2006). The 2.5 m telescope of the sloan digital sky survey. The Astronomical Journal, 131(4):2332.
- Guth, A. H. (1981). Inflationary universe: A possible solution to the horizon and flatness problems. Physical Review D, 23(2):347.
- Guy, J., Bailey, S., Kremin, A., Alam, S., Alexander, D., Prieto, C. A., BenZvi, S., Bolton, A., Brooks, D., Chaussidon, E., et al. (2023). The spectroscopic data processing pipeline for the dark energy spectroscopic instrument. The Astronomical Journal, 165(4):144.
- Hamann, F., Capellupo, D., Chartas, G., McGraw, S., Hidalgo, P. R., Shields, J., Charlton, J., and Eracleous, M. (2013). The physics and physical properties of quasar outflows. arXiv preprint arXiv:1302.0201.
- Hambye, T., Lucca, M., and Vanderheyden, L. (2020). Dark matter as a heavy thermal hot relic. Physics Letters B, 807:135553.
- Harrison, E. R. (1970). Fluctuations at the threshold of classical cosmology. Physical review D, 1(10):2726.
- Heckman, T. (1980). An optical and radio survey of the nuclei of bright galaxies-activity in normal galactic nuclei. Astronomy and Astrophysics, vol. 87, no. 1-2, July 1980, p. 152-164. Research supported by the University of Washington., 87:152–164.
- Hernquist, L., Katz, N., Weinberg, D. H., and Miralda-Escude, J. (1996). The lyman-alpha forest in the cold dark matter model. The Astrophysical Journal, 457(2):L51.
- Hubble, E. (1929). A relation between distance and radial velocity among extra-galactic nebulae. Proceedings of the national academy of sciences, 15(3):168–173.
- Hui, L. and Gnedin, N. Y. (1997). Equation of state of the photoionized intergalactic medium. Monthly Notices of the Royal Astronomical Society, 292(1):27–42.
- Irsic, V., Viel, M., Berg, T. A., D’Odorico, V., Haehnelt, M. G., Cristiani, S., Cupani, G., Kim, T.-S., Lopez, S., Ellison, S., et al. (2017). The lyman  $\alpha$  forest power spectrum from the xq-100 legacy survey. Monthly Notices of the Royal Astronomical Society, 466(4):4332–4345.

- Iršič, V., Viel, M., Haehnelt, M. G., Bolton, J. S., and Becker, G. D. (2017a). First constraints on fuzzy dark matter from lyman- $\alpha$  forest data and hydrodynamical simulations. *Physical review letters*, 119(3):031302.
- Iršič, V., Viel, M., Haehnelt, M. G., Bolton, J. S., Cristiani, S., Becker, G. D., D’Odorico, V., Cupani, G., Kim, T.-S., Berg, T. A., et al. (2017b). New constraints on the free-streaming of warm dark matter from intermediate and small scale lyman- $\alpha$  forest data. *Physical Review D*, 96(2):023522.
- Jamkhedkar, P., Feng, L.-L., Zheng, W., Kirkman, D., Tytler, D., and Fang, L.-Z. (2003). Power spectrum and intermittency of the transmitted flux from the lyman  $\alpha$  absorption spectra of quasi-stellar objects. *Monthly Notices of the Royal Astronomical Society*, 343(4):1110–1122.
- Jansky, K. G. (1933). Electrical disturbances apparently of extraterrestrial origin. *Proceedings of the Institute of Radio Engineers*, 21(10):1387–1398.
- Jeakel, A. P., da Silva, J. P., and Velten, H. (2024). Revisiting  $f(r, t)$  cosmologies. *Physics of the Dark Universe*, 43:101401.
- Jenkins, A., Frenk, C., Pearce, F., Thomas, P., Colberg, J., White, S. D., Couchman, H., Peacock, J., Efstathiou, G., and Nelson, A. (1998). Evolution of structure in cold dark matter universes. *The Astrophysical Journal*, 499(1):20.
- Kaiser, N. (1987). Clustering in real space and in redshift space. *Monthly Notices of the Royal Astronomical Society*, 227(1):1–21.
- Kaiser, N. and Peacock, J. (1991). Power-spectrum analysis of one-dimensional redshift surveys. *Astrophysical Journal, Part 1 (ISSN 0004-637X)*, vol. 379, Oct. 1, 1991, p. 482-506. Research supported by Canadian Institute for Theoretical Astrophysics and NSERC., 379:482–506.
- Kaplinghat, M., Valli, M., and Yu, H.-B. (2019). Too big to fail in light of gaia. *Monthly Notices of the Royal Astronomical Society*, 490(1):231–242.
- Karaçaylı, N. G., Font-Ribera, A., and Padmanabhan, N. (2020). Optimal 1d ly  $\alpha$  forest power spectrum estimation–i. desi-lite spectra. *Monthly Notices of the Royal Astronomical Society*, 497(4):4742–4752.
- Karaçaylı, N. G., Martini, P., Guy, J., Ravoux, C., Karim, M. L. A., Armengaud, E., Walther, M., Aguilar, J., Ahlen, S., Bailey, S., et al. (2023). Optimal 1d ly  $\alpha$  forest power spectrum estimation–iii. desi early data. *arXiv preprint arXiv:2306.06316*.
- Karaçaylı, N. G., Padmanabhan, N., Font-Ribera, A., Iršič, V., Walther, M., Brooks, D., Gaztañaga, E., Kehoe, R., Levi, M., Ntelis, P., et al. (2022). Optimal 1d ly  $\alpha$  forest power spectrum estimation–ii. kodiaq, squad, and xq-100. *Monthly Notices of the Royal Astronomical Society*, 509(2):2842–2855.
- Karim, M. L. A., Armengaud, E., Mention, G., Chabanier, S., Ravoux, C., and Lukic, Z. (2023). Measurement of the small-scale 3d lyman- $\alpha$  forest power spectrum. *Submitted on 13 Oct 2023*.
- Khachikian, E. Y. and Weedman, D. W. (1974). An atlas of seyfert galaxies. *Astrophysical Journal*, vol. 192, Sept. 15, 1974, pt. 1, p. 581-589., 192:581–589.
- Kim, T.-S., Viel, M., Haehnelt, M., Carswell, R., and Cristiani, S. (2004). The power spectrum of the flux distribution in the lyman  $\alpha$  forest of a large sample of uves qso absorption spectra (luqas). *Monthly Notices of the Royal Astronomical Society*, 347(2):355–366.
- Klimchitskaya, G. L. and Mostepanenko, V. M. (2022). Centenary of alexander friedmann’s prediction of the universe expansion and the quantum vacuum. *Physics*, 4(3):981–994.
- Knobel, C. (2012). An introduction into the theory of cosmological structure formation. *arXiv preprint arXiv:1208.5931*.
- Kooistra, R., Lee, K.-G., and Horowitz, B. (2022). Constraining the fluctuating gunn–peterson approximation using ly $\alpha$  forest tomography at  $z=2$ . *The Astrophysical Journal*, 938(2):123.
- Kragh, H. (2018). Hubble law or hubble-lemaitre law? the iau resolution. *arXiv preprint arXiv:1809.02557*.
- Lahav, O. and Liddle, A. R. (2004). The cosmological parameters. *arXiv preprint astro-ph/0406681*.
- Lambourne, R. J. (2010). *Relativity, gravitation and cosmology*. Cambridge University Press.
- Lemaître, G. (1927). Un univers homogène de masse constante et de rayon croissant rendant compte de la vitesse radiale des nébuleuses extra-galactiques. *Annales de la Société Scientifique de Bruxelles*, A47, p. 49-59, 47:49–59.
- Lesgourgues, J. (2011). The cosmic linear anisotropy solving system (class) i: overview. *arXiv preprint arXiv:1104.2932*.

- Liddle, A. (2015). An introduction to modern cosmology. John Wiley & Sons.
- Liddle, A. R. (2004). How many cosmological parameters. Monthly Notices of the Royal Astronomical Society, 351(3):L49–L53.
- Linde, A. D. (1982). A new inflationary universe scenario: a possible solution of the horizon, flatness, homogeneity, isotropy and primordial monopole problems. Physics Letters B, 108(6):389–393.
- López-Corredoira, M. and Marmet, L. (2022). Alternative ideas in cosmology. International Journal of Modern Physics D, 31(08):2230014.
- Lovell, M. R., Eke, V., Frenk, C. S., Gao, L., Jenkins, A., Theuns, T., Wang, J., White, S. D., Boyarsky, A., and Ruchayskiy, O. (2012). The haloes of bright satellite galaxies in a warm dark matter universe. Monthly Notices of the Royal Astronomical Society, 420(3):2318–2324.
- Lumsden, S., Heavens, A., and Peacock, J. (1989). The clustering of peaks in a random gaussian field. Monthly Notices of the Royal Astronomical Society, 238(2):293–318.
- Lyke, B. W., Higley, A. N., McLane, J., Schurhammer, D. P., Myers, A. D., Ross, A. J., Dawson, K., Chabanier, S., Martini, P., Des Bourboux, H. D. M., et al. (2020). The sloan digital sky survey quasar catalog: Sixteenth data release. The Astrophysical Journal Supplement Series, 250(1):8.
- Lynden-Bell, D. (1969). Galactic nuclei as collapsed old quasars. Nature, 223(5207).
- Lynds, R. (1971). The absorption-line spectrum of 4c 05.34. The Astrophysical Journal, 164:L73.
- Madau, P. (2001). The intergalactic medium. In Encyclopedia of Astronomy & Astrophysics, pages 1–5. CRC Press.
- Markovič, K. and Viel, M. (2014). Lyman- $\alpha$  forest and cosmic weak lensing in a warm dark matter universe. Publications of the Astronomical Society of Australia, 31:e006.
- Martins, C., Marques, C., Fernandes, C., Oliveira, J., Pinheiro, D., and Rocha, B. (2023). Alternatives to  $\lambda$ : Torsion, generalized couplings, and scale invariance. In The Sixteenth Marcel Grossmann Meeting on Recent Developments in Theoretical and Experimental General Relativity, Astrophysics and Relativistic Field Theories: Proceedings of the MG16 Meeting on General Relativity; 5–10 July 2021, pages 907–920. World Scientific.
- Martins, J. S., Rosenfeld, R., and Sobreira, F. (2018). Forecasts for warm dark matter from photometric galaxy surveys. Monthly Notices of the Royal Astronomical Society, 481(1):1290–1299.
- McDonald, P., Miralda-Escude, J., Rauch, M., Sargent, W. L., Barlow, T. A., Cen, R., and Ostriker, J. P. (2000). The observed probability distribution function, power spectrum, and correlation function of the transmitted flux in the  $\text{Ly}\alpha$  forest. The Astrophysical Journal, 543(1):1.
- McDonald, P., Seljak, U., Burles, S., Schlegel, D. J., Weinberg, D. H., Cen, R., Shih, D., Schaye, J., Schneider, D. P., Bahcall, N. A., et al. (2006). The  $\text{Ly}\alpha$  forest power spectrum from the sloan digital sky survey. The Astrophysical Journal Supplement Series, 163(1):80.
- McQuinn, M. (2016). The evolution of the intergalactic medium. Annual Review of Astronomy and Astrophysics, 54:313–362.
- Meiksin, A. A. (2009). The physics of the intergalactic medium. Reviews of modern physics, 81(4):1405.
- Mertens, S. (2016). Direct neutrino mass experiments. In Journal of Physics: Conference Series, volume 718, page 022013. IOP Publishing.
- Miller, J. S., French, H. B., and Hawley, S. A. (1978). The spectrum and magnitude of the galaxy associated with bl lacertae. The Astrophysical Journal, 219:L85–L87.
- Miller, T. N., Besuner, R. W., Levi, M. E., Lampton, M., Jelinsky, P., Heetderks, H., Schlegel, D. J., Edelman, J., Doel, P., Brooks, D., et al. (2018). Fabrication of the desi corrector lenses. In Advances in Optical and Mechanical Technologies for Telescopes and Instrumentation III, volume 10706, pages 256–264. SPIE.
- Miralda-Escude, J., Cen, R., Ostriker, J. P., and Rauch, M. (1996). The  $\text{Ly}\alpha$  forest from gravitational collapse in the cold dark matter+  $\lambda$  model. The Astrophysical Journal, 471(2):582.
- Mishra, N. and Gnedin, N. Y. (2022). Cosmic reionization on computers: Evolution of the flux power spectrum. The Astrophysical Journal, 928(2):174.



- Moon, J., Valcin, D., Rashkovetskyi, M., Saulder, C., Aguilar, J. N., Ahlen, S., Alam, S., Bailey, S., Baltay, C., Blum, R., et al. (2023). First detection of the bAO signal from early desi data. Monthly Notices of the Royal Astronomical Society, 525(4):5406–5422.
- Mortonson, M. J. (2009). Testing flatness of the universe with probes of cosmic distances and growth. Physical Review D, 80(12):123504.
- Mucket, J. (1996). The distribution of the Ly- $\alpha$  absorption clouds tracing the dark matter filaments. In Mapping, Measuring, and Modelling the Universe, volume 94, page 137.
- Nagamine, K. (2007). DLA and galaxy formation. Modern Physics Letters A, 22(32):2413–2427.
- Nesseris, S. and Perivolaropoulos, L. (2008). Testing  $\Lambda$ CDM with the growth function  $\delta$  (a): Current constraints. Physical Review D, 77(2):023504.
- Norman, M. L. (2010). Simulating galaxy clusters. arXiv preprint arXiv:1005.1100.
- Noterdaeme, P., Petitjean, P., Carithers, W., Pâris, I., Font-Ribera, A., Bailey, S., Aubourg, E., Bizyaev, D., Ebelke, G., Finley, H., et al. (2012). Column density distribution and cosmological mass density of neutral gas: Sloan digital sky survey-iii data release 9. Astronomy & Astrophysics, 547:L1.
- Novosyadlyj, B., Pelykh, V., Shtanov, Y., and Zhuk, A. (2015). Dark energy: observational evidence and theoretical models. arXiv preprint arXiv:1502.04177.
- Nunes, R. C. and Vagnozzi, S. (2021). Arbitrating the  $s_8$  discrepancy with growth rate measurements from redshift-space distortions. Monthly Notices of the Royal Astronomical Society, 505(4):5427–5437.
- Palanque-Delabrouille, N., Yeche, C., Baur, J., Magneville, C., Rossi, G., Lesgourgues, J., Borde, A., Burtin, E., LeGoff, J.-M., Rich, J., et al. (2015). Neutrino masses and cosmology with Lyman- $\alpha$  forest power spectrum. Journal of Cosmology and Astroparticle Physics, 2015(11):011.
- Palanque-Delabrouille, N., Yeche, C., Borde, A., Le Goff, J.-M., Rossi, G., Viel, M., Aubourg, E., Bailey, S., Bautista, J., Blomqvist, M., et al. (2013). The one-dimensional Ly $\alpha$  forest power spectrum from BOSS. Astronomy & Astrophysics, 559:A85.
- Palanque-Delabrouille, N., Yeche, C., Schöneberg, N., Lesgourgues, J., Walther, M., Chabanier, S., and Armengaud, E. (2020). Hints, neutrino bounds, and  $w$ dm constraints from SDSS DR14 Lyman- $\alpha$  and Planck full-survey data. Journal of Cosmology and Astroparticle Physics, 2020(04):038.
- Pan, C.-J., Su, C.-Y., Li, M.-S., and Huang, W.-R. (2014). Identification of metal absorption lines on quasar spectra of SDSS DR9. Journal of Astrophysics and Astronomy, 35:529–531.
- Pâris, I., Petitjean, P., Aubourg, É., Myers, A. D., Streblyanska, A., Lyke, B. W., Anderson, S. F., Armengaud, É., Bautista, J., Blanton, M. R., et al. (2018). The Sloan Digital Sky Survey quasar catalog: fourteenth data release. Astronomy & Astrophysics, 613:A51.
- Parks, D., Prochaska, J. X., Dong, S., and Cai, Z. (2018). Deep learning of quasar spectra to discover and characterize damped Ly $\alpha$  systems. Monthly Notices of the Royal Astronomical Society, 476(1):1151–1168.
- Patrignani, C., Agashe, K., Aielli, G., Amsler, C., Antonelli, M., Asner, D., Baer, H., Banerjee, S., Barnett, R., Basaglia, T., et al. (2016). Review of particle physics. Chinese Physics C.
- Peacock, J. (2003). Large-scale surveys and cosmic structure. arXiv preprint astro-ph/0309240.
- Peebles, P. J. and Yu, J. (1970). Primeval adiabatic perturbation in an expanding universe. Astrophysical Journal, vol. 162, p. 815, 162:815.
- Peebles, P. J. E. (1993). Principles of physical cosmology, volume 27. Princeton University Press.
- Penzias, A. and Wilson, R. (1965). A measurement of excess antenna temperature at 4080 Mc/s.
- Perivolaropoulos, L. and Skara, F. (2022). Challenges for  $\Lambda$ CDM: An update. New Astronomy Reviews, page 101659.
- Perlmutter, S., Aldering, G., Goldhaber, G., Knop, R., Nugent, P., Castro, P. G., Deustua, S., Fabbro, S., Goobar, A., Groom, D. E., et al. (1999). Measurements of  $\omega$  and  $\lambda$  from 42 high-redshift supernovae. The Astrophysical Journal, 517(2):565.
- Philcox, O. H. and Ivanov, M. M. (2022). BOSS DR12 full-shape cosmology:  $\Lambda$ CDM constraints from the large-scale galaxy power spectrum and bispectrum monopole. Physical Review D, 105(4):043517.

- Planck-Collaboration, Ade, P. A., Aghanim, N., Arnaud, M., Ashdown, M., Aumont, J., Baccigalupi, C., Banday, A., Barreiro, R., Bartlett, J., Bartolo, N., et al. (2016). Planck 2015 results-xiii. cosmological parameters. *Astronomy & Astrophysics*, 594:A13.
- Planck-Collaboration, Aghanim, N., Akrami, Y., Ashdown, M., Aumont, J., Baccigalupi, C., Ballardini, M., Banday, A., Barreiro, R., Bartolo, N., Basak, S., et al. (2020a). Planck 2018 results-vi. cosmological parameters. *Astronomy & Astrophysics*, 641:A6.
- Planck-Collaboration, Aghanim, N., Akrami, Y., Ashdown, M., Aumont, J., Baccigalupi, C., Ballardini, M., Banday, A. J., Barreiro, R., Bartolo, N., Basak, S., et al. (2020b). Planck 2018 results-v. cmb power spectra and likelihoods. *Astronomy & Astrophysics*, 641:A5.
- Planck-Collaboration, Aghanim, N., Akrami, Y., Ashdown, M., Aumont, J., Baccigalupi, C., Ballardini, M., Banday, A. J., Barreiro, R., Bartolo, N., Basak, S., et al. (2020c). Planck 2018 results-viii. gravitational lensing. *Astronomy & Astrophysics*, 641:A8.
- Planck-Collaboration, Aghanim, N., Polastri, L., Rubiño-Martín, J., Dupac, X., Liguori, M., Kim, J., Matarrese, S., Génova-Santos, R., Huang, Z., Forastieri, F., et al. (2018). Planck 2018 results. i. overview and the cosmological legacy of planck. *Astron. Astrophys.*, 641(arXiv: 1807.06205):A1.
- Pontzen, A., Governato, F., Pettini, M., Booth, C., Stinson, G., Wadsley, J., Brooks, A., Quinn, T., and Haehnelt, M. (2008). Damped lyman  $\alpha$  systems in galaxy formation simulations. *Monthly Notices of the Royal Astronomical Society*, 390(4):1349–1371.
- Pound, R. V. and Rebka Jr, G. A. (1960). Apparent weight of photons. *Physical review letters*, 4(7):337.
- Preuss, P. (2012). The first public data release from boss, the baryon oscillation spectroscopic survey - berkeley lab.
- Primack, J. R. (2015). Cosmological structure formation. *The Philosophy of Cosmology*, pages 136–160.
- Pritchard, J. R. and Loeb, A. (2012). 21 cm cosmology in the 21st century. *Reports on Progress in Physics*, 75(8):086901.
- Qin, Y., Mesinger, A., Bosman, S. E., and Viel, M. (2021). Reionization and galaxy inference from the high-redshift ly  $\alpha$  forest. *Monthly Notices of the Royal Astronomical Society*, 506(2):2390–2407.
- Ramírez-Pérez, C., Pérez-Ràfols, I., Font-Ribera, A., Karim, M. A., Armengaud, E., Bautista, J., Beltran, S., Cabayol-Garcia, L., Cai, Z., Chabanier, S., et al. (2023). The lyman-alpha forest catalog from the dark energy spectroscopic instrument early data release. *arXiv preprint arXiv:2306.06312*.
- Rankine, A. L., Hewett, P. C., Banerji, M., and Richards, G. T. (2020). Bal and non-bal quasars: continuum, emission, and absorption properties establish a common parent sample. *Monthly Notices of the Royal Astronomical Society*, 492(3):4553–4575.
- Rauch, M. (1998). The lyman alpha forest in the spectra of quasistellar objects. *Annual Review of Astronomy and Astrophysics*, 36(1):267–316.
- Ravoux, C. (2022). *One-and three-dimensional measurements of the matter distribution from eBOSS and first DESI Lyman- $\alpha$  forest samples*. PhD thesis, Université Paris-Saclay.
- Ravoux, C., Armengaud, E., Walther, M., Etourneau, T., Pomarede, D., Palanque-Delabrouille, N., Yeche, C., Bautista, J., Des Bourboux, H. D. M., Chabanier, S., et al. (2020). A tomographic map of the large-scale matter distribution using the eboss-stripe 82 ly  $\alpha$  forest. *Journal of Cosmology and Astroparticle Physics*, 2020(07):010.
- Ravoux, C., Karim, M. L. A., Armengaud, E., Walther, M., Karaçaylı, N. G., Martini, P., Guy, J., Aguilar, J. N., Ahlen, S., Bailey, S., et al. (2023). The dark energy spectroscopic instrument: One-dimensional power spectrum from first lyman- $\alpha$  forest samples with fast fourier transform. *arXiv preprint arXiv:2306.06311*.
- Reber, G. (1944). Cosmic static. *The Astrophysical Journal*, 100:279.
- Reid, B. A., Percival, W. J., Eisenstein, D. J., Verde, L., Spergel, D. N., Skibba, R. A., Bahcall, N. A., Budavari, T., Frieman, J. A., Fukugita, M., et al. (2010). Cosmological constraints from the clustering of the sloan digital sky survey dr7 luminous red galaxies. *Monthly Notices of the Royal Astronomical Society*, 404(1):60–85.
- Reisenegger, A. and Miralda-Escude, J. (1995). The gunn-peterson effect from underdense regions in a photoionized intergalactic medium. *arXiv preprint astro-ph/9502063*.

- Riess, A. G., Anand, G. S., Yuan, W., Casertano, S., Dolphin, A., Macri, L. M., Breuval, L., Scolnic, D., Perrin, M., and Anderson, R. I. (2023). Crowded no more: The accuracy of the hubble constant tested with high-resolution observations of cepheids by jwst. The Astrophysical Journal Letters, 956(1):L18.
- Riess, A. G., Filippenko, A. V., Challis, P., Clocchiatti, A., Diercks, A., Garnavich, P. M., Gilliland, R. L., Hogan, C. J., Jha, S., Kirshner, R. P., et al. (1998). Observational evidence from supernovae for an accelerating universe and a cosmological constant. The astronomical journal, 116(3):1009.
- Risaliti, G. and Elvis, M. (2004). A panchromatic view of agn. In Supermassive Black Holes in the Distant Universe, pages 187–224. Springer.
- Robertson, H. P. (1935). Kinematics and world-structure. Astrophysical Journal, vol. 82, p. 284, 82:284.
- Robertson, H. P. (1936a). Kinematics and world-structure ii. Astrophysical Journal, vol. 83, p. 187, 83:187.
- Robertson, H. P. (1936b). Kinematics and world-structure iii. Astrophysical Journal, vol. 83, p. 257, 83:257.
- Rossi, G., Yeche, C., Palanque-Delabrouille, N., and Lesgourgues, J. (2015). Constraints on dark radiation from cosmological probes. Physical Review D, 92(6):063505.
- Rubin, D., Aldering, G., Betoule, M., Fruchter, A., Huang, X., Kim, A. G., Lidman, C., Linder, E., Perlmutter, S., Ruiz-Lapuente, P., et al. (2023). Union through unity: Cosmology with 2,000 sne using a unified bayesian framework. arXiv preprint arXiv:2311.12098.
- Rubin, V. C. and Ford Jr, W. K. (1970). Rotation of the andromeda nebula from a spectroscopic survey of emission regions. Astrophysical Journal, vol. 159, p. 379, 159:379.
- Rybicki, G. B. and Lightman, A. P. (1991). Radiative processes in astrophysics. John Wiley & Sons.
- Salpeter, E. (1964). Accretion of interstellar matter by massive objects. Publications, 1:165.
- Sargent, W. L., Young, P. J., Boksenberg, A., and Tytler, D. (1980). The distribution of lyman-alpha absorption lines in the spectra of six qos-evidence for an intergalactic origin. The Astrophysical Journal Supplement Series, 42:41–81.
- Schmidt, M. (1963). 3 c 273: a star-like object with large red-shift. Nature, 197(4872):1040–1040.
- Schneider, P. (2014). Extragalactic astronomy and cosmology: an introduction. Springer.
- Schöneberg, N., Abellán, G. F., Sánchez, A. P., Witte, S. J., Poulin, V., and Lesgourgues, J. (2022). The h0 olympics: A fair ranking of proposed models. Physics Reports, 984:1–55.
- Schutz, B. (2022). A first course in general relativity. Cambridge University Press.
- Seljak, U., Slosar, A., and McDonald, P. (2006). Cosmological parameters from combining the lyman- $\alpha$  forest with cmb, galaxy clustering and sn constraints. Journal of Cosmology and Astroparticle Physics, 2006(10):014.
- Seyfert, C. K. (1943). Nuclear emission in spiral nebulae. apj, 97:28.
- Shields, G. A. (1999). A brief history of active galactic nuclei. Publications of the Astronomical Society of the Pacific, 111(760):661.
- Slosar, A., Font-Ribera, A., Pieri, M. M., Rich, J., Le Goff, J.-M., Aubourg, É., Brinkmann, J., Carithers, B., Charlassier, R., Cortês, M., et al. (2011). The lyman- $\alpha$  forest in three dimensions: measurements of large scale flux correlations from boss 1st-year data. Journal of Cosmology and Astroparticle Physics, 2011(09):001.
- Smee, S. A., Gunn, J. E., Uomoto, A., Roe, N., Schlegel, D., Rockosi, C. M., Carr, M. A., Leger, F., Dawson, K. S., Olmstead, M. D., et al. (2013). The multi-object, fiber-fed spectrographs for the sloan digital sky survey and the baryon oscillation spectroscopic survey. The Astronomical Journal, 146(2):32.
- Sola Peracaula, J. (2022). The cosmological constant problem and running vacuum in the expanding universe. Philosophical Transactions of the Royal Society A, 380(2230):20210182.
- Springel, V., Frenk, C. S., and White, S. D. (2006). The large-scale structure of the universe. nature, 440(7088):1137–1144.
- Springel, V., White, S. D., Jenkins, A., Frenk, C. S., Yoshida, N., Gao, L., Navarro, J., Thacker, R., Croton, D., Helly, J., et al. (2005). Simulating the joint evolution of quasars, galaxies and their large-scale distribution. arXiv preprint astro-ph/0504097.

- Steigman, G. (2007). Primordial nucleosynthesis in the precision cosmology era. *Annu. Rev. Nucl. Part. Sci.*, 57:463–491.
- Tawfik, A. N. and El Dahab, E. A. (2019). Review on dark energy models. *Gravitation and Cosmology*, 25:103–115.
- Tegmark, M. and Zaldarriaga, M. (2002). Separating the early universe from the late universe: Cosmological parameter estimation beyond the black box. *Physical Review D*, 66(10):103508.
- Theuns, T. (2016). Physical cosmology. *Lectures at Durham University*([icc.dur.ac.uk/tt/Lectures/UA/L4](http://icc.dur.ac.uk/tt/Lectures/UA/L4)).
- Thorne, J., Robotham, A., Davies, L., and Bellstedt, S. (2022). Agn unification diagram. Was originally created to be included in the introduction of Thorne J. E., et al., 2022, *MNRAS*, 509, 4940.
- Tikhonov, A. V. and Klypin, A. (2009). The emptiness of voids: yet another overabundance problem for the  $\lambda$  cold dark matter model. *Monthly Notices of the Royal Astronomical Society*, 395(4):1915–1924.
- Tomlinson, J., Vogeley, M. S., and Cen, R. (2018). Using the low-redshift lyman alpha forest to trace dark filaments in large-scale voids. In *American Astronomical Society Meeting Abstracts# 231*, volume 231, pages 357–01.
- Troxel, M. A., MacCrann, N., Zuntz, J., Eifler, T., Krause, E., Dodelson, S., Gruen, D., Blazek, J., Friedrich, O., Samuroff, S., et al. (2018). Dark energy survey year 1 results: Cosmological constraints from cosmic shear. *Physical Review D*, 98(4):043528.
- Turner, M. S. (2022). The road to precision cosmology. *Annual Review of Nuclear and Particle Science*, 72:1–35.
- Vázquez, J. A., Padilla, L. E., and Matos, T. (2018). Inflationary cosmology: from theory to observations. *arXiv preprint arXiv:1810.09934*.
- Villasenor, B., Robertson, B., Madau, P., and Schneider, E. (2022). Inferring the thermal history of the intergalactic medium from the properties of the hydrogen and helium  $\text{ly}\alpha$  forest. *The Astrophysical Journal*, 933(1):59.
- Villasenor, B., Robertson, B., Madau, P., and Schneider, E. (2023). New constraints on warm dark matter from the lyman- $\alpha$  forest power spectrum. *Physical Review D*, 108(2):023502.
- Vogelsberger, M., Genel, S., Springel, V., Torrey, P., Sijacki, D., Xu, D., Snyder, G., Nelson, D., and Hernquist, L. (2014). Introducing the illustris project: simulating the coevolution of dark and visible matter in the universe. *Monthly Notices of the Royal Astronomical Society*, 444(2):1518–1547.
- Walker, A. G. (1937). On milne’s theory of world-structure. *Proceedings of the London Mathematical Society*, 2(1):90–127.
- Walther, M., Armengaud, E., Ravoux, C., Palanque-Delabrouille, N., Yèche, C., and Lukić, Z. (2021). Simulating intergalactic gas for desi-like small scale lyman $\alpha$  forest observations. *Journal of Cosmology and Astroparticle Physics*, 2021(04):059.
- Walther, M., Hennawi, J. F., Hiss, H., Onorbe, J., Lee, K.-G., Rorai, A., and O’Meara, J. (2017). A new precision measurement of the small-scale line-of-sight power spectrum of the  $\text{ly}\alpha$  forest. *The Astrophysical Journal*, 852(1):22.
- Walther, M., Onorbe, J., Hennawi, J. F., and Lukic, Z. (2019). New constraints on igm thermal evolution from the  $\text{ly}\alpha$  forest power spectrum. *The Astrophysical Journal*, 872(1):13.
- Wang, F., Yang, J., Fan, X., Hennawi, J. F., Barth, A. J., Banados, E., Bian, F., Boutsia, K., Connor, T., Davies, F. B., et al. (2021). A luminous quasar at redshift 7.642. *The Astrophysical Journal Letters*, 907(1):L1.
- Weinberg, D. H., Dave, R., Katz, N., and Kollmeier, J. A. (2003). The lyman- $\alpha$  forest as a cosmological tool. In *AIP Conference Proceedings*, volume 666, pages 157–169. American Institute of Physics.
- Weinberg, S. (1989). The cosmological constant problem. *Reviews of modern physics*, 61(1):1.
- Whalen, D. J., Latif, M. A., and Mezcua, M. (2023). Radio emission from  $\text{az}= 10.1$  black hole in uhz1. *The Astrophysical Journal*, 956(2):133.
- White, S. D., Frenk, C. S., Davis, M., and Efstathiou, G. (2012). Clusters, filaments, and voids in a universe dominated by cold dark matter. *Part. Phys. Cosmol.: Dark Matter*, 6:129.
- Wolfe, A. M., Gawiser, E., and Prochaska, J. X. (2005). Damped  $\text{ly}\alpha$  systems. *Annu. Rev. Astron. Astrophys.*, 43:861–918.
- Yèche, C., Palanque-Delabrouille, N., Baur, J., and des Bourboux, H. d. M. (2017). Constraints on neutrino masses from lyman-alpha forest power spectrum with boss and xq-100. *Journal of Cosmology and Astroparticle Physics*, 2017(06):047.

- York, D. G., Adelman, J., Anderson Jr, J. E., Anderson, S. F., Annis, J., Bahcall, N. A., Bakken, J., Barkhouser, R., Bastian, S., Berman, E., et al. (2000). The sloan digital sky survey: Technical summary. The Astronomical Journal, 120(3):1579.
- Youles, S. (2021). Cosmology with the Lyman Alpha Forest. PhD thesis, University of Portsmouth.
- Zasov, A. V., Saburova, A. S., Khoperskov, A. V., and Khoperskov, S. A. (2017). Dark matter in galaxies. Physics-Uspekhi, 60(1):3.
- Zavarygin, E. O. and Webb, J. K. (2019). A search for cosmological anisotropy using the lyman alpha forest from sdss quasar spectra. Monthly Notices of the Royal Astronomical Society, 489(3):3966–3980.
- Zel'Dovich, Y. B. (1970). Gravitational instability: An approximate theory for large density perturbations. Astronomy and astrophysics, 5:84–89.
- Zhan, H., Dave, R., Eisenstein, D., and Katz, N. (2005).  $\text{Ly}\alpha$  flux power spectrum and its covariance. Monthly Notices of the Royal Astronomical Society, 363(4):1145–1154.
- Zwicky, F. (1933). On the masses of nebulae and of clusters of nebulae. In A Source Book in Astronomy and Astrophysics, 1900–1975, pages 729–737. Harvard University Press.

## ADDENDUM ON COSMOLOGY

### A.1 $\Lambda$ CDM parameters

This section is intended to give a brief description of the six free independent parameters referred in equation (2.2), and some probes related to them. The following estimations are based on the fiducial  $\Lambda$ CDM cosmology by [Planck-Collaboration et al. \(2016, 2018\)](#):

- \* The baryon density ( $\Omega_b h^2$ ) and the dark matter density ( $\Omega_{CDM} h^2$ ) parameters are the physical densities related with equation (2.14). They represent the mean present day fractional energy density of baryonic and dark matter.

Both parameters can be estimated by measuring the peaks in the CMB power spectrum ([Planck-Collaboration et al., 2020b,a](#)). Baryonic density parameter can be estimated by measuring the primordial deuterium abundance ([Copi et al., 1995](#); [Cooke et al., 2018](#)). The measurement of the growth rate of structure out of LSS galaxy surveys ([Bahcall et al., 1995](#); [Nesseris and Perivolaropoulos, 2008](#)), BAO measurements ([Addison et al., 2013](#)) and the Ly- $\alpha$  P<sub>FID</sub> (section 3.4) may also be used to constrain these parameters:

$$\Omega_b h^2 = 0.0224 \pm 0.0001, \quad \Omega_{CDM} h^2 = 0.120 \pm 0.001. \quad (\text{A.1})$$

- \* The Hubble constant ( $H_0$ ) represents the present ( $z = 0$ ) expansion rate of the Universe, and it is strictly related to the age of the Universe ( $t_0 = 13.787 \pm 0.020$  Gyr, see equation (2.19)).  $H_0$  is very important because it tells us in what form the Universe has evolved through time considering its contents (recalling equation (2.18)).

Nowdays, there is the so-called "Hubble tension" ([Ezquiaga and Zumalacárregui, 2018](#); [Di-Valentino et al., 2021](#); [Perivolaropoulos and Skara, 2022](#); [Akarsu et al., 2024](#)), this is, the discrepancy ( $> 4\sigma$ ) between the distance ladder estima-

tion method (which uses the distance ladder to estimate the Hubble constant) and  $\Lambda$ CDM dependant estimation methods.

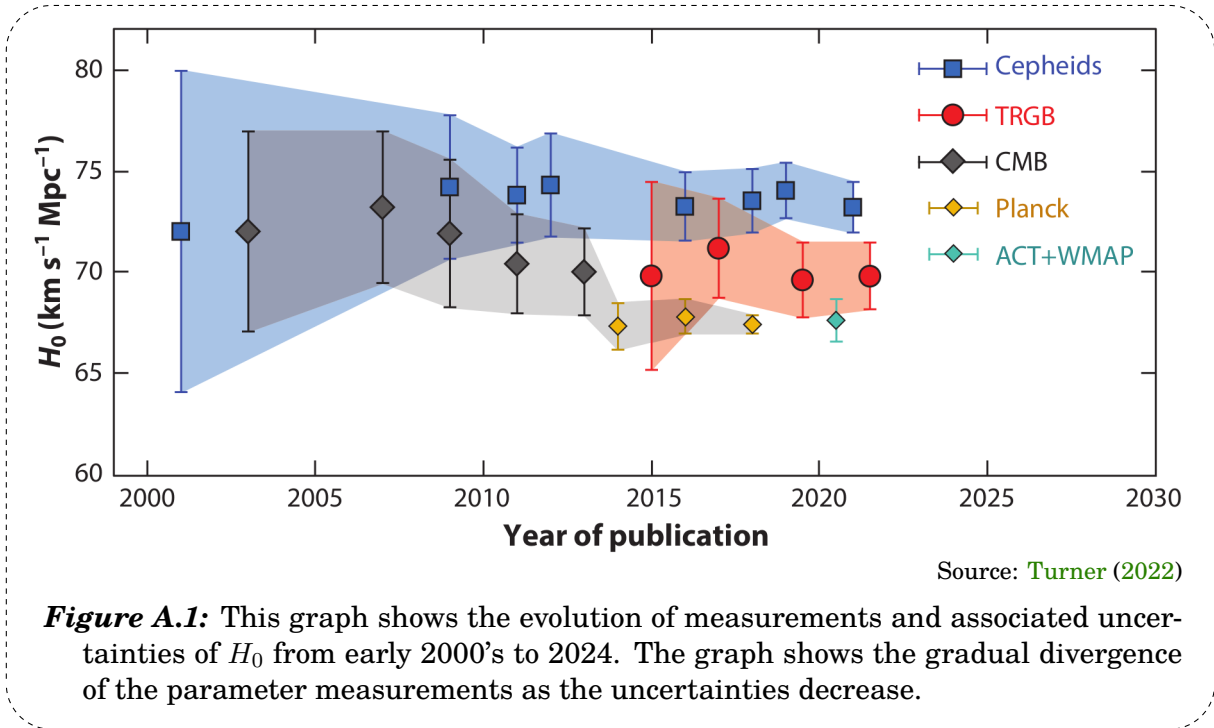


**Figure A.1:** This graph shows the evolution of measurements and associated uncertainties of  $H_0$  from early 2000's to 2024. The graph shows the gradual divergence of the parameter measurements as the uncertainties decrease.

The distance ladder method make use of several procedures like SnIa-Cepheid calibrations, the tip of the red giant branch (TRGB), gravitational waves and weak lensing, megamaser distance estimation technique, among others. One of the most recent studies using the JWST and the distance ladder estimation method has reaffirmed previous estimations made by the HST (Riess et al., 2023), thus reaffirming the tension.

$$H_0 = 73.0 \pm 1.0 \text{ km s}^{-1} \text{ Mpc}^{-1} . \quad (\text{A.2})$$

On the other hand, the  $\Lambda$ CDM (high redshift) dependent methods rely on CMB data and the BAO scale, among others (like Ly- $\alpha$  P<sub>FID</sub>).

$$H_0 = 67.4 \pm 0.5 \text{ km s}^{-1} \text{ Mpc}^{-1} . \quad (\text{A.3})$$

\* The way matter is distributed in the Universe today obeys the evolution of primordial perturbations (possibly) generated after inflation. Nowadays, the



cosmological paradigm assumes that the amplitude of those primordial perturbations could behave as

$$P_L(k, a) = \frac{8\pi^2}{25} \frac{A_s}{\Omega_m^2} D_+^2(a) T^2(k) \frac{k^{n_s}}{H_0^4 k_p^{n_s-1}}, \quad (\text{A.4})$$

where  $P_L$  is the linear matter power spectrum,  $A_s$  is the scalar amplitude of the primordial power spectrum (evaluated at a pivot scale  $k_p$ ) and  $n_s$  is the tilt of the primordial power spectrum (the scalar spectral index) (Dodelson and Schmidt, 2020).

The scalar spectral index ( $n_s$ ) represents the way primordial fluctuations should behave in the primeval Universe, a value of one of  $n_s$  is equivalent to a flat power spectrum overall physical scales. The scalar spectral index is estimated by measuring the angular relations of the anisotropies of the CMB (Planck-Collaboration et al., 2020b,a), LSS clustering statistics (Vázquez et al., 2018) and the Ly- $\alpha$  P<sub>F1D</sub> (section 3.4) to constrain this parameter:

$$n_s = 0.965 \pm 0.004. \quad (\text{A.5})$$

- \* The amplitude of the primordial power spectrum is of wide interest of cosmology (depicted in equation (A.4)), because it define the level of structure of the current Universe. In order to retrieve this parameter, it is necessary to measure the overdensity field  $\delta(\mathbf{x})$  smoothed over some volume, that is,

$$\sigma^2(R) = \frac{1}{2\pi^2} \int P(k) |W(k)|^2 k^2 dk, \quad (\text{A.6})$$

where  $W(k)$  is a window function (commonly defined as a spherical top top hat function of radius  $R$ ). The common choice for  $R$  is  $8 h^{-1}\text{Mpc}$ , that is,  $\sigma_8$ , the variance of the mass distribution or the root-mean-square matter fluctuation.  $\sigma_8$  gives a clue about how matter in the Universe is clumped at a standard scale.

If one defines a matter power spectrum, its amplitude can be parameterized in terms of the amplitude of linear matter fluctuations defined as the RMS of the  $z = 0$  density perturbations on scales of  $8 h^{-1}\text{Mpc}$ . To estimate this clumpiness parameter at different scales and epochs, one can take advantage of CMB data (Aiola et al., 2020), weak lensing (Abbott et al., 2022), galaxy

clustering (Philcox and Ivanov, 2022), cluster counts (Costanzi et al., 2018), redshift space distortions (Nunes and Vagnozzi, 2021), the Sunyaev–Zeldovich effect (Bocquet et al., 2019) and the Ly- $\alpha$  P<sub>F1D</sub> (section 3.4) to constrain this parameter:

$$\sigma_8 = 0.811 \pm 0.006 . \quad (\text{A.7})$$

In literature, it is common to find the  $S_8$  value as representation of matter clumpiness, parameterized as,

$$S_8 = \sigma_8 \sqrt{\frac{\Omega_m}{0.3}} , \quad (\text{A.8})$$

which is combination of  $\sigma_8$  and  $\Omega_m$ , approaching the degeneracy of the two parameters.

As with the Hubble constant, the measured values of  $S_8$  from different probes present a discrepancy of  $2 - 3\sigma$  (Abdalla et al., 2022; Perivolaropoulos and Skara, 2022; Akarsu et al., 2024). Values coming from weak lensing, galaxy clustering, galaxy cluster counts and redshift space distortions present a concordance of  $S_8 \sim 0.75$ , while one of the most recent estimations from CMB data (in concordance with previous measurements) gives a value of  $S_8 = 0.840 \pm 0.030$  (Aiola et al., 2020).

- \* Once radiation decouples from matter, a following epoch called the "Dark Ages" leads to the period when most of the hydrogen was purely neutral and the first stars and quasars begin to form (see Table 2.2). As expected, this Universe is told to be very "dark" for two reasons: the absence of luminous sources, and mostly, the high opaqueness of the medium.

The reionization optical depth  $\tau^1$  is a dimensionless quantity that provides a measure of the line-of-sight free-electron opacity to CMB radiation (equation (2.22)). This parameter is useful because it defines the level of interaction of CMB photons with neutral hydrogen in the Dark Ages and how this can alter the measurements of the CMB power spectrum and, on the other hand, the time structures begin to form according to the level of ionization

---

<sup>1</sup>To a better comprehension of this parameter see equation (2.22) and section 3.3.

of the medium. So, it is common to relate the estimation of this parameter to the anisotropies and polarization measurements of the CMB (Planck Collaboration et al., 2020b,a) and, on the other hand, look at the Gunn-Petterson trough of quasars at  $z \sim 6$  (Fan et al., 2006)<sup>2</sup>,

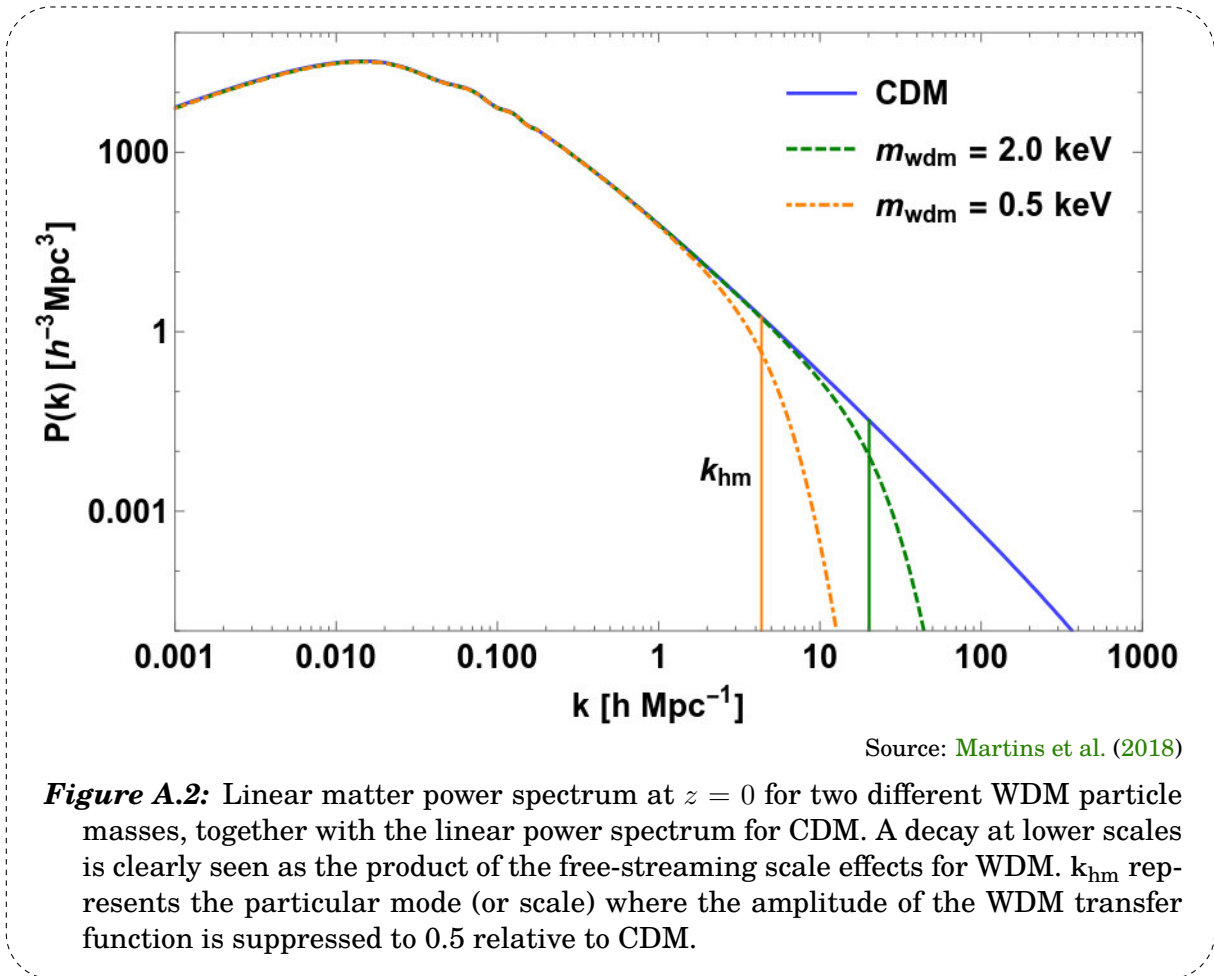
$$\tau = 0.054 \pm 0.007 . \tag{A.9}$$

## A.2 Warm dark matter

As mentioned in chapter 2, the Warm Dark Matter (WDM) hypothesis proposes an intermediate kind of dark matter, between hot and cold dark matter. This postulate leads structure formation occurring bottom-up from above their free-streaming scale, and top-down below their free-streaming scale. The free-streaming scale refers to the scale which dark matter has travelled at the moment it became cold (non-relativistic; Fazio et al., 2018; Fairbairn, 2022). Possible candidates for WDM are sterile neutrinos (Dodelson and Widrow, 1994) and dark matter as a thermal relic (Hambye et al., 2020), among many others.

---

<sup>2</sup>An explanation of this phenomena could be found in 3.3

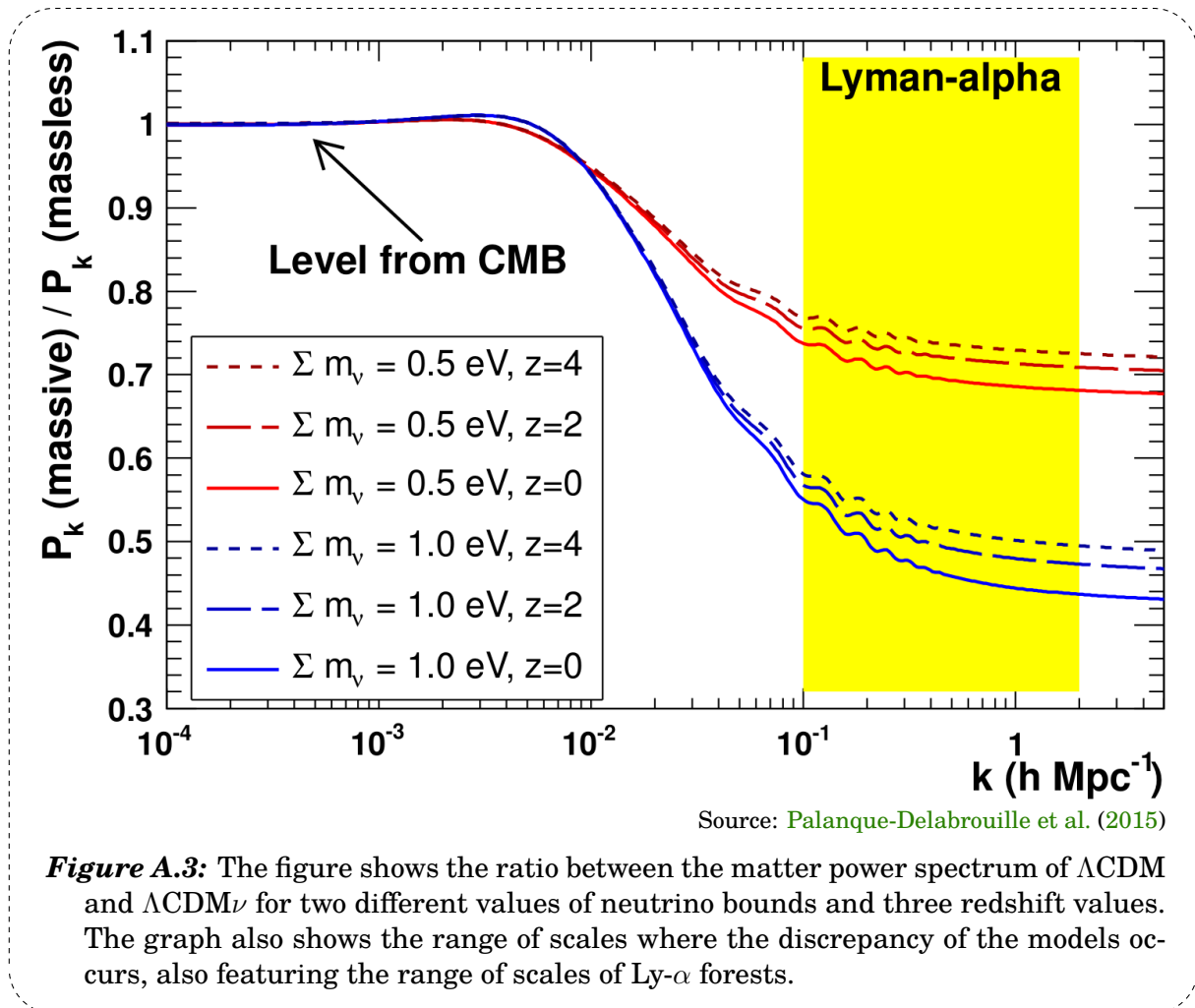


As Figure A.1 shows, WDM would suppress the amplitude of the power spectrum at small scales, thus encompassing the small-structure formation problems named in sections 2.1. Given that the presence of dark matter is very sensitive to small scales, it should be noted that only small scale probes are sensitive to the influence of WDM on the matter power spectrum.

### A.3 $\Lambda\text{CDM}_\nu$

Neutrinos are extremely light and neutral subatomic particles that interact very weakly with matter and they are characterized by three leptonic flavors ( $\nu_e, \nu_\mu, \nu_\tau$ ). While the masses of neutrinos are much smaller than those of other fundamental fermions, they can collectively contribute to the overall mass density of the Universe as pointed in the Friedmann equations above ([Dolgov, 2002](#)). As mentioned

in section 2.2, neutrinos were expected to be relativistic species (massless), however, today it is well-accepted that there exist three distinct masses for neutrinos, and each flavor state of a neutrino is a combination of these three discrete mass eigenstates (Capozzi et al., 2016). Figure out the mass of neutrinos is a current challenge in fundamental physics.



In the context of a cosmological model with massive neutrinos ( $\Lambda\text{CDM}\nu$ ), as the Universe expands and cool, these neutrinos become non-relativistic, and their influence on cosmic structure formation becomes more pronounced because of free-streaming (see Figure A.3). The presence of massive neutrinos should also affects the growth of cosmic structures, influencing the distribution of galaxies and dark matter (Capozzi et al., 2016; Mertens, 2016; Aviles et al., 2021).

---

Neutrinos free-streaming in the early universe erase small perturbations, affecting the growth of structures on small scales by modifying the perturbed gravitational potential. Ly- $\alpha$  forests are sensitive to the matter distribution on these scales, therefore, they can be used to constrain the sum of the neutrino masses. Measuring the Ly- $\alpha$   $P_{\text{FID}}$ , and coupling this measurement with other probes and hydrodynamical simulations, one can put constraints on WDM models and on the neutrino masses (Palanque-Delabrouille et al., 2015; Yèche et al., 2017; Palanque-Delabrouille et al., 2020).

---

## INSTRUMENTS DESCRIPTION

---

This section was intended to give a brief summary of the technical characteristics of the instruments the data come from, this in order to offer a general perspective and support of some concepts cited in the chapters before. The technical description for eBOSS is based on [York et al. \(2000\)](#); [Gunn et al. \(2006\)](#); [Smee et al. \(2013\)](#); [eBOSS Collaboration et al. \(2021\)](#) and for DESI [Flaugher and Bebek \(2014\)](#); [Aghamousa et al. \(2016\)](#); [DESI-Collaboration et al. \(2016\)](#); [Miller et al. \(2018\)](#); [Abareshi et al. \(2022\)](#); [Guy et al. \(2023\)](#).

---

### B.1 The extended Baryon Oscillation Spectroscopic Survey (eBOSS)

The Extended Baryon Oscillation Spectroscopic Survey (eBOSS) is part of the fourth generation of the SDSS project (Sloan Digital Sky Survey). One of the main goals of the SDSS project is to map extragalactic objects at a wide range of redshifts. Over a quarter of the night sky has been mapped using a dedicated 2.5m telescope (Sloan) at the Apache Point Observatory (New Mexico, USA). The Sloan telescope is a Ritchey-Chrétien type with a field of view of  $3 \text{ deg}^2$  (Figure [B.2](#)).

As a subsidiary project of SDSS, eBOSS is a spectroscopic survey that aims to measure the Universe's expansion history. eBOSS uses two identical spectrographs belonging to its predecessor (BOSS) with a resolution of  $1560 - 2650$  ( $R(\bar{\lambda}) \sim 2000$ ) and a spectral range between  $3600$  and  $10400 \text{ \AA}$ . The eBOSS spectra acquisition was carried out setting the spectroscopic mode. The spectroscopic mode refers to the installation of the spectrograph fiber cartridge to the focal plane of the telescope, also setting the connections with the two spectrographs.

The spectrograph fiber cartridge is a system constituted by perforated plates and a set of optical fibers manually inserted. Aluminum plates, like that of Figure [B.3](#) (designated for fiber placement) were pre-drilled to align with the specific field of



view corresponding to the selected target objects. A total of 1000 fibers established connections from the plate to the two spectrographs (these were positioned besides the telescope). Each of these fibers has a diameter of  $120\ \mu\text{m}$ , corresponding to a 2" field of view.

Once light reaches each spectrograph, it was received from 500 fibers through a slit plate, which is mounted within the slithead (Figure B.1). A beam splitter and two red and blue grisms were employed to divide and direct the optical beam towards the red and blue cameras. These cameras were equipped with CCDs of  $4096 \times 4096$  pixels.

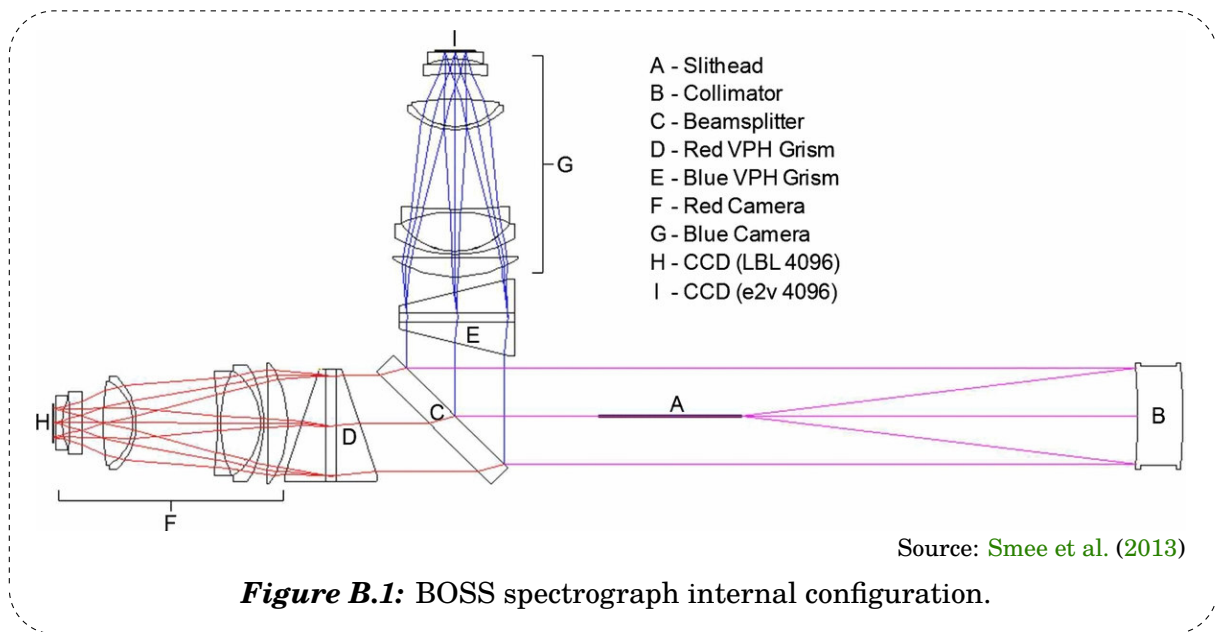
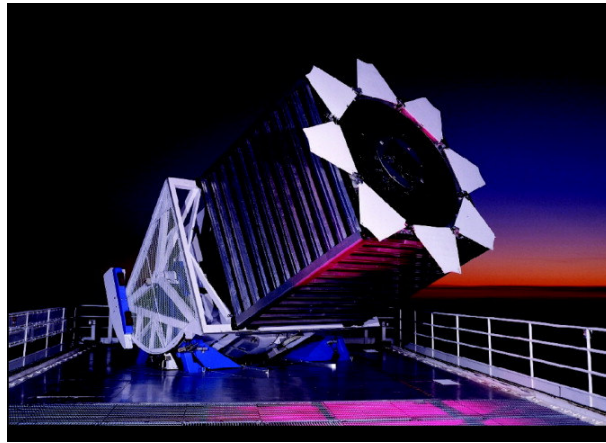


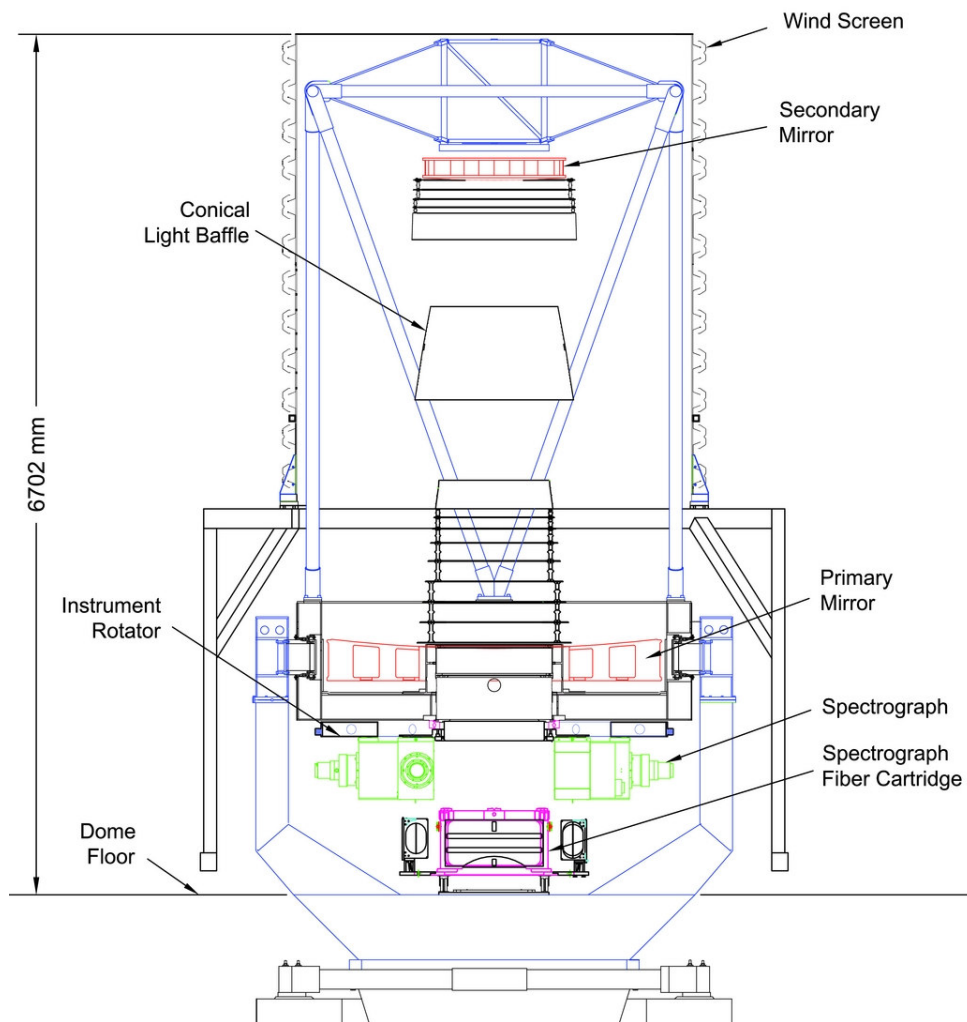
**Figure B.1:** BOSS spectrograph internal configuration.

The blue camera operates within the wavelength range of  $3600$  to  $6350\ \text{\AA}$ , while the red camera covers the spectral range from  $5650$  to  $10000\ \text{\AA}$ . The lower limit is determined by the ultraviolet atmospheric cut-off at  $\sim 3000\ \text{\AA}$ , while the upper limit is designated by the limitations sensor technology. So forth, the spectrographs achieved spectral resolutions in the range of  $1500$  to  $2300$  for the blue cameras and  $1800$  to  $2700$  for the red cameras<sup>1</sup>. The temperature of each CCD was maintained at  $180 \pm 0.5\ \text{K}$  with a refrigeration system in order to lessen dark current effects and undesired contributions.

<sup>1</sup>The spectral resolution is denoted by  $R = \lambda/\Delta\lambda$ .  $R$  is sometimes referred as chromatic resolving power.



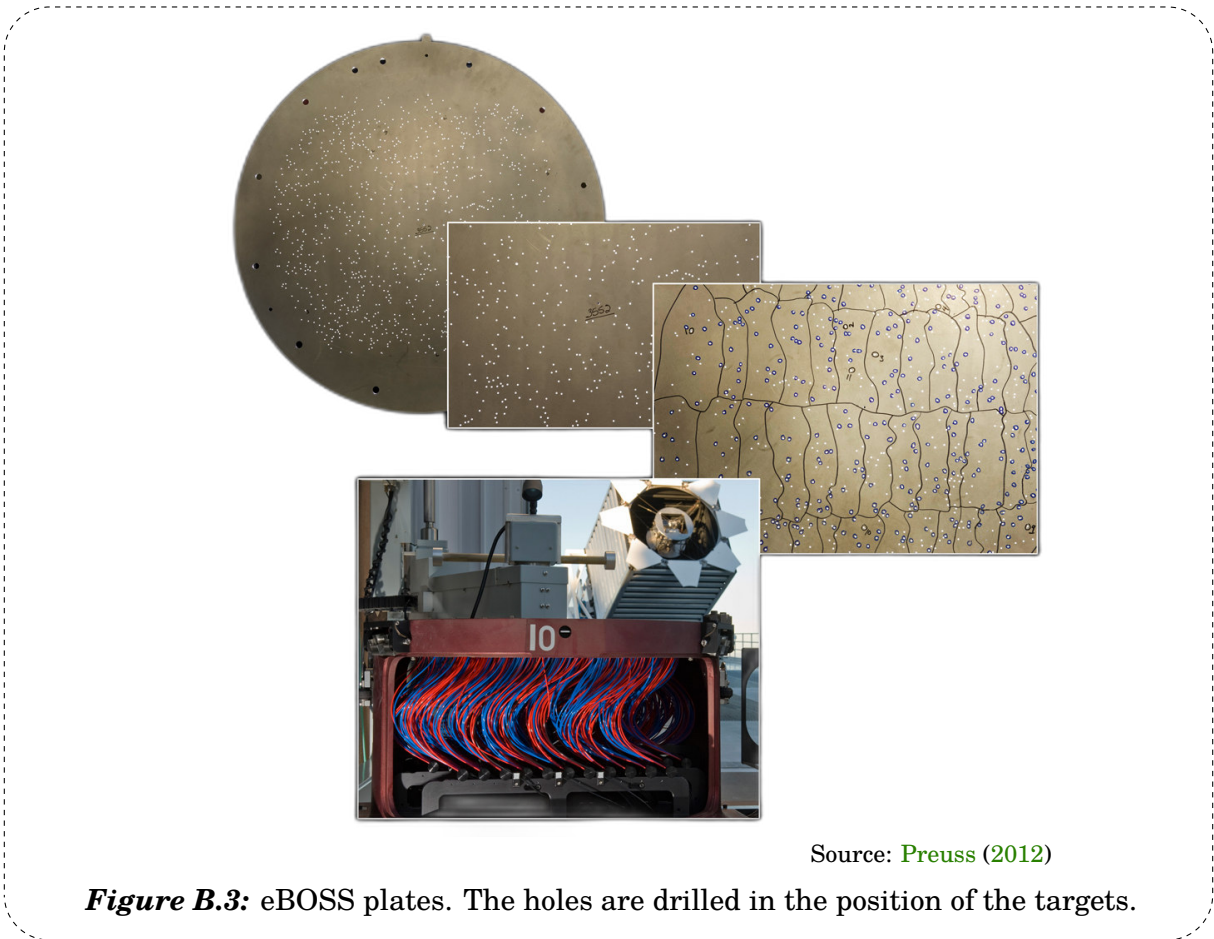
(a) Sloan telescope photograph



(b) Sloan telescope internal schematic representation

Source: (a) Gunn et al. (2006) (b) Smee et al. (2013)

**Figure B.2:** Sloan Telescope



## B.2 The Dark Energy Spectroscopic Instrument (DESI)

The Dark Energy Spectroscopic Instrument (DESI Experiment) aims to study 40 million galaxies and quasars with the goal of estimating the matter power spectrum and measure the expansion history of the Universe aiming to unveil the nature of dark energy. DESI has a better spectral resolution with respect to previous surveys (DESI is intended to be the scientific descendant of the SDSS project). DESI uses the 4-m Mayall telescope at the Kitt Peak National Observatory (Arizona, USA). The Mayall telescope is a reflective prime-focus telescope with a prime focus corrector capable of reaching a field of view of  $7.5 \text{ deg}^2$ . A schematic representation of the telescope internal structure is given in figures [B.4](#) and [B.5](#).

In contrast to eBOSS, DESI is composed of 5000 robot fibers ( $107 \mu\text{m}$  diameter each, see Figure [B.7](#)) which can modify its configuration to aim at the objects of interest

previously selected. Each optical fiber redirects the light of the observed objects to a separate compartment (thermally regulated) containing 10 spectrographs. These spectrographs have a resolution of  $2000 - 5500 (R(\lambda) \sim 3750)$  with a spectral range between  $3600$  and  $9800 \text{ \AA}$ . Each spectrograph also operates with three CCD cameras ( $4096 \times 4096 \text{ pix}$ ) encompassing the following features (see Table B.1 and Figure B.6).

Channel	Spectral range ( $\text{\AA}$ )	Resolving power
Blue (B)	3600 – 5930	2000 – 3200
Blue (R)	5600 – 7720	3200 – 4100
Near Infrared (Z)	7470 – 9800	4100 – 5100

**Table B.1:** DESI CCD cameras resolution. Taken from [Ramírez-Pérez et al. \(2023\)](#).

In contrast to eBOSS, where optical fibers required manual configuration, DESI uses a robotic automated system which precisely directs the fibers towards the objects of interest (see Figure B.7). The positioning of the fibers creates a hexagonal grid with a  $10.4 \text{ mm}$  gap between them. For the sake of comparison, in eBOSS the fiber positioning could take two hours long, meanwhile, DESI achieves the same task for the 5000 fiber in a matter of minutes. This is, perhaps, one of the most important technological breakthroughs and distinctive features of this survey.

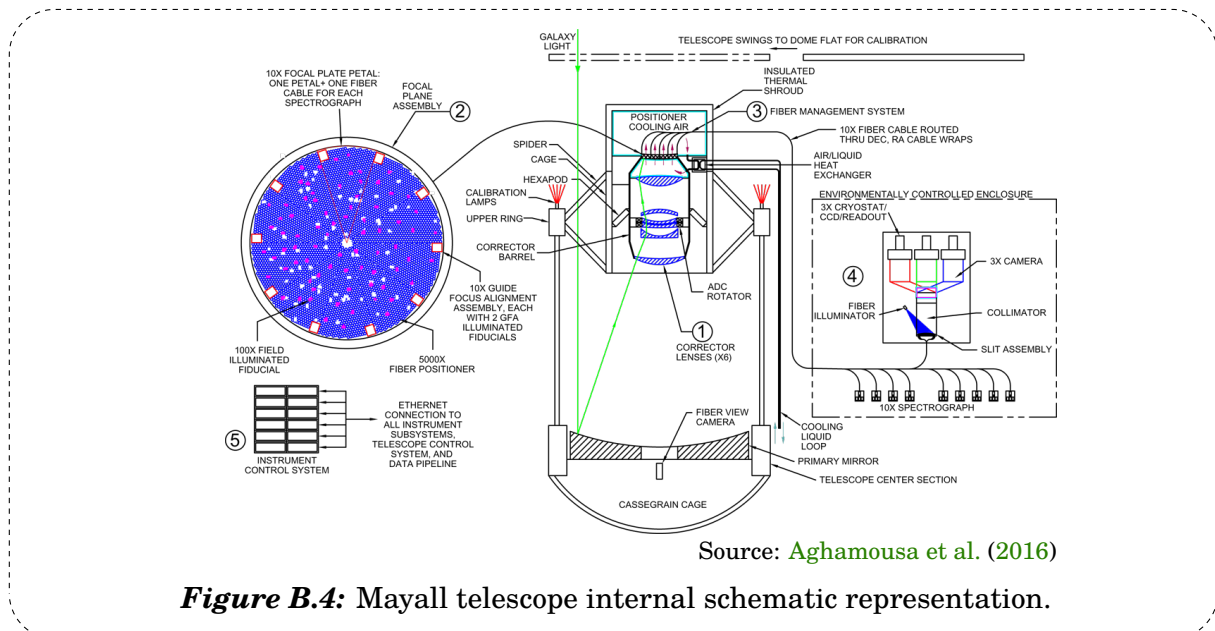
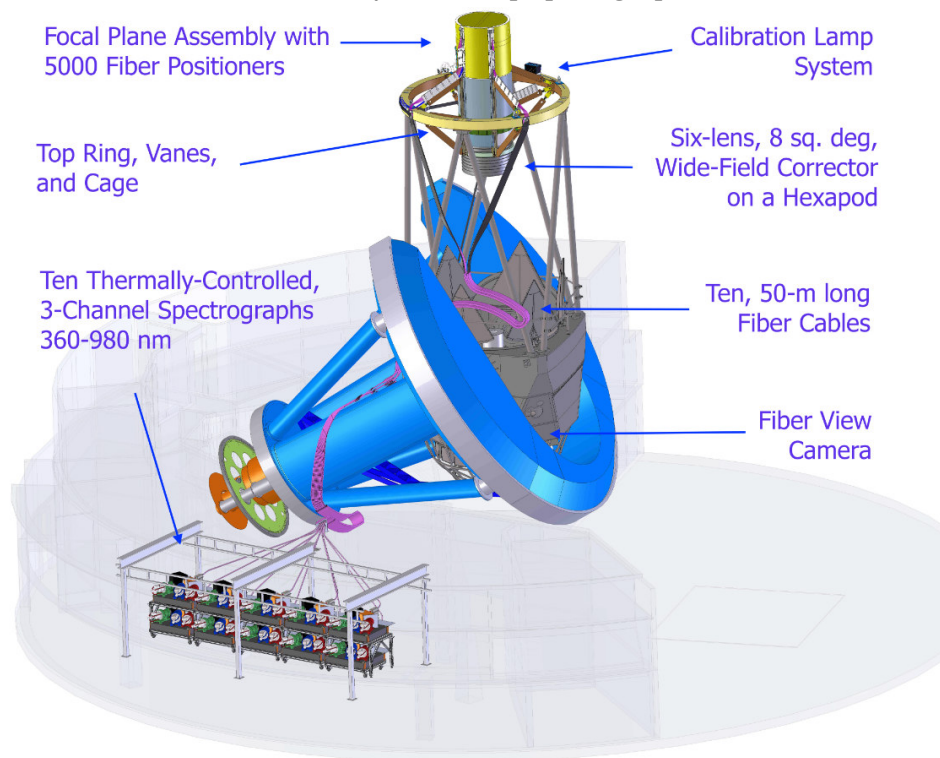


**Figure B.4:** Mayall telescope internal schematic representation.





(a) Mayall telescope photograph



(b) Mayall telescope schematic representation

Source: (a) KPNO/NOIRLab/NSF/AURA/P. Marenfeld (b) [Abareshi et al. \(2022\)](#)

**Figure B.5:** Mayall Telescope

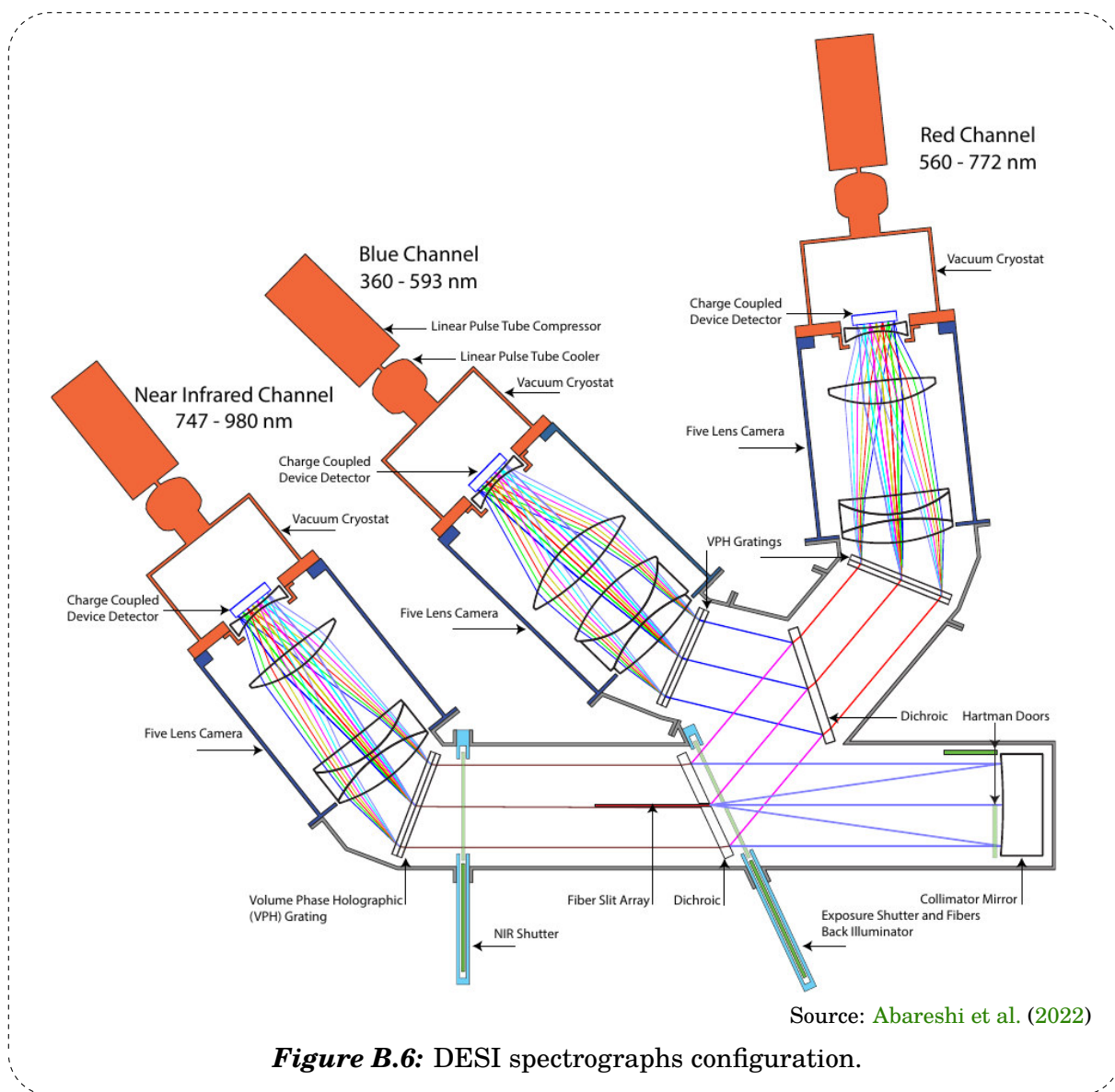
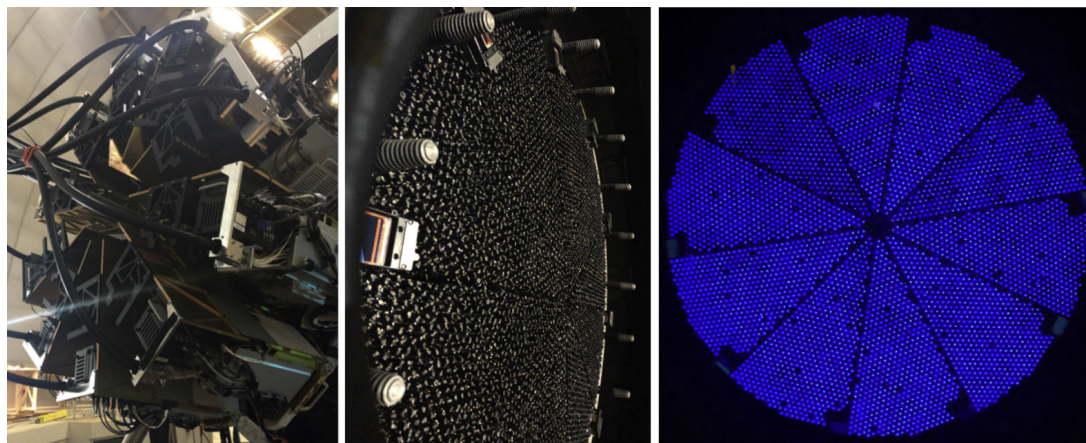
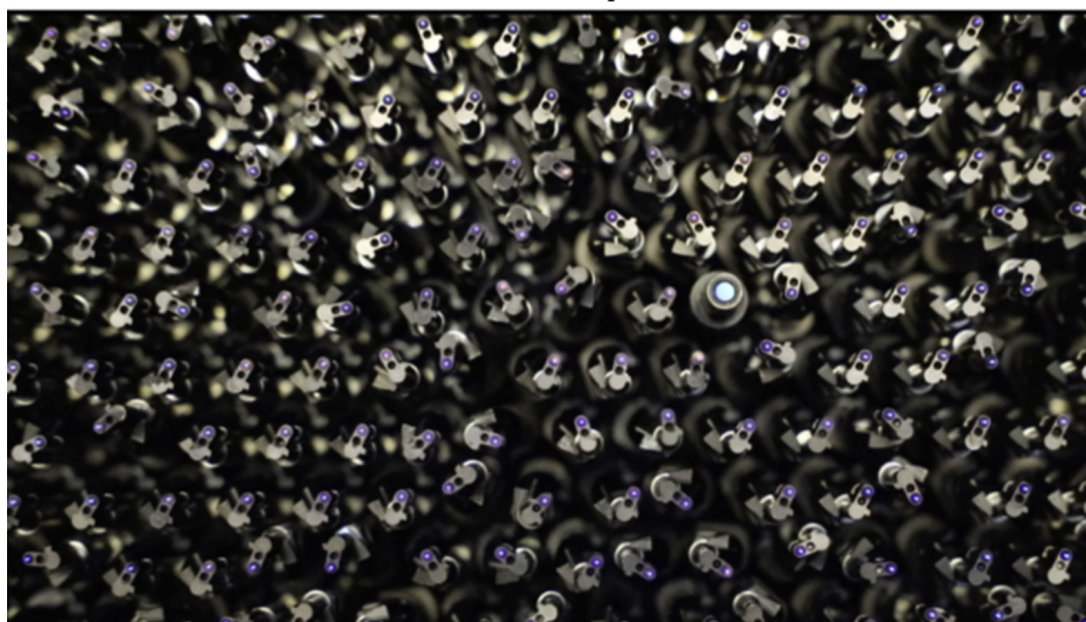


**Figure B.6:** DESI spectrographs configuration.



(a) DESI focal plane.



(b) DESI robotic fibers. In order to visualize how robotic fibers work see this footage of [NOIRLabAstro](#).

Source: (a) - (b) [Abareshi et al. \(2022\)](#)

**Figure B.7:** DESI focal plane system.





## DECLARATION

I declare the work discussed in this dissertation, submitted by me, Holman Daniel Quintero Salazar, entitled as *The 1-D Lyman alpha power spectrum from eBOSS and DESI EDR data sets*, is my own original work and represents the research carried out during my master's degree in astrophysics.

On the other hand, I acknowledge the use of [ChatGPT](#) to revise the grammar and orthography of the text considering English is not my mother language and, with the same purpose, improve the quality, comprehension and continuity of the text. In these terms, I also declare non-intention of committing plagiarism or any kind of academic integrity avoidance.



---

***Holman Daniel Quintero Salazar***

March 21, 2024



**Universidad de Guanajuato**  
Campus Guanajuato  
División de Ciencias Naturales y Exactas

**Comité Académico**  
**Posgrado en Ciencias (Astrofísica)**  
**Presente**

Me permito informar a ustedes que después de haber revisado la tesis titulada:

The 1-D Lyman alpha power spectrum from eBOSS and DESI EDR data sets

Presentada por el estudiante: Holman Daniel Quintero Salazar

Considero que: 

Si	X	No	
----	---	----	--

 reúne los méritos necesarios para obtener el grado de:

( ) **DOCTOR** ( X ) **MAESTRO EN CIENCIAS (ASTROFÍSICA)**

Justificación académica del voto\*:

Aunque encontré el inglés de nivel aceptable, tengo tres comentarios importantes sobre la presentación del trabajo: 1) la tesis falta un Resumen, "Abstract", 2) el texto deberá ser más conciso y directo, 3) las figuras deberán ser acompañadas de más explicaciones en el texto mismo. Después de discutir con el estudiante sobre estos puntos, él se comprometió a cambiar el texto siguiendo las sugerencias que yo indique. Otro comentario que yo hice fue que la interpretación física, quiere decir, el significado de los resultados encontrados no estaba suficientemente discutida. Del otro lado, como la meta de esta tesis es más bien a un nivel técnico, el cual consiste en aplicar y probar un método complejo de análisis usando nuevos datos de alta resolución, puedo concluir que de este punto de vista la tesis está completa y por lo tanto lista para ser defendida.

Atentamente,

Dr. Roger Coziol

Grado, nombre completo y firma

Profesor titular A, Departamento de Astronomía, Universidad de Guanajuato

Adscripción (institución de trabajo)

Guanajuato, 26 de enero 2024

Lugar y fecha de elaboración

Elaboró: LPSM  
31/01/2018

\* Puede exceder una página, si necesario



# Universidad de Guanajuato

Campus Guanajuato

División de Ciencias Naturales y Exactas

## Comité Académico Posgrado en Ciencias (Astrofísica) P r e s e n t e

Me permito informar a ustedes que después de haber revisado la tesis de maestría titulada:

**“The 1-D Lyman alpha power spectrum from eBOSS and DESI EDR data set”**

Presentada por: **Lic. Holman Daniel Quintero Salazar**

Considero que: 

Si	X	No	
----	---	----	--

 reúne los méritos necesarios para obtener el grado de:

### **MAESTRA EN CIENCIAS (ASTROFÍSICA)**

Justificación Académica del Voto:

En mi opinión la tesis está completa, ya que incluye toda la información necesaria y suficiente para el entendimiento de los resultados centrales de la misma.

La tesis presenta los resultados de los censos de eBOSS y de DESI EDR. También se mencionando que la principal aportación de esta tesis es la determinación de 1-D Lyman alpha power spectrum.

Por lo tanto, considerando que la tesis de Maestría en cuestión cumple con los requisitos necesarios, recomiendo que se proceda con los trámites requeridos para ser defendida ante el Comité de Sinodales.

A t e n t a m e n t e

Dr. Juan Pablo Torres Papaqui  
Grado, Nombre completo y firma

Departamento de Astronomía, DCNE, CG, UG  
Adscripción

Guanajuato, Guanajuato a 30 de enero de 2024  
Fecha



**Universidad de Guanajuato**  
Campus Guanajuato  
División de Ciencias Naturales y Exactas

**Comité Académico**  
**Posgrado en Ciencias (Astrofísica)**  
**Presente**

Me permito informar a ustedes que después de haber revisado la tesis titulada:

The 1-D Lyman alpha power spectrum from eBOSS and DESI EDR data sets

Presentada por el estudiante: Holman Daniel Quintero Salazar

Considero que: 

Si	X	No	<input type="checkbox"/>
----	---	----	--------------------------

 reúne los méritos necesarios para obtener el grado de:

( ) **DOCTOR** (X) **MAESTRO EN CIENCIAS (ASTROFÍSICA)**

Justificación académica del voto\*:

Es un trabajo completo en términos de repetir el estudio realizado por la colaboración BOSS sobre el espectro de potencias lineal con los datos del bosque del Lyman alfa, con todas las aristas posibles para explicar el resultado. Es cierto, que no se logra reproducir, pero se explica en detalle todas las metodologías para tratar de lograrlo. A su vez, incluye cálculos sobre los nuevos datos de DESI. El trabajo está en inglés, y aunque requiere de cierto pulido en el estilo, si demuestra conocimiento del idioma. Por otro lado, reúne los elementos necesarios para una tesis de Maestría.

Atentamente,

**PhD Gustavo Niz Quevedo**

Grado, nombre completo y firma

División de Ciencias e Ingenierías, Universidad de Guanajuato

Adscripción (institución de trabajo)

León, Gto. a 20 de Enero de 2024.

Lugar y fecha de elaboración

Elaboró: LPSM  
31/01/2018

\* Puede exceder una página, si necesario



**Universidad de Guanajuato**  
Campus Guanajuato  
División de Ciencias Naturales y Exactas

**Comité Académico**  
**Posgrado en Ciencias (Astrofísica)**  
**P r e s e n t e**

Me permito informar a ustedes que después de haber revisado la tesis titulada:

\_\_\_ **The 1-D Lyman alpha power spectrum from eBOSS and DESI EDR data sets** \_\_\_

Presentada por el estudiante: \_\_\_ **Holman Daniel Quintero Salazar** \_\_\_

Considero que: 

Si	x	No	
----	---	----	--

 reúne los méritos necesarios para obtener el grado de:

**( ) DOCTOR ( x ) MAESTRO EN CIENCIAS (ASTROFÍSICA)**

Justificación académica del voto\*:

This thesis deals with measuring the one-dimensional power spectrum of the Lyman-alpha forest using data from eBOSS and DESI. The work presents a complete re-analysis of the eBOSS DR14 and DESI EDR data samples. An exclusive measurement of the latest eBOSS sample (DR16) is also presented. The manuscript comprises five main chapters, a conclusion (chapter VII), and an introduction (chapter I).

Chapter II gives an excellent introduction to Cosmology, correctly covering various aspects, even some unrelated to Lyman-alpha, which offer a broad view of Cosmology. I found the level of this cosmological introduction largely higher than what I expected from a master's thesis. The comments I provided in this chapter are mainly oriented towards details and potential improvements, in particular on which cosmological probe can constrain which cosmological parameter.

Chapter III introduces the theoretical concepts revolving around the formation of the Lyman-alpha forest in the intergalactic medium. Once again, the thesis covers a wide range of topics and gives a progressive view of the Lyman-alpha forest, from AGN to forest formation, passing by radiative transfer physics. This chapter finishes with a description of the P1D, the main topic of this thesis. It gives a good review of this measurement through historical context. My comments aim to improve this chapter, particularly regarding introducing FGPA and observational considerations.

Chapter IV concisely describes the two telescopes used in this study. In particular, a correct description of the improvements is highlighted. This description is ample enough for the work presented next.

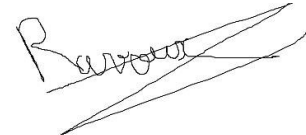
Chapter V starts to present the work realized in this master thesis. In particular, it gives a value-adding visualization of the catalogs and the spectra used to perform the studies. The data description is clear and precise and will be valuable for reproducibility. My comments mainly concern modifications and clarifications regarding the main P1D pipeline (picca).

Chapter VI presents a concise and precise description of the major results of the thesis. All the systematic ratios presented for DESI and eBOSS have a great added value. In my opinion, the main result of this chapter is verifying that the discrepancy between eBOSS and DESI is still present and complicated. It is very valuable for all the P1D analyses performed in DESI, now and in the future.

Finally, the conclusion (chapter VII) provides an excellent summary of the work and results. I suggest placing your work more firmly in the current P1D framework. It will help highlight your work even more.

In conclusion, the work presented in this thesis has a great added value because it provides a better understanding of the one-dimensional power spectrum measurement. In particular, your work allowed to test the new P1D pipeline used for DESI, to improve the reproducibility of eBOSS measurement, and to give new insights regarding the DESI/eBOSS discrepancy. I want to stress again that I found the presented work and the introduction to the topic to be of a quality that far exceeds what is expected of a master's thesis. I am giving Holman a very favorable opinion to defend his master's thesis. I would also be delighted to work with him in the DESI collaboration on new internal data, for which his skills would be highly appreciated and needed.

A t e n t a m e n t e,



**Dr. Corentin Ravoux**

Grado, nombre completo y firma

**Laboratoire de Physique de Clermont – CNRS /IN2P3, Clermont-Ferrand, France**

Adscripción (institución de trabajo)

**Clermont-Ferrand 18/01/24**

Lugar y fecha de elaboración

Elaboró: LPSM  
31/01/2018

\* Puede exceder una página, si necesario



